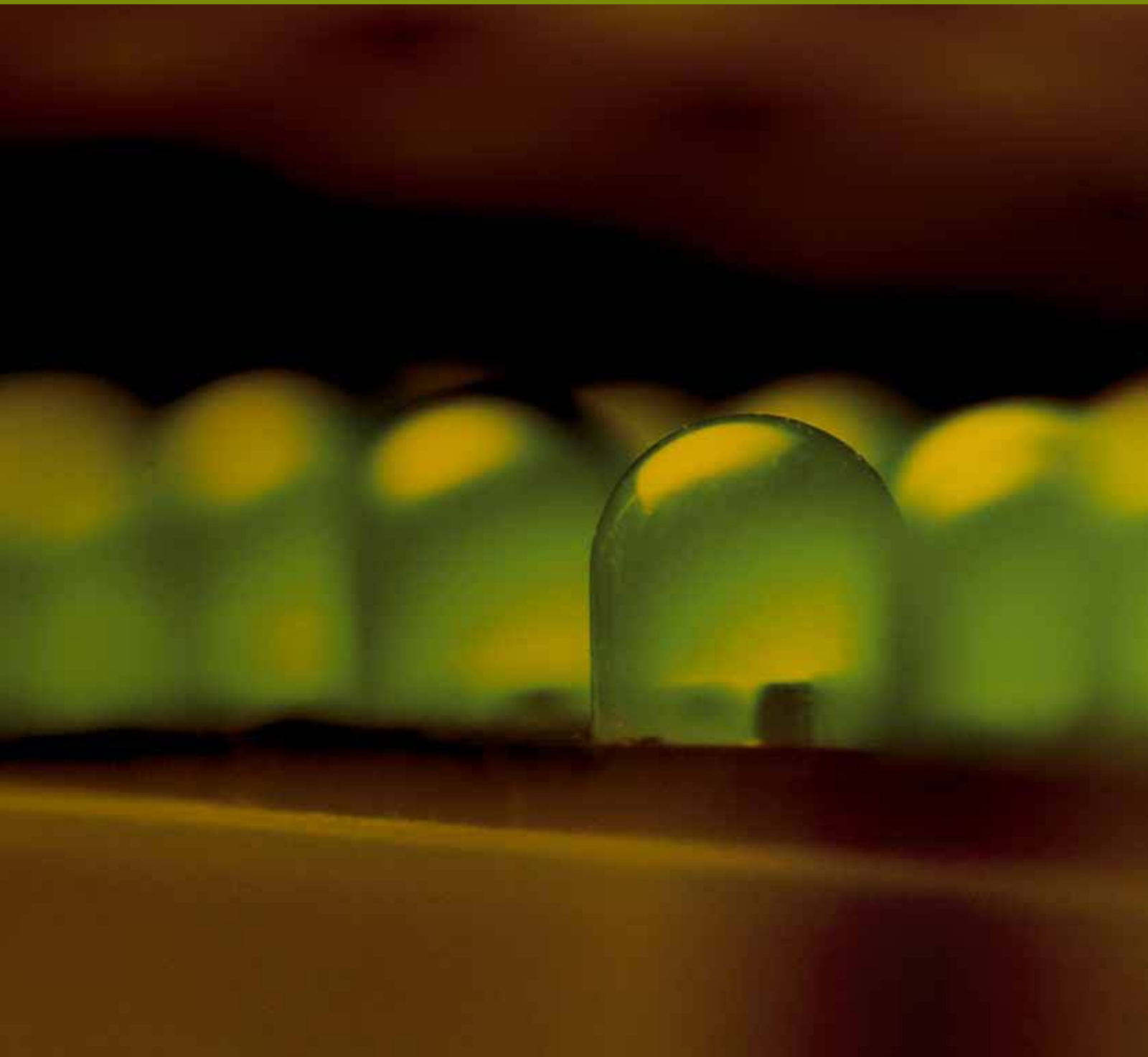


Advances in OptoElectronics

# Optofluidics for Lab-on-a-Chip

Guest Editors: Eric P. Y. Chiou, Aaron T. Ohta,  
Zhihong Li, and Steven T. Wereley





---

# **Optofluidics for Lab-on-a-Chip**

Advances in OptoElectronics

---

## **Optofluidics for Lab-on-a-Chip**

Guest Editors: Eric P. Y. Chiou, Aaron T. Ohta, Zhihong Li,  
and Steven T. Wereley



---

Copyright © 2012 Hindawi Publishing Corporation. All rights reserved.

This is a special issue published in "Advances in OptoElectronics." All articles are open access articles distributed under the Creative Commons Attribution License, which permits unrestricted use, distribution, and reproduction in any medium, provided the original work is properly cited.

## Editorial Board

Armin G. Aberle, Singapore  
Ralf Bergmann, Germany  
Xian An Cao, USA  
Wen-Chang Chen, Taiwan  
Philippe Goldner, France  
Jung Y. Huang, Taiwan  
Anthony J. Kenyon, UK

Yaomin Lin, USA  
Wenning Liu, USA  
Yalin Lu, USA  
Alfred Margaryan, USA  
Samir K. Mondal, India  
Satishchandra B. Ogale, India  
Adrian Podoleanu, UK

Richard Rizk, France  
Lucimara Stolz Roman, Brazil  
Jayanta K. Sahu, UK  
Somenath N. Sarkar, India  
Vasily Spirin, Mexico  
Chang Q. Sun, Singapore  
Yuqin Zong, USA

# Contents

**Optofluidics for Lab-on-a-Chip**, Eric P. Y. Chiou, Aaron T. Ohta, Zhihong Li, and Steven T. Wereley  
Volume 2012, Article ID 935325, 2 pages

***In Situ* Raman Spectroscopy of COOH-Functionalized SWCNTs Trapped with Optoelectronic Tweezers**, Peter J. Pauzauskie, Arash Jamshidi, Joseph M. Zaug, Sarah Baker, T. Y.-J. Han, Joe H. Satcher Jr., and Ming C. Wu  
Volume 2012, Article ID 869829, 4 pages

**An Optically Controlled 3D Cell Culturing System**, Kelly S. Ishii, Wenqi Hu, Swapnil A. Namekar, and Aaron T. Ohta  
Volume 2011, Article ID 253989, 8 pages

**Optoelectrofluidic Manipulation of Nanoparticles and Biomolecules**, Hyundoo Hwang and Je-Kyun Park  
Volume 2011, Article ID 482483, 13 pages

**Light-Driven Droplet Manipulation Technologies for Lab-on-a-Chip Applications**, Sung-Yong Park and Pei-Yu Chiou  
Volume 2011, Article ID 909174, 12 pages

**Fluorescence Detection 400–480 nm Using Microfluidic System Integrated GaP Photodiodes**, Dion McIntosh, Qiugui Zhou, Francisco J. Lara, James Landers, and Joe C. Campbell  
Volume 2011, Article ID 491609, 4 pages

**Electrodes for Microfluidic Integrated Optoelectronic Tweezers**, Kuo-Wei Huang, Sabbir Sattar, Jiang F. Zhong, Cheng-Hsu Chou, Hsiung-Kuang Tsai, and Pei-Yu Chiou  
Volume 2011, Article ID 375451, 10 pages

**Optoelectronic Heating for Fabricating Microfluidic Circuitry**, Gauvain Haulot and Chih-Ming Ho  
Volume 2011, Article ID 237026, 10 pages

**Assembly of Carbon Nanotubes between Electrodes by Utilizing Optically Induced Dielectrophoresis and Dielectrophoresis**, Pei-Fang Wu and Gwo-Bin Lee  
Volume 2011, Article ID 482741, 6 pages

**From Spheric to Aspheric Solid Polymer Lenses: A Review**, Kuo-Yung Hung, Po-Jen Hsiao, Fang-Gang Tseng, and Miao-Chin Wei  
Volume 2011, Article ID 197549, 14 pages

**Moldless PEGDA-Based Optoelectrofluidic Platform for Microparticle Selection**, Shih-Mo Yang, Tung-Ming Yu, Ming-Huei Liu, Long Hsu, and Cheng-Hsien Liu  
Volume 2011, Article ID 394683, 8 pages

## Editorial

# Optofluidics for Lab-on-a-Chip

**Eric P. Y. Chiou,<sup>1</sup> Aaron T. Ohta,<sup>2</sup> Zhihong Li,<sup>3</sup> and Steven T. Wereley<sup>4</sup>**

<sup>1</sup> Department of Mechanical and Aerospace Engineering, University of California, Los Angeles, CA, USA

<sup>2</sup> Department of Electrical Engineering, University of Hawaii at Manoa, Honolulu, HI, USA

<sup>3</sup> National Key Laboratory of Science and Technology on Micro/Nano Fabrication, Institute of Microelectronics, Peking University, Beijing, China

<sup>4</sup> Birck Nanotechnology Center, Purdue University, West Lafayette, IN, USA

Correspondence should be addressed to Eric P. Y. Chiou, [pychiou@seas.ucla.edu](mailto:pychiou@seas.ucla.edu)

Received 22 December 2011; Accepted 22 December 2011

Copyright © 2012 Eric P. Y. Chiou et al. This is an open access article distributed under the Creative Commons Attribution License, which permits unrestricted use, distribution, and reproduction in any medium, provided the original work is properly cited.

Optofluidic devices are gaining popularity due to the flexibility and ease of optical actuation and detection. These features are important for miniaturized lab-on-a-chip systems, which are often tricky to interface with larger benchtop equipment. Droplets, fluids, and particles can be manipulated using optofluidic devices. Simply adjusting the optical source can often reconfigures the type of manipulation, making optofluidics very adaptable compared to other methods. One unique feature of this special issue is its focus on indirect optical manipulation methods, in which light energy is used to trigger electric field, generate heat, or trigger rapidly expanding bubbles to achieve various manipulation functions, instead of using direct optical forces.

“*Light-driven droplet manipulation technologies for lab-on-a-chip applications*” by S.-Y. Park and E. P. Y. Chiou reviews various optical methods for droplet manipulation. Digital microfluidics is quite popular due to the compartmentalization and reduced cross-contamination provided by individual droplets. “*Optoelectrofluidic manipulation of nanoparticles and biomolecules*” by H. Hwang and J.-K. Park reviews techniques that combine optical and electrical effects in fluidic environments for the manipulation of nanoparticles and biomolecules such as proteins and DNA.

“*Optoelectronic heating for fabricating microfluidic circuitry*” by G. Haulot and C.-M. Ho demonstrates the formation of microfluidic channels by using optoelectronic heaters to melt frozen liquids. This can potentially be used to

create fluidic structures on demand. “*Moldless PEGDA-based optoelectrofluidic platform for microparticle selection*” by S.-M. Yang et al. also presents a method for forming microfluidic channels; in this case, using UV-initiated polymerization for creating channels on an optoelectronic device designed to select individual microbeads.

Along with these papers of this issue, other papers involve dielectrophoresis and optically induced dielectrophoresis. The paper by P.-F. Wu and G.-B. Lee uses these two forces to arrange carbon nanotubes between electrodes, towards the goal of creating carbon nanotube sensors. The paper by P. J. Pauzauskie et al. also uses optically induced dielectrophoresis to trap nanotubes, which are detected *in situ* using Raman spectroscopy. The paper by K.-W. Huang et al. presents transparent electrodes that can be used to integrate devices for optically induced dielectrophoresis with microfluidic channels.

“*An optically controlled 3D cell culturing system*” by K. S. Ishii et al. uses optothermal heating to trigger a polymer phase transition that can be used to trap cells that are to be cultured. This can potentially be used to create cell cultures with minimal contamination. “*From spheric to aspheric solid polymer lenses: a review*” by K.-Y. Hung et al. presents methods for creating lenses for optical and optofluidic devices. The paper by D. McIntosh et al. demonstrates a microfluidic chip integrated with photodiode-based fluorescence detector that was used to detect the concentration of an antibiotic.

Together, the papers in this special issue cover a wide range of topics in the growing field of optofluidics.

*Eric P. Y. Chiou*  
*Aaron T. Ohta*  
*Zhihong Li*  
*Steven T. Wereley*

## Research Article

# In Situ Raman Spectroscopy of COOH-Functionalized SWCNTs Trapped with Optoelectronic Tweezers

Peter J. Pauzauskie,<sup>1,2</sup> Arash Jamshidi,<sup>3</sup> Joseph M. Zaugg,<sup>1</sup> Sarah Baker,<sup>1</sup> T. Y.-J. Han,<sup>1</sup> Joe H. Satcher Jr.,<sup>1</sup> and Ming C. Wu<sup>3</sup>

<sup>1</sup>Chemical Sciences Division, Lawrence Livermore National Laboratory, 7000 East Avenue L-231, Livermore, CA 94551, USA

<sup>2</sup>Department of Materials Science and Engineering, University of Washington, Seattle, WA 98195, USA

<sup>3</sup>Department of Electrical Engineering, University of California, Berkeley, CA 94720, USA

Correspondence should be addressed to Peter J. Pauzauskie, peterpz@uw.edu

Received 2 May 2011; Revised 2 November 2011; Accepted 16 November 2011

Academic Editor: Eric Pei Yu Chiou

Copyright © 2012 Peter J. Pauzauskie et al. This is an open access article distributed under the Creative Commons Attribution License, which permits unrestricted use, distribution, and reproduction in any medium, provided the original work is properly cited.

Optoelectronic tweezers (OETs) were used to trap and deposit aqueous dispersions of carboxylic-acid-functionalized single-walled carbon nanotube bundles. Dark-field video microscopy was used to visualize the dynamics of the bundles both with and without virtual electrodes, showing rapid accumulation of carbon nanotubes when optical virtual electrodes are actuated. Raman microscopy was used to probe SWCNT materials following deposition onto metallic fiducial markers as well as during trapping. The local carbon nanotube concentration was observed to increase rapidly during trapping by more than an order of magnitude in less than one second due to localized optical dielectrophoresis forces. This combination of enrichment and spectroscopy with a single laser spot suggests a broad range of applications in physical, chemical, and biological sciences.

## 1. Introduction

One persistent challenge in molecular sensing is the enriching of candidate analytes to concentrations high enough for detection. Optoelectronic tweezers (OET) recently have been used as a versatile platform for trapping objects such as polystyrene spheres, living cells [1], and solid-state nanowires [2], and both [3] single- and [4] multi-walled samples of carbon nanotubes using 100,000x less optical power than single-beam laser traps. Based on a combination of dielectrophoresis and optical image patterning, OET has the unique capability of massively parallel localization of organic and inorganic nanoscale structures for both direct visualization and spectroscopic characterization. In this paper, we use carboxylic-acid- (COOH-) functionalized single-walled carbon nanotubes as a model system to demonstrate analyte enrichment by over an order of magnitude with a low-power OET trapping laser that serves simultaneously as a Raman spectroscopic probe.

## 2. Materials and Methods

**2.1. Carbon Nanotube Sample Preparation.** COOH-functionalized carbon nanotubes have been used as a surfactant-free alternative for aqueous SWCNT suspensions, with the hydrophilic COOH-surface functional groups serving as a means to suspend the nanotubes on polar solvents such as water [5]. In this work, COOH functionalized SWCNTs (P3, Carbon Solutions, Inc., ~4 atomic % COOH-functionalization) were dispersed as made in Milli-Q deionized water, bath-sonicated for 30 min, and centrifuged for 30 min at 16,000 g to remove large bundles and other metallic catalyst particles yielding a semitransparent solution.

**2.2. Carbon Nanotube Sample Characterization.** Transmission electron microscopy (JEOL CM-300) and atomic force microscopy (Veeco) were used to characterize the physical dimensions for the nanotube bundles. Atomic force microscopy measurements provide a diameter distribution

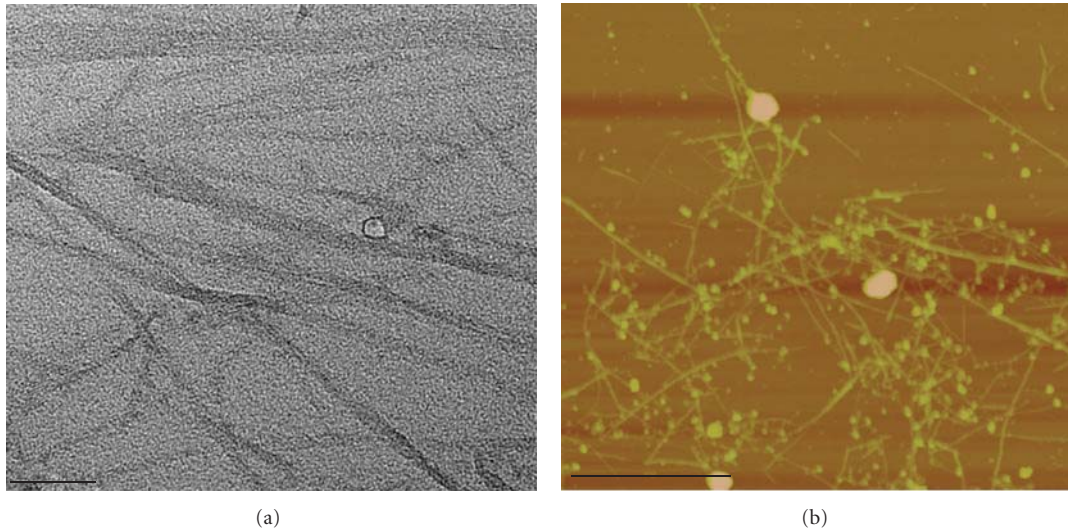


FIGURE 1: Characterization of COOH-functionalized SWCNTs used in this study. (a) Bright-field transmission electron micrograph. Scale bar = 50 nm. (b) Atomic force micrograph of SWCNTs on an aminopropylsilane-coated mica wafer. Scale bar = 1  $\mu\text{m}$ .

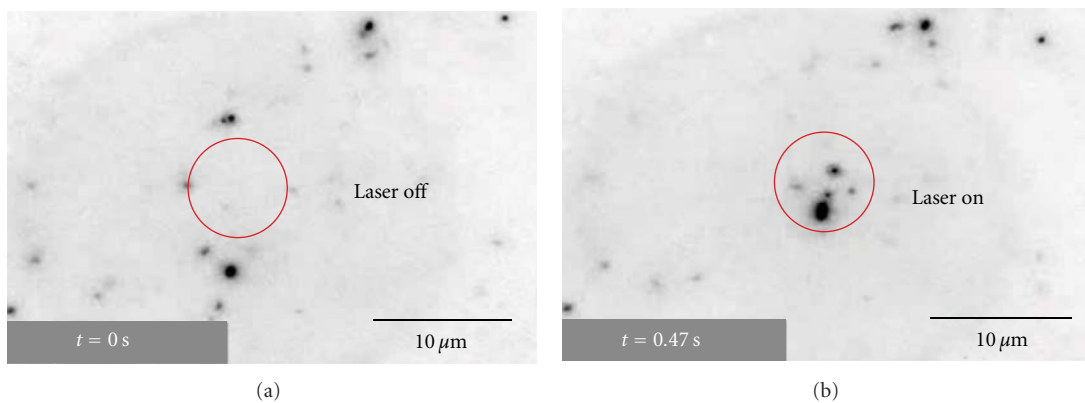


FIGURE 2: Dark-field EMCCD video microscopy of optoelectronic trapping of COOH-SWCNTs with laser off (a) and on (b) at an AC bias of 15 Vpp, 100 kHz. Images are inverted to enhance visibility of faint light scattering from SWCNT bundles. The laser line ( $\text{Ar}^+$ , 488 nm) is blocked by a holographic notch filter.

for the carbon nanotube bundles ranging from 2 to 11 nm, and lengths ranging from 0.1 to 2  $\mu\text{m}$  (Figures 1(a) and 1(b)), with a mean bundle diameter of  $6.4 \pm 2.4$  nm.

**2.3. Dark-Field Imaging with Optoelectronic Tweezers.** OET chambers were fabricated as reported previously [1], and images were collected during trapping with a Nikon Eclipse LV150 microscope equipped with long working distance dark-field objective lenses. Dark-field optical microscopy was used [6] to image aqueous suspensions of SWCNT bundles with a video-rate, thermoelectrically cooled, back-illuminated electron multiplying charge-coupled device camera (Andor, iXon). Standard chamber depths were fixed with double-sided adhesive tape with a standard thickness measured at 75 microns with a hand-held micrometer. During darkfield imaging, the trapping was performed with an argon-ion laser using the 488 nm emission line. The laser

power was measured to be 100  $\mu\text{W}$  focused to a spot size of 5 microns. The laser spot is filtered from the dark-field image using a holographic notch filter.

**2.4. Raman Microscopy.** Raman measurements were made with the 632.8 nm line of a helium-neon laser. Laser light was focused onto samples using a long working distance 20x near-IR corrected apochromatic objective lens (Mitutoyo). Scattered light was collected using the same objective and was focused onto a pinhole (to improve spatial resolution) before being collimated and directed into the spectrometer. A holographic filter (Kaiser Optics) was used to reject elastically scattered laser light. The spectrometer was a 0.3 m Jobin Yvon LabRam system equipped with 1,200 lines/mm and 1,800 lines/mm gratings. The detector was an LN<sub>2</sub>-cooled CCD (Roper Scientific). The system was calibrated

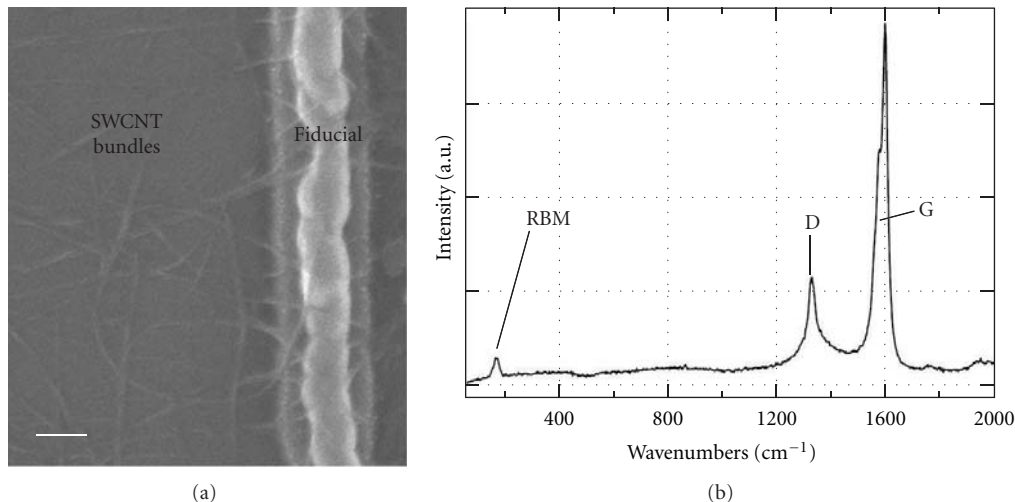


FIGURE 3: *Ex situ* characterization of COOH-SWCNTs following deposition with optoelectronic tweezers at high peak-to-peak voltages. (a) SEM image of SWCNT bundles deposited next to a Ti/Au fiducial marker. Scale bar = 100 nm. (b) Raman spectrum of deposited SWCNT bundles showing radial breathing mode (RBM), D, and G bands; a-Si background subtracted.

using a neon lamp. In all experiments, laser power was measured with a hand-held power meter.

### 3. Results and Discussion

When a 15 V<sub>pp</sub>, 100 kHz trapping voltage is applied across the OET chamber, the SWCNTs are observed to move away from one another (Figure 2(a)) due to repulsive, in-phase dipole-dipole interactions. When the trapping laser is turned on, SWCNT bundles are observed to migrate into the laser spot (Figure 2(b)), agreeing with previous reports of positive dielectrophoresis forces for metallic SWCNTs [7] as well as with recent calculations for MWCNTs predicting forces in the range of piconewtons [4]. At high trapping voltages (20 V<sub>pp</sub>, 100 kHz), the SWCNTs are observed to attach irreversibly to the a-Si surface. Electron beam lithography is used to pattern a grid of metallic fiducial markers (20 nm Ti, 50 nm Au) on top of the polished a-Si layer, which are then used to locate regions on the OET surface following Raman deposition experiments. Using scanning electron microscopy (SEM) (Figure 3(a)) and micro-Raman (Figure 3(b)) for *ex situ* characterization confirms that the deposited structures are indeed SWCNT bundles.

Single-beam laser tweezers have been used previously for three-dimensional trapping [8, 9], and Raman characterization [10] of SWCNT suspensions; however, they typically require several milliwatts of power to produce electric field gradients sufficient for trapping. Confocal micro-Raman measurements may also be performed with OET in an upright backscattering configuration. Generally, several hundred  $\mu\text{W}$  from the polarized 632.8 nm line of a CW He:Ne laser (Figure 4(a)) are focused to an area of  $\sim 75 \mu\text{m}^2$ , yielding a maximum local irradiance of  $< 500 \text{ W/cm}^2$ , which is more than sufficient to actuate the OET virtual trapping electrodes while simultaneously providing enough inelastically scattered photons for Raman

spectroscopy. The focal point is positioned in the chamber with a motorized translation stage, using the Raman signal of the a-Si as a means of ensuring that the Raman focal volume coincides directly with the OET-trapping volume.

When Raman spectra are taken from the COOH-SWCNT dispersions, signal levels are low due to both the low concentration of tubes in solution and defects within the carbon lattice that decrease the inelastic scattering cross-section [11]. Raman spectra are acquired both with and without the OET-trapping voltage (6 V<sub>pp</sub>, 100 kHz) at both the a-Si/fluid interface (Figure 4(a)) and  $\sim 20 \mu\text{m}$  above the a-Si. Once the trapping voltage is applied, the in-plane  $E_{2g}$  stretching mode at  $1591 \text{ cm}^{-1}$  collected from the a-Si/fluid interface shows an 18-fold increase based on a ratio of integrated  $1591 \text{ cm}^{-1}$  peak areas. The enhancement exists both when compared to the case with the trapping voltage off, and with the voltage on, but with the focus  $\sim 20 \mu\text{m}$  above the a-Si surface (Figure 4(b)). The signal enhancement is reversible, depending only on whether the laser is present to generate inhomogeneous lateral electric trapping fields. When the AC field is turned off, the signal relaxes to the background level, suggesting that trapped SWCNTs become free to diffuse through solution in agreement with dark-field images (Figure 2).

### 4. Conclusion

In conclusion, we report here the first demonstration of simultaneous trapping and micro-Raman spectroscopy of SWCNT materials with OET, providing a versatile means for locally concentrating dilute samples, therefore, enhancing the detected Raman signals by over an order of magnitude. This signal enrichment can potentially be combined with other Raman enhancement techniques such as surface-enhanced Raman spectroscopy (SERS) to create more sensitive Raman probes. OET is unique in that a few hundred

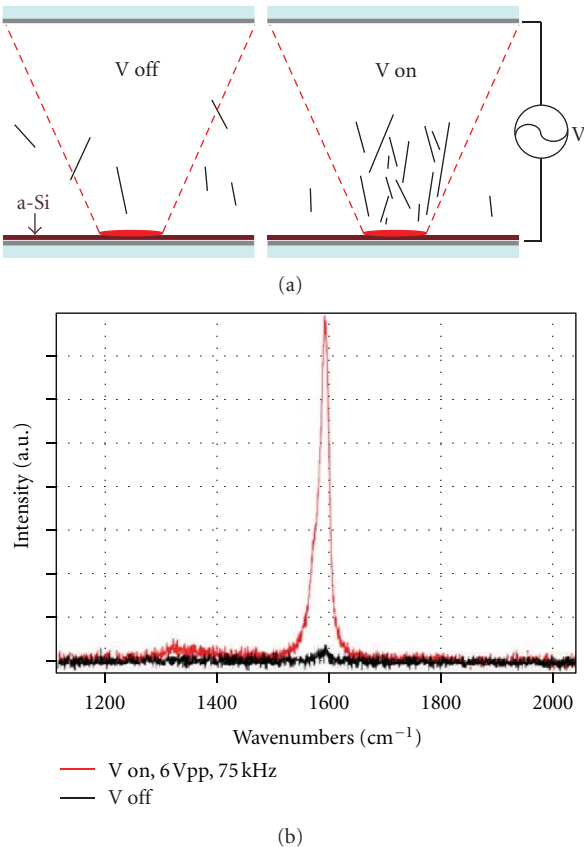


FIGURE 4: Enhanced Raman signal from COOH-SWCNTs trapped with OET. (a) Schematic of micro-Raman experiment and (b) Raman spectrum ( $480 \text{ W/cm}^2$ , 60 s) with (red) and without (black) OET-trapping bias of 6 Vpp, 75 kHz.

micro-Watt laser intensities can be used to enrich the local analyte concentration while simultaneously producing inelastically scattered photons for sample characterization. This combination of enrichment and spectroscopy with a single laser spot suggests a broad range of applications in physical, chemical, and biological sciences. Finally, these results will help guide future experiments with isolated single-walled carbon nanotubes.

## Acknowledgments

P. J. Pauzauskie thanks the LLNL for a Lawrence Fellowship. This work was supported in part by the NIH Roadmap for Medical Research (Grant no. PN2 EY018228) and DARPA. The authors thank Hsan-Yin Hsu, Justin K. Valley, Steven L. Neale, and Marcus Worsley for valuable assistance. This work was performed under the auspices of the U.S. Department of Energy by Lawrence Livermore National Laboratory under Contract no. DE-AC52-07NA27344.

## References

- [1] P. Y. Chiou, A. T. Ohta, and M. C. Wu, "Massively parallel manipulation of single cells and microparticles using optical images," *Nature*, vol. 436, no. 7049, pp. 370–372, 2005.

- [2] A. Jamshidi, P. J. Pauzauskie, P. J. Schuck et al., "Dynamic manipulation and separation of individual semiconducting and metallic nanowires," *Nature Photonics*, vol. 2, no. 2, pp. 86–89, 2008.
- [3] M. W. Lee, Y. H. Lin, and G. B. Lee, "Manipulation and patterning of carbon nanotubes utilizing optically induced dielectrophoretic forces," *Microfluidics and Nanofluidics*, vol. 8, no. 5, pp. 609–617, 2010.
- [4] P. J. Pauzauskie, A. Jamshidi, J. K. Valley, J. H. Satcher, and M. C. Wu, "Parallel trapping of multiwalled carbon nanotubes with optoelectronic tweezers," *Applied Physics Letters*, vol. 95, no. 11, Article ID 113104, 2009.
- [5] K. Balasubramanian and M. Burghard, "Chemically functionalized carbon nanotubes," *Small*, vol. 1, no. 2, pp. 180–192, 2005.
- [6] Z. Yu and L. Brus, "Rayleigh and Raman scattering from individual carbon nanotube bundles," *The Journal of Physical Chemistry B*, vol. 105, no. 6, pp. 1123–1134, 2001.
- [7] R. Krupke, F. Hennrich, H. von Löhnhausen, and M. M. Kappes, "Separation of metallic from semiconducting single-walled carbon nanotubes," *Science*, vol. 301, no. 5631, pp. 344–347, 2003.
- [8] S. Tan, H. A. Lopez, C. W. Cai, and Y. Zhang, "Optical trapping of single-walled carbon nanotubes," *Nano Letters*, vol. 4, no. 8, pp. 1415–1419, 2004.
- [9] O. M. Maragò, P. H. Jones, F. Bqnaccorso et al., "Femtonewton force sensing with optically trapped nanotubes," *Nano Letters*, vol. 8, no. 10, pp. 3211–3216, 2008.
- [10] T. Rodgers, S. Shoji, Z. Sekkat, and S. Kawata, "Selective aggregation of single-walled carbon nanotubes using the large optical field gradient of a focused laser beam," *Physical Review Letters*, vol. 101, no. 12, Article ID 127402, 2008.
- [11] R. Saito, M. S. Dresselhaus, and G. Dresselhaus, *Physical Properties of Carbon Nanotubes*, Imperial College Press, London, UK, 1998.

## Research Article

# An Optically Controlled 3D Cell Culturing System

**Kelly S. Ishii, Wenqi Hu, Swapnil A. Namekar, and Aaron T. Ohta**

*Department of Electrical Engineering, University of Hawaii at Manoa, 2540 Dole Street, Holmes Hall 483, Honolulu, HI 96822, USA*

Correspondence should be addressed to Aaron T. Ohta, [aohta@hawaii.edu](mailto:aohta@hawaii.edu)

Received 2 May 2011; Revised 25 August 2011; Accepted 12 September 2011

Academic Editor: Eric Pei Yu Chiou

Copyright © 2011 Kelly S. Ishii et al. This is an open access article distributed under the Creative Commons Attribution License, which permits unrestricted use, distribution, and reproduction in any medium, provided the original work is properly cited.

A novel 3D cell culture system was developed and tested. The cell culture device consists of a microfluidic chamber on an optically absorbing substrate. Cells are suspended in a thermoresponsive hydrogel solution, and optical patterns are utilized to heat the solution, producing localized hydrogel formation around cells of interest. The hydrogel traps only the desired cells in place while also serving as a biocompatible scaffold for supporting the cultivation of cells in 3D. This is demonstrated with the trapping of MDCK II and HeLa cells. The light intensity from the optically induced hydrogel formation does not significantly affect cell viability.

## 1. Introduction

Drug- and cell-based therapies are being explored for many medical conditions [1, 2], including heart disease [3], cancer [4–6], and diabetes [7–9]. However, the process of identifying suitable treatments is long and complicated. The time from drug discovery to Food and Drug Administration approval is usually 10 to 15 years [10], costing from \$800 million to \$1 billion [11]. Numerous processes contribute to this long lead time, including the testing of drug compounds, drug effects, and drug safety. These tests are conducted in order of increasing complexity: biochemical assays, cell-based assays, animal models, and then clinical trials. It is possible to simplify this testing procedure with improved cell-based assays that could enable the reduction or elimination of animal testing, reducing the time and cost of developing new drugs.

Cell-based drug assays can be improved by culturing cells *in vitro* that remain highly representative of their *in vivo* counterparts, resulting in more realistic testing results, mitigating the risks and costs associated with testing on live subjects, while accelerating the development process. Recent evidence suggests that 3D cultures are more representative of cellular behavior as compared to 2D cultures [12], as 3D cultures more closely simulate *in vivo* cellular microenvironments [13]. For example, cancerous cells grown in 3D

cultures are more resistant to drugs versus cells in 2D cultures [14, 15].

3D cultures have been developed where cells are seeded on porous biomaterials [10, 15, 16] or scaffold-like microstructures [17–19]. Integration of these materials in microfluidic systems can facilitate diffusive transfer of nutrients and waste and minimizes the use of materials and reagents, thereby lowering costs and increasing parallelization of culturing and testing [10, 20]. Thus, appropriately designed microdevices can greatly improve the predictive value of cell-based assays [21–25].

One remaining challenge for microfluidic culture systems is the culturing of specific individual cells. The isolation and culture of specific, individual, and potentially rare cells of interest, such as cancerous cells, can be used to test the effectiveness of drugs, which can lead to the development of treatments that are better tailored to their target. When isolating specific cells, it is desirable to simultaneously select the cells of interest and seed them into a 3D scaffold. This reduces unnecessary handling of the cells, saving time and money, while negating the question of how to recover the selected cells. Minimizing the manipulation required to arrive at the culturing stage also simplifies the equipment necessary to carry out the process.

Here, we demonstrate a microfluidic system that can isolate specific cells from a suspension and seed and culture

them in 3D structures. This system creates 3D hydrogel structures for cell culture using projected light patterns. Specific cells can be captured for homogeneous or heterogeneous 3D culturing while simultaneously creating the scaffolds necessary to support cell growth in 3D. The 3D hydrogel scaffolds are formed using a thermosensitive polymer instead of photoinitiated polymerization [18, 19, 21, 23, 24], which usually is irreversible. The hydrogel formation is reversible, allowing cultured cells to be easily harvested. In this paper, the details of this optically controlled 3D culturing system are presented, along with experimental results demonstrating the optically controlled formation of thermosensitive hydrogels, the trapping of micro-objects within hydrogels, the trapping of mammalian cells, and the testing of cell viability.

## 2. Optically Controlled 3D Cell Culturing System

Our cell culture system uses a device with an optically absorbing substrate that converts the optical energy of the light patterns into heat (Figure 1). This heat is used to trigger a sol-gel transition of a thermoresponsive hydrogel containing cells, allowing selective trapping of cells in a 3D matrix for culturing.

The thermoresponsive hydrogel used is composed of poly(*N*-isopropylacrylamide) (PNIPAAm). This biocompatible polymer dissolves readily in water at room temperature. However, if a PNIPAAm solution is heated above the lower critical solution temperature (LCST) of the PNIPAAm, the polymer undergoes a reversible sol-gel transition, resulting in the creation of a hydrogel [26–28]. As the LCST is approximately 32°C, PNIPAAm is a popular choice as a thermoresponsive polymer for use with cells and other bioparticles. Thus, PNIPAAm solutions are hydrogels at physiological temperatures but liquids at room temperature.

The optically generated heat in the culture device is sufficient to increase the temperature of the PNIPAAm solution above its LCST, thus inducing a sol-gel transition and forming a 3D hydrogel in the heated region. The dimensions of the hydrogel are determined by the heat distribution generated by the optical patterns, and the height of the microfluidic chamber. The height of the microfluidic chamber in these experiments was maintained at 50  $\mu\text{m}$  to ensure sufficient transport of nutrients and waste products into and out of the gels once cells are in culture.

A typical culturing procedure starts by mixing cells at a desired density with a PNIPAAm solution (Figure 2). The solution is introduced into the microfluidic chamber. Optical patterns are then used to form hydrogels around the cells of interest. After trapping the desired cells, the remaining sample is flushed by flowing buffer solution through the device while keeping the gelled region above the LCST. At this point, the optical patterns can be turned off, as long as the device itself is kept above the LCST. The cells can then be cultured. The microfluidic chamber is designed to be removable, providing direct access to the hydrogel, and

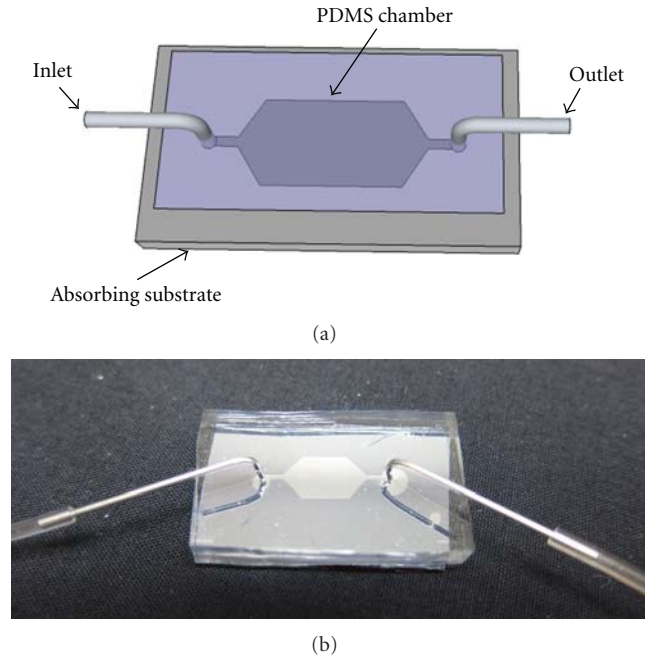


FIGURE 1: (a) Schematic representation of the 3D cell culture device. A microfluidic chamber is imprinted on polydimethylsiloxane (PDMS) using soft lithography and reversibly bonded to an optically absorbent substrate. Tubing is connected at the inlet and outlet ports. Fluid is introduced at the inlet and is drawn through the device by applying negative pressure at the outlet. (b) A prototype device is shown with fluidic tubing connected at the ports. In this design, the hexagonal chamber is approximately 9 mm  $\times$  5 mm; the PDMS piece and accompanying substrate are approximately 30 mm  $\times$  15 mm.

making subsequent culture steps more similar to that of a standard 3D culture.

## 3. Materials and Methods

**3.1. Thermoresponsive Polymer.** A thermoresponsive polymer solution that comprised 10% (w/v) PNIPAAm (Sigma-Aldrich, St. Louis, Mo, USA) dissolved in deionized (DI) water or phosphate-buffered saline (PBS) (ATCC, Manassas, Va, USA) was used in the experiments discussed in this paper.

**3.2. Cells.** Madin Darby Canine Kidney (MDCK II) epithelial cells and HeLa cells were cultivated in a standard 2D culture using Dulbecco's Modified Eagle Medium (DMEM) with 10% fetal bovine serum (FBS) and 1% penicillin streptomycin. The cells were incubated at 37°C in a humidified 95% air, 5% CO<sub>2</sub> environment. The cells were harvested using 0.25% Trypsin/0.53 mM EDTA and mixed into a solution of 10% (w/v) PNIPAAm in PBS for the experiments described here. Viability tests were performed using a LIVE/DEAD assay kit (Invitrogen, Carlsbad, Calif, USA) and fluorescent imaging.

**3.3. Experimental Setup.** The cell culture device is positioned on the stage of an upright microscope, on top of an

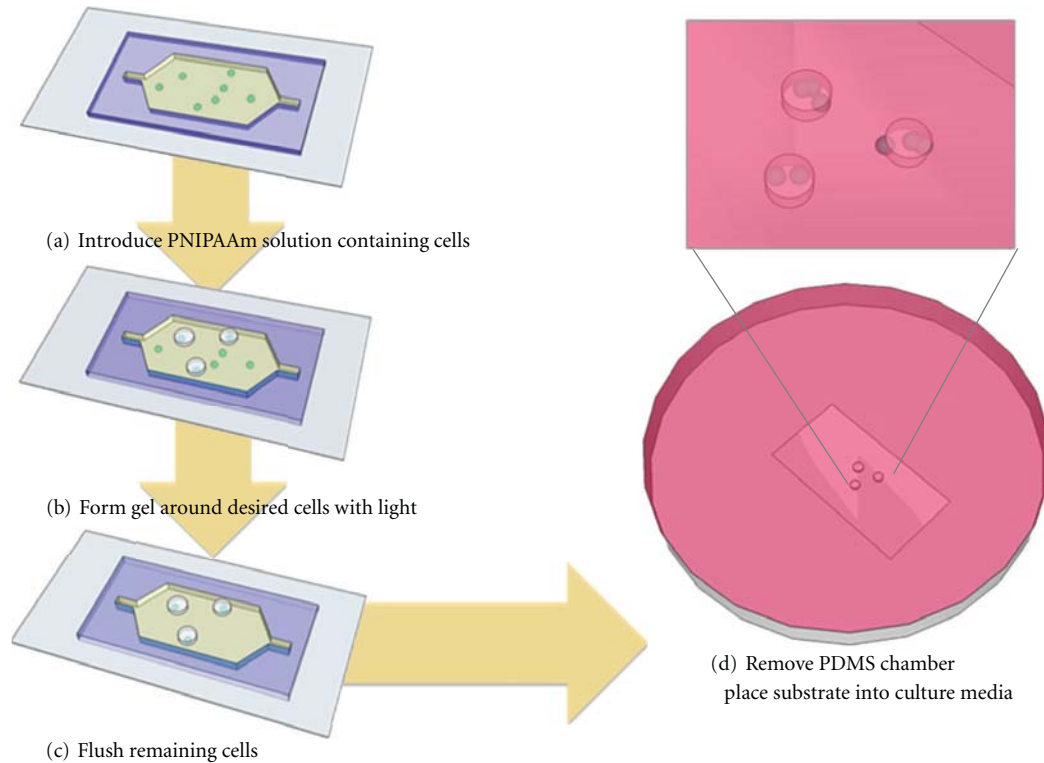


FIGURE 2: Optically controlled 3D culturing process. (a) The cell sample in hydrogel solution is introduced to the device chamber. (b) Desired cells are trapped in PNIPAAm hydrogel (cylindrical volume) using localized optical heating. (c) Undesired cells that remain in solution are flushed from the device. (d) While maintaining the hydrogel above the LCST, the PDMS chamber is removed, and the device substrate with the patterned 3D hydrogel is placed into culture media to allow cell growth.

indium tin oxide (ITO) thin-film heater. The ITO heater is used to warm the device above room temperature, but below the LCST, to facilitate the optically induced gelation. A CCD camera mounted on the microscope provides real-time visualization of the procedure. The thermoresponsive polymer solution containing the cell sample is introduced into the device.

Optical patterns are directed through a hole in the microscope stage to the device substrate. The light patterns are created by focusing the output of a commercial projector (Dell 2400MP) through a 10X objective lens, resulting in an average intensity of  $4.07 \text{ W/cm}^2$ . An alternate light source that can be used to cause gelation is a 635-nm, 10-mW diode laser. Irradiating the absorbing substrate results in localized heating within the device.

The 3D culture device consists of a  $50\text{-}\mu\text{m}$ -high PDMS microfluidic chamber reversibly bonded to an optically absorbent substrate (Figure 1). An inlet port and an outlet port are located at opposite ends of the chamber, and flushing is controlled by negative pressure-driven flow using an external syringe pump.

## 4. Experimental Results

**4.1. Device Characterization.** The temperature profile in the culture device was simulated using COMSOL Multiphysics (Figure 3). The heat source in this simulation is a  $100 \mu\text{m} \times$

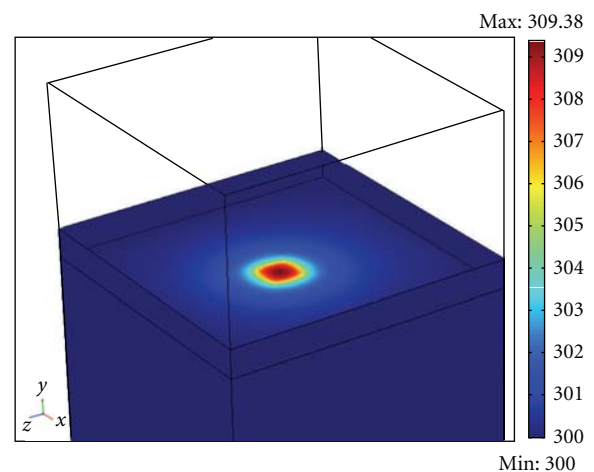


FIGURE 3: Simulated temperature (degrees Kelvin) in the culture device. In this model, two glass layers sandwich a  $100\text{-}\mu\text{m}$  thick layer of water. The heat flux is situated at the bottom of the water layer in a  $100 \mu\text{m} \times 100 \mu\text{m}$  square area.

$100 \mu\text{m}$ , representing a square optical pattern. The heat source is situated at the top surface of the lower glass layer, which corresponds to the location of the optically absorbent layer. This conversion of light to heat is an important parameter in determining the efficacy of the substrate and

ultimately the resolution of the gel that can be achieved. Thus, various light-absorbent substrates were developed and characterized. The materials used to fabricate the substrates were chosen on the basis that they were readily available as well as biocompatible. The primary substrate used consists of a 1.1-mm-thick glass slide coated with a 200-nm-thick layer of ITO and a 1- $\mu\text{m}$ -thick layer of amorphous silicon (a-Si). The a-Si layer absorbs near-infrared, visible, and UV light, converting it to heat. A simpler substrate was also tested, consisting of a 150- $\mu\text{m}$ -thick glass coverslip backed with a layer of black vinyl tape (3M Corp., St. Paul, Minn, USA). Additionally, absorbing polymeric substrates were created by mixing dark particles such as black mineral pigment and carbon black with PDMS.

In order to precisely select single, individual cells for culture, the hydrogel resolution needs to be optimized. While it is desirable to obtain the smallest hydrogel area necessary to fully encompass the cell, the area of hydrogel should also remain relatively constant over the short period of time between trapping and flushing steps. If the heated region of the substrate continues to spread from the point where the light pattern is aimed, the hydrogel region will continue to expand, potentially trapping additional, undesired cells in the immediate area. For this purpose, the various substrates were compared by measuring the area of the hydrogel while exposing the device to the smallest circular light pattern capable of producing gel within the first 30 seconds of exposure. First, the minimum optical pattern dimensions that produced gelling were determined for each substrate. The time point at which hydrogel initially appeared varied across the substrates. The area of the hydrogel was measured over an exposure time of 60 s to include the effects of continued hydrogel formation with time (Figure 4). The diameters of the circular optical patterns used for the different substrates were mineral pigment (450  $\mu\text{m}$ ), electrical tape on a glass coverslip (550  $\mu\text{m}$ ), carbon black (420  $\mu\text{m}$ ) and a-Si (580  $\mu\text{m}$ ). The a-Si substrate was used in the subsequent experiments presented here, as it made the microscope images within the microfluidic chamber clearer. The absorptive nature of the surface of other substrates hinders reflective microscopy, which was used in the experiments here. The ability to visualize the cells is crucial in differentiating anomalous cells from the bulk of a suspension, so the superior imaging qualities of the a-Si substrate made it easier to work with than the other substrates.

The resolution of this technique can be improved by replacing the computer projector with a laser operating in the near-infrared, visible, or UV wavelength range. Hydrogel formation using the computer projector light source is limited by the intensity of the light from the lamp in the projector. The relatively low intensity requires larger illuminated areas to create sufficient heat to trigger the PNI-PAAm gelation. Thus, the resolution of hydrogel formation was examined further using the a-Si substrate and a 635-nm, 10-mW diode laser as the optical source. The laser was focused down to a spot of approximately 108  $\mu\text{m}^2$ . The substrate was irradiated for 30 s at various laser powers, and the resulting hydrogel area was measured (Figure 5).

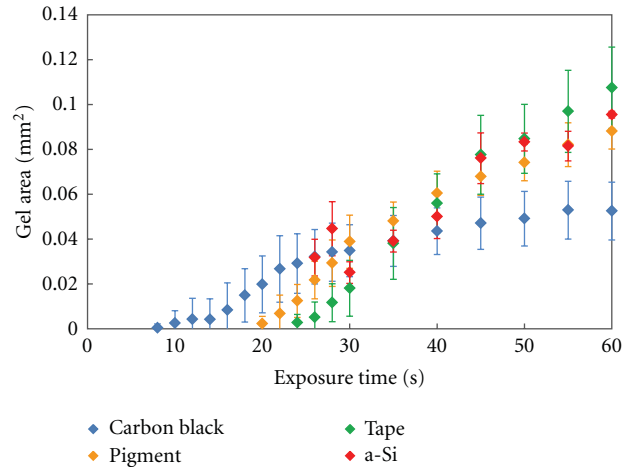


FIGURE 4: Hydrogel area versus time for various optically absorbent substrates. The optically smallest pattern that effectively produced gel was determined for each substrate, using the computer projector light source. The graph shows the average hydrogel area measured across five trials and the standard deviation for each. A two-minute delay between subsequent trials allowed sufficient time for the device to return to room temperature.

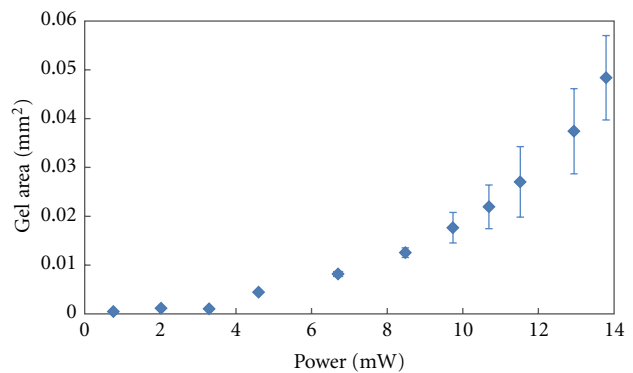


FIGURE 5: Hydrogel area as a function of power, using a 635-nm diode laser as the optical source. The area of the laser spot was approximately 108  $\mu\text{m}^2$ . The substrate was irradiated for a period of 30 seconds to generate each data point. The graph shows the average hydrogel area measured across five trials and the standard deviation of the measurements.

The smallest resultant gel area was 182  $\mu\text{m}^2$ . To remove the effect of accumulated substrate heating, measurement at each power level was performed at a different location in the microfluidic chamber. The gels formed with the laser have a smaller area than those produced using the computer projector. However, since the laser is focused into a single point, it does not provide as much flexibility as the projection of computer-drawn patterns. Thus, the trapping experiments utilized the computer projector setup although more flexibility would be possible by using holographic imaging or spatial light modulators, similar to those used in holographic optical tweezers [29].

**4.2. Microbead Trapping.** The capability of trapping specific objects in 3D hydrogels was demonstrated using polystyrene

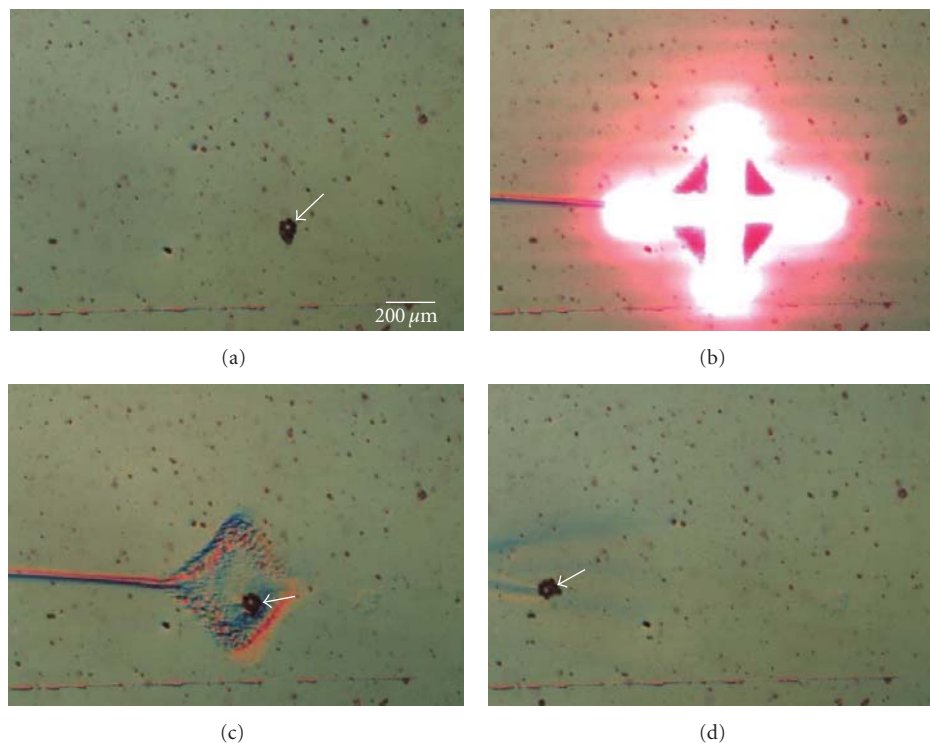


FIGURE 6: Trapping of 20- $\mu\text{m}$ -diameter polystyrene microbeads in an optically patterned hydrogel. The scale bar is 200  $\mu\text{m}$ . (a) A PNIPAAm solution containing 10- and 20- $\mu\text{m}$ -diameter microbeads was introduced into the microfluidic chamber. The solution is flowing from the right to the left at a linear flow rate of 100  $\mu\text{m}/\text{s}$ . A clump of beads was targeted for trapping, as indicated by the arrow. (b) An optical pattern is used to heat the substrate, causing a hydrogel to form in the illuminated area. (c) The hydrogel with the optical pattern removed, showing the trapped target particles. (d) Substrate cooling in the absence of optical heating reverses the trap, and the beads begin to flow away.

beads, which also served as model particles for cells. A group of 20- $\mu\text{m}$ -diameter polystyrene microbeads was selectively trapped from a solution containing 10- and 20- $\mu\text{m}$  beads using optically induced hydrogel formation (Figure 6). Here, polystyrene particles were added to the PNIPAAm solution and flowed through the microfluidic chamber at a linear flow rate of 100  $\mu\text{m}/\text{s}$ . A target was identified, consisting of a clump of beads (Figure 6(a)). An appropriate light pattern was activated to trigger hydrogel formation, trapping the target group of beads (Figures 6(b) and 6(c)). Other beads in the solution were diverted around the hydrogel formation. Switching off the light pattern allows the substrate temperature to decrease, reducing the amount of hydrogel. As the gel reverts back to its sol state, the trapped beads are released, and begin to wash away with the fluid flow (Figure 6(d)).

**4.3. Mammalian Cells.** The optically controlled culturing system was also tested with mammalian cells. Single- and multiple-cell trapping as well as parallel trapping were demonstrated with MDCK II cells. The cells were added to PNIPAAm/PBS solution, resulting in a cell density of approximately  $1 \times 10^5$  cells/mL and 10% (w/v) concentration of PNIPAAm. The MDCK II cells were selectively trapped using optically induced hydrogel formation (Figure 7). Initially, the cell solution was introduced into the microfluidic chamber, and target cells were selected (Figures 7(a) and 7(d)). Under

no-flow conditions, appropriate light patterns were activated to trigger hydrogel formation in the immediate surrounding area, trapping specific cells. Single cells can be trapped, (Figures 7(a)–7(c)) or multiple cells (Figures 7(d)–7(f)). Cells can be trapped in parallel by using multiple light patterns (Figure 7(e)). Cells that are not trapped are flushed by flowing PNIPAAm/PBS or buffer solution until the free cells are flushed away, leaving only the cells within the optically patterned gels (Figures 7(c) and 7(f)). At this point, the light patterns can be turned off as long as the device temperature is maintained above 32°C.

Cell viability tests on MDCK II and HeLa cells were performed immediately after the trapping procedure using a fluorescent LIVE/DEAD assay. The cells were suspended in 10% (w/v) PNIPAAm in PBS. The cells were irradiated with a circular light pattern 200  $\mu\text{m}$  in diameter for approximately 20 minutes while trapping and flushing took place (Figures 8(a) and 9(a)). Buffer solution was used to remove the cells not trapped in the gel from the device, and then, PBS solution containing the viability assay components was flushed in. As soon as flow was stopped, the light pattern was removed, and the temperature of the ITO heater was raised above the LCST to compensate for the loss of heat. The cells were incubated for 25–30 minutes, as the stain was allowed to permeate the hydrogel. Cell viability of a MDCK II sample was approximately 100%, with no dead cells visibly fluorescing (Figure 8(b)). In the experiment with

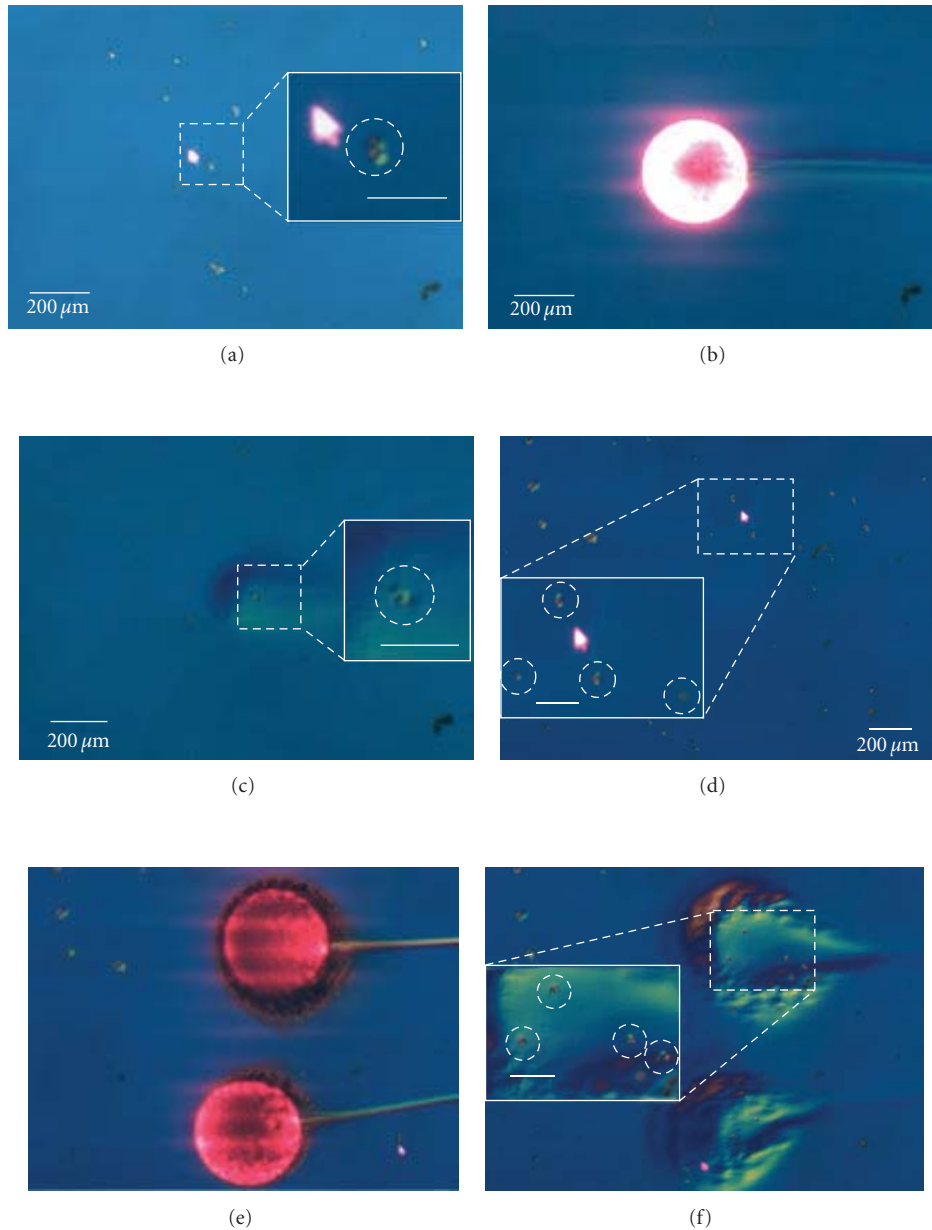


FIGURE 7: Gelation of hydrogels using optical control, demonstrating the trapping of MDCK II cells in 3D hydrogels. (a) Initial cell distribution. The two target cells are circled in the inset. Other cells will be flushed away. The inset scale bar is  $100\ \mu\text{m}$ . (b) A light pattern (bright circle) is used to trigger hydrogel formation (dark circular area), trapping the target cells. Cells not trapped in the gel are flushed away. (c) The two target cells remain in the 3D hydrogel. (d) Initial cell distribution when using parallel optical patterns to trap MDCK II cells in 3D hydrogels. Four target cells are circled in the inset. Other cells will be flushed away, except those trapped by the second optical pattern. The inset scale bar is  $100\ \mu\text{m}$ . (e) Light patterns (bright circles) are used to trigger hydrogel formation (dark circular areas), trapping the target cells while free cells are flushed away. (f) The four target cells remain in the 3D hydrogel.

HeLa cells, over 80% of the cells entrapped in the optically patterned hydrogel fluoresced green, indicating that the cells survive the process (Figure 9(b)). Some cells at the border of the hydrogel exhibited the red fluorescence indicative of cell death (Figure 9(c)). It was expected that the trapping procedure should have an insignificant effect on viability, as PNIPAAm is biocompatible [27, 28]. Furthermore, the cells are exposed to an optical intensity of only  $0.17\ \text{W}/\text{cm}^2$ , as most of the incident light is absorbed by the substrate.

This intensity should not directly cause increased DNA fragmentation [30]. These properties make our technique safe for the culturing of specific cells in 3D.

## 5. Conclusion

In this work, a cell culture system was demonstrated with the ability to trap cells of interest in reversible 3D scaffolds composed of a thermoresponsive hydrogel, PNIPAAm.

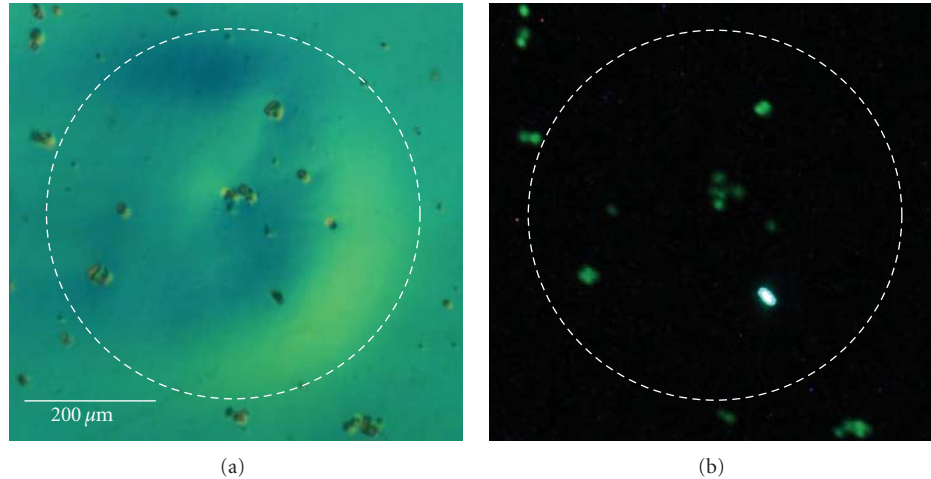


FIGURE 8: Cell viability testing using LIVE/DEAD assay on trapped MDCK II cells. (a) Initial distribution of MDCK II cells after 50 minutes in an optically patterned hydrogel. The starting cell density was approximately  $1 \times 10^5$  cells/mL in solution. The dashed circle encloses the area that was gelled. The circular objects that are visible are the cells. (b) Fluorescent image of the same cells from (a), demonstrating approximately 100% viability. Cells lying outside the gel were not taken into account. Live cells fluoresce green, while dead cells fluoresce red. Fluorescent cells appear as bright spots in these images.

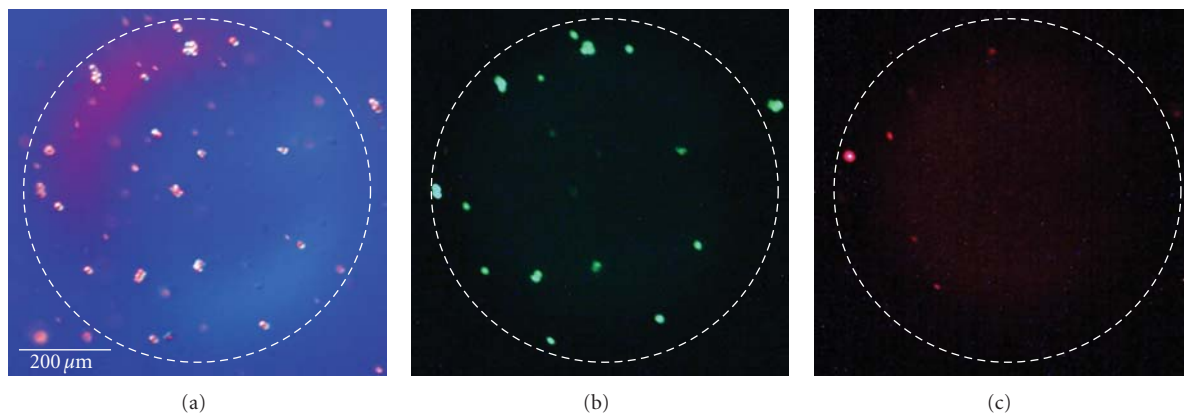


FIGURE 9: Cell viability testing using LIVE/DEAD assay on trapped HeLa cells. (a) Initial distribution of HeLa cells after 45 minutes in an optically patterned hydrogel. The starting cell density was approximately  $1 \times 10^6$  cells/mL in solution. (b-c) Fluorescent images of the same cells from (a), demonstrating approximately 81% viability. Live cells fluoresce green (b), while dead cells fluoresce red (c). Fluorescent cells appear as bright spots in these images.

The culture system utilizes a simple microfluidic device that acts as a repository for the hydrogel solution containing the cell sample while the trapping procedure is performed. Optically generated heating is used to induce localized gelation of cells within the device, enabling the trapping of specific cells. Two possible methods of generating localized heating at the cellular level were shown: using a modified commercial projector as a source of light and using a diode laser. The projector offers a higher degree of flexibility for pattern generation, whereas the higher intensity of the laser provides a stronger heat source and can thus create gels with smaller areas. The intensity of either source is not at a level where it is expected to damage the irradiated cells. To test the trapping capabilities of the culture system, experiments involving microbeads as well as MDCK II and HeLa cells have been performed. With MDCK II cells, single- and multiple-cell trapping was achieved, using a single light pattern or

multiple simultaneous patterns. Preliminary viability tests show that over 80% cells survive the trapping procedure. Future work includes performing further viability tests at later time points during the cell cultivation process.

### Acknowledgments

The authors would like to thank Yujia Li and Dr. Hongwei Li for providing the MDCK II cells and Dr. Ava Dykes and Dr. Shiv Sharma for the HeLa cells. This project is supported by the National Science Foundation, Grant no. EEC09-26632. The project described was also supported by Grant no. U54RR022762 from the National Center for Research Resources (NCRR), a component of the National Institutes of Health (NIH), and its contents are solely the responsibility of the authors and do not necessarily represent the official view of NCRR or NIH.

## References

- [1] A. Dove, "Cell-based therapies go live," *Nature Biotechnology*, vol. 20, no. 4, pp. 339–343, 2002.
- [2] K. H. Wilan, C. T. Scott, and S. Herrera, "Chasing a cellular fountain of youth," *Nature Biotechnology*, vol. 23, no. 7, pp. 807–815, 2005.
- [3] V. F. M. Segers and R. T. Lee, "Stem-cell therapy for cardiac disease," *Nature*, vol. 451, no. 7181, pp. 937–942, 2008.
- [4] W. Xu, L. Liu, and I. G. Charles, "Microencapsulated iNOS-expressing cells cause tumor suppression in mice," *The FASEB Journal*, vol. 16, no. 2, pp. 213–215, 2002.
- [5] M. E. Dudley and S. A. Rosenberg, "Adoptive-cell-transfer therapy for the treatment of patients with cancer," *Nature Reviews Cancer*, vol. 3, no. 9, pp. 666–675, 2003.
- [6] L. Gattinoni, D. J. Powell, S. A. Rosenberg, and N. P. Restifo, "Adoptive immunotherapy for cancer: building on success," *Nature Reviews Immunology*, vol. 6, no. 5, pp. 383–393, 2006.
- [7] Y. Sun, X. Ma, D. Zhou, I. Vacek, and A. M. Sun, "Normalization of diabetes in spontaneously diabetic cynomolgus monkeys by xenografts of microencapsulated porcine islets without immunosuppression," *Journal of Clinical Investigation*, vol. 98, no. 6, pp. 1417–1422, 1996.
- [8] T. Sapir, K. Shternhall, I. Meivar-Levy et al., "Cell-replacement therapy for diabetes: generating functional insulin-producing tissue from adult human liver cells," *Proceedings of the National Academy of Sciences of the United States of America*, vol. 102, no. 22, pp. 7964–7969, 2005.
- [9] J. J. Meier, A. Bhushan, and P. C. Butler, "The potential for stem cell therapy in diabetes," *Pediatric Research*, vol. 59, no. 4, pp. 65R–73R, 2006.
- [10] M. H. Wu, S. B. Huang, and G. B. Lee, "Microfluidic cell culture systems for drug research," *Lab on a Chip*, vol. 10, no. 8, pp. 939–956, 2010.
- [11] Pharmaceutical Research and Manufacturers of America, *Pharmaceutical Industry Profile 2011*, PhRMA, Washington, DC, USA, 2011, <http://www.phrma.org/>.
- [12] U. Marx and V. Sandig, *Drug Testing In Vitro: Breakthroughs and Trends in Cell Culture Technology*, Wiley-VCH, Weinheim, Germany, 2007.
- [13] J. El-Ali, P. K. Sorger, and K. F. Jensen, "Cells on chips," *Nature*, vol. 442, no. 7101, pp. 403–411, 2006.
- [14] Y. S. Torisawa, H. Shiku, T. Yasukawa, M. Nishizawa, and T. Matsue, "Multi-channel 3-D cell culture device integrated on a silicon chip for anticancer drug sensitivity test," *Biomaterials*, vol. 26, no. 14, pp. 2165–2172, 2005.
- [15] D. W. Huttmacher, "Biomaterials offer cancer research the third dimension," *Nature Materials*, vol. 9, no. 2, pp. 90–93, 2010.
- [16] B. A. Justice, N. A. Badr, and R. A. Felder, "3D cell culture opens new dimensions in cell-based assays," *Drug Discovery Today*, vol. 14, no. 1-2, pp. 102–107, 2009.
- [17] R. C. Dutta and A. K. Dutta, "Cell-interactive 3D-scaffold; advances and applications," *Biotechnology Advances*, vol. 27, no. 4, pp. 334–339, 2009.
- [18] L. H. Han, G. Mapili, S. Chen, and K. Roy, "Projection microfabrication of three-dimensional scaffolds for tissue engineering," *Journal of Manufacturing Science and Engineering*, vol. 130, no. 2, article 021005, 4 pages, 2008.
- [19] V. Chan, P. Zorlutuna, J. H. Jeong, H. Kong, and R. Bashir, "Three-dimensional photopatterning of hydrogels using stereolithography for long-term cell encapsulation," *Lab on a Chip*, vol. 10, no. 16, pp. 2062–2070, 2010.
- [20] P. S. Dittrich and A. Manz, "Lab-on-a-chip: microfluidics in drug discovery," *Nature Reviews Drug Discovery*, vol. 5, no. 3, pp. 210–218, 2006.
- [21] V. L. Tsang and S. N. Bhatia, "Three-dimensional tissue fabrication," *Advanced Drug Delivery Reviews*, vol. 56, no. 11, pp. 1635–1647, 2004.
- [22] M. J. Powers, K. Domansky, M. R. Kaazempur-Mofrad et al., "A microfabricated array bioreactor for perfused 3D liver culture," *Biotechnology and Bioengineering*, vol. 78, no. 3, pp. 257–269, 2002.
- [23] S. A. Lee, S. E. Chung, W. Park, S. H. Lee, and S. Kwon, "Three-dimensional fabrication of heterogeneous microstructures using soft membrane deformation and optofluidic maskless lithography," *Lab on a Chip*, vol. 9, no. 12, pp. 1670–1675, 2009.
- [24] D. R. Albrecht, G. H. Underhill, T. B. Wassermann, R. L. Sah, and S. N. Bhatia, "Probing the role of multicellular organization in three-dimensional microenvironments," *Nature Methods*, vol. 3, no. 5, pp. 369–375, 2006.
- [25] T. Braschler, R. Johann, M. Heule, L. Metref, and P. Renaud, "Gentle cell trapping and release on a microfluidic chip by in situ alginate hydrogel formation," *Lab on a Chip*, vol. 5, no. 5, pp. 553–559, 2005.
- [26] Y. H. Bae, T. Okano, and S. Wan Kim, "Temperature dependence of swelling of crosslinked poly(*N,N'*-alkyl substituted acrylamides) in water," *Journal of Polymer Science B*, vol. 28, no. 6, pp. 923–936, 1990.
- [27] R. A. Stile, W. R. Burghardt, and K. E. Healy, "Synthesis and characterization of injectable poly(*N*-isopropylacrylamide)-based hydrogels that support tissue formation in vitro," *Macromolecules*, vol. 32, no. 22, pp. 7370–7379, 1999.
- [28] J. F. Pollock and K. E. Healy, "Mechanical and swelling characterization of poly(*N*-isopropyl acrylamide -co- methoxy poly(ethylene glycol) methacrylate) sol-gels," *Acta Biomaterialia*, vol. 6, no. 4, pp. 1307–1318, 2010.
- [29] D. G. Grier, "A revolution in optical manipulation," *Nature*, vol. 424, no. 6950, pp. 810–816, 2003.
- [30] S. K. Mohanty, A. Rapp, S. Monajembashi, P. K. Gupta, and K. O. Greulich, "Comet assay measurements of DNA damage in cells by laser microbeams and trapping beams with wavelengths spanning a range of 308 nm to 1064 nm," *Radiation Research*, vol. 157, no. 4, pp. 378–385, 2002.

## Review Article

# Optoelectrofluidic Manipulation of Nanoparticles and Biomolecules

**Hyundoo Hwang and Je-Kyun Park**

*Department of Bio and Brain Engineering, Korea Advanced Institute of Science and Technology (KAIST), 291 Daehak-ro, Yuseong-gu, Daejeon 305-701, Republic of Korea*

Correspondence should be addressed to Je-Kyun Park, jekyun@kaist.ac.kr

Received 27 April 2011; Revised 27 July 2011; Accepted 28 July 2011

Academic Editor: Eric Pei Yu Chiou

Copyright © 2011 H. Hwang and J.-K. Park. This is an open access article distributed under the Creative Commons Attribution License, which permits unrestricted use, distribution, and reproduction in any medium, provided the original work is properly cited.

This paper presents optoelectrofluidic technologies for manipulation of nanoparticles and biomolecules. Optoelectrofluidics provides an elegant scheme for the programmable manipulation of particles or fluids in microenvironments based on optically induced electrokinetics. Recent progress on the optoelectrofluidic manipulation of nanoobjects, which include nanospheres, nanowires, nanotubes, and biomolecules, is introduced. Some potential applications of the optoelectrofluidic nanoparticle manipulation, such as nanoparticles separation, nanostructures manufacturing, molecular physics, and clinical diagnostics, and their future directions are also discussed.

## 1. Introduction

A number of advances in micro- and nanomanipulation techniques have been made due to the increase of needs for high performance manipulation—trapping, transportation, separation, concentration, and assembly—of micro-/nanoobjects in a variety of applications. In particular, manipulating nanoobjects such as nanospheres, nanowires, and biomolecules has provided tremendous opportunities in various application fields, including from device manufacturing to chemical analysis. For addressing such nanoparticle applications, numerous techniques based on various forces such as mechanical [1–4], optical [5–9], electrical [10–13], and magnetic [14, 15] forces have been introduced. In this paper, we present the fundamentals of optoelectrofluidics and the major experiments performed to date for manipulating nanoparticles and molecules using the optoelectrofluidic platforms. Recent progress and some potential applications of optoelectrofluidic technology for nanoparticle manipulation, as well as its future direction are discussed.

## 2. Conventional Techniques for Nanoparticle Manipulation: Optical and Electrical Methods

Optical manipulation techniques have attracted much attention for a long time since the appearance of optical tweezers in 1970 [5] and been one of the most frequently used methods because one can directly trap and transport individual particles on demand based on the optical field of a tightly focused laser beam. However, it is well known that a lower bound on the size to which light can be focused is limited by the diffraction limit, which is given by  $d = 1.2\lambda/\text{N.A.}$ , where  $\lambda$  and N.A. are the wavelength of the light and the numerical aperture of the lens, respectively [16]. Despite such limitations, conventional optical tweezers have been used to trap not only viruses [17] and biological cells [18] but also metallic nanoparticles [6], nanowires [7], and carbon nanotubes (CNTs) [8]. When the target object is much smaller than the diffraction limit as the case of nanoparticles, the trap stability is dependent on the polarizability of the particles because they can be treated as

point dipoles in an inhomogeneous electromagnetic field of the optical trap [6]. In the Rayleigh regime, however, the trapping force is proportional to the volume of the particle, thereby an extremely high power laser source is required for trapping nanoparticles. For dielectric nanoparticles such as latex, the situation is more challenging than for metallic nanoparticles because the laser power needed for trapping latex nanoparticles is significantly higher than that for metallic particles of similar size. For biomolecules, most of the researchers have tried to manipulate and characterize the physical properties of the molecules by attaching them onto microbeads and manipulating the beads [9]. In this paper, however, only the direct manipulation of molecules, which are not immobilized onto any supporting substrates as a carrier, would be considered. To our knowledge, there are no studies, in which direct trapping and transporting of biomolecules using a conventional optical tweezers system have been demonstrated.

To deal with the limitation of conventional optical tweezers, several types of advanced optical manipulation techniques using near field photonics have been reported [19]. Silicon waveguides have been applied to directly manipulate nanoparticles and  $\lambda$ DNA molecules [20]. By using the subwavelength slot waveguides, the intensity of the optical field and the sharpness of the gradient could be increased, resulting in the increase of the optical force. Recently, an alternative method based on an optical resonator, which amplifies the local optical fields, has also been demonstrated [21]. They could generate extremely strong optical field gradients in three dimensions while simultaneously enhancing the trap stiffness due to the optical field amplification within the resonator. Methods based on localized surface plasmon resonance (LSPR) have also been applied to trap nanosized particles. For example, excitation of LSPR between two gold nanodots with a focused laser beam could generate strong optical forces to trap [22]. Plasmonic dipole antenna has also been applied to enhance the optical field and to trap 10 nm gold nanoparticles with stronger forces [23]. Although these methods offered a new way to reduce the incident laser power to trap nanoparticles with higher stability compared to the conventional optical tweezers, transportation of trapped nanoparticles at a specific region of interest is not possible because they always require the patterned metal structures in a predefined design to enhance the optical fields and to trap the particles. In addition, these methods still require relatively complicated optical setup for flexible manipulation of the optical pattern and fine alignment of the optical path, which affect the performance of nanoparticle manipulation.

Electrical methods, especially using electrokinetic mechanisms such as electrophoresis, dielectrophoresis (DEP), and AC electroosmosis (ACEO), have been widely used for the manipulation of nanoparticles as well. For example, under a nonuniform electric field formed by patterned microelectrodes, nanospheres, nanowires, and nanotubes as well as biomolecules move towards or repel from the edge of the electrodes, around which an electric field is the strongest, by DEP forces, which depend on the dielectric properties of target matters and surrounding medium. Some drag forces due to the flow effects such as ACEO and electrothermal

(ET) flow also affect the movement of nanoparticles. In 1997, Green and Morgan [10] first demonstrated the DEP-based manipulation of 93 nm latex beads using microelectrode arrays. Precise alignment and placement of semiconducting nanowires onto electrode patterns have been recently demonstrated on the basis of positive DEP, which means the movement of particles towards the strongest electric field area [11]. Separation of metallic single-walled CNTs from semiconducting ones has also been demonstrated based on their different dielectric properties, which cause different DEP behaviors [12]. In addition, gold nanoparticles were concentrated and assembled onto the electrodes by several AC electrokinetic mechanisms such as positive DEP, ACEO, and ET flows [13]. Although these electrical techniques offer simple and versatile setup for nanoparticle manipulation compared to the optical methods, it has been only possible to manipulate them under a fixed electric field distribution formed by predesigned electrode patterns.

### 3. Optoelectrofluidics

To combine their own advantages of optical and electrical manipulation technologies, an alternative manipulation technique, so-called optoelectrofluidics, has been suggested. Optoelectrofluidics refers to the motions of particles or fluids under an electric field, which is induced or perturbed by an optical source [24]. There are two typical approaches for optoelectrofluidic manipulation [25]: (i) direct change of liquid properties by light and (ii) change of surface conductivity by light. Although both methods have been applied for optoelectrofluidic manipulation of nanoparticles including biomolecules, more widely used method is the latter one, which is based on the photoconductivity of a surface, because there is no significant change in the natural properties of sample fluid and more flexible application is available based on several electrokinetic mechanisms such as DEP and ACEO by forming a nonuniform electric field in the fluid.

In the case of the former one, local temperature increase of fluid under an electric field by illuminating a strong light source has been usually used to induce electrohydrodynamic vortices due to local change of electrical conductivity and permittivity of the fluid depending on its temperature (Figure 1(a)). Mizuno et al. [26] have first demonstrated the ET vortices induced by a strong infrared (IR) laser source and applied to transport DNA molecules in 1995. Although they have also simultaneously applied an optical field and an electrical field to manipulate particles and molecules [27–29], those works are not included in this paper since two fields independently worked for different purposes in those studies: an optical force for trapping, positioning, or cutting; and an electrostatic force for rotating or extracting.

In the case of the latter one, a light source is used to make only the partially illuminated area of the surface become more conductive than other area and to form a nonuniform electric field in the liquid sample, resulting in several electrokinetic phenomena (Figure 1(b)). Hayward et al. [30] have first demonstrated the electrokinetic patterning of microbeads under a nonuniform electric field formed

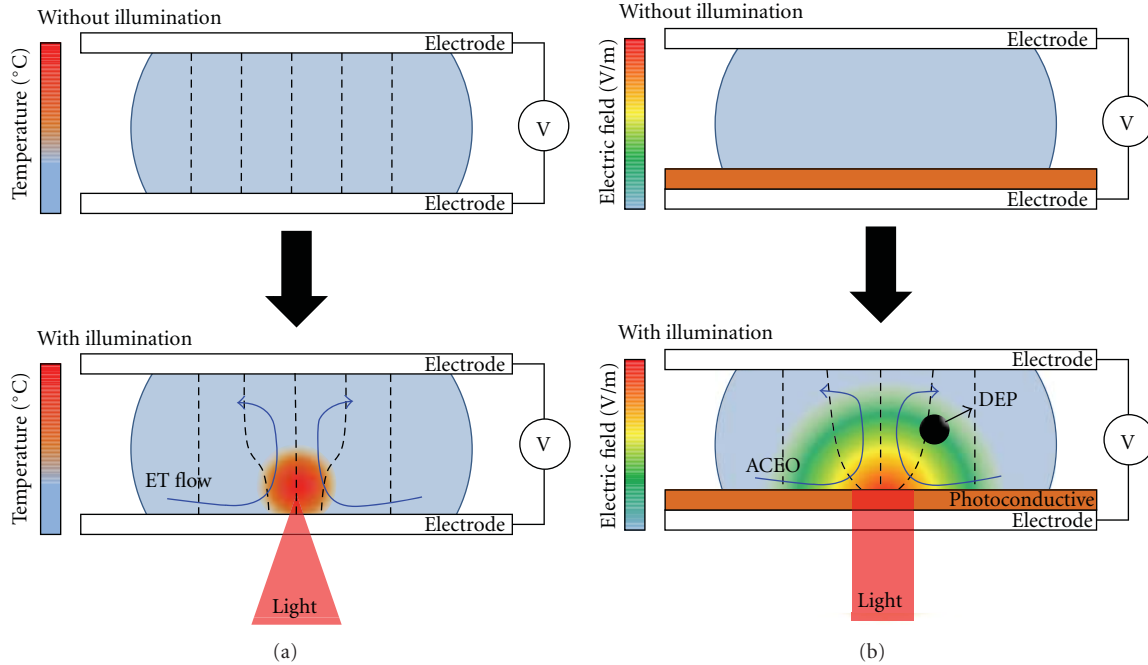


FIGURE 1: Schematic illustration of two typical approaches for optoelectrofluidic particle manipulation: (a) using light for changing sample properties and (b) using light for changing conductivity of the surface.

by an ultraviolet (UV) light pattern projected onto an indium tin oxide surface in 2000. Since the appearance of a technology so-called optoelectronic tweezers (OET) [31] in 2005, photoconductive materials such as hydrogenated amorphous silicon (a-Si:H) have started to be used so that a weak conventional white light source is applicable for inducing electric fields and operating the optoelectrofluidic devices [31–34]. In addition, several types of display devices, such as a digital micromirror device [31], a beam projector [33], and a liquid crystal display [32, 35], have been utilized to generate a dynamic image pattern for programmable manipulation of the electric field distribution.

The OET-based optoelectrofluidic platforms provide many advantages over the conventional methodologies based on optical and electrical mechanisms. Compared to optical manipulation technologies, the OET-based optoelectrofluidic technologies require much less optical power and offer much larger manipulation area. In addition, compared to conventional electrical methods, in which fixed electrode patterns are applied, reconfigurable virtual electrodes formed by an optical manner allow parallel manipulation of massive amount of particles at a specific region of interest in a wide area. Due to those advantages, the optoelectrofluidic platforms have been widely applied to manipulate several kinds of cells, including blood cells [35], motile bacteria [36], and oocytes [37], as well as nonbiological microparticles including polymeric microbeads [38].

Since the optoelectrofluidic devices are originally based on the electrokinetic phenomena under an electric field, which is induced or controlled by an optical source, the operating mechanisms for the manipulation are also the same with the conventional electrokinetic devices except

for those electrokinetic driving forces are controlled in an optical way. Therefore, typical electrokinetic mechanisms, including electrophoresis, DEP, ACEO, and ET flows, have been usually applied to manipulate particles or fluids in the optoelectrofluidic devices. There are some helpful literatures, in which those physical phenomena in the optoelectrofluidic device are presented in detail [25, 39, 40]. In this paper, therefore, we focus on dealing with typical experimental studies for nanoparticle manipulation in optoelectrofluidic devices and the physical mechanisms utilized in those studies.

#### 4. Optoelectrofluidic Manipulation of Nanoparticles

Some research groups have tried to manipulate several types of nanoscale objects from spherical nanoparticles to biological molecules using the optoelectrofluidic platforms. In this section, we will introduce typical experiments, in which various nanoobjects including nanospheres, nanowires, nanotubes, and biomolecules have been manipulated using several types of optoelectrofluidic platforms, with the physical mechanisms applied therein.

**4.1. Nanospheres.** There were a few studies, in which nanospheres were manipulated using an optoelectrofluidic platform. Due to the extremely small volume of nanospheres, relatively small electrode gap and high voltage are required for manipulating them only with the DEP force [41],  $F_{\text{DEP}} \propto r^3 \nabla |E|^2$ , where  $r$  is the particle radius and  $E$  is the electric field, as overcoming the Brownian motion

related to the random force,  $F_{\text{thermal}} \sim k_B T/2r$ , where  $k_B$  is the Boltzmann constant and  $T$  is the temperature [42]. Therefore, spherical nanoparticles have been usually manipulated using the hydrodynamic drag forces,  $F_{\text{drag}} = 6\pi r\eta(u - v)$ , where  $\eta$  is the fluid viscosity,  $u$  is the flow velocity, and  $v$  is the particle velocity, by the optically induced electrohydrodynamic effects—ACEO and ET flows [43–45].

The optically induced ACEO is a fluidic motion generated by the ionic motion within the electric double-layer (EDL) along the tangential electric field,  $E_t$ , which is formed by partial illumination of the photoconductive layer [38]. The ACEO slip velocity,  $u_{\text{slip}}$ , which is the velocity at the top of the EDL, along the surface of the photoconductive layer is proportional to the charges contained in the EDL; the tangential electric field strength; and the Debye length,  $\lambda_D \propto (c_0 Z^2)^{-1/2}$ , where  $Z$  is the valance of the ions and  $c_0$  is the concentration [46]. Chiou et al. [43] have demonstrated the concentration of 50 nm and 200 nm polystyrene nanoparticles and quantum dots using this ACEO in an OET device. When a light pattern was projected onto the photoconductive layer, the ACEO vortices were generated around the pattern and concentrated the nanospheres towards the pattern within several tens of seconds. They could determine the concentration of nanospheres through increase of the fluorescence intensity in the illuminated area as shown in Figure 2(a).

The optically induced ET effect, which is due to the thermal gradient in a fluid, has also been applied to concentrate and to pattern nanospheres. The thermal gradient, which can be generated by local illumination of a strong light source [26] or by Joule heating [39], induces a gradient in the fluid permittivity and conductivity, resulting in a fluidic motion under an electric field [47]. Williams et al. [44] have applied the ET vortices, which were created by IR-induced local heating of a fluid under an electric field, to concentrate and pattern 49 nm and 100 nm polystyrene nanoparticles. They also characterized those concentration phenomena against the applied AC frequency and voltage (Figure 2(b)). On the other hand, Jamshidi et al. [45] have concentrated and patterned metal nanoparticles using the ET vortices, which were induced by Joule heating in an OET device as shown in Figure 2(c). The Joule heating-based ET effect requires much weaker light source than that for sample heating-based ET effect and is dominant in the OET-based optoelectrofluidic platforms, in which virtual electrodes are formed by partial illumination of the photoconductive layer, because the heat is originally generated by an electrical source, not by an optical source.

**4.2. Nanowires and Nanotubes.** Nonspherical nanoparticles such as nanowires and nanotubes have also been manipulated on the basis of the optoelectrofluidic methods. In the case of nanowires or nanotubes, DEP force acting on them can be defined as  $F_{\text{DEP}} \propto r^2 l \text{Re}[K] \nabla |E|^2$ , where  $l$  is the length of nanowires or nanotubes and  $\text{Re}[K]$  is the real part of the Clausius-Mossotti factor [41]. Thus, the DEP force acting on the nanowires or nanotubes can become much larger than that on spherical nanoparticles, which have the

same  $r$  with the nanowires or nanotubes, depending on their length.

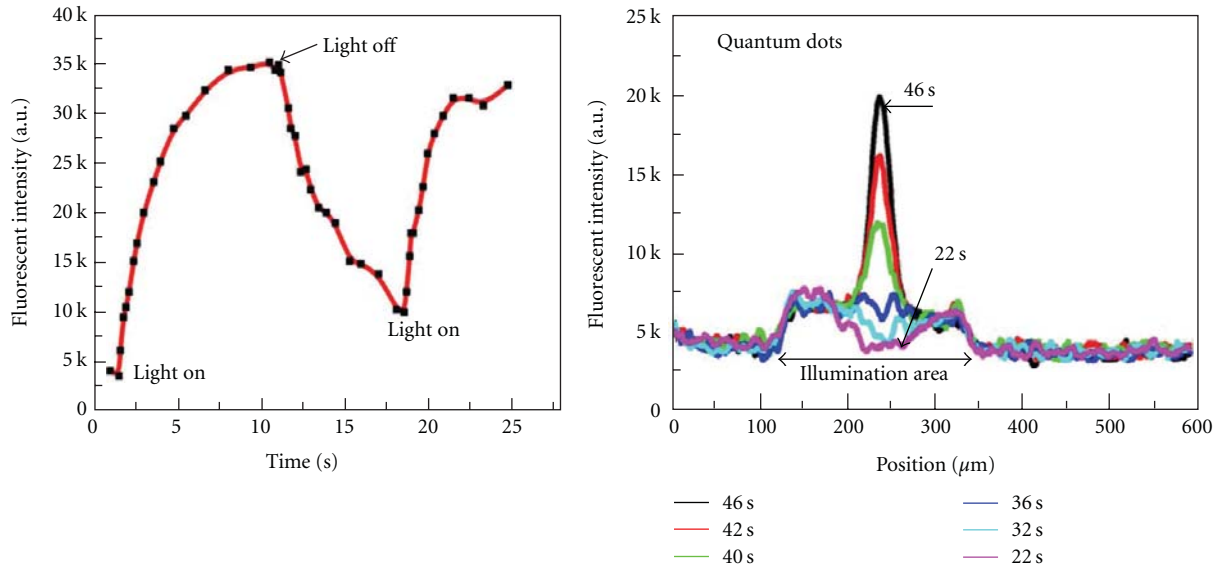
Jamshidi et al. [48] have utilized these characteristics of DEP for trapping and transporting silver nanowires (100 nm diameter and 5  $\mu\text{m}$  length) with positive DEP force induced by a laser source in an OET device. The metal nanowires were much more polarizable than the surrounding media, thus the  $\text{Re}[K]$  was larger than 1, resulting in the positive DEP, in which the particles move towards a light pattern where the electric field strength is larger than other area. They could also separate silver nanowires from silicon nanowires based on their different DEP mobility depending on the  $\text{Re}[K]$  (Figure 3(a)). Based on the same principles, Pauzauskie et al. [49] have successfully addressed multiwalled CNTs with high translation velocity over 200  $\mu\text{m}/\text{s}$ . They could also modulate the density of CNTs based on their repulsive interactions (Figure 3(b)). The repulsion among those concentrated CNTs might be due to the electrostatic interaction force which depends on the distances among the particles, the polarizability of the particles, the electric field, and the particle size [50]. Therefore, the density of nanoparticles within a specific area would also be controllable based on the intensity and the shape of an image pattern, which correlates with the strength and the direction of an electric field, respectively.

**4.3. Molecules.** Several types of optoelectrofluidic platforms and various mechanisms have been applied to manipulate biological molecules such as DNA and proteins [43, 51–54]. Here we will review them according to the underlying mechanisms for manipulation.

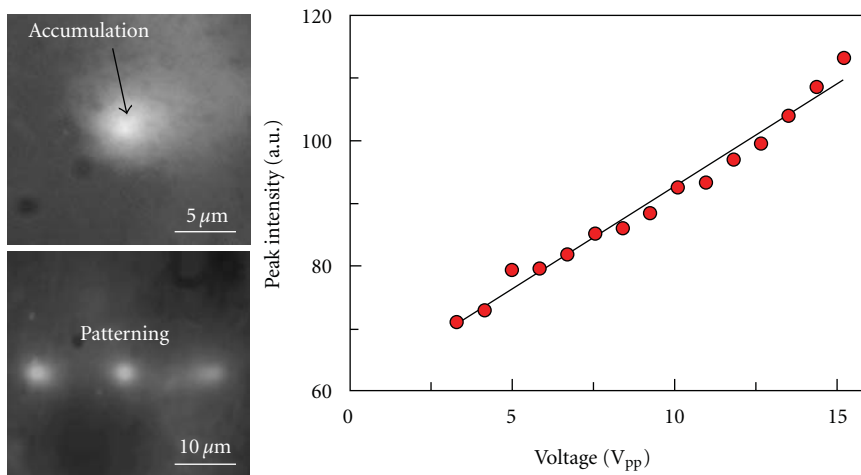
Most biomolecules are charged under a specific pH of the solution, thus the electrophoretic force acting on a charged objects in an electric field, which is defined by  $F_{\text{EP}} = qE$ , where  $q$  is the net charge of the particle, is very useful to manipulate them. The optoelectrofluidic devices, in which  $\text{TiO}_2$  and Ge photoanodes were used as the photoconductive layer, have been applied for transport and separation of charged proteins such as bovine serum albumin (BSA) and cytochrome c under an optically modulated DC electric field within agarose gel (Figure 4(a)) [51]. They also applied this technique to separate DNA fragments based on their size—10 bp and 3000 bp [52]. It took relatively long time over several tens of minutes because they applied a gel system, which is much more viscous than a liquid system, resulting in much stronger drag force.

The optically induced DEP and ET flows in an OET device have also been applied to manipulate DNA molecules. Hoeb et al. [53] have tried to manipulate DNA with DEP induced by projecting a diode laser onto the a-Si:H layer. They could also observe some convection-like motions of DNA molecules due to the local heating of the sample fluids by a strong laser source. The moving characteristics of DNA molecules after correcting the motion by thermal flows were agreed well with the calculated DEP characteristics of DNA as shown in Figure 4(b).

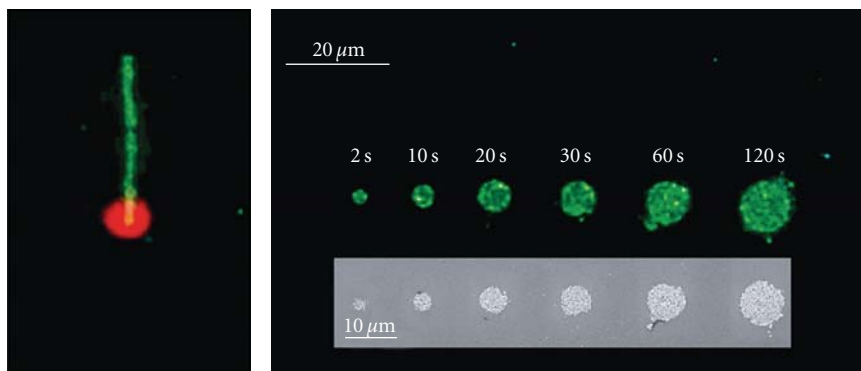
DNA has been manipulated with the optically induced ACEO as well. Chiou et al. [43] could successfully concentrate  $\lambda$ -phage DNA with the light-induced ACEO vortices



(a)



(b)



(c)

FIGURE 2: Optoelectrofluidic concentration and patterning of nanospheres. (a) Fluorescent polymeric nanoparticles and quantum dots using optically induced ACEO flows (adapted with permission from Chiou et al. [43] Copyright 2008 IEEE). (b) Voltage-dependent concentration of fluorescent polymeric nanoparticles using a laser-induced electrothermal (ET) effect (Williams et al. [44]—reproduced by permission of The Royal Society of Chemistry). (c) Dynamic concentration and patterning of metal nanoparticles using a Joule heating-induced ET effect and DEP-mediated immobilization (adapted with permission from Jamshidi et al. [45], Copyright 2009 American Chemical Society).

as like polymeric nanoparticles and quantum dots. Hwang and Park [54] have manipulated proteins such as BSA, polysaccharides such as dextran, and fluorescent dyes such as fluorecein and bisbenzimidazole using the same phenomena. They investigated the frequency-dependent concentration effect of those molecules depending on several electrokinetic mechanisms including DEP and electrostatic interactions as well as ACEO (Figure 4(c)). Moreover, they could control their local concentration in both temporal and spatial manner by controlling the applied AC signal and the light pattern.

Not only the OET devices, but also the optically induced ET effect in microelectrode system have also been applied for manipulating molecules. Mizuno et al. [26] have first demonstrated transport of DNA molecules by the ET flows induced by a laser spot focused in the middle of an AC electric field. Nakano et al. [55] have applied the laser-induced ET flows in a microelectrode system to trap and stretch long DNA molecules based on high-shear rate as shown in Figure 4(d).

## 5. Applications

Much research has been actively conducted on the optoelectrofluidic manipulation of nanoparticles over worldwide as mentioned above, but most of them have focused only on demonstrating the concentration and patterning of nanoparticles or molecules. Only a few practical applications, in which the optoelectrofluidic platforms provide their own advantages over other conventional tools for the same purposes, have been developed to date. Here we introduce some studies, in which potential applications of the optoelectrofluidic technologies for nanoparticle manipulation are shown, and discuss about the future directions of this technology for its more practical uses.

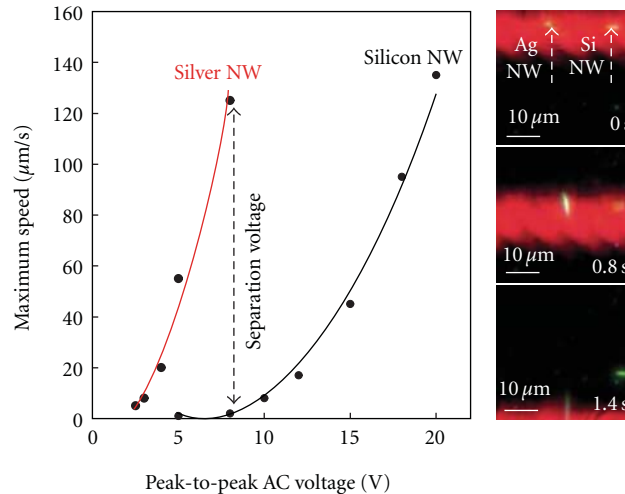
**5.1. Separation of Nanoparticles.** Purification of nanoparticles remains as one of significant challenging issues in the preparation of well-defined materials. For separating or purifying nanoobjects using the optoelectrofluidic phenomena, the separation criteria might be almost the same with that for conventional electrokinetic separation technologies—size, dielectric constant, or charge of the target particle. For example, size-based separation of synthesized metal nanoparticles [56, 57] or purification of single-walled CNTs from catalytic impurities [58, 59] would be possible based on the differences in their size or dielectric properties using the optoelectrofluidic mechanisms such as optically induced DEP. In practice, silver nanowires could be separated from semiconducting silicon nanowires based on their DEP characteristics in an optoelectrofluidic device (Figure 3(a)) [48]. This study is the first demonstration of optoelectrofluidic separation of nanowires. However, it might be more meaningful if one could apply this elegant scheme not only for simple demonstration to show what kind of particles they can move, but also for more practical uses. For example, separation of metallic single-walled CNTs from semiconducting CNTs would be more practical in the

perspective of purification of CNTs prepared by a chemical vapor deposition method—it has been demonstrated using DEP in metal microelectrodes [12].

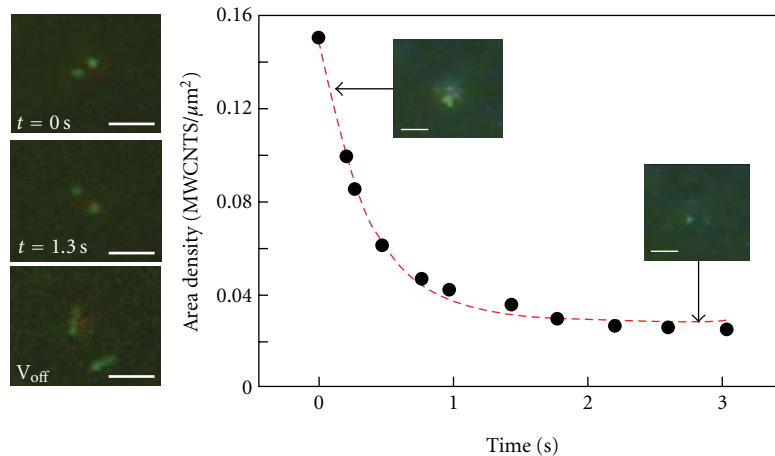
In addition, in the perspective of separation performances such as purity, recovery, resolution, and throughput, it is still questionable whether the optoelectrofluidic techniques are more practically useful or have better performances compared to conventional separation technologies. Even if continuous processing for injection of mixtures and recollection of the separated samples is available based on integrated microchannel structures [60], the reasons, why we should use the optically induced virtual electrodes, which requires the photoconductive layer in addition to an electrode, instead of just-patterned microelectrodes, might still remain as an unanswered question. On the same line with this, for practical uses of the optoelectrofluidic technologies for nanoparticle separation, fully integrated processing from sample preparation or separation to applications—assembly or detection—in a tiny volume of sample droplet without any fluidic components would be required.

**5.2. Manufacturing of Nanostructures.** For the application of optoelectrofluidic platforms in nanoscience except biology and chemistry, manufacturing or synthesis of nanostructures might be one of the most potential applications, in which they can be applied to practical uses, because most of the research in this field have focused on the concentration, alignment, assembly, or patterning of various nanoobjects. For example, dynamic manipulation of individual nanowires (Figure 3(a)) [48] and patterning of metal nanoparticles (Figure 2(c)) [45] based on optoelectrofluidics showed the potential of this technology on nanofabrication well.

Jamshidi et al. [45] have shown that a metal nanostructure patterned by the optoelectrofluidic concentration is applicable as a photonic nanostructure like surface-enhanced Raman scattering (SERS) substrate. However, compared to conventional techniques for manufacturing photonic structures, such as chemical self-assembly [61], electron beam lithography [62], focused ion beam milling [63], the optoelectrofluidic patterning of nanoparticles has still a lot of room for improvements in the view-points of reproducibility and tenability. In addition, such approaches to fabricate SERS-active substrates, in which metal nanoparticles were concentrated and patterned into a predefined area, could be achieved not only by the optoelectrofluidic methods but also by conventional electrokinetic methods based on prepatterned microelectrodes [64, 65]. To overcome those conventional technologies and to develop more practical tools based on the optoelectrofluidics, the own intrinsic advantages of the optoelectrofluidic platforms, in which dynamic control of virtual electrodes is available using a light pattern, could be applied. For example, the nanostructures, which are actively controllable using a light pattern, could be generated in a specific area of interest by projecting a light pattern into the desired area. Such an on-demand formation of nanostructures would be useful for constructing an active SERS platform for detecting chemicals with enhanced Raman scattering signals in a specific area of interest whenever we want. Recently, such an optoelectrofluidic-active



(a)



(b)

FIGURE 3: Optoelectrofluidic trapping and manipulation of nanowires and nanotubes. (a) Separation of metal nanowires from semiconducting nanowires based on their different dielectric characteristics (adapted by permission from Jamshidi et al. [48], Copyright Macmillan Publishers Ltd. 2008). (b) Trapping of carbon nanotubes using optically induced dielectrophoresis and their electrostatic repulsion (adapted with permission from Pauzauskie et al. [49], Copyright 2009, American Institute of Physics).

SERS platform has been reported [66]. In that study, active generation of SERS substrate by optoelectrofluidic concentration of gold nanoparticles into a specific area of interest and *in situ* measurement of SERS signals from small molecules around the area has been demonstrated as shown in Figure 5(a).

**5.3. Molecular Physics.** Hwang and Park [67] have developed a new system based on an optoelectrofluidic manipulation platform for measuring the mobility of molecules in a liquid solution (Figure 5(b)). They utilized the phenomena that the molecules were immediately depleted from the illuminated area in the application of extremely low AC frequency around 100 Hz. After turning off the voltage, the depleted molecules were diffused into the area, resulting in the recovery of the fluorescence signal. By measuring the recovery rate, the diffusion coefficient of molecules could be measured.

Compared to the conventional techniques such as fluorescence recovery after photobleaching [68] or fluorescence correlation spectroscopy [69], this method does not require high-power lasers, high-speed camera, photobleaching of the sample, fluidic components, and complicated optical components. In addition, this technology provides wider operation range because the molecular depletion area can be controlled by adjusting the light pattern size. However, the optoelectrofluidic technique is not applicable for *in vivo* measurements and always requires an electrical source, which is not necessary for the conventional optical technologies.

Elongation of DNA molecules by the optically induced ET vortices has also been demonstrated by Nakano et al. [55] in 2006. They trapped  $\lambda$ - and T4-phage DNA molecules within the ET vortices induced by a laser spot focused into an AC electric field and observed their coil-stretching transitions by strong shear flows (Figure 4(d)). They could

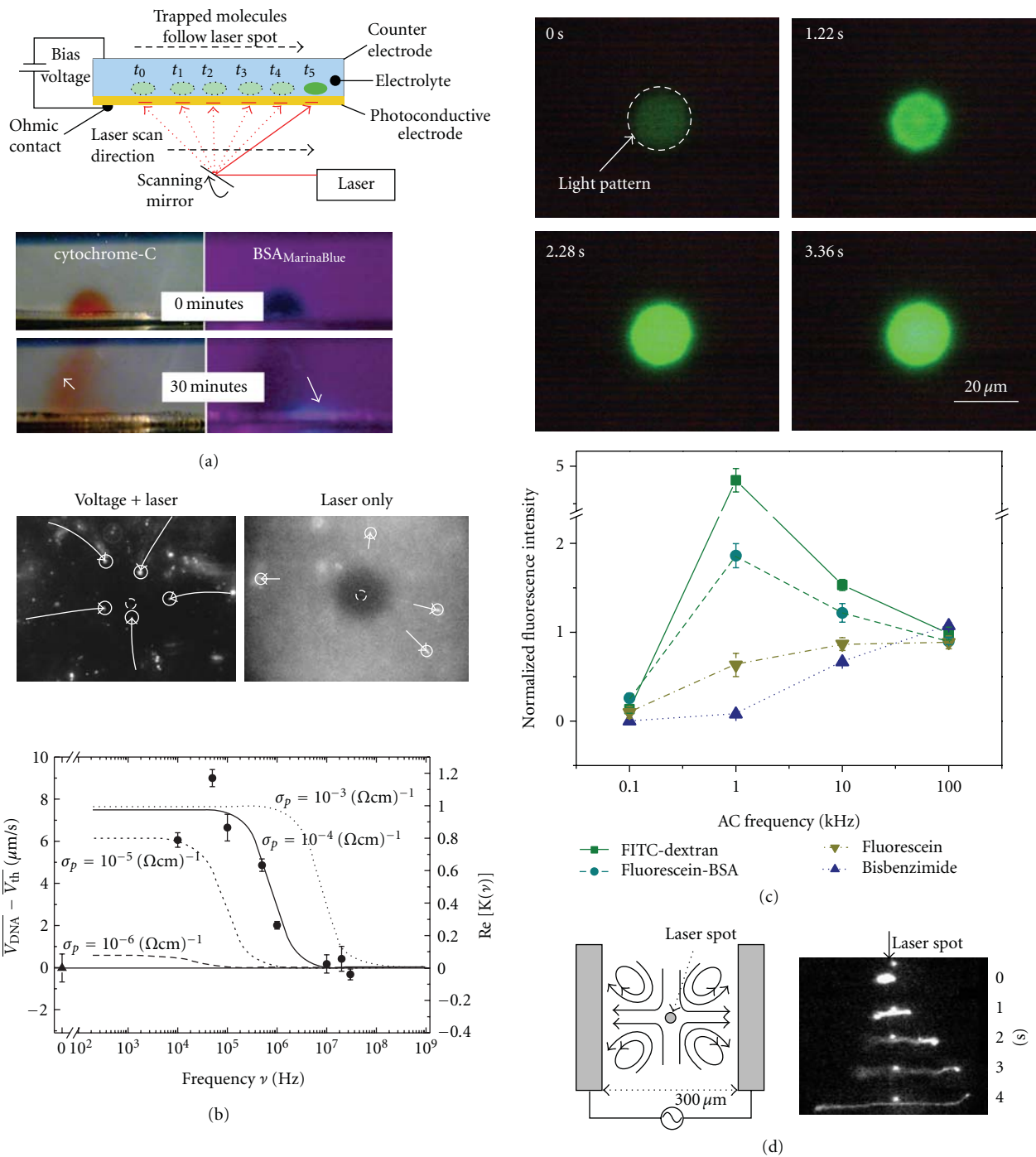


FIGURE 4: Optoelectrofluidic manipulation of biomolecules. (a) Electrophoretic separation of proteins based on optically modulated DC electric field (adapted by permission from Hafeman et al. [51], Copyright 2006 National Academy of Sciences, USA). (b) Concentration of DNA molecules using optically induced dielectrophoresis (DEP) and quantification of their DEP mobility (adapted from Hoeb et al. [53], Copyright 2007, with permission from Elsevier). (c) Dynamic control of local concentration of proteins, polysaccharides, and fluorescent dyes using optically induced ACEO vortices and their characteristics depending on the applied AC voltage and frequency (adapted with permission from Hwang and Park [54], Copyright 2009 American Chemical Society). (d) Trapping and stretching of long DNA molecule using ET flows induced by a laser source focused into an AC electric field (adapted with permission from Nakano et al. [55], Copyright 2006, American Institute of Physics).

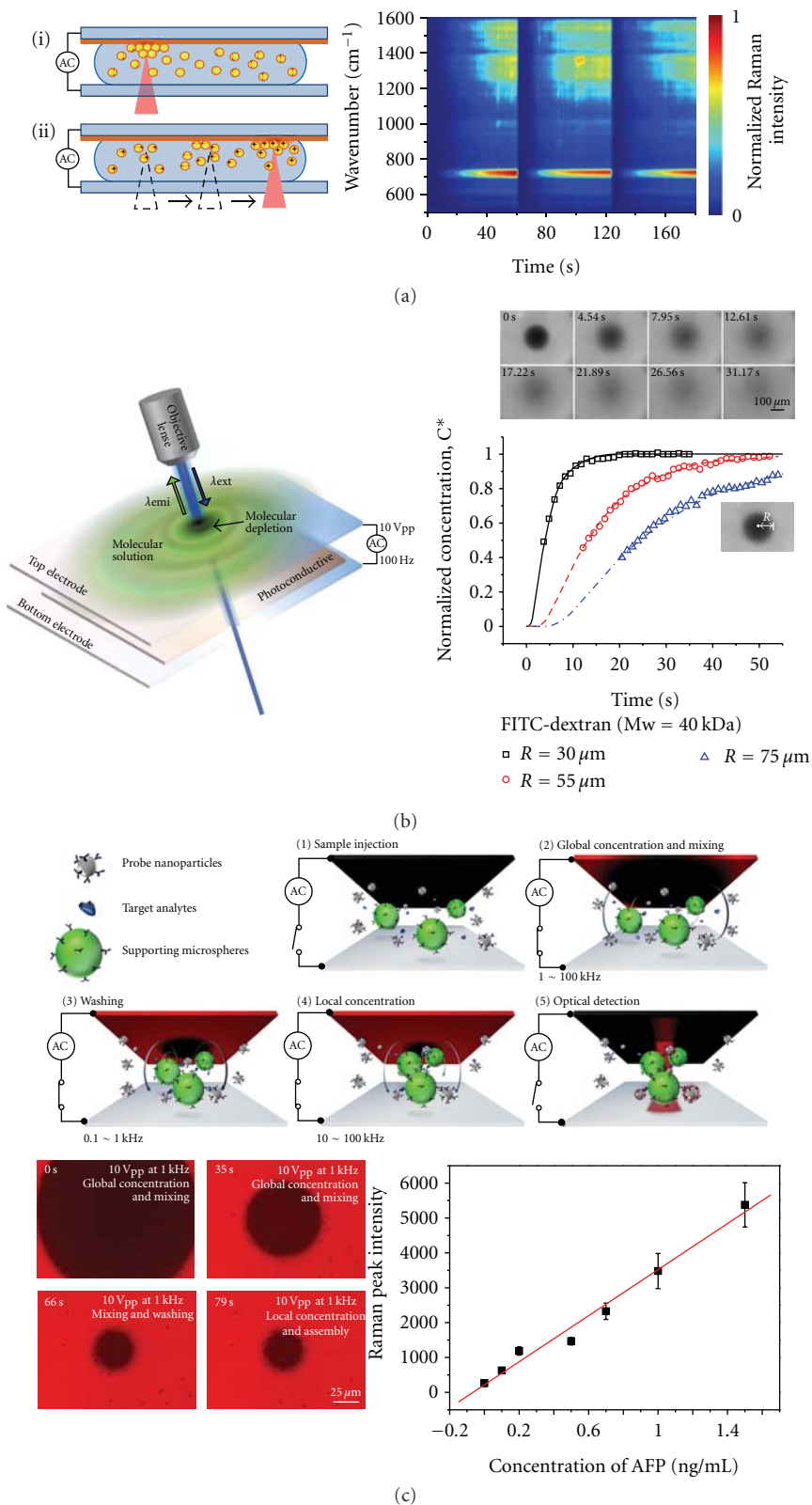


FIGURE 5: Optoelectrofluidic tools for biological and chemical applications. (a) Active surface-enhanced Raman scattering (SERS) substrate for *in situ* detection of molecules in a specific area at a specific time of interest (Hwang et al. [66])—reproduced by permission of The Royal Society of Chemistry). (b) Measurement of molecular diffusion coefficient by analyzing recovery rate after optoelectrofluidic molecular depletion from the illuminated area at a low AC frequency condition (adapted with permission from Hwang and Park [67], Copyright 2009 American Chemical Society). (c) Sandwich immunoassays driven by a dynamic image pattern and optoelectrofluidic mechanisms for detection of human tumor marker using SERS probe nanoparticles (adapted with permission from Hwang et al. [76], Copyright 2010 American Chemical Society).

also adjust the flow velocity by controlling the laser power. The higher laser power was applied, the faster ET flows occurred, resulting in longer extended length of DNA.

In spite of these studies, the area of molecular physics, which can be studied with the direct manipulation of molecules, is restricted. Thus, many people applied some supporting substrates such as polymeric microbeads capturing the target molecules to make it easier or possible to accurately manipulate molecules and measure their physical properties using the manipulation tools. Although we did not review those cases, various manipulation tools such as optical tweezers [70, 71], magnetic tweezers [72], and atomic force microscopy [73] have been applied for those purposes [74]. Molecular manipulation through the indirect manipulation of a supporting microbead, on which DNA molecules were attached, has also been demonstrated in an optoelectrofluidic device. They could stretch DNA molecules by moving the supporting microbeads based on the optically induced DEP [75]. This method showed the potential of optoelectrofluidic technologies as a single molecule force spectroscopy, but quantification of the force acting on those molecules might be much more difficult than other technologies, in which only one kind of forces works on deforming the molecules, differently from the optoelectrofluidic devices wherein various AC electrokinetic mechanisms such as DEP, ACEO, ET flows, and electrostatic forces simultaneously exist. In addition, the limitation of the optoelectrofluidic platforms that the driving forces are dependent on the electrical properties of the sample fluid also interferes with the flexible application of those platforms to the studies using chemical and biological samples, of which properties are also sensitive to the buffer conditions.

**5.4. Immunoassays.** The first optoelectrofluidic tool for clinical diagnostics has been recently developed by Hwang et al. [76]. They demonstrated sandwich immunoassays for detection of human tumor marker using an optoelectrofluidic platform (Figure 5(c)). They could simultaneously control the motions of the probe nanoparticles and the supporting microbeads as well as the target molecules based on their frequency-dependent optoelectrofluidic behaviors. All the steps for sandwich immunoassay, including mixing, washing, and detection, were automatically conducted in an OET-based optoelectrofluidic device with various electrokinetic mechanisms such as DEP and ACEO, which were controlled by a dynamic light pattern generated from an LCD and by the applied AC signals. Simple and quantitative SERS-based immunoassay of human tumor marker, alpha-fetoprotein, with lower detection limit of about 0.1 ng/mL has been possible in a ~500 nL total sample droplet within 5 min. Compared to the conventional microfluidic devices for immunoassays [77, 78], this optoelectrofluidic platform does not require any fluidic components and spends less dead volumes and disposables. They also showed the simultaneous control of multiple assays using a programmed LCD image. However, as like the molecular studies based on the optoelectrofluidic devices, the conductivity of physiological samples significantly affects the manipulation performance of the optoelectrofluidic

devices. For the direct analysis of salty solutions such as blood plasma, therefore, an optoelectrofluidic device with much higher photoconductivity is necessary. However, the devices developed to date such as a phototransistor-based OET device [79] are so complicated and require high costs and long time for the fabrication. Therefore, more research for developing the optoelectrofluidic devices which can be operated even under physiological conditions should be promoted. More studies on the interactions of proteins or nanoparticles under an electric field as well as the development of stable nanoprobe should be accomplished to increase the sensitivity of the optoelectrofluidic immunoassays.

## 6. Conclusions

In this paper, we reviewed recent progress in optoelectrofluidics for nanoparticle manipulation and discussed future challenges for development of practical applications. Some typical experiments for manipulation of nanoparticles—nanospheres, nanowires, nanotubes, and biomolecules—using various optoelectrofluidic mechanisms such as electrophoresis, DEP, ACEO, and ET flows induced in an optical manner were introduced. In addition, potential applications of the optoelectrofluidic nanoparticle manipulation such as separation of nanoparticles, manufacturing of nanostructures, molecular physics, and immunoassays were suggested and their future directions for overcoming the current challenging issues were discussed.

There were a lot of advances in this optoelectrofluidic field especially during a few past years. Several types of optoelectrofluidic devices from the optically induced ET systems, which were constructed with simple plate electrodes and a strong laser source, to the OET devices based on a photoconductive layer and a display device have been developed and applied for manipulation of various target particles from polymeric microbeads and nanoparticles to cells and biomolecules. Various physical mechanisms have also been investigated including electrostatic particle-particle interactions and surface-particle interactions as well as electrokinetic mechanisms such as electrophoresis, DEP, ACEO, and ET flows. This optoelectrofluidics, which is the combination of optics, electrokinetics, and fluidics, might be one of the most powerful tools for noncontact manipulation of nano- and microparticles and would provide valuable capabilities for creating novel applications and extraordinary advances in nanoscience and nanotechnology.

## Acknowledgments

This research was supported by the National Research Laboratory (NRL) Program Grant (R0A-2008-000-20109-0) and by the Nano/Bio Science and Technology Program Grant (2008-00771) through the National Research Foundation of Korea (NRF) funded by the Ministry of Education, Science and Technology (MEST).

## References

- [1] I. W. Lyo and P. Avouris, "Field-induced nanometer- to atomic-scale manipulation of silicon surfaces with the STM," *Science*, vol. 253, no. 5016, pp. 173–176, 1991.
- [2] J. A. Stroscio and D. M. Eigler, "Atomic and molecular manipulation with the scanning tunneling microscope," *Science*, vol. 254, no. 5036, pp. 1319–1326, 1991.
- [3] P. H. Beton, A. W. Dunn, and P. Moriarty, "Manipulation of C<sub>60</sub> molecules on a Si surface," *Applied Physics Letters*, vol. 67, no. 8, pp. 1075–1077, 1995.
- [4] T. A. Jung, R. R. Schlittler, J. K. Gimzewski, H. Tang, and C. Joachim, "Controlled room-temperature positioning of individual molecules: molecular flexure and motion," *Science*, vol. 271, no. 5246, pp. 181–184, 1996.
- [5] A. Ashkin, "Acceleration and trapping of particles by radiation pressure," *Physical Review Letters*, vol. 24, no. 4, pp. 156–159, 1970.
- [6] K. Svoboda and S. M. Block, "Optical trapping of metallic Rayleigh particles," *Optics Letters*, vol. 19, no. 13, pp. 930–932, 1994.
- [7] P. J. Pauzauskie, A. Radenovic, E. Trepagnier, H. Shroff, P. Yang, and J. Liphardt, "Optical trapping and integration of semiconductor nanowire assemblies in water," *Nature Materials*, vol. 5, no. 2, pp. 97–101, 2006.
- [8] J. Plewa, E. Tanner, D. M. Mueth, and D. G. Grier, "Processing carbon nanotubes with holographic optical tweezers," *Optics Express*, vol. 12, no. 9, pp. 1978–1981, 2004.
- [9] T. Nishizaka, H. Miyata, H. Yoshikawa, S. Ishiwata, and K. Kinoshita, "Unbinding force of a single motor molecule of muscle measured using optical tweezers," *Nature*, vol. 377, no. 6546, pp. 251–254, 1995.
- [10] N. G. Green and H. Morgan, "Dielectrophoretic separation of nano-particles," *Journal of Physics D*, vol. 30, no. 11, pp. L41–L44, 1997.
- [11] S. Raychaudhuri, S. A. Dayeh, D. Wang, and E. T. Yu, "Precise semiconductor nanowire placement through dielectrophoresis," *Nano Letters*, vol. 9, no. 6, pp. 2260–2266, 2009.
- [12] R. Krupke, F. Hennrich, H. V. Löhneysen, and M. M. Kappes, "Separation of metallic from semiconducting single-walled carbon nanotubes," *Science*, vol. 301, no. 5631, pp. 344–347, 2003.
- [13] B. C. Gierhart, D. G. Howitt, S. J. Chen, R. L. Smith, and S. D. Collins, "Frequency dependence of gold nanoparticle superassembly by dielectrophoresis," *Langmuir*, vol. 23, no. 24, pp. 12450–12456, 2007.
- [14] B. B. Yellen, O. Hovorka, and G. Friedman, "Arranging matter by magnetic nanoparticle assemblers," *Proceedings of the National Academy of Sciences of the United States of America*, vol. 102, no. 25, pp. 8860–8864, 2005.
- [15] C. S. Lee, H. Lee, and R. M. Westervelt, "Microelectromagnets for the control of magnetic nanoparticles," *Applied Physics Letters*, vol. 79, no. 20, pp. 3308–3310, 2001.
- [16] M. Born and E. Wolf, *Principles of Optics*, Cambridge University Press, New York, NY, USA, 1999.
- [17] A. Ashkin and J. M. Dziedzic, "Optical trapping and manipulation of viruses and bacteria," *Science*, vol. 235, no. 4795, pp. 1517–1520, 1987.
- [18] A. Ashkin, J. M. Dziedzic, and T. Yamane, "Optical trapping and manipulation of single cells using infrared laser beams," *Nature*, vol. 330, no. 6150, pp. 769–771, 1987.
- [19] D. Erickson, X. Serey, Y. F. Chen, and S. Mandal, "Nanomanipulation using near field photonics," *Lab on a Chip*, vol. 11, no. 6, pp. 995–1009, 2011.
- [20] A. H. J. Yang, S. D. Moore, B. S. Schmidt, M. Klug, M. Lipson, and D. Erickson, "Optical manipulation of nanoparticles and biomolecules in sub-wavelength slot waveguides," *Nature*, vol. 457, no. 7225, pp. 71–75, 2009.
- [21] S. Mandai, X. Serey, and D. Erickson, "Nanomanipulation using silicon photonic crystal resonators," *Nano Letters*, vol. 10, no. 1, pp. 99–104, 2010.
- [22] A. N. Grigorenko, N. W. Roberts, M. R. Dickinson, and Y. Zhang, "Nanometric optical tweezers based on nanostructured substrates," *Nature Photonics*, vol. 2, no. 6, pp. 365–370, 2008.
- [23] W. Zhang, L. Huang, C. Santschi, and O. J. F. Martin, "Trapping and sensing 10 nm metal nanoparticles using plasmonic dipole antennas," *Nano Letters*, vol. 10, no. 3, pp. 1006–1011, 2010.
- [24] H. Hwang and J. K. Park, "Rapid and selective concentration of microparticles in an optoelectrofluidic platform," *Lab on a Chip*, vol. 9, no. 2, pp. 199–206, 2009.
- [25] H. Hwang and J. K. Park, "Optoelectrofluidic platforms for chemistry and biology," *Lab on a Chip*, vol. 11, no. 1, pp. 33–47, 2011.
- [26] A. Mizuno, M. Nishioka, Y. Ohno, and L. D. Dascalescu, "Liquid microvortex generated around a laser focal point in an intense high-frequency electric field," *IEEE Transactions on Industry Applications*, vol. 31, no. 3, pp. 464–468, 1995.
- [27] A. Mizuno, H. Sakano, and Y. Ohno, "Opto-electrostatic micro-manipulation of cells and fine particles," *Review of Laser Engineering*, vol. 19, no. 9, pp. 895–900, 1991.
- [28] A. Mizuno, M. Imamura, and K. Hosoi, "Manipulation of single fine particle in liquid by electrical force in combination with optical pressure," *IEEE Transactions on Industry Applications*, vol. 27, no. 1, pp. 140–146, 1991.
- [29] M. Nishioka, T. Tanizoe, S. Katsura, and A. Mizuno, "Micro manipulation of cells and DNA molecules," *Journal of Electrostatics*, vol. 35, no. 1, pp. 83–91, 1995.
- [30] R. C. Hayward, D. A. Saville, and I. A. Aksay, "Electrophoretic assembly of colloidal crystals with optically tunable micropatterns," *Nature*, vol. 404, no. 6773, pp. 56–59, 2000.
- [31] P. Y. Chiou, A. T. Ohta, and M. C. Wu, "Massively parallel manipulation of single cells and microparticles using optical images," *Nature*, vol. 436, no. 7049, pp. 370–372, 2005.
- [32] W. Choi, S. H. Kim, J. Jang, and J. K. Park, "Lab-on-a-display: a new microparticle manipulation platform using a liquid crystal display (LCD)," *Microfluidics and Nanofluidics*, vol. 3, no. 2, pp. 217–225, 2007.
- [33] Y. S. Lu, Y. P. Huang, J. A. Yeh, C. Lee, and Y. H. Chang, "Controllability of non-contact cell manipulation by image dielectrophoresis (iDEP)," *Optical and Quantum Electronics*, vol. 37, no. 13–15, pp. 1385–1395, 2005.
- [34] H. Hwang, Y. Oh, J. J. Kim et al., "Reduction of nonspecific surface-particle interactions in optoelectronic tweezers," *Applied Physics Letters*, vol. 92, no. 2, Article ID 024108, 2008.
- [35] H. Hwang, Y. J. Choi, W. Choi, S. H. Kim, J. Jang, and J. K. Park, "Interactive manipulation of blood cells using a lens-integrated liquid crystal display based optoelectronic tweezers system," *Electrophoresis*, vol. 29, no. 6, pp. 1203–1212, 2008.
- [36] W. Choi, S. W. Nam, H. Hwang, S. Park, and J. K. Park, "Programmable manipulation of motile cells in optoelectronic tweezers using a grayscale image," *Applied Physics Letters*, vol. 93, no. 14, Article ID 143901, 2008.
- [37] H. Hwang, D. H. Lee, W. Choi, and J. K. Park, "Enhanced discrimination of normal oocytes using optically induced pulling-up dielectrophoretic force," *Biomicrofluidics*, vol. 3, no. 1, Article ID 014103, 2009.

- [38] H. Hwang, Y. H. Park, and J. K. Park, "Optoelectrofluidic control of colloidal assembly in an optically induced electric field," *Langmuir*, vol. 25, no. 11, pp. 6010–6014, 2009.
- [39] J. K. Valley, A. Jamshidi, A. T. Ohta, H. Y. Hsu, and M. C. Wu, "Operational regimes and physics present in optoelectronic tweezers," *Journal of Microelectromechanical Systems*, vol. 17, no. 2, pp. 342–350, 2008.
- [40] A. Kumar, S. J. Williams, H.-S. Chuang, N. G. Green, and S. T. Wereley, "Hybrid opto-electric manipulation in microfluidics—opportunities and challenges," *Lab on a Chip*, vol. 11, pp. 2135–2148, 2011.
- [41] T. B. Jones, *Electromechanics of Particles*, Cambridge University Press, New York, NY, USA, 1995.
- [42] L. Zheng, J. P. Brody, and P. J. Burke, "Electronic manipulation of DNA, proteins, and nanoparticles for potential circuit assembly," *Biosensors and Bioelectronics*, vol. 20, no. 3, pp. 606–619, 2004.
- [43] P. Y. Chiou, A. T. Ohta, A. Jamshidi, H. Y. Hsu, and M. C. Wu, "Light-actuated AC electroosmosis for nanoparticle manipulation," *Journal of Microelectromechanical Systems*, vol. 17, no. 3, pp. 525–531, 2008.
- [44] S. J. Williams, A. Kumar, N. G. Green, and S. T. Wereley, "A simple, optically induced electrokinetic method to concentrate and pattern nanoparticles," *Nanoscale*, vol. 1, no. 1, pp. 133–137, 2009.
- [45] A. Jamshidi, S. L. Neale, K. Yu et al., "Nanopen: dynamic, low-power, and light-actuated patterning of nanoparticles," *Nano Letters*, vol. 9, no. 8, pp. 2921–2925, 2009.
- [46] A. Ajdari, "Pumping liquids using asymmetric electrode arrays," *Physical Review E*, vol. 61, no. 1, pp. R45–R48, 2000.
- [47] A. Ramos, H. Morgan, N. G. Green, and A. Castellanos, "AC electrokinetics: a review of forces in microelectrode structures," *Journal of Physics D*, vol. 31, no. 18, pp. 2338–2353, 1998.
- [48] A. Jamshidi, P. J. Pauzauskie, P. J. Schuck et al., "Dynamic manipulation and separation of individual semiconducting and metallic nanowires," *Nature Photonics*, vol. 2, no. 2, pp. 86–89, 2008.
- [49] P. J. Pauzauskie, A. Jamshidi, J. K. Valley, J. H. Satcher, and M. C. Wu, "Parallel trapping of multiwalled carbon nanotubes with optoelectronic tweezers," *Applied Physics Letters*, vol. 95, no. 11, Article ID 113104, 2009.
- [50] H. Hwang, J. J. Kim, and J. K. Park, "Experimental investigation of electrostatic particle-particle interactions in optoelectronic tweezers," *Journal of Physical Chemistry B*, vol. 112, no. 32, pp. 9903–9908, 2008.
- [51] D. G. Hafeman, J. B. Harkins, C. E. Witkowski et al., "Optically directed molecular transport and 3D isoelectric positioning of amphoteric biomolecules," *Proceedings of the National Academy of Sciences of the United States of America*, vol. 103, no. 17, pp. 6436–6441, 2006.
- [52] A. Braiman, F. Rudakov, and T. Thundat, "Highly selective separation of DNA fragments using optically directed transport," *Applied Physics Letters*, vol. 96, no. 5, Article ID 053701, 2010.
- [53] M. Hoeb, J. O. Rädler, S. Klein, M. Stutzmann, and M. S. Brandt, "Light-induced dielectrophoretic manipulation of DNA," *Biophysical Journal*, vol. 93, no. 3, pp. 1032–1038, 2007.
- [54] H. Hwang and J. K. Park, "Dynamic light-activated control of local chemical concentration in a fluid," *Analytical Chemistry*, vol. 81, no. 14, pp. 5865–5870, 2009.
- [55] M. Nakano, H. Kurita, J. Komatsu, A. Mizuno, and S. Katsura, "Stretching of long DNA molecules in the microvortex induced by laser and ac electric field," *Applied Physics Letters*, vol. 89, no. 13, Article ID 133901, 2006.
- [56] X. Sun, S. M. Tabakman, W. S. Seo et al., "Separation of nanoparticles in a density gradient: FeCo@C and gold nanocrystals," *Angewandte Chemie International Edition*, vol. 48, no. 5, pp. 939–942, 2009.
- [57] S. F. Sweeney, G. H. Woehrle, and J. E. Hutchison, "Rapid purification and size separation of gold nanoparticles via diafiltration," *Journal of the American Chemical Society*, vol. 128, no. 10, pp. 3190–3197, 2006.
- [58] J. H. Kang and J. K. Park, "Magnetophoretic continuous purification of single-walled carbon nanotubes from catalytic impurities in a microfluidic device," *Small*, vol. 3, no. 10, pp. 1784–1791, 2007.
- [59] Y. Q. Xu, H. Peng, R. H. Hauge, and R. E. Smalley, "Controlled multistep purification of single-walled carbon nanotubes," *Nano Letters*, vol. 5, no. 1, pp. 163–168, 2005.
- [60] Y. H. Lin and G. B. Lee, "Optically induced flow cytometry for continuous microparticle counting and sorting," *Biosensors and Bioelectronics*, vol. 24, no. 4, pp. 572–578, 2008.
- [61] R. G. Freeman, K. C. Grabar, K. J. Allison et al., "Self-assembled metal colloid monolayers: an approach to SERS substrates," *Science*, vol. 267, no. 5204, pp. 1629–1632, 1995.
- [62] L. Gunnarsson, E. J. Bjerneld, H. Xu, S. Petronis, B. Kasemo, and M. Käll, "Interparticle coupling effects in nanofabricated substrates for surface-enhanced Raman scattering," *Applied Physics Letters*, vol. 78, no. 6, pp. 802–804, 2001.
- [63] A. Dhawan, Y. Du, F. Yan, M. D. Gerhold, V. Misra, and T. Vo-Dinh, "Methodologies for developing surface-enhanced Raman scattering (SERS) substrates for detection of chemical and biological molecules," *IEEE Sensors Journal*, vol. 10, no. 3, Article ID 5419269, pp. 608–616, 2010.
- [64] I. F. Cheng, C. C. Lin, D. Y. Lin, and H. C. Chang, "A dielectrophoretic chip with a roughened metal surface for on-chip surface-enhanced Raman scattering analysis of bacteria," *Biomicrofluidics*, vol. 4, no. 3, Article ID 034104, pp. 1–11, 2010.
- [65] Y. S. Huh, A. J. Chung, B. Cordovez, and D. Erickson, "Enhanced on-chip SERS based biomolecular detection using electrokinetically active microwells," *Lab on a Chip*, vol. 9, no. 3, pp. 433–439, 2009.
- [66] H. Hwang, D. Han, Y. J. Oh, Y. K. Cho, K. H. Jeong, and J. K. Park, "In situ dynamic measurements of the enhanced SERS signal using an optoelectrofluidic SERS platform," *Lab on a Chip*, vol. 11, no. 15, pp. 2518–2525, 2011.
- [67] H. Hwang and J. K. Park, "Measurement of molecular diffusion based on optoelectrofluidic fluorescence microscopy," *Analytical Chemistry*, vol. 81, no. 21, pp. 9163–9167, 2009.
- [68] D. Axelrod, D. E. Koppel, J. Schlessinger, E. Elson, and W. W. Webb, "Mobility measurement by analysis of fluorescence photobleaching recovery kinetics," *Biophysical Journal*, vol. 16, no. 9, pp. 1055–1069, 1976.
- [69] E. L. Elson and D. Magde, "Fluorescence correlation spectroscopy. I. Conceptual basis and theory," *Biopolymers*, vol. 13, no. 1, pp. 1–27, 1974.
- [70] S. M. Block, L. S. B. Goldstein, and B. J. Schnapp, "Bead movement by single kinesin molecules studied with optical tweezers," *Nature*, vol. 348, no. 6299, pp. 348–352, 1990.
- [71] E. A. Abbondanzieri, W. J. Greenleaf, J. W. Shaevitz, R. Landick, and S. M. Block, "Direct observation of base-pair stepping by RNA polymerase," *Nature*, vol. 438, no. 7067, pp. 460–465, 2005.

- [72] T. R. Strick, V. Croquette, and D. Bensimon, "Single-molecule analysis of DNA uncoiling by a type II topoisomerase," *Nature*, vol. 404, no. 6780, pp. 901–904, 2000.
- [73] M. Rief, F. Oesterhelt, B. Heymann, and H. E. Gaub, "Single molecule force spectroscopy on polysaccharides by atomic force microscopy," *Science*, vol. 275, no. 5304, pp. 1295–1297, 1997.
- [74] K. C. Neuman and A. Nagy, "Single-molecule force spectroscopy: optical tweezers, magnetic tweezers and atomic force microscopy," *Nature Methods*, vol. 5, no. 6, pp. 491–505, 2008.
- [75] Y. H. Lin, C. M. Chang, and G. B. Lee, "Manipulation of single DNA molecules by using optically projected images," *Optics Express*, vol. 17, no. 17, pp. 15318–15329, 2009.
- [76] H. Hwang, H. Chon, J. Choo, and J. K. Park, "Optoelectrofluidic sandwich immunoassays for detection of human tumor marker using surface-enhanced Raman scattering," *Analytical Chemistry*, vol. 82, no. 18, pp. 7603–7610, 2010.
- [77] X. Jiang, J. M. K. Ng, A. D. Stroock, S. K. W. Dertinger, and G. M. Whitesides, "A miniaturized, parallel, serially diluted immunoassay for analyzing multiple antigens," *Journal of the American Chemical Society*, vol. 125, no. 18, pp. 5294–5295, 2003.
- [78] P. Yager, T. Edwards, E. Fu et al., "Microfluidic diagnostic technologies for global public health," *Nature*, vol. 442, no. 7101, pp. 412–418, 2006.
- [79] H. Y. Hsu, A. T. Ohta, P. Y. Chiou, A. Jamshidi, S. L. Neale, and M. C. Wu, "Phototransistor-based optoelectronic tweezers for dynamic cell manipulation in cell culture media," *Lab on a Chip*, vol. 10, no. 2, pp. 165–172, 2010.

## Review Article

# Light-Driven Droplet Manipulation Technologies for Lab-on-a-Chip Applications

**Sung-Yong Park and Pei-Yu Chiou**

*Department of Mechanical and Aerospace Engineering, University of California, Los Angeles, CA 90095-1597, USA*

Correspondence should be addressed to Pei-Yu Chiou, [pchiou@seas.ucla.edu](mailto:pchiou@seas.ucla.edu)

Received 15 June 2011; Accepted 20 August 2011

Academic Editor: Aaron T. Ohta

Copyright © 2011 S.-Y. Park and P.-Y. Chiou. This is an open access article distributed under the Creative Commons Attribution License, which permits unrestricted use, distribution, and reproduction in any medium, provided the original work is properly cited.

Droplet-based (digital) microfluidics has been demonstrated in many lab-on-a-chip applications due to its free cross-contamination and no dispersion nature. Droplet manipulation mechanisms are versatile, and each has unique advantages and limitations. Recently, the idea of manipulating droplets with light beams either through optical forces or light-induced physical mechanisms has attracted some interests, since light can achieve 3D addressing, carry high energy density for high speed actuation, and be patterned and dynamically reconfigured to generate a large number of light beams for massively parallel manipulation. This paper reviews recent developments of various optical technologies for droplet manipulation and their applications in lab-on-a-chip.

## 1. Introduction

Microfluidic devices promise a broad range of biomedical and chemical applications due to their potentials of small volume requirement, short analysis and diagnostic time, high sensitivity, and high throughput analysis [1–3]. Recently, particular attention has been paid to droplet-based (digital) microfluidic devices since droplets isolated in immiscible oil or air can be free from cross-contamination and dispersion [4]. Numerous droplet-based applications including protein crystallization [5, 6], polymerase chain reaction (PCR) [7, 8], enzyme kinetic assays [3, 9], and synthesis of organic molecules or nanoparticles [10, 11] have been demonstrated.

Droplet manipulation mechanisms that have been investigated cover a broad range of physical principles, including electrowetting on dielectric (EWOD) [12, 13], dielectrophoresis (DEP) [14, 15], thermocapillary force [16, 17], surface acoustic wave [18], magnetic force [19, 20], and optical forces [21]. In recent years, many light-driven droplet actuation mechanisms have been demonstrated, aiming to provide more functionalities, flexibility, lower cost, and higher throughput droplet manipulation tools or platforms [22, 23].

In general, optical-based droplet manipulation technologies can provide several unique advantages. First, light can be patterned and reconfigured to provide dynamic images, which in turn provides dynamic control of the triggered physical mechanisms without using complex control circuitry on chip. Millions of optical pixels can be readily generated by commercial spatial light modulators such as a LCD or DMD display to provide control of millions of electrodes in parallel on a low-cost and disposable device. Second, some optical methods can provide 3D manipulation of droplets since light can be propagated and focused in free space without needing any media. The energy can be delivered to any arbitrary locations in space to trigger an event.

This paper reviews optical manipulation mechanisms that have been utilized for manipulating droplets. A brief comparison of these technologies is summarized in Table 1.

## 2. Optical Droplet Manipulation Technologies

Light-driven droplet manipulation technologies are in general based on three basic concepts: (1) direct optical forces, (2) opto-electrical, and (3) optothermal. Figure 1 shows

TABLE I: Various optical technologies for droplet manipulation.

Platform	Manipulation principles	Targets	Functions and applications	Light sources	References
Pure optics	Optical levitation	Aerosol droplets (about tens of $\mu\text{m}$ in diameter)	Droplet levitation, atmospheric physics, chemistry, and hygroscopy	Ar <sup>+</sup> laser (488 nm, 1.2 W) Nd:YVO <sub>4</sub> laser (532 nm, 150 mW)	Jordanov and Zellner [37] Kohira et al. [36]
	Optical tweezers	Aerosol droplets (1 ~ 10 $\mu\text{m}$ in diameter)	Droplet trap, atmospheric chemistry and physics (Brownian dynamics), combustion science, and drug delivery	Nd:YAG laser (1064 nm, 5 mW) Nd:YAG laser (532 nm, 2 W)	Magome et al. [40], McGloin et al. [21] Leonardo et al. [43]
	Optical vortex traps	Aqueous droplets in oil (1 ~ 10 $\mu\text{m}$ in diameter)	Droplet trap, transport, fusion, dynamic control of concentration	Nd:YAG laser to create Laguerre-Gaussian beam	Gabagan and Swartzlander [47], Lorenz et al. [49]
Optothermal	Photothermocapillary in microfluidic channels	Aqueous droplets in oil (pL ~ $\mu\text{L}$ )	Droplet transport, trapping, high-speed sorting, and protein assay	Holographic laser (532 nm, 4 W) Argon-ion laser (514.5 nm in vacuum, 159 mW) Projector	Cordero et al. [52] Vincent et al. [53], Kotz et al. [54] Hu and Ohta [55]
	Photothermal cavitations in microfluidic channels	Picoliter aqueous droplets in oil	High-speed droplet generation, and fast droplet merging	Q-switched Nd:YVO <sub>4</sub> pulse laser (532 nm, 15 ns width, 100 $\mu\text{J}$ ) Nd:YAG pulse laser (532 nm, 6 ns width, 100 $\mu\text{J}$ )	Park et al. [56] Li et al. [57]
Optoelectronic	Optoelectrowetting (OEW) Open-OEW COEW SCOEW	Aqueous droplets in air or oil (pL ~ $\mu\text{L}$ )	Droplet transport, mixing, splitting, dispensing, and integration with an external reservoir	Laser (532 nm, 636 mW/cm <sup>2</sup> ) Laser (760 nm, 15 mW/cm <sup>2</sup> ) Laser (632 nm, 254 W/cm <sup>2</sup> ) Projector, or LCD	Chiou et al. [58, 59] Chuang et al. [60] Chiou et al. [61] Park et al. [62]
	OET FEOET	Aqueous droplets in oil (nL ~ $\mu\text{L}$ )	Droplet transport, mixing, integration with microfluidic channel, and microwell structures	LCD Laser (532 nm, 400 $\mu\text{W/cm}^2$ ) or projector	Lee et al. [63] Park et al. [23, 64]
	Combination of OET and COEW	Nanoliter aqueous droplets in air	Droplet splitting for enhancing particle concentration, and single-cell encapsulation	Projector	Valley et al. [22]

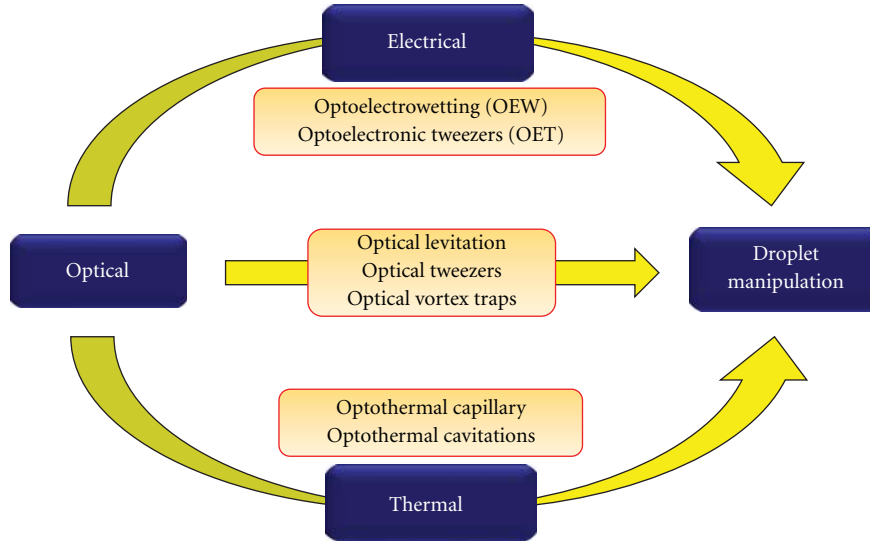


FIGURE 1: Illustration of optical energy transduction pathways used in optical methods for droplet manipulation.

the energy transduction pathways of mechanisms that have been applied for droplet manipulation. The principles, applications, and limitations of these mechanisms will be discussed in the following sections.

**2.1. Droplet Actuation Using Direct Optical Forces.** Optical tweezers is an useful technology in several fields of physics, chemistry, and biology [24]. It has been applied to trap, transport, pattern, and sort microscopic objects ranging from dielectric particles, viruses, living cells, bacteria, and small metal particles [24–31]. Two different types of forces are involved in optical manipulation. Scattering forces generate forces on particles in the light beam propagation direction [32], while gradient forces attract particles to regions of high intensity [24]. Since an optical force is typically in the range of pN, only small size of droplets can be effectively manipulated.

**2.1.1. Optical Levitation.** Optical levitation is a method using a lightly focused light beam to irradiate an aerosol droplet and create a scattering force to balance the gravitation force of the droplet [33–35]. The size of suspended droplets is in the range of tens of micrometers. This technique has been used in measuring the droplet size and phase in thermodynamic equilibrium, which is controlled by temperature, composition of atmospheric aerosols, and relative humidity [36, 37].

**2.1.2. Optical Tweezers and Optical Vortex Traps.** A tightly focused laser beam is used to generate large gradient force to form a stable trap for an aerosol droplet smaller than  $10\ \mu\text{m}$  in diameter, and prevent external perturbation from gas flow or collision of other aerosols [38]. The enhanced droplet position stability can provide excellent signal-to-noise ratio

in data acquisition in short timescales. This gradient force of the optical tweezers can be expressed by [31]

$$F = Q \frac{nP}{c}, \quad (1)$$

where  $c/n$  is the light speed in the medium,  $Q$  is the dimensionless trapping efficiency, and  $P$  is the power of the incident light.

Figure 2 shows a typical experimental setup of an optical tweezers system for trapping dual aerosol droplets in gas [39]. An intense laser beam is focused through a high N.A objective lens to maximize the gradient force for optical trapping in a specially designed cell. Aerosols are generated from an ultrasonic nebulizer and introduced into the cell. The relative humidity is controlled by the flow rate of humidified nitrogen gas into the cell.

Magome et al. has demonstrated droplet trapping in air using optical tweezers [40]. The size and compositions of trapped droplets can be investigated using droplet cavity enhanced Raman spectroscopy (CERS) [41, 42]. This technique has shown that the droplet volume is preserved with extremely high precision when undergoing coagulation. Leonardo et al. have used optical trapping to study the Brownian dynamics of a water droplet, whose displacement is determined by the viscosity of the gas phase and the optical power for trapping [43]. Reid's group has studied extensively the relative humidity effects on the equilibrium droplet size, thermodynamic properties of an aerosol, chemical compositions, and coagulation using optical tweezers and Raman spectroscopy [44, 45]. Holographic optical tweezers was also utilized to create multiple optical traps to manipulate an array of aerosol droplets in air and characterize the coagulation and mixing of multiple aerosols [21, 46].

Optical trapping using a strongly focused laser beam with a Gaussian profile allows trapping high refractive index objects ( $n_o$ ) in a low refractive index medium ( $n_m$ ) such as

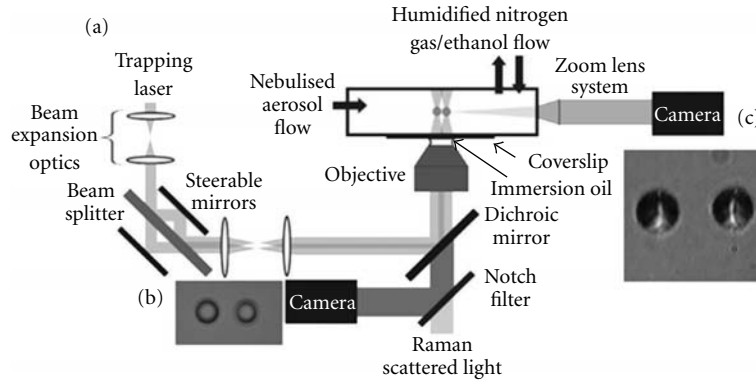


FIGURE 2: (a) Experimental setup of a dual trapping optical tweezers system. Reproduced with permission from [39] (b) In-plane image and (c) Side image of two optically trapped NaCl/aqueous aerosol droplets.

beads or cells dispersed in an aqueous buffer or aqueous droplets in air.

However, optical trapping of aqueous droplets dispersed in immiscible oil, which is a situation commonly used in digital microfluidics, cannot be achieved with this simple Gaussian beam, since the refractive index of water is lower than that of oil ( $n_{\text{water}} < n_{\text{oil}}$ ). The optical gradient force repels an oil-immersed water droplet, instead of trapping it.

To overcome this issue, Gahagan and Swartzlander have demonstrated three-dimensional trapping of low-index particles in water using a single dark optical vortex laser beam [47, 48]. Instead of using Gaussian beam profile, optical vortex traps are based on the ring-shaped laser beam profile with a dark core in the focal point (Figure 3). Optical gradient force pushes a low-index particle away from the region of high light intensity. As a result, the ring-shaped laser beam forms a potential barrier and trap a low-index particle at the dark core, where a net force of all gradient forces is zero [49]. Compared to optical tweezers, optical vortex trapping provides several advantages. First, it enables a stable optical trap of low-index particles such as water droplets dispersed in oil. Second, the potential barrier created by an optical vortex trap allows isolating a single droplet from potential contamination from other droplets. Utilizing the optical vortex trapping technique, Chiu's group has demonstrated optical manipulation of femtoliter volume droplets immersed in oil such as droplet trap, fusion, and dynamic control of concentrations of dissolved species [50, 51].

**2.2. Optothermal Droplet Actuation.** Optics has been commonly used as heating sources in many biomedical and manufacturing areas [65]. Recently optothermal effects have been applied in manipulating droplets in digital microfluidics. Compared to direct optical forces, optothermal mechanisms could provide much larger forces to allow faster droplet manipulation in high-throughput applications.

**2.2.1. Optothermal Capillary.** The Marangoni effect is a phenomenon of liquid movement induced by surface tension

difference. Thermocapillary is the Marangoni effect associated with surface tension difference induced by temperature gradient. This thermocapillary phenomenon was first investigated by Young et al. who observed air bubble motion in silicone oil induced by temperature gradient [66]. In an unconfined fluid, thermocapillary migration speed,  $U_{\text{Th}}$ , of a droplet can be expressed by [67]

$$U_{\text{Th}} = -\frac{2}{2\mu_o + 3\mu_i} \left( \frac{\partial\sigma}{\partial T} \right) \frac{R}{2 + \Lambda_i/\Lambda_o} \nabla T, \quad (2)$$

where  $R$  is the droplet radius,  $\mu_o$  and  $\mu_i$  are the shear viscosity, and  $\Lambda_o$  and  $\Lambda_i$  the thermal conductivities of the fluid inside and outside the droplet. The thermocapillary migration speed is proportional to droplet size ( $R$ ), the ratio of change of surface tension with temperature ( $\partial\sigma/\partial T$ ), and temperature gradient ( $\nabla T$ ). It is noted that when  $\partial\sigma/\partial T < 0$ , the droplet is attracted to the light illumination region, the hot zone, while it is repelled if  $\partial\sigma/\partial T > 0$ .

Conventional thermocapillary devices typically use microfabricated electrical resistors to generate heat and temperature gradient for droplet transport, trapping, and sorting on trajectories of prepatterned structures [68, 69]. Optothermal capillary induces the Marangoni effect by localized laser heating at a droplet interface. This increases the local temperature and decreases the surface tension at the heated site. The light-induced surface tension gradient causes a droplet to move toward the colder region [54]. Optically induced thermocapillary forces have been used for demonstrating many droplet-based microfluidic phenomena. Baroud et al. showed the interfacial flow induced by a thermocapillary force at the water/oil interface (Figure 4(a)) [70]. In the case of droplets carried by immiscible oil flow in microchannels ( $\partial\sigma/\partial T > 0$ ), laser focusing at the front of a droplet causes a thermocapillary force to balance against the drag force from the hydrodynamic oil flow [70]. In addition, shaping a laser beam with holographic technology allows multidroplet patterning and merging [52]. Vincent et al. showed high-speed sorting and 100% sorting efficiency for droplets moving at speed up to 1.3 cm/s in microfluidic devices [53].

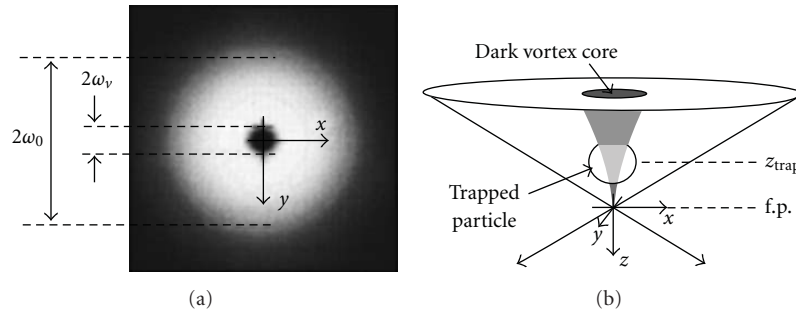
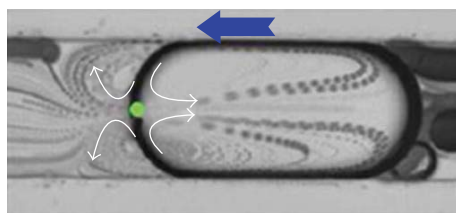
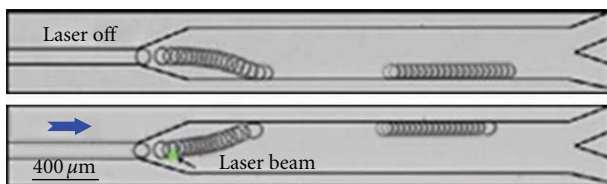


FIGURE 3: (a) Intensity profile of an optical vortex beam with beam waist  $\omega_0$  and vortex waist  $\omega_v$  at input aperture of focusing objective. (b) Schematic diagram of stable tapping for a low-index particle in an optical vortex trap. Reproduced with permission from [47].



(a)



(b)

FIGURE 4: (a) Superposition of 100 frames from a video sequence showing the motion of seeding particles near the hot spot. Note that the motion along the interface is directed towards the hot spot. Reproduced with permission from [70]. (b) Superposition of successive frames illustrating drop switching by local thermocapillary actuation. The arrow indicates the laser location observed by the fluorescence of the water-dye solution. Reproduced with permission from [53].

Recently, Ohta et al. have also reported droplet manipulation driven by the optothermal capillary effect on a light absorbing a-Si:H coated glass substrate using an optical projector [55, 71].

**2.2.2. Optothermal Cavitation Bubbles.** Laser-induced cavitation is a phenomenon caused by tightly focusing an intense laser pulse in water to generate a rapidly expanding vapor bubble through nonlinear optical absorption [72]. Figure 5 illustrates the principle of laser-induced plasma formation followed by the emission of shock wave and the generation of a cavitation bubble. When a laser pulse is intensively focused into a liquid medium, such as water, strong optical fields can breakdown water molecules and produce hot plasma at the focal point (Figure 5(a)). This hot plasma leads to an explosive vapor bubble that expand

at high speed and collapse rapidly (Figures 5(b) and 5(c)) [73–77]. The expansion speed of a laser-induced cavitation bubble is fast and can go up to hundreds of m/s within  $1 \mu\text{s}$ . Such high-speed cavitation bubbles have been used in many microfluidic applications such as cell lysing [77], microfluidic mixing [78], pumping [79], and switching [80].

Park et al. have demonstrated a high-speed, on-demand droplet generation device using such ultrafast microfluidic flow triggered by pulse laser induced cavitation bubbles. This mechanism is called pulse laser driven droplet generation (PLDG) [56]. It enables on-demand water droplet generation in microfluidic channels at a speed up to 10,000 droplets/sec with less than 1% droplet volume variation. PLDG devices have a simple structure, consisting of only two channels, one for water and one for oil, connected by a nozzle-shaped opening in a single-layer PDMS microfluidic chip (Figure 6). An intense laser pulse is focused in the middle of the water channel and induces a cavitation bubble to push water into the oil channel for droplet formation. By adjusting the laser energy and pulsing location, Park has demonstrated tunable droplet generation with volume ranging from 1 pL to 150 pL. Recently, Li et al. also utilized laser induced cavitation bubbles to trigger on-demand droplet fusion in microfluidic devices [57].

**2.3. Optoelectronic Droplet Actuation.** Electrokinetics is one of the most commonly used methods for manipulating small-scale particles and microfluidic flows. Electrowetting on dielectric (EWOD) and dielectrophoresis (DEP) are the most effective electrical based mechanisms for droplet manipulation. DEP manipulates droplets by patterning non-uniform electric fields. Droplets do not necessarily contact the electrodes [82], while EWOD manipulates droplets by changing surface energy between droplets and the underneath dielectric material through electrostatic energy. It provides large actuation forces and fast responses [83, 84].

Optical control of electrokinetic phenomena is usually through photoconductive materials. Light illumination on a photoconductive layer can generate virtual electrodes to locally modify electric field distribution, which in turn controls the local DEP or EWOD effects for manipulating droplets.

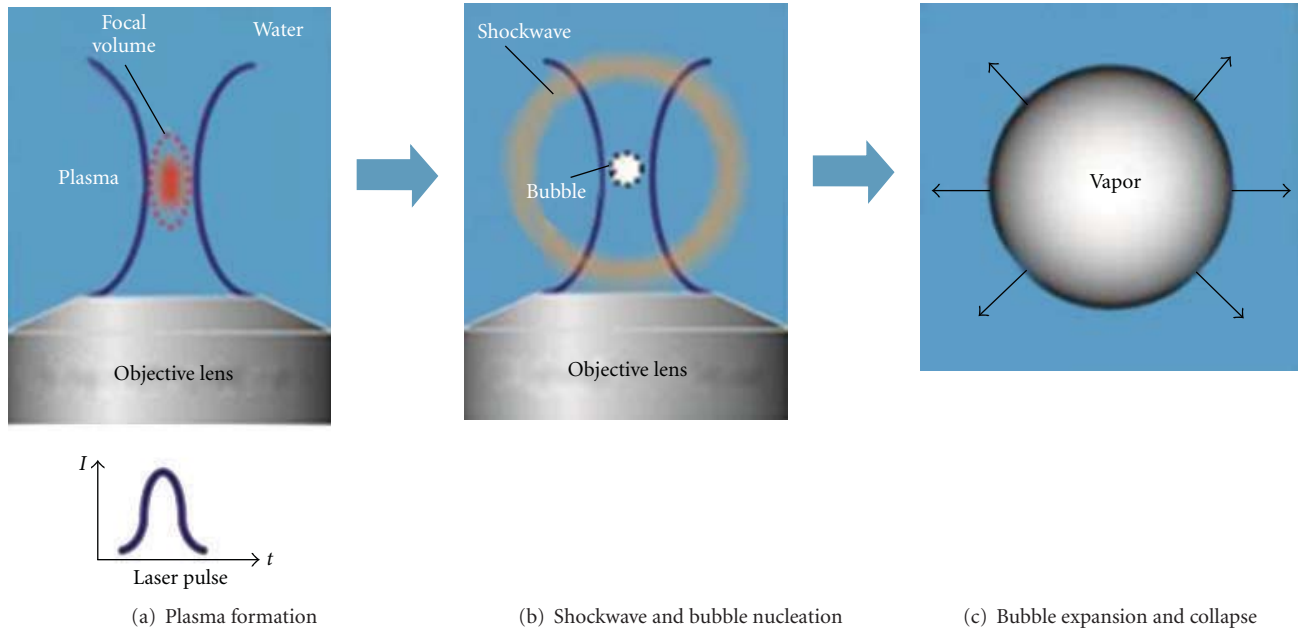


FIGURE 5: Schematic of pulse-laser induced plasma formation and the following shock wave emission and cavitation bubble generation in liquid medium. Reproduced with permission from [81].

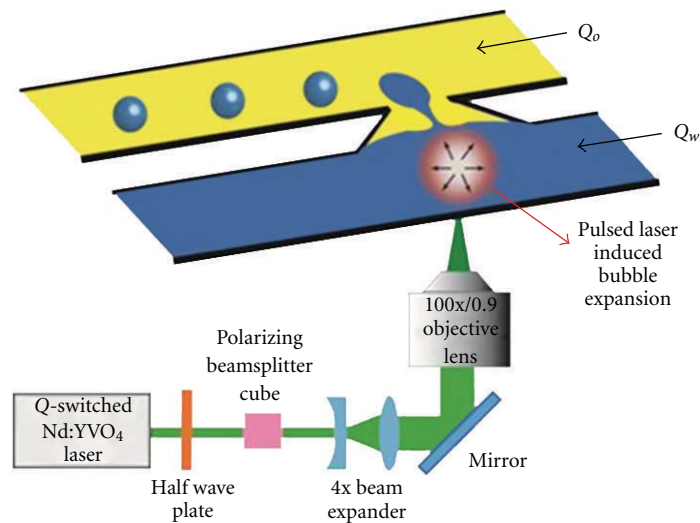


FIGURE 6: Schematic of a PLDG device that consists of two microfluidic channels connected by a nozzle-shape opening. A tightly focused laser pulse induces a rapid expanding bubble to push nearby water into the oil channel and form droplet. Reproduced with permission from [56].

**2.3.1. Optoelectrowetting (OEW).** EWOD is an effective method for manipulating microdroplets. It utilizes electrostatic energy stored in the dielectric layer between a water droplet and an electrode to change local surface tension and droplet contact angle. The difference of contact angle at edges of a droplet induces a net capillary force to actuate the droplet [84]. EWOD has been shown to be able to provide a complete droplet functions from droplet injection, transportation, merging, mixing, and splitting [12, 85–87].

Young-Lippmann equation describes that the relationship between the contact angle  $\theta$  of a droplet and the local

voltage across a dielectric layer between the droplet and the underlying electrodes [88]

$$\cos \theta = \cos \theta_0 + \frac{1}{2\gamma} \frac{\epsilon_r \epsilon_0}{t} V^2, \quad (3)$$

where  $\theta_0$  is the original contact angle,  $\gamma$  is the surface tension between the droplet and surrounding medium,  $\epsilon_0$  is vacuum permittivity,  $\epsilon_r$  is the dielectric constant,  $t$  is the thickness of the dielectric layer, and  $V$  is the voltage drop across a dielectric layer in the vertical direction at the three-phase contact line.

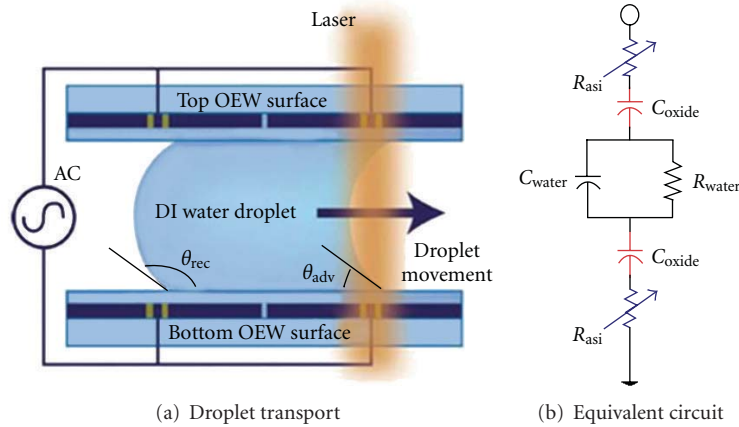


FIGURE 7: (a) Schematic of droplet actuation on an optoelectrowetting (OEW) device. (b) Its equivalent circuit model for one unit cell of OEW. Reproduced with permission from [58].

Droplet actuation on EWOD devices is typically realized by electrical activation of pixelated physical electrodes. Optoelectrowetting (OEW) uses optical images to trigger local electrowetting effects either on patterned digital electrodes or on a featureless photoconductive thin film. OEW solves the issues of complex wiring and interconnection when a large number of electrodes or droplets need to be controlled in parallel without interference.

The concept of OEW was first reported by Chiou et al. [58, 59]. He demonstrated that all droplet manipulation functions including injection, transport, separation, and multidroplet manipulation could be achieved by light beam scanning on a photoconductive chip with tens of thousands of digital electrodes with only two electrical bias wires. Figure 7 shows the configuration of an OEW device and its equivalent circuit model of one unit cell. Each plate consists of patterned indium-tin-oxide (ITO) electrodes that are bridged by photoconductive hydrogenated amorphous silicon (a-Si:H). Silicon dioxide ( $\text{SiO}_2$ ) and thin Teflon layers are deposited to provide dielectric and hydrophobic properties on top of the ITO electrodes. An AC bias with frequency at 500 Hz is used for optimal operation and a light beam causes voltage switching between the oxide capacitors ( $C_{oxide}$ ) and the photoconductors ( $R_{asi}$ ). In the absence of light illumination, the electrical impedance of  $R_{asi}$  dominates and most voltage drops across the photoconductive bridges. Therefore, ITO electrodes cannot be activated and droplet contact angle does not change. When light illuminates the photoconductive bridges nearby a droplet, the electric conductivity of the photoconductive bridges increases and ITO electrodes are activated to induce electrowetting for droplet actuation.

Conventional OEW configuration has two main drawbacks. First, it requires a sandwich structure consisting of two glass substrates. This increases the difficulty of interfacing with other microfluidic components. Second, minimum droplet size that can be actuated is limited by the size of digital electrodes as in regular EWOD devices. To overcome these limitations, several different OEW configurations have

been proposed. Chuang et al. reported an open OEW configuration enabling droplet actuation on a single-sided photoconductive surface [60]. This open configuration provides a flexible interface to allow easy integration, but the patterned pixelated electrodes still limit the controllable minimum droplet size. Chiou et al. proposed a continuous optoelectrowetting (COEW) that allows continuous transport of picoliter droplets sandwiched between two featureless photoconductive electrodes [61], but it was faced with issues of device interfacing. Later Pei et al. reported the improved COEW device and showed more reliable fabrication that consequently enabled large array of manipulation of droplets [89].

Park et al. demonstrated a single-sided continuous optoelectrowetting mechanism (SCOEW) to enable continuous, light patterned electrowetting on a featureless photoconductive surface [62]. Unlike conventional OEW, droplet actuation on SCOEW is based on optical modulation of lateral electric fields. Under uniform light illumination, the contact angle of an oil-immersed water droplet remains larger than  $90^\circ$  on top of the hydrophobic surface. As shown in Figure 8, the dark pattern illumination nearby the droplet locally increases the voltage drop across the dielectric layer. The decreased contact angle moves the droplet toward the dark region. SCOEW not only provides advantages of open configuration for easy integration and continuous manipulation to solve the size limitation issue but requires 3 orders of magnitude lower light intensity ( $\sim 400 \mu\text{W}/\text{cm}^2$ ) for droplet actuation than other OEW devices ( $\sim 1 \text{ W}/\text{cm}^2$ ). This unique advantage allows SCOEW to be operated by directly positioning a device on top of a LCD, an iPhone or an iPad screen without any extra light sources or lenses. One major limitation of SCOEW is that it requires high voltage (a few kV) in actuation and optical control of droplet motion is less straightforward than conventional OEW.

2.3.2. *Optoelectronic Tweezers (OET)*. Another widely applied principle for droplet manipulation is dielectrophoresis (DEP). It refers to an electrostatic force exerted on a

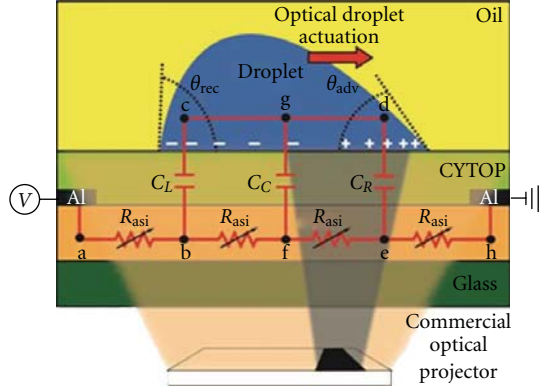


FIGURE 8: Schematic of a SCOEW device and its equivalent circuit model. Reproduced with permission from [62].

field induced electric dipole on a particle in a nonuniform electric field. This force can be approximated as [90]

$$\mathbf{F} = (\mathbf{p} \cdot \nabla)\mathbf{E}, \quad (4)$$

where  $\mathbf{p}$  represents the dipole moment and  $\mathbf{E}$  is the electric field. For a homogenous dielectric sphere, the well-known expression for DEP force is given by [91]

$$\langle \mathbf{F}_{\text{dep}} \rangle = 2\pi\epsilon_m R^3 \text{Re}[K^*(\omega)] \nabla (\mathbf{E}_{\text{rms}}^2),$$

$$K^*(\omega) = \frac{\epsilon_p^* - \epsilon_m^*}{\epsilon_p^* + 2\epsilon_m^*}, \quad \epsilon_m^* = \epsilon_m + \frac{\sigma_m}{j\omega}, \quad \epsilon_p^* = \epsilon_p + \frac{\sigma_p}{j\omega}, \quad (5)$$

where  $\langle \mathbf{F}_{\text{dep}} \rangle$  represents the timeaverage of  $\mathbf{F}_{\text{dep}}$ ,  $\mathbf{E}_{\text{rms}}$  is the root-mean square magnitude of the electric field,  $R$  is the particle radius,  $\epsilon_m$  and  $\epsilon_p$  are the permittivity of the surrounding medium and the particle, respectively,  $\sigma_m$  and  $\sigma_p$  are the electric conductivities of the medium and the particle, respectively,  $\omega$  is the angular frequency of the applied electric field, and  $K^*(\omega)$  is known as the frequency dependent Clausius-Mossotti (CM). The real part of  $K^*(\omega)$  has a value,  $0.5 \leq \text{Re}[K^*(\omega)] \leq 1.0$ , depending on the polarization of the medium and the particle at a certain frequency. In digital microfluidic devices where aqueous droplets are typically immersed in electrically insulating oil medium,  $\text{Re}[K^*(\omega)]$  has a positive value close to 1, aqueous droplets in oil experience positive DEP forces that move them toward the strong electric field regions.

Chiou et al. have demonstrated a mechanism called optoelectronic tweezers (OET) to allow light images to pattern non-uniform electric fields to induce DEP forces for microparticle [92]. OET was commonly used for manipulating particles suspended in aqueous media. Due to an electrical impedance matching issue, OET is not ideal to operate in air or in oil environment since the large electrical impedance of these media will take over most voltage even without light illumination and optical modulation of electric field is difficult in principle. In some special cases in which droplet sizes are close to the gap space between two electrodes, optical actuation could still be accomplished. Park's group achieved droplet manipulation in oil using

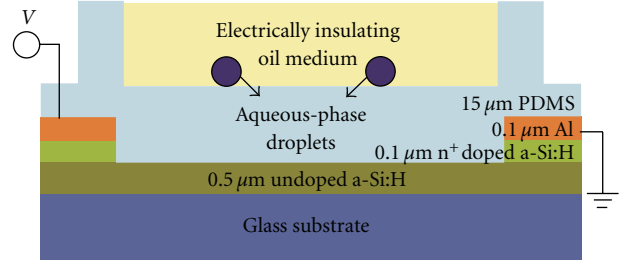


FIGURE 9: Schematic of a FEOET device. Reproduced with permission from [64].

a sandwiched OET platform integrated with microfluidic channels and showed the manipulation of picoliter droplets by optically induced DEP forces [63].

Park et al. have recently demonstrated a mechanism, called floating electrode optoelectronic tweezers (FEOET), specifically aiming for manipulating aqueous droplets suspended in electrically insulating oil and air media (Figure 9) [64]. FEOET utilizes lateral electric field as in SCOEW. The device structure of FEOET and SCOEW looks similar except that the thickness of the dielectric layer between droplets and the photoconductive layer is different. In SCOEW, this layer has to be as thin as  $1 \mu\text{m}$  to allow large contact angle modulation. In FEOET, this dielectric layer can be as thick as  $1 \text{mm}$ . The operation principle of FEOET is based the electrostatic interactions between a droplet induced dipole and the light induced dipole on the photoconductive layer under the application of a lateral field across the entire device. Both FEOET and SCOEW devices require extremely low light intensity in droplet actuation ( $\sim 400 \mu\text{W}/\text{cm}^2$ ) owing to the fact that in lateral electric field configuration, the virtual electrode is turned on as long as the light illumination can create a small photoconductivity difference between the illuminated and dark regions. This is different from other OET and OEW devices that require light to switch voltages between a photoconductor and a dielectric layer or a liquid layer. In other words, FEOET and SCOEW turn on virtual electrodes based on relative photoconductivity difference, not the absolute photoconductivity as in other devices. Using FEOET, Park has achieved transporting a  $160\text{-nL}$  droplet at a speed of  $85.1 \mu\text{m}/\text{s}$  using a light beam with an intensity of  $400 \mu\text{W}/\text{cm}^2$ . Since FEOET allows a thick dielectric layer on top of the photoconductive surface, it provides a flexible interface for integration with other microfluidic components such as microwells and microchannels [23].

Recently, Valley et al. also reported an integrated platform enabling both COEW and OET manipulation on the same chip [22]. This platform allows light beams to manipulate not only droplets but also individual cells inside these droplets. They have demonstrated concentration enhancement of cells and single-cell encapsulation in droplet.

### 3. Conclusion and Prospectus

This paper reviews various optical manipulation methods that have been demonstrated so far for manipulating liquid

droplets. These methods can be categorized into three types: (1) direct optical force, (2) optothermal, and (3) optoelectrical. Methods using direct optical forces can provide precise trapping of micrometer scale droplets in three dimensional spaces and are ideal tools for fundamental science studies. However, the high optical power requirement limits its throughput and applications in other areas.

Methods using optothermal effects can provide large forces for high-throughput and high-speed manipulation. Localized optical heating can generate temperature gradient to change surface tension, which is the dominating force in the micrometer scale, for droplet manipulation via the Marangoni effect. Optothermal actuation can also be accomplished by using intense short laser pulses to induce explosive cavitation bubbles which can generate large and transient pressure for high-speed microfluidic actuation. This novel actuation phenomenon has been utilized to demonstrate on-demand droplet injection up to 10,000 droplet/sec and on-demand droplet fusion.

Methods using optoelectrical effects could potentially provide a high throughput platform via massively parallel processing a large number of droplets across a large area. The major difference between optoelectrical from optothermal or direct optical force is that the optical energy is used to switch on electrical driving force to drive droplet motion, while in direct optical forces or in optothermal, the optical energy is directly used to power the droplet movement. This allows opto-electrical methods to actuate droplets with much lower optical power and induce minimum optical heating effect across a large area.

Optical methods for droplet manipulation are an emerging field that has already shown great promises for many applications. It provides several unique advantages that are difficult to achieve with other methods. It provides 3D addressing capability without the need of any physical electrical or mechanical interconnects that can be difficult to fabricate. Second, optical methods can deliver the highest energy density far beyond any other physical mechanisms can possibly achieve. If such energy can be properly converted into actuation forces through clever engineering designs, it can realize many novel high-speed droplet manipulation functions. Third, optical addressing provides a method to realize massively parallel droplet manipulation on a low cost and disposable platform.

Despite many promising potential applications for this technology, there are still many challenges that need to be overcome. First, many of the optical experiments still require bulky optics and lasers. Miniaturization of optical systems is critical to reduce footprint size of the integrated system, which is important for broadening future applications. A portable integrated system would be the goal. Most of the optical methods presented are enabling technologies that have to be integrated with other subsystems for real applications. Solving the interfacing issues will also be important. With the rapid progresses in photonics and optoelectronics, low-cost, compact, and high-power light sources, switches, and other components can be realized. More fundamental studies and research efforts need to be put on finding more novel and useful optical actuation mechanisms that have

higher optical energy conversion efficiency to droplet manipulation, lower optical power requirement, more reliable devices and materials, and mechanisms that can be easily interfaced with other subsystems such as microfluidic devices.

## Acknowledgments

This work is gratefully supported by an NSF CAREER Award (ECCS 0747950), NSF DBI-0852701, and NSF ECCS 0901154.

## References

- [1] H. Wang, K. Liu, K. J. Chen et al., "A rapid pathway toward a superb gene delivery system: programming structural and functional diversity into a supramolecular nanoparticle library," *ACS Nano*, vol. 4, no. 10, pp. 6235–6243, 2010.
- [2] C. C. Lee, G. Sui, A. Elizarov et al., "Multistep synthesis of a radiolabeled imaging probe using integrated microfluidics," *Science*, vol. 310, no. 5755, pp. 1793–1796, 2005.
- [3] L. S. Roach, H. Song, and R. F. Ismagilov, "Controlling non-specific protein adsorption in a plug-based microfluidic system by controlling interfacial chemistry using fluorosurfactants," *Analytical Chemistry*, vol. 77, no. 3, pp. 785–796, 2005.
- [4] H. Song, D. L. Chen, and R. F. Ismagilov, "Reactions in droplets in microfluidic channels," *Angewandte Chemie—International Edition*, vol. 45, no. 44, pp. 7336–7356, 2006.
- [5] B. T. C. Lau, C. A. Baitz, X. P. Dong, and C. L. Hansen, "A complete microfluidic screening platform for rational protein crystallization," *Journal of the American Chemical Society*, vol. 129, no. 3, pp. 454–455, 2007.
- [6] D. L. Chen, G. J. Gerdts, and R. F. Ismagilov, "Using microfluidics to observe the effect of mixing on nucleation of protein crystals," *Journal of the American Chemical Society*, vol. 127, no. 27, pp. 9672–9673, 2005.
- [7] W. Li, H. H. Pham, Z. Nie, B. MacDonald, A. Güenther, and E. Kumacheva, "Multi-step microfluidic polymerization reactions conducted in droplets: the internal trigger approach," *Journal of the American Chemical Society*, vol. 130, no. 30, pp. 9935–9941, 2008.
- [8] Z. Hua, J. L. Rouse, A. E. Eckhardt et al., "Multiplexed real-time polymerase chain reaction on a digital microfluidic platform," *Analytical Chemistry*, vol. 82, no. 6, pp. 2310–2316, 2010.
- [9] A. Huebner, M. Srisa-Art, D. Holt et al., "Quantitative detection of protein expression in single cells using droplet microfluidics," *Chemical Communications*, vol. 2, no. 12, pp. 1218–1220, 2007.
- [10] L. H. Hung, K. M. Choi, W. Y. Tseng, Y. C. Tan, K. J. Shea, and A. P. Lee, "Alternating droplet generation and controlled dynamic droplet fusion in microfluidic device for CdS nanoparticle synthesis," *Lab on a Chip*, vol. 6, no. 2, pp. 174–178, 2006.
- [11] T. Hatakeyama, D. L. Chen, and R. F. Ismagilov, "Microgram-scale testing of reaction conditions in solution using nanoliter plugs in microfluidics with detection by MALDI-MS," *Journal of the American Chemical Society*, vol. 128, no. 8, pp. 2518–2519, 2006.

- [12] J. Gong and C. J. Kim, "All-electronic droplet generation on-chip with real-time feedback control for EWOD digital microfluidics," *Lab on a Chip*, vol. 8, no. 6, pp. 898–906, 2008.
- [13] A. R. Wheeler, "Chemistry: putting electrowetting to work," *Science*, vol. 322, no. 5901, pp. 539–540, 2008.
- [14] K. Ahn, C. Kerbage, T. P. Hunt, R. M. Westervelt, D. R. Link, and D. A. Weitz, "Dielectrophoretic manipulation of drops for high-speed microfluidic sorting devices," *Applied Physics Letters*, vol. 88, no. 2, Article ID 024104, pp. 1–3, 2006.
- [15] J. R. Millman, K. H. Bhatt, B. G. Prevo, and O. D. Velev, "Anisotropic particle synthesis in dielectrophoretically controlled microdroplet reactors," *Nature Materials*, vol. 4, no. 1, pp. 98–102, 2005.
- [16] J. Z. Chen, S. M. Troian, A. A. Darhuber, and S. Wagner, "Effect of contact angle hysteresis on thermocapillary droplet actuation," *Journal of Applied Physics*, vol. 97, no. 1, Article ID 014906, pp. 014906–9, 2005.
- [17] E. F. Greco and R. O. Grigoriev, "Thermocapillary migration of interfacial droplets," *Physics of Fluids*, vol. 21, no. 4, Article ID 042105, 2009.
- [18] T. Franke, A. R. Abate, D. A. Weitz, and A. Wixforth, "Surface acoustic wave (SAW) directed droplet flow in microfluidics for PDMS devices," *Lab on a Chip*, vol. 9, no. 18, pp. 2625–2627, 2009.
- [19] M. Okochi, H. Tsuchiya, F. Kumazawa, M. Shikida, and H. Honda, "Droplet-based gene expression analysis using a device with magnetic force-based-droplet-handling system," *Journal of Bioscience and Bioengineering*, vol. 109, no. 2, pp. 193–197, 2009.
- [20] Y. Zhang, S. Park, K. Liu, J. Tsuan, S. Yang, and T. H. Wang, "A surface topography assisted droplet manipulation platform for biomarker detection and pathogen identification," *Lab on a Chip*, vol. 11, no. 3, pp. 398–406, 2011.
- [21] D. McGloin, D. R. Burnham, M. D. Summers, D. Rudd, N. Dewar, and S. Anand, "Optical manipulation of airborne particles: techniques and applications," *Faraday Discussions*, vol. 137, pp. 335–350, 2008.
- [22] J. K. Valley, S. Ningpei, A. Jamshidi, H. Y. Hsu, and M. C. Wu, "A unified platform for optoelectrowetting and optoelectronic tweezers," *Lab on a Chip*, vol. 11, no. 7, pp. 1292–1297, 2011.
- [23] S. Y. Park, S. Kalim, C. Callahan, M. A. Teitell, and E. P. Y. Chiou, "A light-induced dielectrophoretic droplet manipulation platform," *Lab on a Chip*, vol. 9, no. 22, pp. 3228–3235, 2009.
- [24] A. Ashkin, J. M. Dziedzic, J. E. Bjorkholm, and S. Chu, "Observation of a single-beam gradient force optical trap for dielectric particles," *Optics Letters*, vol. 11, no. 5, pp. 288–290, 1986.
- [25] J. E. Curtis, B. A. Koss, and D. G. Grier, "Dynamic holographic optical tweezers," *Optics Communications*, vol. 207, no. 1–6, pp. 169–175, 2002.
- [26] K. Sasaki, M. Koshioka, H. Misawa, N. Kitamura, and H. Masuhara, "Optical trapping of a metal particle and a water droplet by a scanning laser beam," *Applied Physics Letters*, vol. 60, no. 7, pp. 807–809, 1992.
- [27] A. Ashkin and J. M. Dziedzic, "Optical trapping and manipulation of viruses and bacteria," *Science*, vol. 235, no. 4795, pp. 1517–1520, 1987.
- [28] A. Ashkin, J. M. Dziedzic, and T. Yamane, "Optical trapping and manipulation of single cells using infrared laser beams," *Nature*, vol. 330, no. 6150, pp. 769–771, 1987.
- [29] D. G. Grier, "A revolution in optical manipulation," *Nature*, vol. 424, no. 6950, pp. 810–816, 2003.
- [30] U. Bockelmann, P. Thomen, B. Essevez-Roulet, V. Viasnoff, and F. Heslot, "Unzipping DNA with optical tweezers: high sequence sensitivity and force flips," *Biophysical Journal*, vol. 82, no. 3, pp. 1537–1553, 2002.
- [31] J. E. Molloy and M. J. Padgett, "Lights, action: optical tweezers," *Contemporary Physics*, vol. 43, no. 4, pp. 241–258, 2002.
- [32] A. Ashkin, "Acceleration and trapping of particles by radiation pressure," *Physical Review Letters*, vol. 24, no. 4, pp. 156–159, 1970.
- [33] A. Ashkin and J. M. Dziedzic, "Optical levitation by radiation pressure," *Applied Physics Letters*, vol. 19, no. 8, pp. 283–285, 1971.
- [34] A. Ashkin and J. M. Dziedzic, "Optical levitation of liquid drops by radiation pressure," *Science*, vol. 187, no. 4181, pp. 1073–1075, 1975.
- [35] P. T. Nagy and G. P. Neitzel, "Optical levitation and transport of microdroplets: proof of concept," *Physics of Fluids*, vol. 20, no. 10, Article ID 101703, 2008.
- [36] M. I. Kohira, A. Isomura, N. Magome, S. Mukai, and K. Yoshikawa, "Optical levitation of a droplet under a linear increase in gravitational acceleration," *Chemical Physics Letters*, vol. 414, no. 4–6, pp. 389–392, 2005.
- [37] N. Jordanov and R. Zellner, "Investigations of the hygroscopic properties of ammonium sulfate and mixed ammonium sulfate and glutaric acid micro droplets by means of optical levitation and Raman spectroscopy," *Physical Chemistry Chemical Physics*, vol. 8, no. 23, pp. 2759–2764, 2006.
- [38] R. J. Hopkins, L. Mitchem, A. D. Ward, and J. P. Reid, "Control and characterisation of a single aerosol droplet in a single-beam gradient-force optical trap," *Physical Chemistry Chemical Physics*, vol. 6, no. 21, pp. 4924–4927, 2004.
- [39] L. Mitchem, R. J. Hopkins, J. Buajarern, A. D. Ward, and J. P. Reid, "Comparative measurements of aerosol droplet growth," *Chemical Physics Letters*, vol. 432, no. 1–3, pp. 362–366, 2006.
- [40] N. Magome, M. I. Kohira, E. Hayata, S. Mukai, and K. Yoshikawa, "Optical trapping of a growing water droplet in air," *Journal of Physical Chemistry B*, vol. 107, pp. 3988–3990, 2003.
- [41] K. J. Knox, J. P. Reid, K. L. Hanford, A. J. Hudson, and L. Mitchem, "Direct measurements of the axial displacement and evolving size of optically trapped aerosol droplets," *Journal of Optics A*, vol. 9, no. 8, article S10, pp. S180–S188, 2007.
- [42] R. Symes, R. M. Sayer, and J. P. Reid, "Cavity enhanced droplet spectroscopy: principles, perspectives and prospects," *Physical Chemistry Chemical Physics*, vol. 6, no. 3, pp. 474–487, 2004.
- [43] R. D. Leonardo, G. Ruocco, J. Leach et al., "Parametric resonance of optically trapped aerosols," *Physical Review Letters*, vol. 99, no. 1, Article ID 010601, 2007.
- [44] L. Mitchem, J. Buajarern, R. J. Hopkins et al., "Spectroscopy of growing and evaporating water droplets: exploring the variation in equilibrium droplet size with relative humidity," *Journal of Physical Chemistry A*, vol. 110, no. 26, pp. 8116–8125, 2006.
- [45] L. Mitchem, J. Buajarern, A. D. Ward, and J. P. Reid, "A strategy for characterizing the mixing state of immiscible aerosol components and the formation of multiphase aerosol particles through coagulation," *Journal of Physical Chemistry B*, vol. 110, no. 28, pp. 13700–13703, 2006.
- [46] D. R. Burnham and D. McGloin, "Holographic optical trapping of aerosol droplets," *Optics Express*, vol. 14, no. 9, pp. 4176–4181, 2006.
- [47] K. T. Gahagan and G. A. Swartzlander, "Trapping of low-index microparticles in an optical vortex," *Journal of the Optical Society of America B*, vol. 15, no. 2, pp. 524–534, 1998.

- [48] K. T. Gahagan and G. A. Swartzlander, "Optical vortex trapping of particles," *Optics Letters*, vol. 21, no. 11, pp. 827–829, 1996.
- [49] R. M. Lorenz, J. S. Edgar, G. D. M. Jeffries, Y. Zhao, D. McGloin, and D. T. Chiu, "Vortex-trap-induced fusion of femtoliter-volume aqueous droplets," *Analytical Chemistry*, vol. 79, no. 1, pp. 224–228, 2007.
- [50] G. D. M. Jeffries, J. S. Kuo, and D. T. Chiu, "Dynamic modulation of chemical concentration in an aqueous droplet," *Angewandte Chemie—International Edition*, vol. 46, no. 8, pp. 1326–1328, 2007.
- [51] D. T. Chiu and R. M. Lorenz, "Chemistry and biology in femtoliter and picoliter volume droplets," *Accounts of Chemical Research*, vol. 42, no. 5, pp. 649–658, 2009.
- [52] M. L. Cordero, D. R. Burnham, C. N. Baroud, and D. McGloin, "Thermocapillary manipulation of droplets using holographic beam shaping: microfluidic pin ball," *Applied Physics Letters*, vol. 93, no. 3, Article ID 034107, 2008.
- [53] M. R. D. S. Vincent, R. Wunenburger, and J. P. Delville, "Laser switching and sorting for high speed digital microfluidics," *Applied Physics Letters*, vol. 92, no. 15, Article ID 154105, 2008.
- [54] K. T. Kotz, K. A. Noble, and G. W. Faris, "Optical microfluidics," *Applied Physics Letters*, vol. 85, no. 13, pp. 2658–2660, 2004.
- [55] W. Hu and A. T. Ohta, "Aqueous droplet manipulation by optically induced Marangoni circulation," *Microfluidics and Nanofluidics*, vol. 11, no. 3, pp. 307–316, 2011.
- [56] S. Y. Park, T. H. Wu, Y. Chen, M. A. Teitell, and P. Y. Chiou, "High-speed droplet generation on demand driven by pulse laser-induced cavitation," *Lab on a Chip*, vol. 11, no. 6, pp. 1010–1012, 2011.
- [57] Z. G. Li, K. Ando, J. Q. Yu, A. Q. Liu, J. B. Zhang, and C. D. Ohl, "Fast on-demand droplet fusion using transient cavitation bubbles," *Lab on a Chip*, vol. 11, no. 11, pp. 1879–1885, 2011.
- [58] P. Y. Chiou, Z. Chang, and M. C. Wu, "Droplet manipulation with light on optoelectrowetting device," *Journal of Microelectromechanical Systems*, vol. 17, no. 1, pp. 133–138, 2008.
- [59] P. Y. Chiou, H. Moon, H. Toshiyoshi, C. J. Kim, and M. C. Wu, "Light actuation of liquid by optoelectrowetting," *Sensors and Actuators A*, vol. 104, no. 3, pp. 222–228, 2003.
- [60] H. S. Chuang, A. Kumar, and S. T. Wereley, "Open optoelectrowetting droplet actuation," *Applied Physics Letters*, vol. 93, no. 6, Article ID 064104, 2008.
- [61] P. Y. Chiou, S. Y. Park, and M. C. Wu, "Continuous optoelectrowetting for picoliter droplet manipulation," *Applied Physics Letters*, vol. 93, no. 22, Article ID 221110, 2008.
- [62] S. Y. Park, M. A. Teitell, and E. P. Y. Chiou, "Single-sided continuous optoelectrowetting (SCOEW) for droplet manipulation with light patterns," *Lab on a Chip*, vol. 10, no. 13, pp. 1655–1661, 2010.
- [63] D. H. Lee, H. Hwang, and J. K. Park, "Generation and manipulation of droplets in an optoelectrofluidic device integrated with microfluidic channels," *Applied Physics Letters*, vol. 95, no. 16, Article ID 164102, 2009.
- [64] S. Park, C. Pan, T. H. Wu et al., "Floating electrode optoelectronic tweezers: light-driven dielectrophoretic droplet manipulation in electrically insulating oil medium," *Applied Physics Letters*, vol. 92, no. 15, Article ID 151101, 2008.
- [65] L. J. Radziemski and D. A. Cremers, *Laser-Induced Plasmas and Applications*, Marcel Dekker, New York, NY, USA, 1989.
- [66] N. O. Young, J. S. Goldstein, and M. J. Block, "The motion of bubbles in a vertical temperature gradient," *Journal of Fluid Mechanics*, vol. 6, pp. 350–356, 1959.
- [67] K. D. Barton and R. S. Subramanian, "The migration of liquid drops in a vertical temperature gradient," *Journal of Colloid and Interface Science*, vol. 133, no. 1, pp. 211–222, 1989.
- [68] B. Selva, V. Miralles, I. Cantat, and M. C. Jullien, "Thermocapillary actuation by optimized resistor pattern: bubbles and droplets displacing, switching and trapping," *Lab on a Chip*, vol. 10, no. 14, pp. 1835–1840, 2010.
- [69] A. A. Darhuber, J. P. Valentino, J. M. Davis, S. M. Troian, and S. Wagner, "Microfluidic actuation by modulation of surface stresses," *Applied Physics Letters*, vol. 82, no. 4, pp. 657–659, 2003.
- [70] C. N. Baroud, J. P. Delville, F. Gallaire, and R. Wunenburger, "Thermocapillary valve for droplet production and sorting," *Physical Review E*, vol. 75, no. 4, Article ID 046302, 2007.
- [71] A. T. Ohta, A. Jamshidi, J. K. Valley, H. Y. Hsu, and M. C. Wu, "Optically actuated thermocapillary movement of gas bubbles on an absorbing substrate," *Applied Physics Letters*, vol. 91, no. 7, Article ID 074103, 2007.
- [72] Y. R. Shen, *The Principles of Nonlinear Optics*, Wiley, New York, NY, USA, 1984.
- [73] E. A. Brujan, K. Nahen, P. Schmidt, and A. Vogel, "Dynamics of laser-induced cavitation bubbles near an elastic boundary," *Journal of Fluid Mechanics*, vol. 433, pp. 251–281, 2001.
- [74] R. K. Chang, J. H. Eickmans, W.-F. Hsieh, C. F. Wood, J.-Z. Zhang, and J.-b. Zheng, "Laser-induced breakdown in large transparent water droplets," *Applied Optics*, vol. 27, no. 12, pp. 2377–2385, 1988.
- [75] A. Vogel, S. Busch, and U. Parlitz, "Shock wave emission and cavitation bubble generation by picosecond and nanosecond optical breakdown in water," *Journal of the Acoustical Society of America*, vol. 100, no. 1, pp. 148–165, 1996.
- [76] E. Zwaan, S. Le Gac, K. Tsuji, and C. D. Ohl, "Controlled cavitation in microfluidic systems," *Physical Review Letters*, vol. 98, no. 25, Article ID 254501, 2007.
- [77] K. R. Rau, P. A. Quinto-Su, A. N. Hellman, and V. Venugopalan, "Pulsed laser microbeam-induced cell lysis: time-resolved imaging and analysis of hydrodynamic effects," *Biophysical Journal*, vol. 91, no. 1, pp. 317–329, 2006.
- [78] A. N. Hellman, K. R. Rau, H. H. Yoon et al., "Laser-induced mixing in microfluidic channels," *Analytical Chemistry*, vol. 79, no. 12, pp. 4484–4492, 2007.
- [79] R. Dijkink and C. D. Ohl, "Laser-induced cavitation based micropump," *Lab on a Chip*, vol. 8, no. 10, pp. 1676–1681, 2008.
- [80] T. H. Wu, L. Gao, Y. Chen, K. Wei, and P. Y. Chiou, "Pulsed laser triggered high speed microfluidic switch," *Applied Physics Letters*, vol. 93, no. 14, Article ID 144102, 2008.
- [81] P.-Y. Chiou, T.-H. Wu, S. Park, and Y. Chen, "Pulse laser driven ultrafast micro and nanofluidic system," in *Proceedings of the SPIE*, vol. 7759, p. 77590Z, San Diego, Calif, USA, 2010.
- [82] P. R. C. Gascoyne, J. V. Vykoukal, J. A. Schwartz et al., "Dielectrophoresis-based programmable fluidic processors," *Lab on a Chip*, vol. 4, no. 4, pp. 299–309, 2004.
- [83] H. J. Verheijen and M. W. J. Prins, "Reversible electrowetting and trapping of charge: model and experiments," *Langmuir*, vol. 15, no. 20, pp. 6616–6620, 1999.
- [84] H. Moon, S. K. Cho, R. L. Garrell, and C. J. Kim, "Low voltage electrowetting-on-dielectric," *Journal of Applied Physics*, vol. 92, no. 7, pp. 4080–4087, 2002.
- [85] A. R. Wheeler, H. Moon, C. A. Bird et al., "Digital microfluidics with in-line sample purification for proteomics analyses with MALDI-MS," *Analytical Chemistry*, vol. 77, no. 2, pp. 534–540, 2005.

- [86] S. K. Cho, H. Moon, and C. J. Kim, "Creating, transporting, cutting, and merging liquid droplets by electrowetting-based actuation for digital microfluidic circuits," *Journal of Microelectromechanical Systems*, vol. 12, no. 1, pp. 70–80, 2003.
- [87] M. Abdelgawad, S. L. S. Freire, H. Yang, and A. R. Wheeler, "All-terrain droplet actuation," *Lab on a Chip*, vol. 8, no. 5, pp. 672–677, 2008.
- [88] M. Vallet, B. Berge, and L. Vovelle, "Electrowetting of water and aqueous solutions on poly(ethylene terephthalate) insulating films," *Polymer*, vol. 37, no. 12, pp. 2465–2470, 1996.
- [89] S. N. Pei, J. K. Valley, S. L. Neale, A. Jamshidi, H. Y. Hsu, and M. C. Wu, "Light-actuated digital microfluidics for large-scale, parallel manipulation of arbitrarily sized droplets," in *Proceedings of the 23rd IEEE International Conference on Micro Electro Mechanical Systems (MEMS '10)*, pp. 252–255, January 2010.
- [90] T. B. Jones, *Electromechanics of Particles*, Cambridge University Press, 1995.
- [91] H. Pohl, *Dielectrophoresis*, Cambridge University Press, Cambridge, UK, 1978.
- [92] P. Y. Chiou, A. T. Ohta, and M. C. Wu, "Massively parallel manipulation of single cells and microparticles using optical images," *Nature*, vol. 436, no. 7049, pp. 370–372, 2005.

## Research Article

# Fluorescence Detection 400–480 nm Using Microfluidic System Integrated GaP Photodiodes

Dion McIntosh,<sup>1</sup> Qiugui Zhou,<sup>1</sup> Francisco J. Lara,<sup>2</sup> James Landers,<sup>2</sup> and Joe C. Campbell<sup>1</sup>

<sup>1</sup>Department of Electrical Engineering, University of Virginia, 351 McCormick Road, Charlottesville, VA 22904, USA

<sup>2</sup>Department of Chemistry, University of Virginia, McCormick Road, P.O. Box 400319, Charlottesville, VA 22904, USA

Correspondence should be addressed to Joe C. Campbell, jcc7s@virginia.edu

Received 29 April 2011; Revised 14 August 2011; Accepted 21 August 2011

Academic Editor: Zhihong Li

Copyright © 2011 Dion McIntosh et al. This is an open access article distributed under the Creative Commons Attribution License, which permits unrestricted use, distribution, and reproduction in any medium, provided the original work is properly cited.

Ciprofloxacin is a commonly used antibiotic and the active ingredient in a veterinary antibiotic. Detecting its presence allows us to understand its absorption process in blood as well as tissue. A portable microfluidic system has been fabricated. It operates at low bias voltage and shows a linear relationship between concentration levels and system response. Detection of concentrations down to 1 ppb of ciprofloxacin in microliters of solution was achieved.

## 1. Introduction

As the medical industry has evolved, it has become necessary to have accurate testing available in the shortest possible time [1–5]. Miniaturizing UV and fluorescence detectors and extending them to fluid analysis is one way of bridging this gap [6–9].

Detecting ciprofloxacin has become increasingly important because it is the active ingredient in enrofloxacin an antibiotic used in veterinary medicine [10, 11]. Interest in monitoring ciprofloxacin levels in the tissues of animals raised for food and in the milk of cows has led to improvements in current technology and a search for new detection techniques. Ciprofloxacin absorbs strongly in the UV ( $\leq 280$  nm) and emits at  $\sim 440$  nm [10].

Currently, online detection is carried out by analytical methods such as high-performance liquid chromatography (HPLC), which involves a relatively costly investment in hardware [12, 13], or by capillary electrophoresis. Capillary electrophoresis (CE), while simpler than the aforementioned HPLC, still requires complex sample preparation methods utilizing pH adjustment to reach lower detection limits and requires very high bias voltage (kV) [12, 14]. These two methods usually employ photomultiplier tubes (PMTs) for photodetection.

PMTs have been used in applications such as low-level ultraviolet detection in laser-induced fluorescence

biological-agent warning systems [15]. Other applications in this wavelength range are under-water detection at 400 nm, the wavelength at which water is transparent, and detection of 440 nm-wavelength light from scintillation crystals that are used to sense gamma rays from nuclear material.

While PMTs are among the most sensitive detectors currently available, semiconductor photodiodes offer the advantages of being less expensive and more robust. Si photodiodes have high responsivities at 440 nm; however, GaP exhibits a detection cutoff wavelength of 550 nm, which makes it an attractive alternative to Si, which requires expensive filters to reject extraneous wavelengths.

This paper expands on our previous success in integrating photodiodes with microfluidics for ciprofloxacin detection [16]. In that work, linear detection of 0.01 ppm ciprofloxacin was achieved. The best published results for the widely used techniques are 0.01 ppm HPLC and 0.015 ppm CE [12, 14]. We note however that these detection limits were obtained in physiological samples. It should also be pointed out that HPLC and CE provide richer spectral results than the technique reported here, which provides simple confirmation of the presence of ciprofloxacin.

## 2. Fabrication

GaP wafers were grown by metal organic chemical vapor deposition. The wafer structure was as follows: an n-type

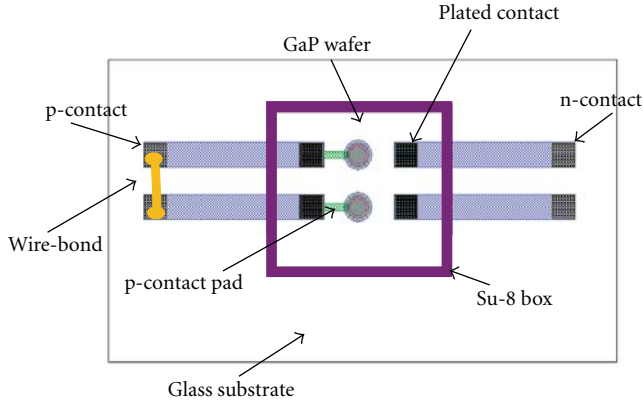


FIGURE 1: Detector system as viewed through the glass substrate.

substrate with a 650 nm-thick  $n^+$ -doped ( $1.4 \times 10^{19} \text{ cm}^{-3}$ ) first layer, an 800 nm-thick unintentionally undoped ( $4 \times 10^{16} \text{ cm}^{-3}$ ) second layer, and a 300 nm  $p^+$ -doped ( $1.1 \times 10^{19} \text{ cm}^{-3}$ ) top layer.

Mesa structure devices were fabricated by standard clean-room processes. First, a mesa was defined by photolithography and etched to the bottom  $n^+$  layer by inductively coupled plasma. This was followed by a 5-second etch in  $\text{HNO}_3:\text{HCl}:\text{DI}$  water in equal parts to remove damage to the sidewall caused by the inductively coupled plasma etch. Plasma enhanced chemical-vapor deposition was used to deposit  $\text{SiO}_2$  which served as both a passivation and an antireflection coating. After contacts were formed by metal evaporation of AuGe-Ni-Au (40 nm, 10 nm, 110 nm), the contacts were annealed for ten seconds at  $430^\circ\text{C}$  in a mixture of nitrogen and hydrogen [17]. A Ti-Au p-contact pad was evaporated and both the p-contact pad and n contact were Au plated to a final thickness of  $\sim 2 \mu\text{m}$ . The wafer was diced into  $1 \text{ mm}^2$  chips consisting of a  $2 \times 1$  array of GaP photodiodes. In order to flip the contacts a corresponding metal contact Ti-Au was evaporated on a thin glass slide. These contacts were Au plated at each end; the GaP photodiodes were bonded to the inner contacts and the outer contacts served as bias pads after flip-chip bonding. Using SU-8 photoresist, a box slightly larger than the chip and approximately  $30 \mu\text{m}$  in height was defined by photolithography. Its function was to facilitate alignment of the contacts on the GaP chips with those on the glass. The chips were bonded to the contact pads at  $220^\circ\text{C}$ . The p-contact pads of two adjacent devices were wire bonded together placing the photodiodes in parallel with each other (see Figure 1).

### 3. Device Characteristics

The dark currents of the individual devices were 0.06 and 0.04 pA at 2 V reverse bias with breakdown voltage  $\sim 38 \text{ V}$ . After wire bonding the devices in parallel, they had a combined dark current of  $\sim 0.15 \text{ pA}$  at 2 V reverse bias. A peak quantum efficiency of 38% was achieved at 440 nm after

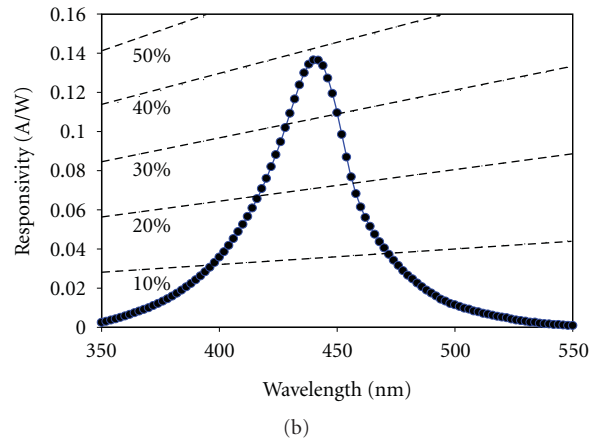
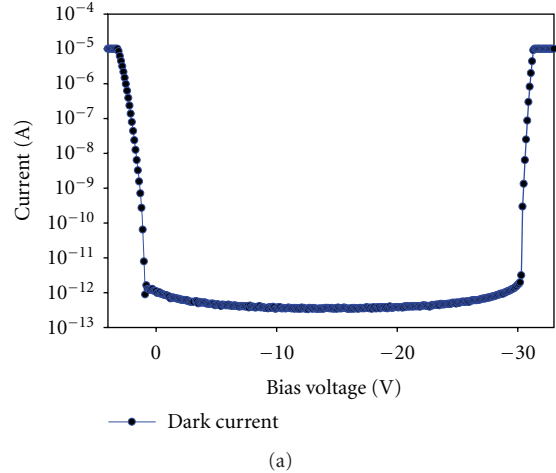


FIGURE 2: (a) Dark current versus voltage for two devices combined in parallel; (b) quantum efficiency versus wavelength for a single bonded device.

bonding; this reflects a 10% loss in efficiency due to bonding. Figure 2 shows the device characteristics.

### 4. Measurement Setup

Fused silica capillaries with inner and outer diameters of  $320 \mu\text{m}$  and  $435 \mu\text{m}$ , respectively, were purchased from Polymicro Technologies. A window was opened in the capillary by removing a short strip of the polyimide coating. This window was aligned with the photodiodes, and the capillary was affixed to the detector system, thus integrating the two parts. Forced air was used to push solution from a vial in order to fill the capillary. The whole system was placed on a flat holder with openings for both the capillary and the excitation light. A 266 nm pulsed laser with 7.3 kHz repetition rate and a 400 ps pulse width was used as the excitation light source. The laser is a compact model and consists of controller box length 6.5 inches, width 5 inches, and height 4 inches as well as the actual laser which is 6 by 3 by 2 inches. The capillary was illuminated by focusing the laser signal with a microscope objective at 90 degrees to the photodiodes. Any light from the laser that is detected

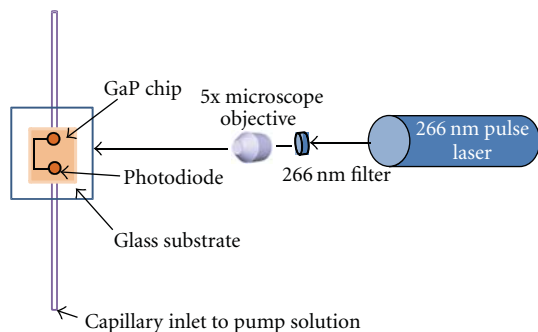


FIGURE 3: Schematic depiction of measurement setup.

by the photodiodes contributes to the background noise level; to reduce the scattered laser light, a narrow-band filter  $266 \pm 10$  nm was placed before the microscope objective. A schematic of the measurement apparatus is depicted in Figure 3.

## 5. Linear Fluorescence Detection

Ciprofloxacin powder was purchased from Fluka, Sigma-Aldrich, and a stock solution of 100 ppm of ciprofloxacin with equal parts of methanol and deionized water was prepared. The stock solution was further diluted with equal parts of methanol and de-ionized to prepare varying concentrations.

Two GaP photodiodes connected in parallel were used for these measurements. Each device was  $220 \mu\text{m}$  in diameter. For linear detection, the devices were biased at  $-2$  V and the average current was measured with a Keithley 6430 SourceMeter. The laser was focused to a spot size of  $\sim 150 \mu\text{m}$ . For light incident perpendicular to the detector  $<1\%$  of the scattered is detected. In operation, light is incident perpendicular to the detector and the scattered light accounts for  $<1\%$  of the signal. When the laser is focused on the capillary directly adjacent to either detector, the scattered light signal in the other detector is below the detection limit. The lowest background current was therefore achieved when the laser was positioned on the capillary adjacent to one of the detectors. Since the fluorescence from the ciprofloxacin is anisotropic, the fluorescence was detected by both photodiodes even though the sample was illuminated only under the first detector. Placing the two detectors in parallel effectively increases the fluorescence detection area while the excitation was proximate to a single device, which significantly reduced the background level.

The photodiode current was measured as ciprofloxacin of different concentrations were pumped through the capillary. When the current reached a stable maximum, a ten data point average was recorded. Methanol was pumped through the capillary after each ciprofloxacin concentration. The methanol flushes any traces on ciprofloxacin from the capillary. This process was continued until the total current returned to the background level. Each concentration was measured three times, and the averaged data along with standard deviation bars is shown in Figure 4. Concentrations

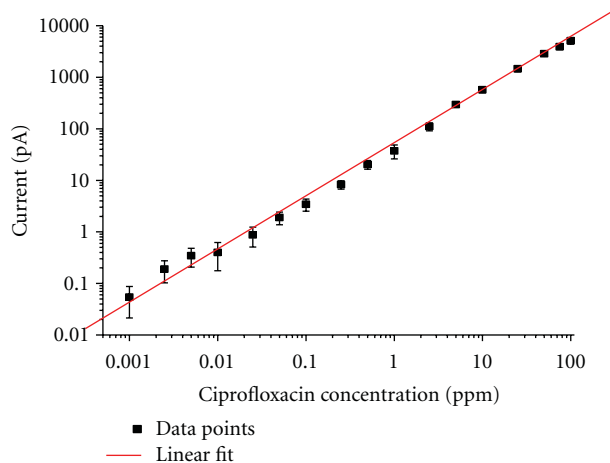


FIGURE 4: Linear detection photocurrent versus ciprofloxacin concentration.

from 1 ppb to 100 ppm were measured. The system showed a linear response for concentrations in this range.

## 6. Conclusion

Integration of two parallel connected photodiodes with a microcapillary was investigated. Individual devices had a peak quantum efficiency of 38%, and the connected parallel devices had a combined dark current of 0.15 pA, both at reverse bias 2 V. This system is a simple and effective way of detecting fluorescence from solutions in the wavelength range 400–480 nm. It can potentially be used for initial measurements but, due to its inability to separate analytes, is not a replacement for HPLC or CE. Linear detection of ciprofloxacin concentrations from 100 ppm down to 1 ppb was achieved.

## References

- [1] L. M. Smith, J. Z. Sanders, and R. J. Kaiser, "Fluorescence detection in automated DNA sequence analysis," *Nature*, vol. 321, no. 6071, pp. 674–679, 1986.
- [2] M. L. Chabinye, D. T. Chiu, J. C. McDonald et al., "An integrated fluorescence detection system in poly(dimethylsiloxane) for microfluidic applications," *Analytical Chemistry*, vol. 73, no. 18, pp. 4491–4498, 2001.
- [3] J. R. Webster, M. A. Burns, D. T. Burke, and C. H. Mastrangelo, "Monolithic capillary electrophoresis device with integrated fluorescence detector," *Analytical Chemistry*, vol. 73, no. 7, pp. 1622–1626, 2001.
- [4] R. A. Mathies, T. Kamei, B. M. Paegel, J. R. Scherer, A. M. Skelley, and R. A. Street, "Integrated hydrogenated amorphous Si photodiode detector for microfluidic bioanalytical devices," *Analytical Chemistry*, vol. 75, no. 20, pp. 5300–5305, 2003.
- [5] R. M. Hoffman, "The multiple uses of fluorescent proteins to visualize cancer in vivo," *Nature Reviews Cancer*, vol. 5, no. 10, pp. 796–806, 2005.
- [6] M. K. Araz, C. H. Lee, and A. Lal, "Ultrasonic separation in microfluidic capillaries," in *Proceedings of the 2003 IEEE Ultrasonics Symposium*, pp. 1111–1114, October 2003.

- [7] S. Jeonggi and L. P. Lee, "Fluorescence amplification by self-aligned integrated microfluidic optical systems," in *Proceedings of the 12th International Conference in TRANSDUCERS, Solid-State Sensors, Actuators and Microsystems*, vol. 2, pp. 1136–1139, 2003.
- [8] C. J. Easley, J. M. Karlinsey, J. M. Bienvenue et al., "A fully integrated microfluidic genetic analysis system with sample-in-answer-out capability," *Proceedings of the National Academy of Sciences of the United States of America*, vol. 103, no. 51, pp. 19272–19277, 2006.
- [9] P. K. Wong, Y. K. Lee, and C. M. Ho, "Deformation of DNA molecules by hydrodynamic focusing," *Journal of Fluid Mechanics*, no. 497, pp. 55–65, 2003.
- [10] L. Kaartinen, M. Salonen, L. Alli, and S. Pyorala, "Pharmacokinetics of enrofloxacin after single intravenous, intramuscular and subcutaneous injections in lactating cows," *Journal of Veterinary Pharmacology and Therapeutics*, vol. 18, no. 5, pp. 357–362, 1995.
- [11] O. R. Idowu and J. O. Peggins, "Simple, rapid determination of enrofloxacin and ciprofloxacin in bovine milk and plasma by high-performance liquid chromatography with fluorescence detection," *Journal of Pharmaceutical and Biomedical Analysis*, vol. 35, no. 1, pp. 143–153, 2004.
- [12] X. Zhou, D. Xing, D. Zhu, Y. Tang, and L. Jia, "Development and application of a capillary electrophoresis-electrochemiluminescent method for the analysis of enrofloxacin and its metabolite ciprofloxacin in milk," *Talanta*, vol. 75, no. 5, pp. 1300–1306, 2008.
- [13] O. Ballesteros, I. Toro, V. Sanz-Nebot, A. Navalón, J. L. Vilchez, and J. Barbosa, "Determination of fluoroquinolones in human urine by liquid chromatography coupled to pneumatically assisted electrospray ionization mass spectrometry," *Journal of Chromatography B*, vol. 798, no. 1, pp. 137–144, 2003.
- [14] K. H. Bannefeld, H. Stass, and G. Blaschke, "Capillary electrophoresis with laser-induced fluorescence detection, an adequate alternative to high-performance liquid chromatography, for the determination of ciprofloxacin and its metabolite desethyleneciprofloxacin in human plasma," *Journal of Chromatography B*, vol. 692, no. 2, pp. 453–459, 1997.
- [15] G. A. Wilson and J. Brady, "Design considerations and signal processing algorithms for laser-induced fluorescence airborne pathogen sensors," in *Proceedings of the International Society for Optical Engineering, (SPIE 5617)*, pp. 1–13, London, UK, 2004.
- [16] J. Campbell, D. McIntosh, Q. Z. F. J. Lara, and J. Landers, "Flip-chip bonded GaP photodiodes for detection of 400–480 nm fluorescence," *Photonics Technology Letters*, vol. 23, no. 13, pp. 878–880, 2011.
- [17] A. L. Beck, B. Yang, S. Wang et al., "Quasi-direct UV/blue GaP avalanche photodetectors," *IEEE Journal of Quantum Electronics*, vol. 40, no. 12, pp. 1695–1699, 2004.

## Research Article

# Electrodes for Microfluidic Integrated Optoelectronic Tweezers

**Kuo-Wei Huang,<sup>1</sup> Sabbir Sattar,<sup>1</sup> Jiang F. Zhong,<sup>2</sup> Cheng-Hsu Chou,<sup>3</sup>  
Hsiung-Kuang Tsai,<sup>3</sup> and Pei-Yu Chiou<sup>1</sup>**

<sup>1</sup> Department of Mechanical and Aerospace Engineering, University of California, Los Angeles, CA 90095, USA

<sup>2</sup> Department of Neurology, University of Southern California, Los Angeles, CA 90033, USA

<sup>3</sup> Chimei-Innolux Inc., Tainan County, Southern Taiwan Science Park 744, Taiwan

Correspondence should be addressed to Kuo-Wei Huang, kuoweih@gmail.com

Received 11 May 2011; Accepted 25 June 2011

Academic Editor: Aaron T. Ohta

Copyright © 2011 Kuo-Wei Huang et al. This is an open access article distributed under the Creative Commons Attribution License, which permits unrestricted use, distribution, and reproduction in any medium, provided the original work is properly cited.

We report on two types of electrodes that enable the integration of optoelectronic tweezers (OETs) with multilayer poly(dimethylsilane)- (PDMS-) based microfluidic devices. Both types of electrodes, Au-mesh and single-walled carbon nanotube- (SWNT-) embedded PDMS thin film, are optically transparent, electrically conductive, and can be mechanically deformed and provide interfaces to form strong covalent bonding between an OET device and PDMS through standard oxygen plasma treatment. Au-mesh electrodes provide high electrical conductivity and high transparency but are lack of flexibility and allow only small deformation. On the other hand, SWNT-embedded PDMS thin film electrodes provide not only electrical conductivity but also optical transparency and can undergo large mechanical deformation repeatedly without failure. This enables, for the first time, microfluidic integrated OET with on-chip valve and pump functions, which is a critical step for OET-based platforms to conduct more complex and multistep biological and biochemical analyses.

## 1. Introduction

Optoelectronic tweezers (OETs) demonstrated by Chiou et al. in 2005 have promised a platform for high-throughput single cell manipulation and analysis [1, 2]. The principle of manipulating microscale objects and cells on an OET platform is based on light-patterned virtual electrodes and the induced dielectrophoretic (DEP) forces [1]. Types of objects that have been manipulated using OET are versatile, including polystyrene beads [1, 2], semiconductor microdisks [3], nanowires [4], DNA molecules [5], proteins [6], sperm [7], and bacteria and mammalian cells [1, 2, 8–10]. Recent development of OET technologies also broadened the type of media in which OET can operate. Phototransistor OET enabled OET to function in regular physiological buffers with high electrical conductivity (1.5 S/m) [11]. Floating electrode OET enabled the manipulation of aqueous droplets in electrically insulating media such as oils and air [12, 13]. OET can also be integrated with digital microfluidic platform for manipulating objects carried in droplets [13, 14]. A universal platform successfully integrating OET and

optoelectrowetting (OEW) further allows optical manipulation of objects and droplets on the same featureless OET device [15]. Integration of OET with continuous phase microfluidic devices has also been realized [16, 17]. However, the integration is currently limited to simple microfluidic channels without other functional components such as valves and pumps due to the rigid and brittle property of ITO electrodes. This has limited OET's potentials for performing complex protocols.

To realize microfluidic integrated OET with more functions, here, we demonstrate two types of enabling electrodes, Au-mesh electrode and SWNT-embedded thin film electrode, that allow integrating OET with multilayer PDMS-based microfluidic devices that can provide on-chip valve and pump function through deformable thin PDMS membranes. PDMS is widely used in fabricating microfluidic devices due to its elastic mechanical property, gas permeability, and simple fabrication process [18–24]. Thousands of membrane valves and pumps can be integrated on the same chip to conduct complex and multistep biochemical analysis and synthesis protocols. OET

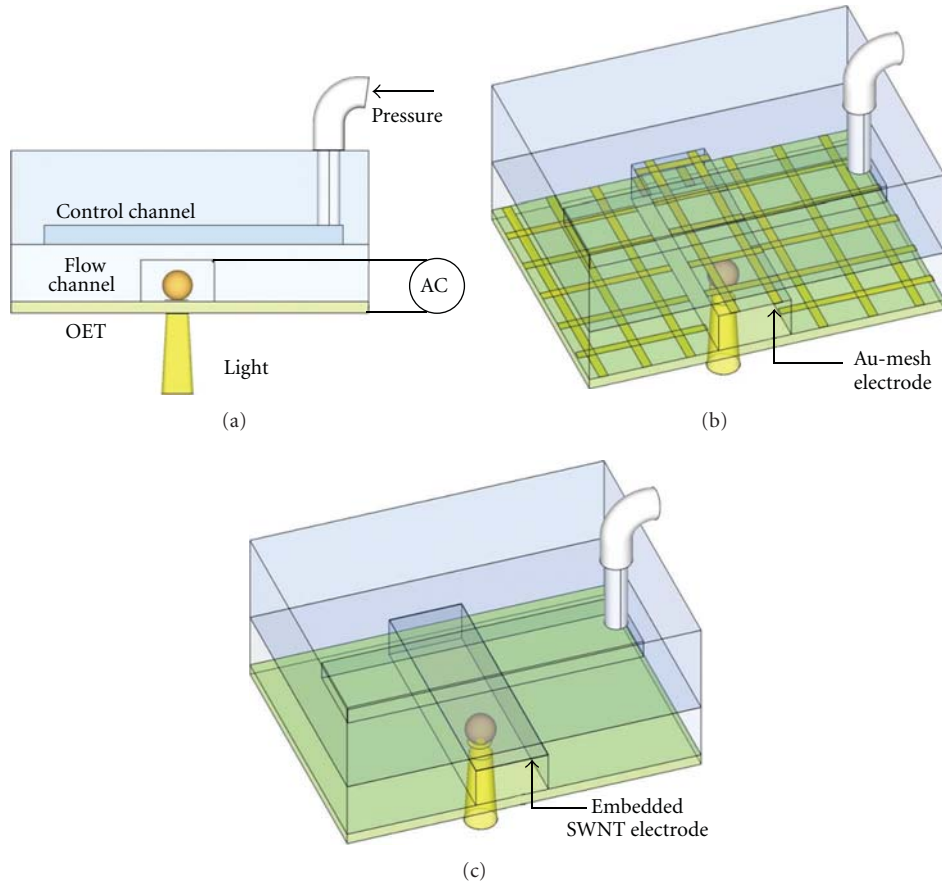


FIGURE 1: (a) Schematic of a microfluidic integrated OET device. (b) Devices using an Au-mesh electrode or (c) an SWNT-embedded PDMS thin film electrode as the top channel surface and the deformable check valve.

and PDMS microfluidic devices provide complementary functions. OET is a powerful tool enabling massively parallel single cell manipulation with light but not effective in manipulating fluid. On the other hand, PMDS microfluidic device is effective in controlling the delivery of fluid but ineffective in manipulating particles or cells carried by the fluid. Integration of OET with PDMS microfluidic devices promises a platform for high throughput and parallel control not only complex microfluidic circuitry but also individual cells carried by fluid.

Several requirements need to be satisfied to realize such integration. First, the electrode needs to be optically transparent to allow optical imaging and diagnostics. This is important since the amorphous silicon used in OET strongly absorbs visible lights with wavelength shorter than 632 nm (red). Fluorescence excitation and observation through the amorphous silicon side is difficult and has to come from the transparent electrode side. Second, the electrode needs to be electrically conductive after deposited on the elastic PDMS surface. ITO electrodes usually crack after deposition on PDMS and cannot conduct current. Third, the PDMS device needs to provide an interface after electrode coating that can form strong bonding with the OET surface to provide good sealing and prevent liquid leakage during manipulation.

This paper shows the fabrication process, theory, OET manipulation performance, and limitations of Au-mesh and SWNT-embedded PDMS thin film electrodes.

## 2. Device Structures of Microfluidic Integrated OET

The schematic of a microfluidic integrated OET consisting of an upper PDMS microfluidic channel and a bottom photoconductive OET surface is illustrated in Figure 1(a). Unlike a conventional OET device in which a fluid chamber is formed between an ITO electrode and a photoconductive substrate, the proposed multilayer PDMS microfluidic integrated OET can have two or more layers of channels. The bottom channel contains aqueous solutions carrying biological cells or particles and the top channel is used to control the membrane valve formed at the region where the top and bottom channels intersect. This elastic membrane works as a mechanical valve that can be controlled by pneumatic pressure to close the bottom channel and stop the fluid flow. A peristaltic pump can be achieved by actuating three valves along a channel in series.

The OET surface comprises of multiple layers including an ITO, a 50-nm n+ hydrogenated amorphous silicon (a-Si:H), a 1- $\mu\text{m}$  undoped a-Si:H, and a 100-nm silicon dioxide. The layer of silicon dioxide is deposited for bonding with PDMS. The Au-mesh electrode (Figure 1(b)) or the SWNT-embedded PDMS thin film (Figure 1(c)) is fabricated on the top surface of the bottom PDMS channel.

### 3. Au-Mesh Electrode

An Au-mesh electrode is formed by two-perpendicular periodic Au/Ti stripes coated on the top surface of a PDMS channel by directional e-beam evaporation through shadow masks (Figure 1(b)). Au-mesh electrodes provide high electrical conductivity in the same order of magnitude as regular metal electrodes. The empty regions between wires control its optical transparency. Since Au covers only a small area on an Au-mesh electrode, strong bonding between PDMS and the OET can be formed through plasma treatment to provide tight sealing during fluid delivery. Figure 2 shows the fabrication process of Au-mesh electrodes. A shadow mask with an array of strips is used to create periodic metal strips through e-beam deposition on the top surface of a PDMS channel. The fabrication process of the shadow mask starts from a commercial 100  $\mu\text{m}$  thick silicon wafer. A thin layer of PECVD oxide was deposited on the wafer as an etch mask for deep reactive-ion etching (DRIE). A strip pattern with a line width of 5- $\mu\text{m}$  and a spacing of 50- $\mu\text{m}$  was patterned on the etch mask by standard photolithography. The PDMS microfluidic channels and chambers are fabricated through standard soft lithography processes. After peeling off the PDMS structures from the mold, the periodic electrodes formed by 1 nm Ti and 100 nm Au stripes are deposited by e-beam evaporation on the PDMS surface through the shadow mask twice. In the second deposition, the shadow mask was rotated by 90 degrees.

Figure 3 shows both the bright and fluorescence images of 10- $\mu\text{m}$  fluorescent particles positioned 100  $\mu\text{m}$  underneath an Au-mesh electrode. The particles can be clearly observed under a 10x and a 50x objective lens even for particles positioned right underneath Au wires. Since Au-mesh and particles are not at the same focal plane, the Au-mesh image blurs out when the imaging plane is on the OET surface. It can be expected that the larger the separation gap between OET and the electrode, the larger the blurring. Also, the higher the magnification of the objective lens is, the less is the shadowing effect. Furthermore, decreasing the width of Au wires can further reduce the shadow effect of Au-mesh.

To verify the performance of OET manipulation using an Au-mesh electrode, an HeNe laser was used as the light source to induce a virtual electrode on the photoconductive surface. Nalm 6 cells were first suspended in an isotonic buffer and then flowed into the microchannels using a syringe pump. After a light beam turned on a virtual electrode, Nalm 6 cells experiencing positive DEP forces are observed to move toward the light spot as shown in Figures 4(a) and 4(b). To evaluate the DEP forces, we can translate the velocity of Nalm 6 cell into DEP force by Stock's formula,

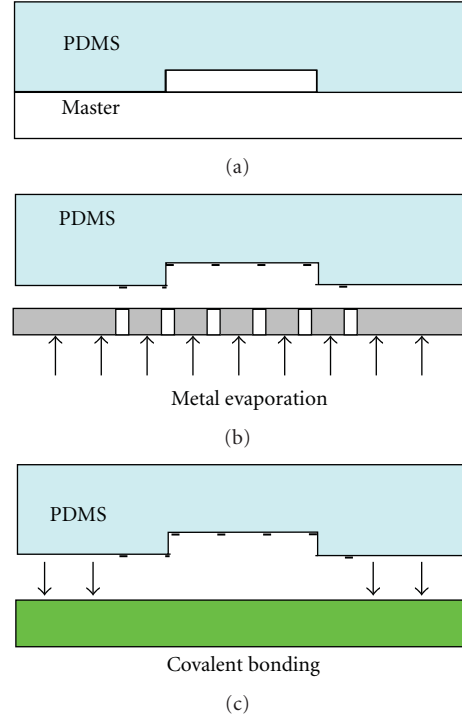


FIGURE 2: (a) A master mold fabricated by SU-8 is used to define the PDMS microfluidic channels. (b) Evaporating through a shadow mask placed near the PDMS enables the fabrication of patterned Au/Ti wires on the upper surface of channels. (c) Covalent bonding is formed between the Au/Ti-mesh PDMS and the OET chip after oxygen plasma treatment on the bonding surfaces.

$V_{\text{DEP}} = (F_{\text{DEP}} + F_{\text{friction}})/6\pi\eta R$ , where  $\eta$  is the viscosity of the media,  $R$  is the radius of the cells, and the  $F_{\text{friction}}$  is the friction force between cells and the OET surfaces. Based on our experimental observation and ignoring the friction forces, the speed was found to be 14  $\mu\text{m}/\text{sec}$  giving a force of 1.3 pN.

One potential drawback of Au-mesh electrode is the highly nonuniform electric field near Au wires. If cells or particles are near these wires, strong DEP forces will be induced on them. This effect turns out to be not severe when particles or cells are manipulated near the OET surface since this highly nonuniform field decreases rapidly away from the wires. This property allows Au-mesh OET to manipulate cells or particles near the photoconductive surface smoothly as a continuous electrode. This can be confirmed by the finite element method (FEM) simulation showing the electric-field distribution induced by a light beam on an Au-mesh OET device as shown in Figure 5(a). The geometry parameters used in simulation are based on real device dimensions. The width of Au-wire electrodes is 5  $\mu\text{m}$  and the spacing is 50  $\mu\text{m}$ . A 50- $\mu\text{m}$  high chamber is filled with medium having a conductivity of 0.01 S/m. The photoconductivity of a-Si:H is assumed to follow the Gaussian distribution profile with a peak conductivity of 0.1 S/m and an FWHM spot diameter of 16.6  $\mu\text{m}$ . The nonuniform electric field induced by Au-mesh is limited to regions close to the top surface (shown in the 47.2  $\mu\text{m}$  curve in Figure 5(b)) and quickly decays in the

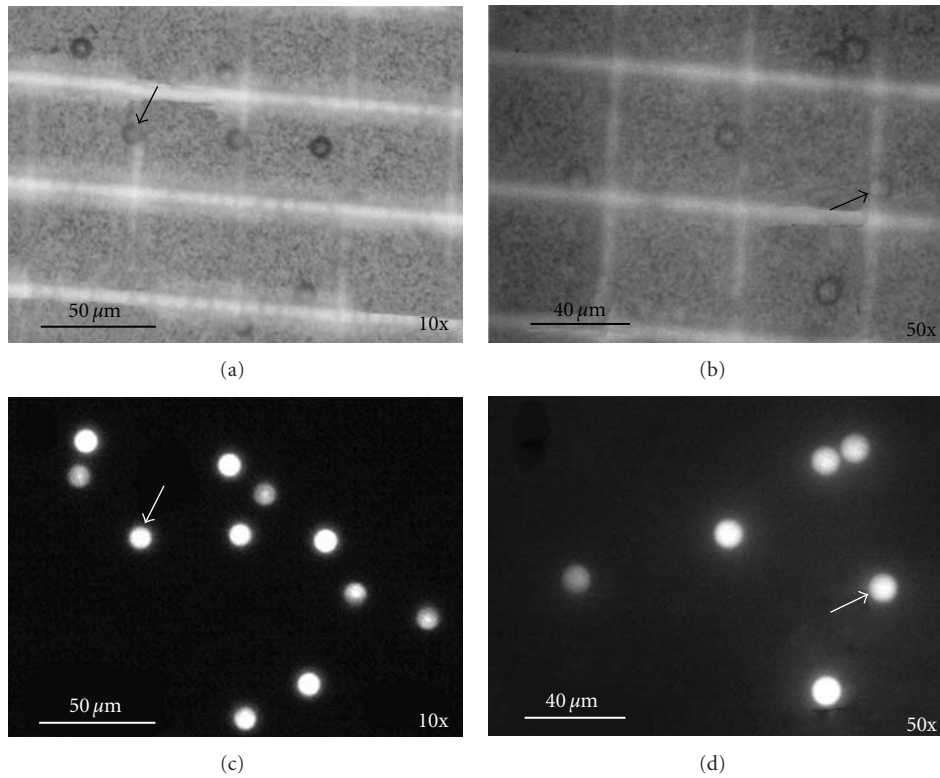


FIGURE 3: (a, b) Bright-field images and (c, d) fluorescent images of 10- $\mu\text{m}$  particles underneath an Au-mesh electrode. The gap spacing between the electrode and the OET surface where the particles sit is 100  $\mu\text{m}$ . The arrows point to the particles below Au wires.

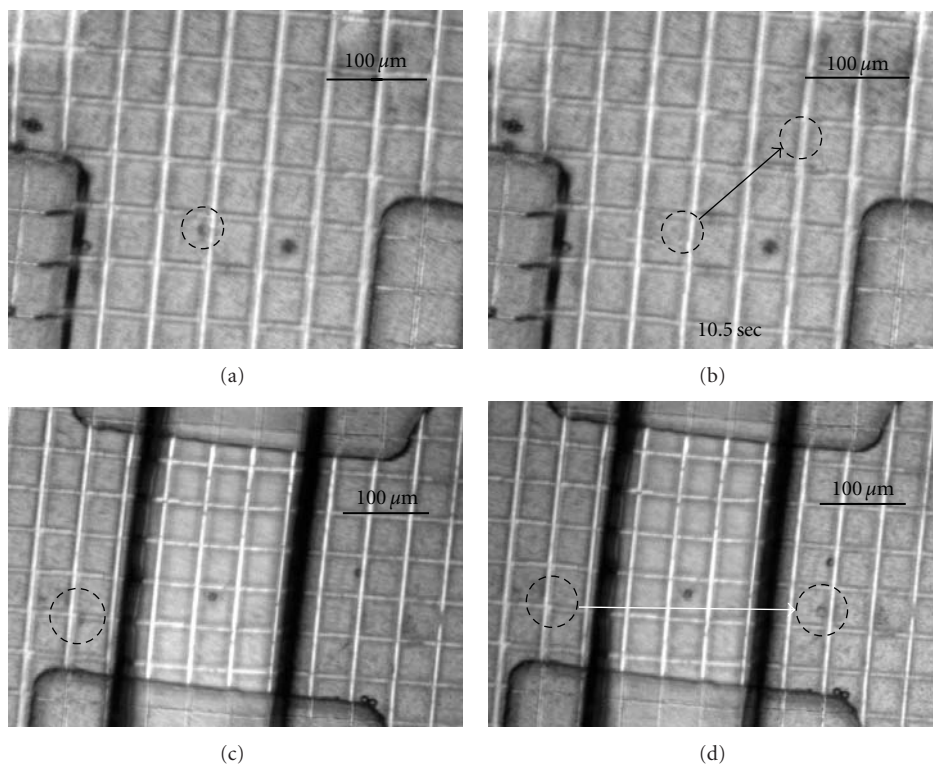


FIGURE 4: (a, b) A Nalm 6 cell trapped by a light spot (the dish circle) is transported in a microfluidic channel. (c, d) Transport of a single Nalm 6 cell trapped by OET in multilayer PDMS channels. The region between two black lines is a control channel above the flowing channel where the cells are.

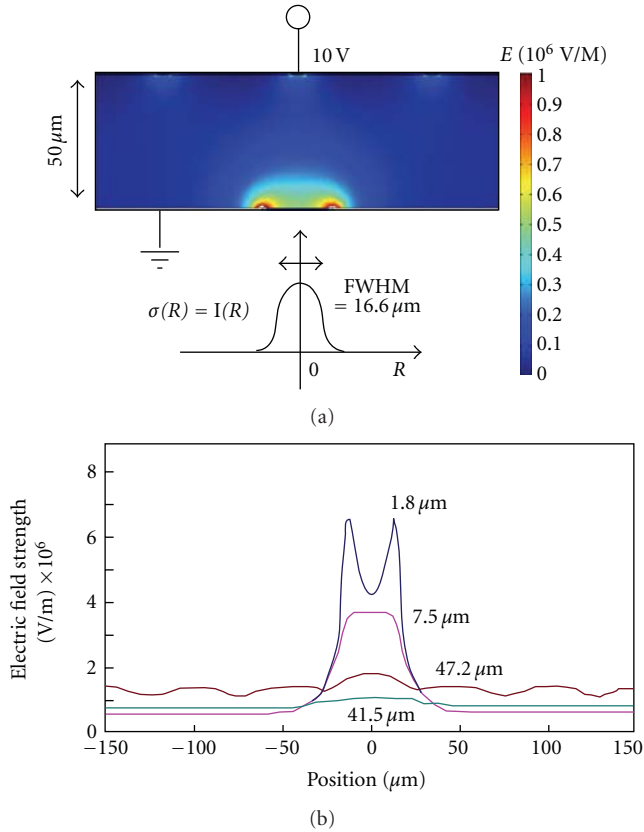


FIGURE 5: (a) Finite element simulation of the electric field pattern in the liquid layer when a  $16.6\ \mu\text{m}$  wide light beam illuminates the photoconductive layer. (b) The electric field distribution at different heights above the photoconductive layer.

vertical direction. At regions near the OET surface, Au-mesh-induced field gradient is negligible compared to that induced by the light beam ( $1.8\ \mu\text{m}$  and  $7.5\ \mu\text{m}$  curves in Figure 5(b)).

Although Au-mesh electrodes provide high electrical conductivity and high optical transparency, there are several drawbacks. First, there is a trade-off between the height of channels and the density of Au-mesh since the electrode is discrete. The nonuniform electric field induced near Au wires will affect OET manipulation when the height of channels becomes small. Increasing the channel height or reducing the spacing between Au wires can help reducing this effect. Another limitation comes from the fact that metallic films, despite more deformable than ITO, tend to peel off from PDMS surface after large deformation which also creates cracks. As a result, Au-mesh electrodes can only undergo large mechanical deformation once before failure. In Figures 4(c) and 4(d), a Nalm 6 cell was transported across a deformable PDMS membrane valve coated with Au-mesh electrode. This Au-mesh electrode failed after the PDMS membrane valve was pushed down to close the flow channel.

#### 4. SWNT-Embedded PDMS Thin Film Electrode

Motivated by the cracking issue of Au-mesh electrodes, we investigate SWNT-embedded PDMS thin film electrodes to

solve this problem. SWNTs exhibit high electrical conductivity. Films made by randomly distributed SWNT have shown potentials for flexible electronics [25]. SWNT thin films with thickness in the range of 10–100 nm can have low sheet resistance and high optical transparency as well as robust mechanical flexibility [26]. SWNT thin films have been demonstrated in devices including solar cells [27], thin film transistors [28], light emitting diodes [29], and electrowetting [30]. Recent researches suggested that the electrical stability and mechanical robustness of SWNT films could be improved by embedding SWNT thin film into polymers [31–33]. Devices made by SWNT films within polymer membranes also show promising potentials for applications on microfluidic platforms [34].

Here, we demonstrate microfluidic integrated OET using SWNT-embedded PDMS thin film electrode as shown in Figure 1(c). This electrode is continuous, optically transparent, and electrically conductive and has robust mechanical flexibility allowing large deformation without failure.

The fabrication process of SWNT embedded PDMS thin film is illustrated Figure 6. The vacuum filtration method is used to get uniform SWNT thin films [35]. The suspension of SWNT is filtered through a filtration membrane to form a thin layer of SWNT network. The highly dense SWNT suspension was made by high purity (>90%) arc discharge nanotubes from Carbon Solutions, Inc. SWNTs were dissolved in 1 wt% sodium dodecyl sulfate (SDS) solution to prepare solution-based SWNT. This highly concentrated SWNT suspension was ultrasonically agitated using a probe sonicator for ~10 minutes. To remove the carbon particles and impurities, the suspension was centrifuged at 14000 rpm for 30 minutes. A porous anodic aluminum oxide (AAO) filter (Anodisc 47, Whatman Inc.) was used in vacuum filtration. The suspension flows through the pores and leaves a thin film of an SWNT network on the surface of the AAO filter. The concentration and the volume of the flow suspension can control the density of SWNT network.

A PDMS stamp is then used to transfer the SWNT thin film from the filtration membrane [36]. To fabricate the PDMS stamp, a master mold was made by using standard photolithography using a negative photoresist (SU-8 2025, MicroChem corporation) on a silicon wafer. Polydimethylsiloxane (Sylgard 184, Dow Corning) with a ratio of 10 base: 1 curing agent was poured onto the master mold and cured at  $65^\circ\text{C}$  for 4 hours. A PDMS stamp with a pattern of microfluidic channels could be peeled off from the Si wafer. Before the stamp contacts the filtration membrane, it was treated by trichloro(1H, 1H, 2H, 2H-perfluorooctyl)silane (Sigam-Aldrich, Inc.), a chemical release agent that lowers the adhesive forces between the PDMS stamp and the SWNT thin film [37]. The treated PDMS stamp was then pressed in contact with the SWNT network on the AAO filter paper (Figure 6(a)). After the PDMS stamp is removed, the SWNT network is transferred onto the extruding surface of the PDMS stamp. This PDMS stamp with an SWNT thin film was then used as the mold for casting microfluidic channels.

To cast the microfluidic channels, an uncured PDMS precursor at the ratio of 10 base: 1 curing agent was poured

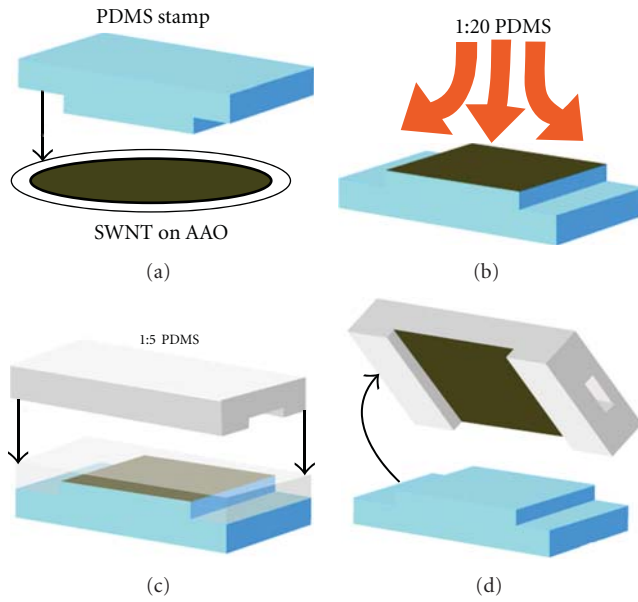


FIGURE 6: The fabrication process of embedding a thin layer SWNT network in a multi-layer PDMS microfluidic structure.

onto the PDMS stamp and baked in an oven. The uncured gel-like PDMS precursor infiltrates the vacant regions in the SWNT network during the curing process. The cured microfluidic channels were then be peeled off from the mold with an SWNT thin film embedded near the top surface of channels. This fabrication technique can be used to embed SWNT thin film on multilayer PDMS microfluidic devices. To achieve that, the uncured PDMS precursor at a ratio of 20 base: 1 curing agent was spin-coated on the PDMS stamp to create a thin membrane (Figure 6(b)). A top thick PDMS layer made with a ratio of 5 base: 1 curing agent is pressed to contact the thin PDMS layer. These two layers are bonded after cured (Figure 6(c)). The cured PDMS with a top control channel and a thin film SWNT embedded bottom PDMS channel can be peeled off from the first PDMS stamp as shown in Figure 6(d). This multilayer PDMS channel with an embedded SWNT thin film electrode on the top surface of bottom channels including the membrane valve locations was then bonded with an OET device through oxygen plasma treatment.

In our fabrication process, the PDMS stamp is used as the mold for not only casting other microfluidic channels but also transferring an SWNT thin film to the top surface of a channel. This fabrication process is compatible with the standard soft lithography process. Figure 7(a) shows the microscopic image of the SWNT electrode embedded in a multi-layer PDMS microfluidic device. Since the SWNT electrode exists only on the top surface of the flow channels, this promises a clean surface for forming strong covalent bonding between PDMS and silicon dioxide surface of an OET device. Figure 7(b) shows the SEM image of a thin film SWNT embedded into the cured PDMS matrix. Embedded SWNT networks can provide better electrical stability and mechanical robustness.

To examine the optical transparency of SWNT electrodes,  $10\text{-}\mu\text{m}$  fluorescent particles were pumped into an SWNT OET device. Figures 7(c) and 7(d) are the bright field and the fluorescence images of  $10\text{-}\mu\text{m}$  fluorescent particles underneath an SWNT electrode. Three particles highlighted with arrows are located in the membrane valve location where two layers of PDMS channels cross. The relation between the measured sheet resistance and the optical transmittance at  $632\text{ nm}$  is plotted in Figure 7(e). The optical transparency and electrical conductivity of SWNT electrodes are highly dependent on the carbon nanotube purity, tube length, and dispersion quality of the films. The transparency and the sheet resistance can be controlled by the thickness of SWNT films, which can be adjusted by the amount of SWNT in the dispersion solution. Experimental results have shown a linear relationship between sheet resistance and optical transparency. The electrodes with sheet resistance from  $\sim 350$  to  $\sim 550$  ohm per square have from 55 to 80% optical transparency measured at  $632\text{ nm}$ . In an SWNT OET device, all the flow channels (top layer) and the control channels (bottom layer) are  $300\text{-}\mu\text{m}$  wide, so the area of the valve was  $300\text{ }\mu\text{m} \times 300\text{ }\mu\text{m}$ , and the height of bottom channel was  $18\text{ }\mu\text{m}$ . The valve could be pushed down to completely close the bottom flow channel by applying a pressure in the top channel. Figure 7(f) shows a series of pictures of valve function. The dye solution was pumped into an SWNT OET device by a constant pressure of  $1.5\text{ psi}$ . The white arrows are the flow directions of dye solution. First, a pressure of  $25\text{ psi}$  was applied into the top channel in the right-hand side, the PDMS membranes deformed, and the dye solution was stopped by the two closed valves. The dye solution moved when the two valves were open and the valve in left-hand side was close. After the dye solution was filled in the entire flow channel, the color change in the valve region indicates the closing of the valves. The electrical resistance of the SWNT electrode increased when the valve deformed. After releasing the pressure, the resistance decreased back to its original value before deformation. The SWNT-embedded PDMS thin film electrode is capable of reproducing their electrical conductivity for strain up to 40%.

In the experimental setup, a DMD-based projector with its projection lens and color filters being removed is used as the light source for generating dynamic optical images. These images are projected onto the photoconductive layer by a  $4\times$  objective lens. The microfluidic integrated OET device was positioned on an inverted microscope. An ac bias of  $100\text{ kHz}$ ,  $10\text{ V}_{pp}$  is applied to the SWNT electrode in the PDMS channel and the ITO electrode on the OET device. Figures 8(a) and 8(b) are the snapshots of images showing a  $10\text{-}\mu\text{m}$  particle being transported across a deformable PDMS membrane valve by dynamic light images.

The performance of OET manipulation using an SWNT embedded PDMS thin film electrode has been compared with a regular ITO electrode. An HeNe laser which was set on an up-right microscope was used as the light source to trigger virtual electrodes. Therefore, the incident laser light is from the bottom side of the photoconductive layers, avoiding the optical transmittance difference between two top electrodes (ITO and SWNT).  $10\text{-}\mu\text{m}$  particles were

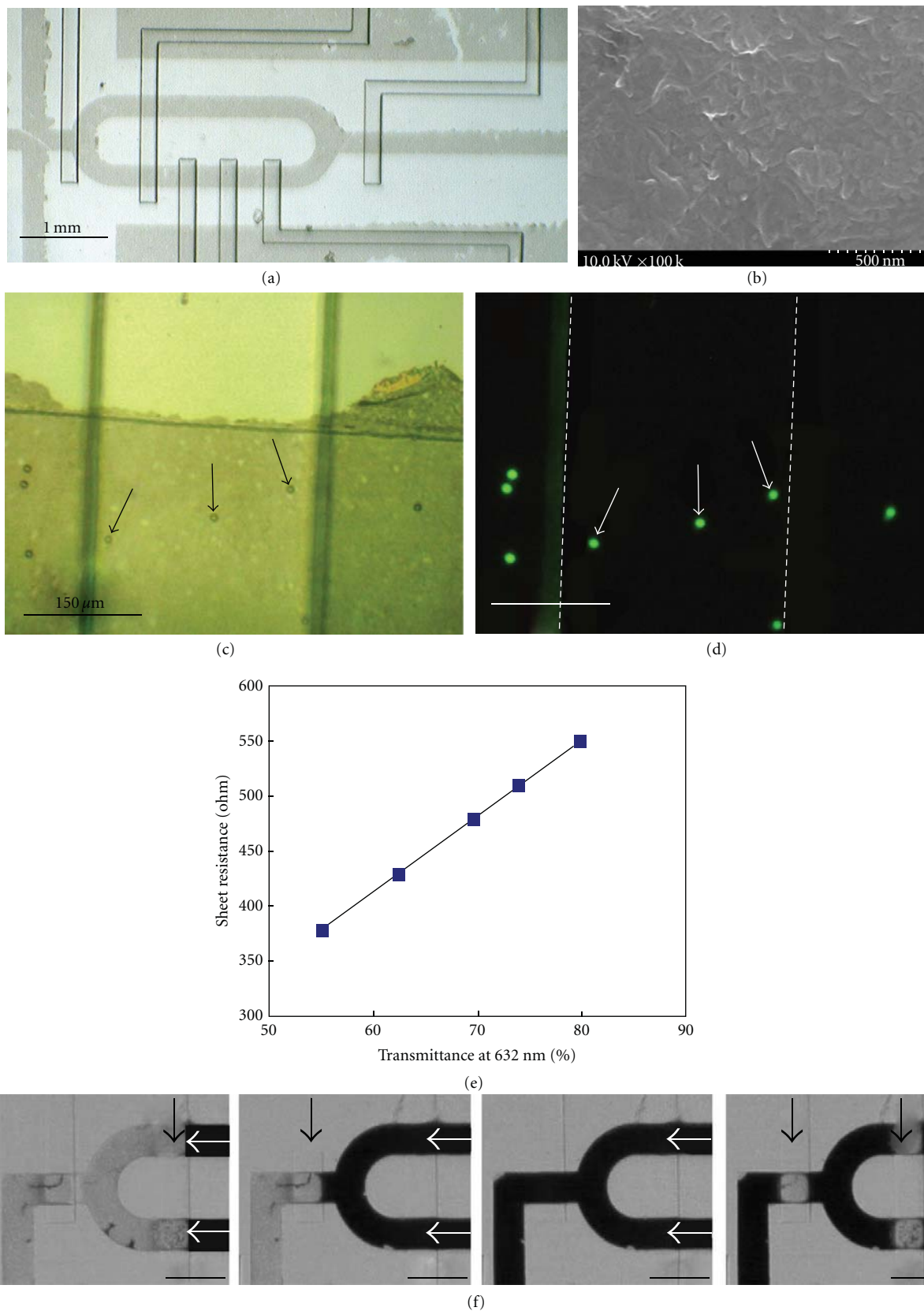


FIGURE 7: (a) A microscopic image of SWNT-embedded valves and channels in multilayer PDMS microfluidic structures. The channel is bonded on an OET chip. (b) A SEM image of SWNT network embedded in the surface of PDMS. (c, d) Bright field and fluorescence image of 10 μm fluorescence particles underneath an SWNT electrode. (e) Measured sheet resistance of SWNT-embedded PDMS electrodes and its relation with optical transmittance at 632 nm. (f) A series of pictures showing the valve function by deforming the SWNT membrane electrode. The white arrows are the flow directions of the dye solution in the flow channels. The black arrows show the pressure sources to deform the membranes. The dye solution can be stopped by pushing down the membrane. The scale bars are 600 μm.

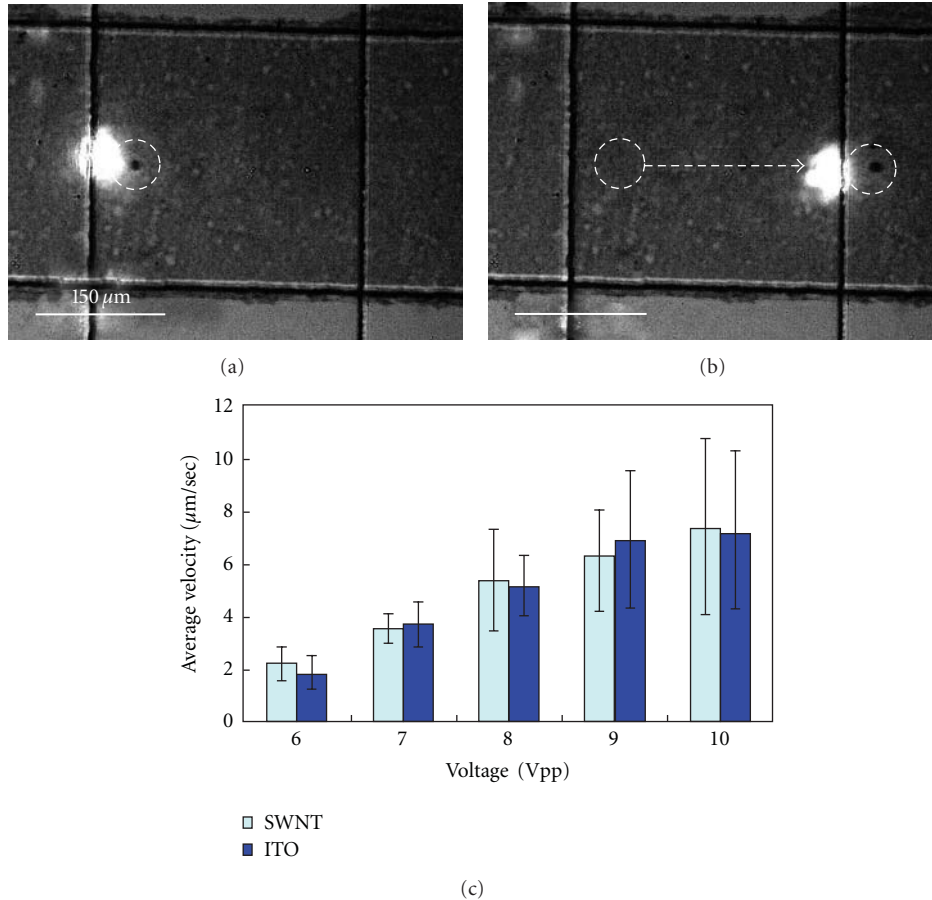


FIGURE 8: (a, b) Transport of a 10- $\mu\text{m}$  particle by light across a membrane valve on an OET-integrated multilayer PDMS device. The scale bars are 150  $\mu\text{m}$ . (c) Comparison of particle moving speed in OET using ITO electrode and SWNT-embedded PDMS electrode. The light intensity is 1.5 W/cm<sup>2</sup> and the applied frequency is 100 kHz.

diluted in KCl solution of 0.07 mS/cm and injected into a liquid chamber which was formed by an ITO electrode or an SWNT electrode. The tests were under the application of an ac bias with different voltage but in the same liquid chamber and at the same frequency, 100 kHz. Figure 8(c) shows the average velocities of 10- $\mu\text{m}$  particles under different voltages. The SWNT electrodes behave like regular ITO electrodes under these operation conditions. The particle transport speed using the SWNT electrode is similar to a regular ITO electrode. We can estimate that the DEP forces in both electrodes are almost the same.

## 5. Conclusion

We have successfully demonstrated two types of enabling electrodes that permit OET devices to integrate with multilayer PDMS microfluidic devices with on-chip valve and pump functions for conducting multistep and complex biological diagnostic protocols. Au-mesh electrodes provide high electrical conductivity and high optical transparency but lack of robust mechanical flexibility. Au-mesh electrode cracks after large mechanical deformation. SWNT-embedded PDMS thin film electrode solves this cracking

issue and also provides required electrical conductivity and optical transparency for effective OET operation in a microfluidic integrated OET device. Sheet resistance of 350~550 ohm/square can be obtained with optical transparency of 55% to 80%. The SWNT-embedded PDMS thin film electrode has robust mechanical flexibility, can tolerate a maximum strain of 40%, and can be used as a membrane valve to completely close a flow channel repeatedly without losing its electrical conductivity property.

## Acknowledgments

The authors thank Professor Chih-Ming Ho's group for supporting experimental facilities, Professor Hsian-Rong Tseng's group for their helps with fabrication of PDMS devices, and Dr. Liangbing Hu and Professor George Gruner for their discussion about SWNT thin films. The appreciation is extended to the staff at UCLA Nanoelectronics Research Facility for their helps with microfabrication. This work has been funded by NSF CAREER AWARD ECCS 0747950 and DBI 0852701.

## References

- [1] P. Y. Chiou, A. T. Ohta, and M. C. Wu, "Massively parallel manipulation of single cells and microparticles using optical images," *Nature*, vol. 436, no. 7049, pp. 370–372, 2005.
- [2] A. T. Ohta, P. Y. Chiou, T. H. Han et al., "Dynamic cell and microparticle control via optoelectronic tweezers," *Journal of Microelectromechanical Systems*, vol. 16, no. 3, pp. 491–499, 2007.
- [3] M. C. Tien, A. T. Ohta, K. Yu, S. L. Neale, and M. C. Wu, "Heterogeneous integration of InGaAsP microdisk laser on a silicon platform using optofluidic assembly," *Applied Physics A*, vol. 95, no. 4, pp. 967–972, 2009.
- [4] A. Jamshidi, P. J. Pauzauskie, P. J. Schuck et al., "Dynamic manipulation and separation of individual semiconducting and metallic nanowires," *Nature Photonics*, vol. 2, no. 2, pp. 86–89, 2008.
- [5] P. Y. Chiou, A. T. Ohta, A. Jamshidi, H. Y. Hsu, and M. C. Wu, "Light-actuated AC electroosmosis for nanoparticle manipulation," *Journal of Microelectromechanical Systems*, vol. 17, no. 3, pp. 525–531, 2008.
- [6] H. Hwang and J. K. Park, "Measurement of molecular diffusion based on optoelectrofluidic fluorescence microscopy," *Analytical Chemistry*, vol. 81, no. 21, pp. 9163–9167, 2009.
- [7] A. T. Ohta, M. Garcia, J. K. Valley et al., "Motile and non-motile sperm diagnostic manipulation using optoelectronic tweezers," *Lab on a Chip*, vol. 10, no. 23, pp. 3213–3217, 2010.
- [8] A. T. Ohta, P. Y. Chiou, H. L. Phan et al., "Optically controlled cell discrimination and trapping using optoelectronic tweezers," *IEEE Journal on Selected Topics in Quantum Electronics*, vol. 13, no. 2, pp. 235–242, 2007.
- [9] J. K. Valley, S. Neale, H. Y. Hsu, A. T. Ohta, A. Jamshidi, and M. C. Wu, "Parallel single-cell light-induced electroporation and dielectrophoretic manipulation," *Lab on a Chip*, vol. 9, no. 12, pp. 1714–1720, 2009.
- [10] W. Choi, S. W. Nam, H. Hwang, S. Park, and J. K. Park, "Programmable manipulation of motile cells in optoelectronic tweezers using a grayscale image," *Applied Physics Letters*, vol. 93, no. 14, Article ID 143901, 2008.
- [11] H. Y. Hsu, A. T. Ohta, P. Y. Chiou, A. Jamshidi, S. L. Neale, and M. C. Wu, "Phototransistor-based optoelectronic tweezers for dynamic cell manipulation in cell culture media," *Lab on a Chip*, vol. 10, no. 2, pp. 165–172, 2010.
- [12] S. Park, C. Pan, T. H. Wu et al., "Floating electrode optoelectronic tweezers: light-driven dielectrophoretic droplet manipulation in electrically insulating oil medium," *Applied Physics Letters*, vol. 92, no. 15, Article ID 151101, 2008.
- [13] S. Y. Park, S. Kalim, C. Callahan, M. A. Teitell, and E. P. Y. Chiou, "A light-induced dielectrophoretic droplet manipulation platform," *Lab on a Chip*, vol. 9, no. 22, pp. 3228–3235, 2009.
- [14] G. J. Shah, A. T. Ohta, E. P. Y. Chiou, M. C. Wu, and C. J. C. Kim, "EWOD-driven droplet microfluidic device integrated with optoelectronic tweezers as an automated platform for cellular isolation and analysis," *Lab on a Chip*, vol. 9, no. 12, pp. 1732–1739, 2009.
- [15] J. K. Valley, S. Ningpei, A. Jamshidi, H.-Y. Hsu, and M. C. Wu, "A unified platform for optoelectrowetting and optoelectronic tweezers," *Lab on a Chip*, vol. 11, no. 7, pp. 1292–1297, 2011.
- [16] Y. H. Lin and G. B. Lee, "Optically induced flow cytometry for continuous microparticle counting and sorting," *Biosensors and Bioelectronics*, vol. 24, no. 4, pp. 572–578, 2008.
- [17] D. H. Lee, H. Hwang, and J. K. Park, "Generation and manipulation of droplets in an optoelectrofluidic device integrated with microfluidic channels," *Applied Physics Letters*, vol. 95, no. 16, Article ID 164102, 2009.
- [18] G. M. Whitesides, "The origins and the future of microfluidics," *Nature*, vol. 442, no. 7101, pp. 368–373, 2006.
- [19] J. C. McDonald, D. C. Duffy, J. R. Anderson et al., "Fabrication of microfluidic systems in poly(dimethylsiloxane)," *Electrophoresis*, vol. 21, no. 1, pp. 27–40, 2000.
- [20] M. A. Unger, H. P. Chou, T. Thorsen, A. Scherer, and S. R. Quake, "Monolithic microfabricated valves and pumps by multilayer soft lithography," *Science*, vol. 288, no. 5463, pp. 113–116, 2000.
- [21] T. Thorsen, S. J. Maerkl, and S. R. Quake, "Microfluidic large-scale integration," *Science*, vol. 298, no. 5593, pp. 580–584, 2002.
- [22] D. J. Laser and J. G. Santiago, "A review of micropumps," *Journal of Micromechanics and Microengineering*, vol. 14, no. 6, pp. R35–R64, 2004.
- [23] N. T. Nguyen and Z. Wu, "Micromixers—a review," *Journal of Micromechanics and Microengineering*, vol. 15, no. 2, pp. R1–R16, 2005.
- [24] J. W. Hong and S. R. Quake, "Integrated nanoliter systems," *Nature Biotechnology*, vol. 21, no. 10, pp. 1179–1183, 2003.
- [25] Q. Cao and J. A. Rogers, "Ultrathin films of single-walled carbon nanotubes for electronics and sensors: a review of fundamental and applied aspects," *Advanced Materials*, vol. 21, no. 1, pp. 29–53, 2009.
- [26] L. Hu, D. S. Hecht, and G. Grüner, "Carbon nanotube thin films: fabrication, properties, and applications," *Chemical Reviews*, vol. 110, no. 10, pp. 5790–5844, 2010.
- [27] M. W. Rowell, M. A. Topinka, M. D. McGehee et al., "Organic solar cells with carbon nanotube network electrodes," *Applied Physics Letters*, vol. 88, no. 23, Article ID 233506, 2006.
- [28] Q. Cao, S. H. Hur, Z. T. Zhu et al., "Highly bendable, transparent thin-film transistors that use carbon-nanotube-based conductors and semiconductors with elastomeric dielectrics," *Advanced Materials*, vol. 18, no. 3, pp. 304–309, 2006.
- [29] D. Zhang, K. Ryu, X. Liu et al., "Transparent, conductive, and flexible carbon nanotube films and their application in organic light-emitting diodes," *Nano Letters*, vol. 6, no. 9, pp. 1880–1886, 2006.
- [30] L. Hu, G. Gruner, J. Gong, C. J. Kim, and B. Hornbostel, "Electrowetting devices with transparent single-walled carbon nanotube electrodes," *Applied Physics Letters*, vol. 90, no. 9, Article ID 093124, 2007.
- [31] L. Hu, D. S. Hecht, and G. Grüner, "A method of fabricating highly transparent and conductive interpenetrated carbon nanotube-parylene networks," *Nanotechnology*, vol. 20, no. 46, Article ID 465304, 5 pages, 2009.
- [32] E. Lahiff, C. Y. Ryu, S. Curran, A. I. Minett, W. J. Blau, and P. M. Ajayan, "Selective positioning and density control of nanotubes within a polymer thin film," *Nano Letters*, vol. 3, no. 10, pp. 1333–1337, 2003.
- [33] K. Lee, S. S. Lee, J. A. Lee, K. C. Lee, and S. Ji, "Carbon nanotube film piezoresistors embedded in polymer membranes," *Applied Physics Letters*, vol. 96, no. 1, Article ID 013511, 2010.
- [34] H. Cao, Z. Gan, Q. Lv et al., "Single-walled carbon nanotube network/poly composite thin film for flow sensor," *Microsystem Technologies*, vol. 16, no. 6, pp. 955–959, 2010.
- [35] Z. Wu, Z. Chen, X. Du et al., "Transparent, conductive carbon nanotube films," *Science*, vol. 305, no. 5688, pp. 1273–1276, 2004.

- [36] Y. Zhou, L. Hu, and G. Grüner, "A method of printing carbon nanotube thin films," *Applied Physics Letters*, vol. 88, no. 12, Article ID 123109, 3 pages, 2006.
- [37] M. Zhang, J. Wu, L. Wang, K. Xiao, and W. Wen, "A simple method for fabricating multi-layer PDMS structures for 3D microfluidic chips," *Lab on a Chip*, vol. 10, no. 9, pp. 1199–1203, 2010.

## Research Article

# Optoelectronic Heating for Fabricating Microfluidic Circuitry

**Gauvain Haulot and Chih-Ming Ho**

*Mechanical and Aerospace Engineering Department, University of California, Los Angeles, Los Angeles, CA 90095, USA*

Correspondence should be addressed to Chih-Ming Ho, [chihming@seas.ucla.edu](mailto:chihming@seas.ucla.edu)

Received 7 June 2011; Accepted 1 August 2011

Academic Editor: Eric Pei Yu Chiou

Copyright © 2011 G. Haulot and C.-M. Ho. This is an open access article distributed under the Creative Commons Attribution License, which permits unrestricted use, distribution, and reproduction in any medium, provided the original work is properly cited.

This work reports on optoelectronic-based heaters that can transduce low-power optical images into high-power heating to melt frozen liquids and form desired microfluidic circuitry. The mechanism of optoelectronic heating (OEH) was studied and characterized. OEH relies on photocurrent heating in the illuminated parts of actuating images. Resolution was affected by dark current heating. Photocurrents and dark currents were measured and related to the operating parameters. Successful melting of a frozen media within seconds with 2 mW light patterns and a 4 V operating voltage was demonstrated with feature sizes down to  $200\ \mu\text{m} \times 200\ \mu\text{m}$ . Strategies to increase resolution were addressed. It was shown that the size and location of heating areas can be reliably and rapidly reconfigured by changing the actuating image.

## 1. Introduction

Microelectromechanical system (MEMS) techniques have enabled thermal control at the microscale and thereby opened up the way to new applications. Microheating has been applied to various chemical and biological processes [1, 2], where accurate control of temperature is often essential, with a particular focus on polymerase chain reaction [3]. It has also been popular for microfluidic flow control; thermal pumps [4] and valves [5] offer elegant solutions for device integration. They are based on thermal expansion or phase transition of specific materials. Other thermal phenomena include the control of viscosity for droplet generation [6], temperature gradient focusing of particles [7], and thermocapillary pumping [8]. Local microheating is usually achieved with thin-film resistive heaters that are deposited and patterned using MEMS fabrication techniques. Optical heating is a convenient alternative.

Existing optical heating often requires a high-power light source and has been successfully demonstrated in chemical and biological applications [9, 10]. Optothermal valves and pumps have also been implemented in microfluidic platforms [11, 12]. They are typically based on thermal expansion of bubbles or nanocomposite materials in prefabricated areas. Biocompatible thermoreversible gelation polymers

offer more flexibility [13]. Those polymers solidify when heated and are biocompatible. They can be mixed with biochemical samples and be used as ubiquitous valves activated upon irradiation [14]. Nonetheless, all those devices are reliant on the optical absorption of liquids, which varies with chemical composition. Photoabsorbing substrates are a convenient alternative. They have been applied to optothermal valves [15] and droplet manipulation based on thermocapillary effects [16].

Optical actuation with low-power light patterns has been recently developed for microfluidics. It offers significant advantages for device integration and parallel manipulation. It is based on optoelectronic amplification of optical signals. So far, it has mainly relied on dielectrophoresis, with the optoelectronic tweezers (OETs) [17], and on optoelectrowetting [18].

In this work, optical actuation with low-power light is extended to microheating. Optoelectronic heating (OEH) constitutes a new technique for thermal control at the microscale. OEH provides high flexibility in thermal operations and is of particular interest for microfluidic applications, especially in the area of phase-transition-based flow control [19]. This paper reports on the fabrication and characterization of newly developed optoelectronic heaters (OEH devices).

## 2. Device Physics and Structure

The device presented in this work enables local microheating controlled by low-power light images. Such process is illustrated in Figure 1. Images are generated by a DMD microdisplay (DMD Discovery 1100 by Texas Instruments) and are projected onto an OEH device. Based on an optoelectronic heating transduction process, OEH devices convert the lighted parts of an image into heating areas. OEH is based on a photoconductive material sandwiched between two electrodes. The bottom electrode is made of transparent indium tin oxide (ITO). The top electrode is highly reflective and contains silver. A voltage bias is imposed between the electrodes, which induces a vertical electric field across the photoconductor. The lighted areas of displayed images create charge carriers in the photoconductive layer that are accelerated by the electric field; they produce heat by the Joule effect. Thus, only low optical power is needed.

The photoconductive layer must absorb light efficiently and thus necessitates a minimum thickness. Meanwhile, lateral heat transfers must be minimized for high resolution; this is why a thin film with low thermal conductivity is required. Hydrogenated amorphous silicon (a-Si:H) meets both those requirements. One-micrometer films can absorb light efficiently (absorption is  $10^{-4} \text{ cm}^{-1}$  at 630 nm), and its thermal conductivity is low, reportedly between  $0.1 \text{ W/m/K}$  [20] and  $2.6 \text{ W/m/K}$  [21] (this last value was measured in pure amorphous silicon films). In comparison, crystalline silicon (cSi) layers must be  $30 \mu\text{m}$  thick to absorb light efficiently, and the material's thermal conductivity is approximately  $140 \text{ W/m/K}$ , leading to poor resolution.

The system's temperature is controlled by a cooler. The cooler is placed underneath the optoelectronic chip to keep the top surface clear for observation and to facilitate access to the OEH device for eventual applications. Since observation requires illumination that would interfere with the actuating light patterns, the patterns are projected from underneath the chip; the cooler thus needs to be transparent.

In the OEH device, heat is generated by the Joule effect. The heating power is defined as

$$P_{\text{heat}} = I \cdot V, \quad (1)$$

where  $I$  is electrical current and  $V$  is the voltage bias. Therefore, the device's performance is monitored with  $I$ - $V$  curves. A typical  $I$ - $V$  characteristic measured on an OEH device is plotted in Figure 2.

The total current is sum of the dark current and the photocurrent:  $I = I_D + I_p$ . Photocurrents are activated by the lighted parts of displayed images. Dark currents emerge from intrinsic properties of the photoconductor, from the dark parts of displayed images, and from light used for observation. A key feature of OEH is resolution, which stems from the difference between heat generated in the lighted areas of a displayed image and heat generated in the dark areas of the image. Therefore the effective heating power depends on the photocurrent, and heating resolution will be improved by reducing dark currents.

The device displays a rectifying behavior (Figure 2). It comes from the metal-semiconductor contact, or the

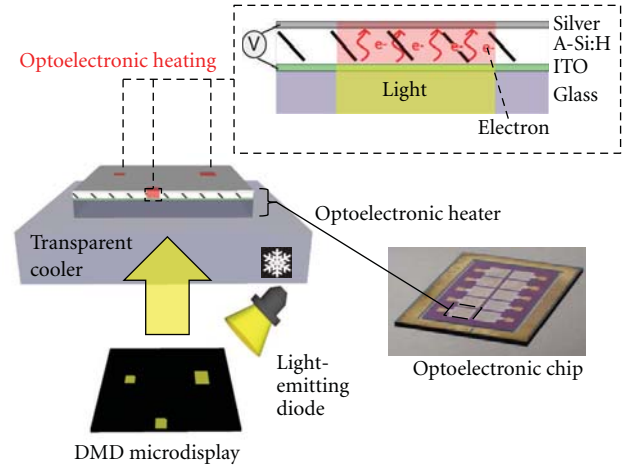


FIGURE 1: Structure and physics of the OEH platform.

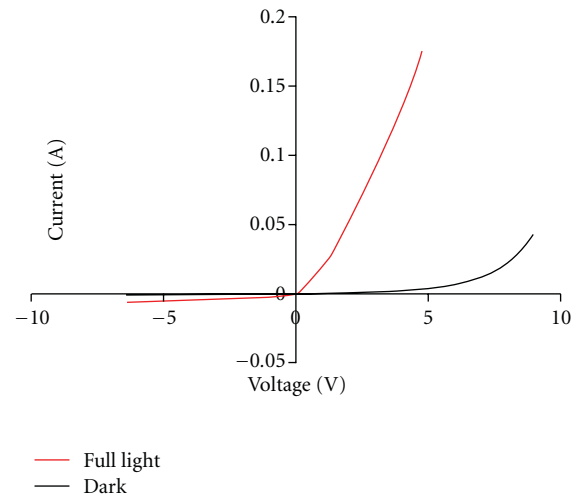


FIGURE 2: Typical  $I$ - $V$  characteristic measured on an OEH device. “Full light” means that the device is lighted throughout its entire surface, and “dark” means that a black image is displayed. Forward/reverse bias (positive/negative voltage) corresponds to a negative/positive potential applied to the bottom ITO electrode.

Schottky contact, at the interface between a-Si:H and the silver electrode. Such contacts have been reported for a-Si:H and used for solar cell applications [22]. The a-Si:H layer is n-doped in the vicinity of its interface with ITO to ensure ohmic contact. Because forward bias (negative potential applied to the bottom electrode) by far gives the highest power output, OEH is performed under such a bias.

Dark currents are expected to be greatly influenced by the Schottky barrier, and photocurrents to a lesser extent. In spite of the fact that the Schottky barriers in a-Si:H have been extensively studied, they are usually investigated under reverse bias and low forward bias. Indeed, high forward bias tends to reduce such barriers: as the forward bias increases, the depletion region decreases. The barrier therefore eventually becomes negligible. Moreover, the series resistance of intrinsic hydrogenated amorphous silicon is high (mobilities are low). At higher voltage, currents become series-resistance

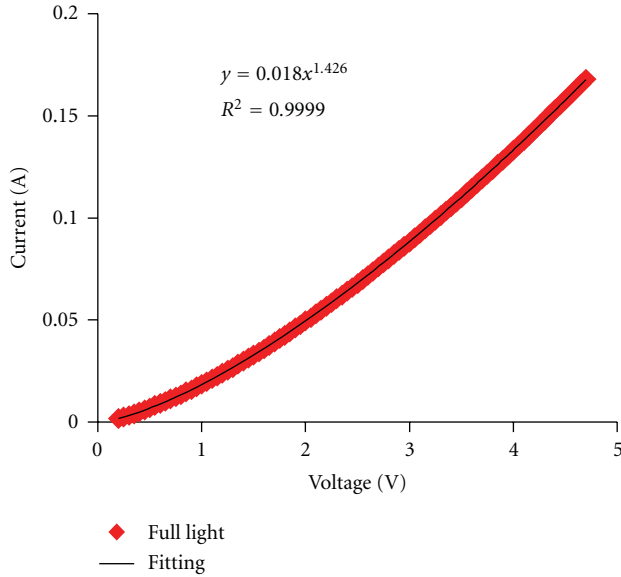


FIGURE 3: Photocurrent under forward bias for a fully lighted image (the entire surface of the OEH device is illuminated).

limited [23, 24], which precludes experimental studies of the barrier. It also entails high heat losses in the device, which is generally a drawback; in this work, it is the effect sought after.

### 3. Materials and Methods

OEH devices were fabricated from hydrogenated amorphous silicon chips purchased from Silicon Digital (Korea). Such chips consisted of a glass substrate, a 200 nm thick indium tin oxide (ITO) electrode, a 50 nm n-doped a-Si:H layer, and a 1  $\mu\text{m}$ -thick intrinsic a-Si:H layer; they were 3 cm wide and 5 cm long. An array of 10 OEH devices was made out of one of those chips. 500 nm of silicon dioxide was deposited by plasma-enhanced chemical vapor deposition (PECVD) and subsequently patterned by wet-etching using buffer oxide etch (BOE, 6 : 1).  $\text{SiO}_2$  filled possible pinholes in the a-Si:H film to prevent shunt currents.  $\text{SiO}_2$  was etched in the future locations of the OEH devices and in the periphery. Amorphous silicon was then etched by RIE in the periphery in order to reveal the underlying ITO. Contact pads for the OEH devices' top electrode and for ITO were subsequently deposited by evaporation and patterned by liftoff. This layer was made of titanium and gold (10 nm and 100 nm). Finally, the OEH devices' top electrodes were deposited and patterned through the same process. They were made of titanium for adhesion (10 nm), platinum as an atomic diffusion shield that protected the semiconductor from silver (50 nm), and silver for high reflection (100 nm). A picture of the final chip is shown in Figure 1.

The chip was then placed on a cooler. The cooler was made of an aluminum plate with a built-in transparent sapphire window. Sapphire has a high thermal conductivity, which is essential to cooling efficiency. To limit light absorption while cooling homogeneously, the cooler's thickness was minimized based on simulations using the COMSOL

Multiphysics software. Temperature was controlled by thermoelectric coolers (PT8-25-40\*80 by Melcor, Trenton, NJ, USA) attached to the aluminum plate.

A DMD microdisplay generated images that were focused on the photoconductive layer using lenses and a mirror (Thorlabs, Inc.). The DMD was integrated with a light source consisting of a red diode emitting at 629 nm and with a projection lens (ViALUX GmbH, Germany). This wavelength provided optimum absorption in the 1  $\mu\text{m}$  thick a-Si:H layer. For most of the experiments, the chip was connected to an electrical setup controlled by LabView.  $I$ - $V$  curves were plotted based on this setup. For melting experiments, however, a dc generator was directly connected to the chip. OEH devices were visualized through a microscope placed above the optoelectronic chip.

For the melting experiments, a layer of liquid hexadecane (ReagentPlus, 99%, Sigma-Aldrich) was placed on the optoelectronic chip at room temperature. The layer was confined using spacers and a glass cover slip. The cooler's temperature was then set to 288 K to freeze hexadecane. Using a 4 V operating voltage and images of square patterns, melting of square-shaped areas was achieved.

### 4. Experimental Section: Characterization of OEH

For high power and high resolution, heating must be maximized in lighted regions and minimized in dark regions. Photocurrents and dark currents are studied by using fully lighted images (the entire surface of the OEH device is illuminated) and black images, respectively. Furthermore, optical control of OEH is investigated using more complex light patterns.

**4.1. Heating Power: Study of Photocurrents.** In this section, photocurrents and their dependence on voltage and on the optical power input are investigated. Dark currents can be subtracted from the current measured under full illumination to study the photocurrents (see Figure 2). The resulting curve is plotted in Figure 3.

Theoretically, in a photoconductor, photocurrents are linearly correlated to voltage [25]. They follow the following equation:

$$I_P = (\mu_n + \mu_p) G_e \tau q \frac{A}{l} V, \quad (2)$$

where  $\mu_n$  and  $\mu_p$  are, respectively, the electron and hole mobilities,  $G_e$  is the carrier generation rate,  $\tau$  is the carrier life time,  $q$  is the elementary charge,  $A$  is the illuminated photoconductor area,  $l$  is the semiconductor thickness, and  $V$  is the voltage bias. A slight nonlinear trend is observed in Figure 3 however. The plot is fitted for voltages greater than 0.3 V, since measurements at very low voltages are noisy. With excellent correlation of  $R^2 = 0.9999$ , the photocurrent follows the following equation:

$$I_P = I_{0P} V^\varphi \quad (3)$$

with  $\varphi = 1.43$  and  $I_{0P} = 1.85 \cdot 10^{-2} \text{A}$ .

The exponent  $\varphi$  is greater than its theoretical value of 1 (see (2)). Such a superohmic photoconductivity has been reported in a-Si:H under high electric fields, typically above 10 kV/cm [26, 27], which is comparable to the ones used in the present study. This behavior, however, decreases with temperature, and those experiments were performed at 100 K and below. The Schottky contact is a more likely cause of superohmic photoconductivity in the present study. Since the depletion region at the corresponding metal-semiconductor interface decreases when forward bias increases, the series resistance is also reduced and thereby causes the observed superohmic trend.

A key aspect of OEH is its low-power light source. This feature is studied by measuring the power output under different optical power inputs. The results are represented in Figure 4(a).

Fully lighted images are displayed at different optical powers. In Figure 4(a), 100% corresponds to the maximum power output of the display system, 2 mW. Percentages of the maximum power are achieved by homogeneously turning off pixels in the projected image. Each millisecond, a new image with newly turned-on and turned-off pixels is displayed to ensure homogeneity. For that purpose, the DMD display is controlled by a Matlab program.  $I$ - $V$  curves are plotted under optical powers varying from 10% to 100%, with 10% increments. A clear saturation trend is observed. It shows that increasing the optical power input above 1 mW (corresponding to 50%) has a limited impact on heat generation.

Those results can be analyzed using the equation found for photocurrents, (3). After subtracting the dark currents, which correspond to the 0% curve in Figure 4(a), excellent fitting is achieved, with  $R^2$  values ranging from 1 to 0.9995 for light intensities above 20%. 10% light intensity gives  $R^2 = 0.9988$ . The corresponding values for  $I_{0P}$  and  $\varphi$  are plotted in Figures 4(b) and 4(c).

$I_{0P}$  increases with the optical power input as illustrated in Figure 4(b), but a slight saturation tendency is observed. Figure 4(c) shows that increasing light intensity decreases  $\varphi$ , leading to a lower response to voltage. Figures 4(b) and 4(c) clearly indicate that photocurrents tend to saturate when the optical power increases.

Furthermore, theoretically  $I_{0P}$  is proportional to the carrier generation rate, which itself is proportional to light intensity. It comes from (2) and from the following equation for the generation rate [25]:

$$G_e = \frac{1}{Al} \eta \frac{P_{\text{opt}}}{h\nu}, \quad (4)$$

where  $\eta$  is the quantum efficiency,  $P_{\text{opt}}$  is the light intensity or incident optical power, and  $h\nu$  is the photon energy. From the data displayed in Figure 4(a), photocurrents are plotted against light intensity for various values of the bias voltage (Figure 4(d)). According to Figure 4(d), photocurrents approximately scale with light intensity following a power law with exponent smaller than one:

$$I_P \propto P_{\text{opt}}^\gamma, \quad \text{with } \gamma < 1. \quad (5)$$

This behavior has been reported previously [28, 29]. The exponent  $\gamma$  is plotted in Figure 4(e). Interestingly,  $\gamma$  decreases with voltage. It shows that the dependence of photocurrents on voltage and their dependence on light intensity are correlated. The literature reports values of  $\gamma$  spanning from 0.5 to 1 [28, 29] depending on the recombination process. If recombination is purely bimolecular (involving an electron and a hole),  $\gamma = 1/2$ ; if recombination is purely monomolecular (involving a single charge carrier at a time),  $\gamma = 1$  [28].

These results show that photocurrents are related to voltage and light intensity through a power law, with a scaling exponent greater than one for voltage and smaller than one for light intensity. These relations are correlated, since the exponent of the power law for voltage ( $\varphi$ ) depends on light intensity and the exponent of the power law for light intensity ( $\gamma$ ) depends on voltage. Increasing voltage is an efficient way to achieve high-power OEH with low-power light. On the contrary, increasing the optical power input above the level currently available on the OEH platform will have little effect.

**4.2. Resolution: Study of Dark Currents.** Resolution is affected by heat generation in the dark areas of the displayed patterns. It stems from two sources: dark currents and background currents. Dark currents are generated by the voltage bias. They can result from thermal excitation of carriers or background doping in a-Si:H. Background currents are excited by background illumination, which comes from the light used for observation and from the dark parts of images. Black images indeed generate a  $3 \mu\text{W}$  optical power. In this work, dark currents and background currents are grouped together and simply designated as dark currents to indicate that they occur in dark regions.

The forward characteristics of an OEH device are measured under complete dark at  $22^\circ\text{C}$ . To assess the influence of background currents, the characteristics are also measured when a black image is displayed and when the device is illuminated for microscope observation. The characteristics are fitted with the diode equation:

$$I_D = I_{0D} \left( \exp\left(\frac{qV}{nk_B T}\right) - 1 \right), \quad (6)$$

where  $V$  is the bias voltage,  $k_B$  is the Boltzmann constant,  $T$  is the temperature, and  $n$  is the ideality factor. The results are plotted in Figure 5. For complete dark, dark with DMD background light, and dark with background light and observation light, values for  $I_{0D}$  are, respectively,  $5 \times 10^{-5}$  A,  $3.3 \times 10^{-4}$  A, and  $1.17 \times 10^{-3}$  A. The corresponding values for  $n$  are 56, 69, and 79, respectively. Background and observation lights expectedly increase both  $I_{0D}$  and  $n$ . The diode model matches the data well. At 4 V, carriers generated by background light approximately result in a three-fold increase of current; adding microscope illumination causes another twofold.

The ideality factors are high compared to reported values. They are usually close to unity, although they can increase up to values of 10 at lower temperature [22, 30]. Nevertheless, values reported in previous works were measured at low

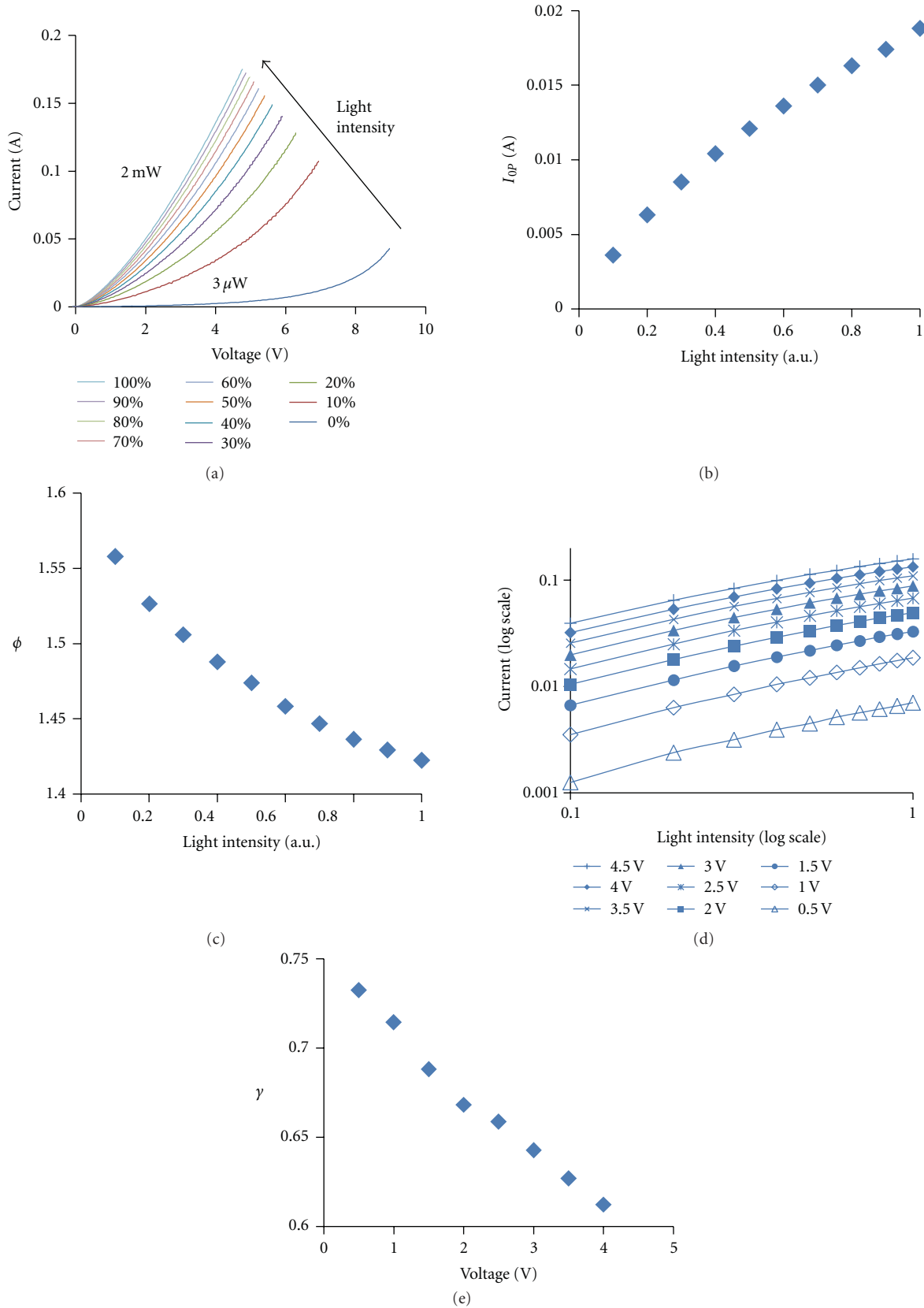


FIGURE 4: Influence of the optical power input on OE. (a)  $I-V$  curves showing the functional dependence of currents on light intensity under fully lighted images (the entire OEH device's surface is illuminated). Light intensities are indicated as percentages of the maximum light intensity ( $2 \text{ mW}$ ), with 10% increment. 0% ( $3 \mu\text{W}$ ) corresponds to a black image. (b) and (c) Influence of light intensity on  $I_{op}$  and  $\phi$  defined in the photocurrent equation as  $I_p = I_{op}V^\phi$ . (d) Current against light intensity for various values of the bias voltage (log-log scale). (e) Functional dependence of  $\gamma$  on voltage, where  $\gamma$  relates photocurrents to light intensity through the power law  $I_p \propto P_{opt}^\gamma$ .

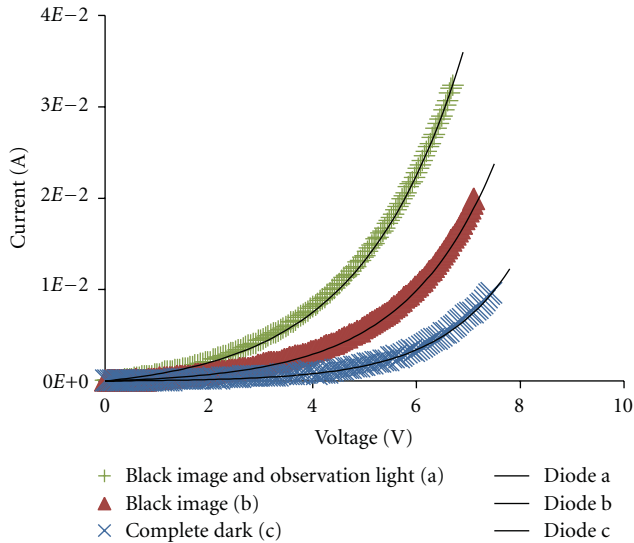


FIGURE 5:  $I$ - $V$  curves for an OEH device under various “dark” conditions and their respective fittings. Fittings are based on the diode equation (6). Measurements are performed in complete dark (a), when a black image is projected onto the OEH device (b), and when a black image is displayed and the top electrode is illuminated for microscope observation (c).

voltages, typically between 0.2 V and 0.6 V (ideality factors close to unity cause the current to reach very high values around 1 V). On the contrary, the study herein investigates a voltage range between 0 V and 8 V. At such far forward bias, series resistance and, at higher voltages, eventual space-charge-limited currents have to be accounted for [23]. Those phenomena limit currents and explain high ideality factors. Furthermore, the prefactor  $I_{0D}$  is higher compared to reported values. It stems from high forward bias and shunt currents. Shunt currents are caused by pinholes in the photoconductive layer and have been reported in a-Si:H films [23].

Resolution can be increased by mitigating dark current heating. It can be done by reducing currents induced by microscope illumination. The related optical power can be reduced to a minimum value, or other visualization strategies can be adopted. Furthermore, observation light is partly reflected by the silver electrode, since the reflectance of silver is between 90% and 95% for most of the visual range of the light spectrum. Some of it is absorbed, however, which causes currents. Improving reflection of the OEH device’s top electrode, for instance, using antireflective coating, should therefore reduce dark heating. Filtering light to a particular range of wavelengths could also optimize reflection. On the contrary, not much can be done to curb background currents originating from the dark parts of displayed patterns. The only option is to use a display device with a higher contrast. Finally, dark currents that do not emerge from background light can be reduced using higher-quality materials, with minimal shunts and background doping. It will increase the series resistance.

For a heater, the effect of temperature variation on device performance is important. The characteristics of dark currents under background and observation light as well as

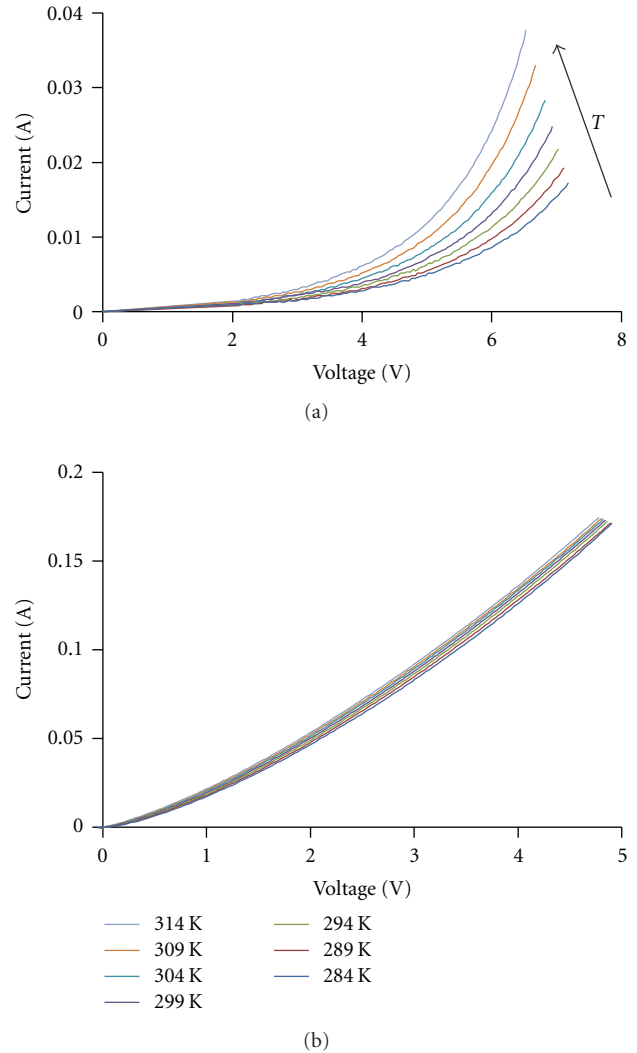


FIGURE 6:  $I$ - $V$  curves showing the influence of temperature ( $T$ ) on dark currents (a) and photocurrents (b). The increase of temperature is illustrated with an arrow.

the characteristics of photocurrents under full illumination are studied at different temperatures. The results are plotted in Figure 6. The temperature range studied spans from 284 K to 314 K. Temperature has a relatively stronger influence on dark currents than on photocurrents. It entails that, when temperature increases, heating power will be maintained but resolution will be affected. This effect is stronger at higher voltages.

**4.3. Optical Control of OEH.** Up to this point, only fully lighted and black images have been used to study the OEH device. The goal for OEH is to offer optically controlled microheating with high flexibility in terms of size, location, and timing. In this section heating is thus studied with more complex images: square patterns of different sizes in a fixed location, square patterns of fixed size in different locations, and finally sequences of fully lighted and black images with varying frequencies to investigate the device’s time response.

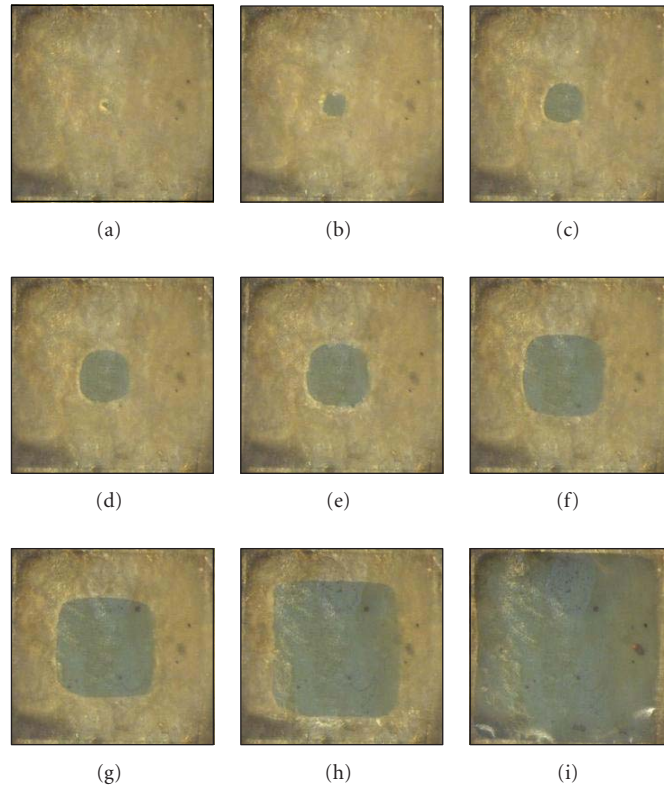


FIGURE 7: Melting of square-shaped areas localized at the OEH device’s center in hexadecane at 15°C. From (a) to (i) in percentage of chip area: 1%, 2.25%, 4%, 6.25%, 9%, 16%, 25%, 56.25%, and 100%. Each image represents a 5 mm × 5 mm area.

An interesting application of OEH is the rapid fabrication and reconfiguration of microfluidic structures by local thawing of a frozen media. Melting actuated by images is demonstrated herein. It is also a convenient way to visualize OEH. The melting material used is hexadecane. It melts at 18°C, and its latent heat is 184 kJ/L (as compared to 332 kJ/L for water). The system temperature is set at 15°C, and the operating voltage is 4 V. Square patterns of different sizes are displayed at the chip center. Figure 7 illustrates the experimental results.

Figure 7 shows square-shaped melted areas ranging from 500 μm × 500 μm to 5 mm × 5 mm. They were melted within seconds, thus proving OEH’s efficiency, and they remained stable thereafter. Steady state was achieved between 2 s and 10 s depending on the feature size—the transient time increased with size. For better visualization, a rather thick layer of hexadecane was used. The thickness was between 150 μm and 200 μm. Since melting was detected only when the layer was thawed throughout its whole thickness, smaller feature sizes were obtained with thinner films.

The melted areas display rounded corners. They are due to the isotropy of heat diffusion, as corroborated by three-dimensional simulations based on the COMSOL Multiphysics software. The simulations also show that temperature within the device does not vary more than a few degrees. Indeed, thermal insulation has not been optimized in this study. In particular, the high thermal conductivity of silver

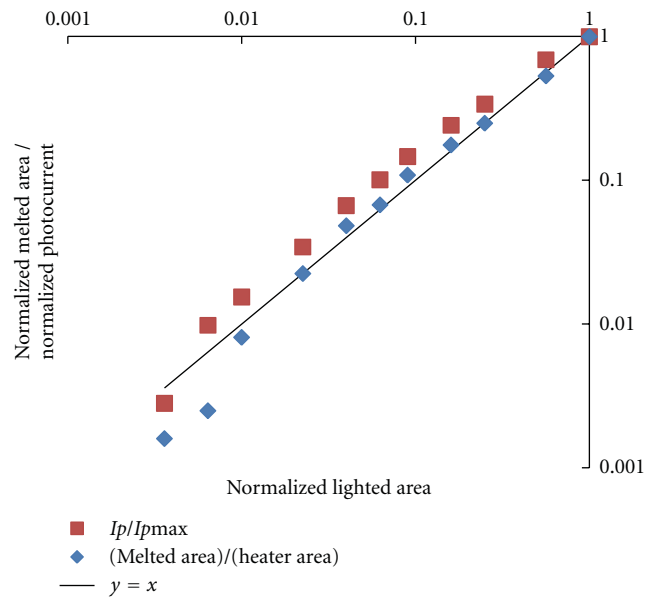


FIGURE 8: Functional dependence of normalized photocurrents and normalized melted areas on the corresponding normalized lighted areas. The expected linear trend is plotted for reference. Photocurrents are normalized to the photocurrent generated by a fully lighted image, where the entire OEH device area is lighted. Melted areas and lighted areas are normalized to the OEH device (heater) area.

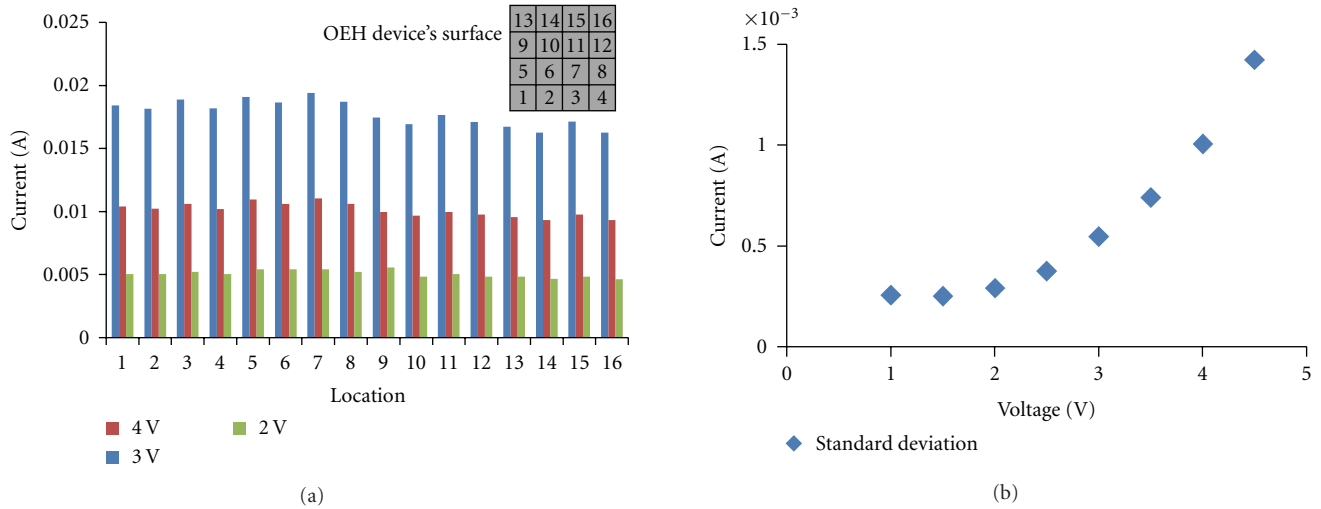


FIGURE 9: Homogeneity of photocurrent actuation throughout an OEH device's surface. (a) Current in 16  $1.25 \text{ mm} \times 1.25 \text{ mm}$  areas covering the entire surface of an OEH device at various voltages. The areas were lighted one at a time. (b) Standard deviation of current values throughout the 16 areas: functional dependence on voltage.

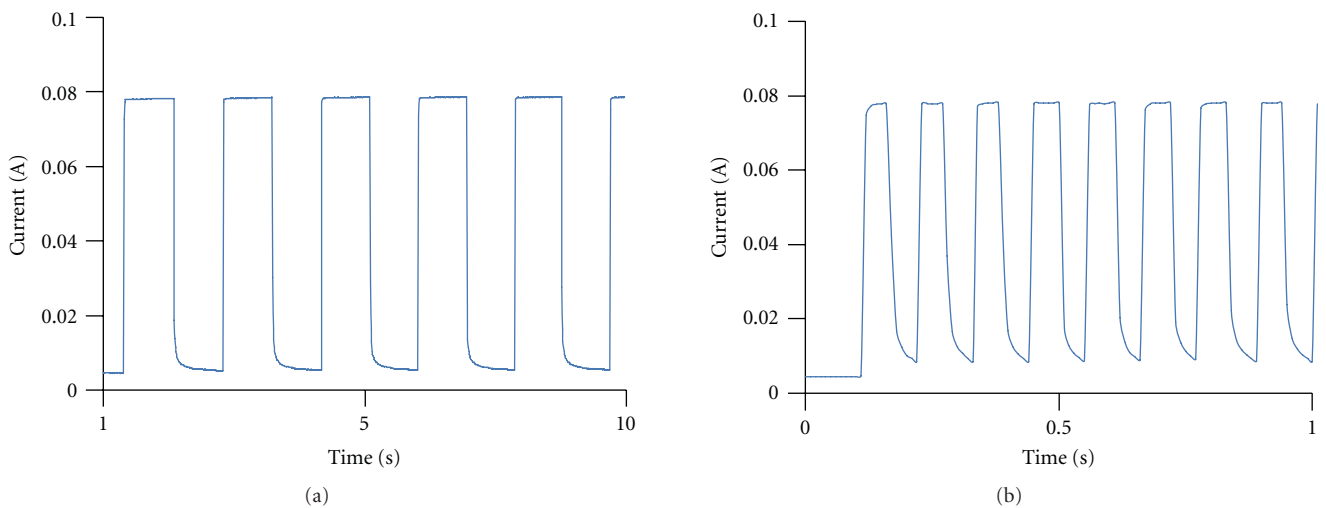


FIGURE 10: Current variation with time when a fully lighted image and a black image are sequentially displayed one after the other, each for 1 s (a) or for 0.05 s (b).

accounts for higher heat fluxes in the OEH device's top electrode.

More measurements were carried out with a  $100 \mu\text{m}$  thick layer of hexadecane. Pictures of melted square patterns were taken and used to evaluate the corresponding areas. Normalized melted areas are plotted against the corresponding normalized lighted areas in Figure 8. Melted areas and lighted areas are normalized to the OEH device's surface area. Photocurrents were also measured. They are plotted against the corresponding normalized lighted areas in Figure 8. Photocurrents are normalized to the maximum photocurrent, which is activated by fully lighted images. Melted areas and photocurrents are accurately controlled by the light patterns down to  $500 \mu\text{m} \times 500 \mu\text{m}$  features. The

preciseness and effectiveness of OEH are thereby demonstrated. Optical control becomes nonlinear below  $500 \mu\text{m} \times 500 \mu\text{m}$  features. This phenomenon is observed on data points corresponding to melted areas of  $200 \mu\text{m} \times 200 \mu\text{m}$  and  $250 \mu\text{m} \times 250 \mu\text{m}$  that are actuated by square patterns of areas  $300 \mu\text{m} \times 300 \mu\text{m}$  and  $400 \mu\text{m} \times 400 \mu\text{m}$ , respectively. As stated hereinbefore, the layer's thickness plays a role in this nonlinear behavior. Besides, dark currents become comparable to photocurrents at lower feature sizes. Thereby, the dark currents affect resolution and also account for this nonlinear response.

Figure 8 shows that for lighted areas larger than  $500 \mu\text{m} \times 500 \mu\text{m}$  the photocurrent can be used as a proxy for OEH and for melting. It will be used in the following. Heating

homogeneity is important for the reliability of OEH devices. To test homogeneity, the OEH device's surface was divided into a four by four array of 16  $1.25\text{ mm} \times 1.25\text{ mm}$  areas. The areas were lighted one at a time, and the current was measured. The experiment was repeated at several voltages; the results for 2 V, 3 V and 4 V are plotted in Figure 9(a).

An OEH device is a square of area  $5\text{ mm} \times 5\text{ mm}$  (cf. Figure 1). Figure 9(a) shows how heating varies throughout the OEH device's surface. Although the values are close to one another, differences appear. No obvious trend such as edge effects stands out however. The standard deviation for the current values throughout the 16 unit areas is plotted against voltage in Figure 9(b). Homogeneity in the areas' response to optical actuation is fairly good throughout the OEH device's surface: the standard deviation stays below 5% of the average value. The highest difference between current values, however, reaches 15%. The reason for this slight heterogeneity is not straightforward. A likely cause is the quality of a-Si:H. The material used in these experiments has proven very rough and contains pinholes. Roughness indicates variations in chemical composition and thickness, which entail variations in conductivity. Pinholes, if not properly passivated by the oxide layer, result in shunt currents. The randomness of those two factors is in agreement with the results presented in Figure 9(a). Better quality amorphous silicon will increase heating homogeneity.

The time response of the device is also an important parameter for the nature of reconfigurable operations. It was tested by serially displaying fully lighted and black images at different frequencies. The results are illustrated in Figure 10.

In these experiments, currents were measured at 2.5 V. A fully lighted image and a black image were displayed one after the other and each for the same amount of time, which varied between experiments from 1 min to 0.01 s. The device could be operated as fast as 0.05 s/image. Current was plotted against time. The curves show rounded corners that are due to capacitive effects. Those effects appear to be the time-response limiting factor. In the case of melting applications, melting takes at least half a second and will thus be the limiting time factor of reconfiguration.

Finally, although a-Si:H is known to degrade when illuminated because of light-induced defects [31], no degradation was noticed during four weeks of device operation.

## 5. Conclusion

In this paper, an optoelectronic-based heater is reported for the first time. It enables heating confined at microscales with low-power light pattern actuation. Optoelectronic heating (OEH) is triggered by photocurrents in the lighted parts of actuating images. Photocurrents highly respond to the operating voltage, and their dependence on the optical power input is limited. Therefore OEH efficiently operates with low-power light. Dark currents cause undesired heating in the dark regions of actuating images. Since they respond exponentially to the operating voltage, they affect resolution at higher voltages. However, dark currents can be mitigated by improving the photoconductor quality and by minimizing background illumination. The versatility of OEH has been

demonstrated by varying the size, location, and timing of the actuating light patterns. In particular, a frozen material was successfully melted within seconds. The melting areas varied from  $5\text{ mm} \times 5\text{ mm}$  to  $200\text{ }\mu\text{m} \times 200\text{ }\mu\text{m}$ . Smaller feature sizes can be achieved by improving the resolution of OEH devices and reducing the frozen material layer's thickness. Thawing of a frozen media by OEH paves the way to the rapid fabrication and reconfiguration of microfluidic structures, as previously reported [19]. This work provides a quantitative analysis of the OEH process for further investigation of reconfigurable microfluidic circuitry controlled by low-power light images.

## Acknowledgments

The authors would like to thank Drs. Hideaki Tsutsui and Eric P.Y. Chiou for their help. This work is supported by the Center for Scalable and Integrated NanoManufacturing (SINAM) (DMI-0327077).

## References

- [1] E. M. Chan, R. A. Mathies, and A. P. Alivisatos, "Size-controlled growth of CdSe nanocrystals in microfluidic reactors," *Nano Letters*, vol. 3, no. 2, pp. 199–201, 2003.
- [2] D. L. Huber, R. P. Manginell, M. A. Samara, B. I. Kim, and B. C. Bunker, "Programmed adsorption and release of proteins in a microfluidic device," *Science*, vol. 301, no. 5631, pp. 352–354, 2003.
- [3] M. U. Kopp, A. J. de Mello, and A. Manz, "Chemical amplification: continuous-flow PCR on a chip," *Science*, vol. 280, no. 5366, pp. 1046–1048, 1998.
- [4] P. Sethu and C. H. Mastrangelo, "Polyethylene glycol (PEG)-based actuator for nozzle-diffuser pumps in plastic microfluidic systems," *Sensors and Actuators A*, vol. 104, no. 3, pp. 283–289, 2003.
- [5] M. E. Harmon, M. Tang, and C. W. Frank, "A microfluidic actuator based on thermoresponsive hydrogels," *Polymer*, vol. 44, no. 16, pp. 4547–4556, 2003.
- [6] N. T. Nguyen, T. H. Ting, Y. F. Yap et al., "Thermally mediated droplet formation in microchannels," *Applied Physics Letters*, vol. 91, no. 8, Article ID 084102, 2007.
- [7] D. Ross and L. E. Locascio, "Microfluidic temperature gradient focusing," *Analytical Chemistry*, vol. 74, no. 11, pp. 2556–2564, 2002.
- [8] A. A. Darhuber, J. P. Valentino, S. M. Troian, and S. Wagner, "Thermocapillary actuation of droplets on chemically patterned surfaces by programmable microheater arrays," *Journal of Microelectromechanical Systems*, vol. 12, no. 6, pp. 873–879, 2003.
- [9] Y. Liu, D. K. Cheng, G. J. Sonek, M. W. Berns, C. F. Chapman, and B. J. Tromberg, "Evidence for localized cell heating induced by infrared optical tweezers," *Biophysical Journal*, vol. 68, no. 5, pp. 2137–2144, 1995.
- [10] M. N. Slyadnev, Y. Tanaka, M. Tokeshi, and T. Kitamori, "Photothermal temperature control of a chemical reaction on a microchip using an infrared diode laser," *Analytical Chemistry*, vol. 73, no. 16, pp. 4037–4044, 2001.
- [11] S. R. Sershen, G. A. Mensing, M. Ng, N. J. Halas, D. J. Beebe, and J. L. West, "Independent optical control of microfluidic valves formed from optomechanically responsive nanocomposite hydrogels," *Advanced Materials*, vol. 17, no. 11, pp. 1366–1368, 2005.

- [12] K. Zhang, A. Jian, X. Zhang, Y. Wang, Z. Li, and H. Y. Tam, "Laser-induced thermal bubbles for microfluidic applications," *Lab on a Chip*, vol. 11, no. 7, pp. 1389–1395, 2011.
- [13] H. Yoshioka, M. Mikami, Y. Mori, and E. Tsuchida, "Synthetic hydrogel with thermoreversible gelation. I. preparation and rheological properties," *Journal of Macromolecular Science—Pure and Applied Chemistry*, vol. A31, no. 1, pp. 113–120, 1994.
- [14] H. Sugino, T. Arakawa, Y. Nara et al., "Integration in a multilayer microfluidic chip of 8 parallel cell sorters with flow control by sol-gel transition of thermoreversible gelation polymer," *Lab on a Chip*, vol. 10, no. 19, pp. 2559–2565, 2010.
- [15] M. Krishnan, J. Park, and D. Erickson, "Optothermoeological flow manipulation," *Optics Letters*, vol. 34, no. 13, pp. 1976–1978, 2009.
- [16] A. T. Ohta, A. Jamshidi, J. K. Valley, H. Y. Hsu, and M. C. Wu, "Optically actuated thermocapillary movement of gas bubbles on an absorbing substrate," *Applied Physics Letters*, vol. 91, no. 7, Article ID 074103, 2007.
- [17] P. Y. Chiou, A. T. Ohta, and M. C. Wu, "Massively parallel manipulation of single cells and microparticles using optical images," *Nature*, vol. 436, no. 7049, pp. 370–372, 2005.
- [18] P. Y. Chiou, H. Moon, H. Toshiyoshi, C. J. Kim, and M. C. Wu, "Light actuation of liquid by optoelectrowetting," *Sensors and Actuators A*, vol. 104, no. 3, pp. 222–228, 2003.
- [19] G. Haulot, A. J. Benahmed, and C. M. Ho, "Optoelectronic reconfigurable microchannels," in *Proceedings of the 24th International Conference on Micro Electro Mechanical Systems (MEMS '11)*, pp. 53–56, January 2011.
- [20] N. Attaf, M. S. Aida, and L. Hadjeris, "Thermal conductivity of hydrogenated amorphous silicon," *Solid State Communications*, vol. 120, no. 12, pp. 525–530, 2001.
- [21] H. J. Goldsmid, M. M. Kaila, and G. L. Paul, "Thermal conductivity of amorphous silicon," *Physica Status Solidi A*, vol. 76, no. 1, pp. K31–K33, 1983.
- [22] C. R. Wronski, D. E. Carlson, and R. E. Daniel, "Schottky-barrier characteristics of metal-amorphous-silicon diodes," *Applied Physics Letters*, vol. 29, no. 9, pp. 602–605, 1976.
- [23] D. E. Heller, R. M. Dawson, C. T. Malone, S. Nag, and C. R. Wronski, "Electron-transport mechanisms in metal Schottky barrier contacts to hydrogenated amorphous silicon," *Journal of Applied Physics*, vol. 72, no. 6, pp. 2377–2384, 1992.
- [24] N. Szydlo, J. Magariño, and D. Kaplan, "Post-hydrogenated chemical vapor deposited amorphous silicon Schottky diodes," *Journal of Applied Physics*, vol. 53, no. 7, pp. 5044–5051, 1982.
- [25] S. M. Sze, *Physics of Semiconductor Devices*, Wiley, 3rd edition, 2007.
- [26] T. Aoki, N. Ohru, C. Fujihashi, and K. Shimakawa, "Enhancement of non-geminate electron-hole pair recombination induced by strong electric field in hydrogenated amorphous silicon (a-Si:H): effective-temperature concept," *Philosophical Magazine Letters*, vol. 88, no. 1, pp. 9–17, 2008.
- [27] K. Jahn, R. Carius, and W. Fuhs, "Photoluminescence and photoconductivity of a-Si:H at high electric fields," *Journal of Non-Crystalline Solids*, vol. 97-98, no. 1, pp. 575–578, 1987.
- [28] W. Paul and D. A. Anderson, "Properties of amorphous hydrogenated silicon, with special emphasis on preparation by sputtering," *Solar Energy Materials*, vol. 5, no. 3, pp. 229–316, 1981.
- [29] J. A. Schmidt, R. R. Koropecski, R. D. Arce, F. A. Rubinelli, and R. H. Buitrago, "Energy-resolved photon flux dependence of the steady state photoconductivity in hydrogenated amorphous silicon: implications for the constant photocurrent method," *Thin Solid Films*, vol. 376, no. 1-2, pp. 267–274, 2000.
- [30] A. Madan, W. Czubytyj, J. Yang, M. S. Shur, and M. P. Shaw, "Observation of two modes of current transport through phosphorus-doped amorphous hydrogenated silicon Schottky barriers," *Applied Physics Letters*, vol. 40, no. 3, pp. 234–236, 1982.
- [31] T. Shimizu, "Staebler-Wronski effect in hydrogenated amorphous silicon and related alloy films," *Japanese Journal of Applied Physics Part 1*, vol. 43, no. 6 A, pp. 3257–3268, 2004.

## Research Article

# Assembly of Carbon Nanotubes between Electrodes by Utilizing Optically Induced Dielectrophoresis and Dielectrophoresis

Pei-Fang Wu<sup>1</sup> and Gwo-Bin Lee<sup>2</sup>

<sup>1</sup>Department of Engineering Science, National Cheng Kung University, Tainan 701, Taiwan

<sup>2</sup>Department of Power Mechanical Engineering, National Tsing Hua University, Hsinchu 30013, Taiwan

Correspondence should be addressed to Gwo-Bin Lee, gwobin@pme.nthu.edu.tw

Received 1 May 2011; Revised 30 June 2011; Accepted 6 July 2011

Academic Editor: Aaron T. Ohta

Copyright © 2011 P.-F. Wu and G.-B. Lee. This is an open access article distributed under the Creative Commons Attribution License, which permits unrestricted use, distribution, and reproduction in any medium, provided the original work is properly cited.

This study reports a new approach for assembling carbon nanotubes (CNTs) between electrodes combination of optically induced dielectrophoresis force and dielectrophoresis force. Metal electrodes and amorphous silicon layer were first patterned and then used to assemble CNTs. By utilizing moving light patterns, the CNTs could be collected to the central area between two metal electrodes. The CNTs with different concentrations can be collected and aligned to form CNTs lines with different widths. The immobilization of preassembled CNTs was also demonstrated by exposing them to an ultraviolet light source such that they can be fixed at the prealigned location. Then photoresist ash was used to get rid of the cured polymer. The development of the new platform can be promising to massively assemble CNTs.

## 1. Introduction

The application of CNTs in various fields has increased dramatically and has made a substantial impact recently since their discovery [1]. For example, they are regarded as promising building blocks for next-generation nanosensing devices due to their high-aspect-ratio structures, unique electronic characteristics, and excellent transducing properties [2, 3]. With advances in micro- and nanotechnologies, these nanosensing devices are capable of metering physical, chemical or biological properties at a micro- or even nano-scale. For instance, CNTs can be trapped and patterned across prefabricated electrode arrays to yield reproducible sensing features in constructing gas sensors [4, 5]. However, there are several issues involved when patterned CNTs across electrodes to form nanosensors. First, reproducible and well-controlled patterns of CNTs must be made such that these nanosensors will behave in a reproducible manner from device to device. Furthermore, parallel assembly of these CNTs is crucial for mass production of any CNT-based nanosensors.

A variety of methods for the manipulation of CNTs have been demonstrated in the literature, including guided

CNTs growth [6, 7], magnetic forces [8, 9], polar molecular patterning [10], and optical tweezers [11]. For instance, organized CNTs structures can be formed by using chemical vapor deposition such that guided CNTs can grow in situ. Alternatively, pregrown CNTs can be aligned and manipulated after they have been formed. However, it is either a lengthy process or remains challenging when attempts are made to align them in parallel between two electrodes for a large-scale fabrication process. Furthermore, a variety of techniques for modifying the surfaces of CNTs may also give rise to self-assembled ordered structure of CNTs on metal substrates [12]. Alternatively, optical tweezers (OTs) have been explored as a flexible method for the manipulation of CNTs [13]. Although OTs can manipulate objects accurately by using high-power laser beams to trap the nanoobjects, they also need a high-precision positioning process for the manipulation of CNTs, hence, hindering their practical applications. Furthermore, the experimental setup for an OT system is relatively costly.

Recently, another technique, dielectrophoresis (DEP) [14], has been commonly used for CNT manipulation. For example, CNTs could be aligned between two metal electrodes with ease by using this approach [15, 16]. However,

the number and the total width of clustered CNTs are difficult to be precisely controlled since the induced DEP force exists only in the neighborhood of the electrodes. Therefore, it may significantly affect the density of the CNT-based nanosensors. Consequently, a primary challenge involved in the fabrication of these nanosensing devices is the controllable manipulation of CNTs, and, thus, it still remains challenging to align a well-controlled number of CNTs between two electrodes. Recently, optically induced dielectrophoresis (ODEP) and optoelectronic tweezers (OET) have been reported to manipulate microparticles [17], or even metal nanowires and CNTs [18, 19]. Furthermore, the manipulation and patterning of CNTs has been demonstrated [20]. The ODEP was further demonstrated as a powerful tool to manipulate CNTs. However, the attempt to assemble CNTs between electrodes to form a CNT-based nanosensor by utilizing ODEP and dielectrophoresis has never been made. In this study, a new method to assemble CNTs on a nanosensor by using the combination of ODEP and DEP forces was reported for the first time. It may allow for large-scale, parallel assembly of CNTs with a well-controlled width across two electrodes, which is crucial for the practical application of CNT-based nanosensors.

## 2. Materials and Methods

**2.1. Operating Principle.** Figure 1 shows a schematic illustration of the new approach for assembling CNTs across electrodes. Briefly, the DEP force was used to attract more CNTs around the electrodes. Then, CNTs were collected and transported to the central area between the two electrodes by using the ODEP force from a projected moving light pattern. The width of the CNTs line can be controlled by either the collection time or the initial concentration of the suspended CNTs. The chip was composed of an upper indium-tin-oxide (ITO) glass and a bottom substrate coated with a photoconductive layer (hydrogenated amorphous silicon, a-Si) and patterned metal electrodes. The gap spacing between the top and the bottom layer is typically defined using double-sided tape with 30- $\mu\text{m}$  thickness. The entire region can induce the ODEP force except the metal electrodes since they are not supplied with alternating current (AC) voltages. When an AC voltage was applied across the metal electrodes patterned on the bottom substrate, a lateral nonuniform electric field can be generated. Afterwards, when a projected light source illuminates the a-Si layer, electron-hole pairs were excited, thus, decreasing the impedance of the a-Si layer by 4 to 5 orders of magnitude. Then the AC voltage dropped across the liquid layer inside the illuminated area such that a non-uniform electric field can be induced. The light-illuminated region can be regarded as the “virtual electrode.” When CNTs were suspended in the non-uniform electric field, a positive ODEP force can be induced when an appropriate frequency was applied and thus CNTs can be manipulated and prealigned across the electrodes by moving the light patterns which has been programmed by a computer. Therefore, a thin line of CNTs can be aligned across the electrodes.

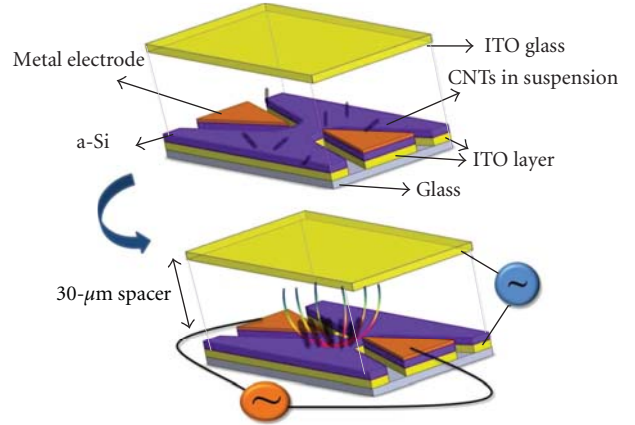


FIGURE 1: Schematic illustration of the new ODEP platform for assembling CNTs between electrodes to form a CNT-based nanosensor. The ODEP chip was composed of an upper ITO glass and a bottom substrate coated with a photoconductive layer (a-Si) and patterned gold electrodes.

The DEP force for nanotubes with a radius of  $r$  and a length of  $l$ , including CNTs, can be represented as follows using an elongated ellipsoid model [21]:

$$F = \left( \frac{\pi r^2 l}{6} \right) \epsilon m \operatorname{Re}[K * (\omega)] \nabla(E^2), \quad (1)$$

where  $l$  denotes the length of the nanotubes,  $\epsilon m$  represents the permittivity of the surrounding medium,  $r$  is the radius of the nanotubes,  $E$  is the electric field, and  $\operatorname{Re}[K * (\omega)]$  is known as the real part of the Clausius-Mossotti (CM) factor. The induced ODEP forces are proportional to the gradient of the square of the electric field strength  $[\nabla(E^2)]$  which is directly related to the efficiency of the photoconductivity effect of the a-Si layer.

**2.2. Fabrication Process.** Figure 3 shows a schematic illustration of the simplified fabrication process for the ODEP chip. The chip is with typical sizes of 4 cm  $\times$  4 cm. A 10-nm thick molybdenum layer, acting as an adhesive and conductive layer, was first deposited onto a 1-mm thick ITO glass substrate. A 0.5- $\mu\text{m}$  thick a-Si was then deposited on top of the adhesive layer by using a plasma-enhanced chemical vapor deposition (PECVD) process. Then, the a-Si layer was patterned by using a reactive ion etching process. Next, a standard wet ITO etching process was used to pattern ITO electrodes. The purpose of this step was to isolate the ITO electrodes from the photoconductive material layer. Next, the fabrication process involved the deposition of an adhesion layer of 150- $\text{\AA}$  chrome and a 1000- $\text{\AA}$  gold electrode layer by using an electron-beam evaporation process. Photolithography was then used to pattern the metal layer into a triangular shape. The two electrodes face inward with a tip-to-tip distance of 70  $\mu\text{m}$ . ODEP and DEP forces can be induced when two AC voltages were applied at different electrodes.

**2.3. Experimental Setup.** CNTs were first dispersed in a 10-mL solution containing 20% w/v poly(ethylene glycol)

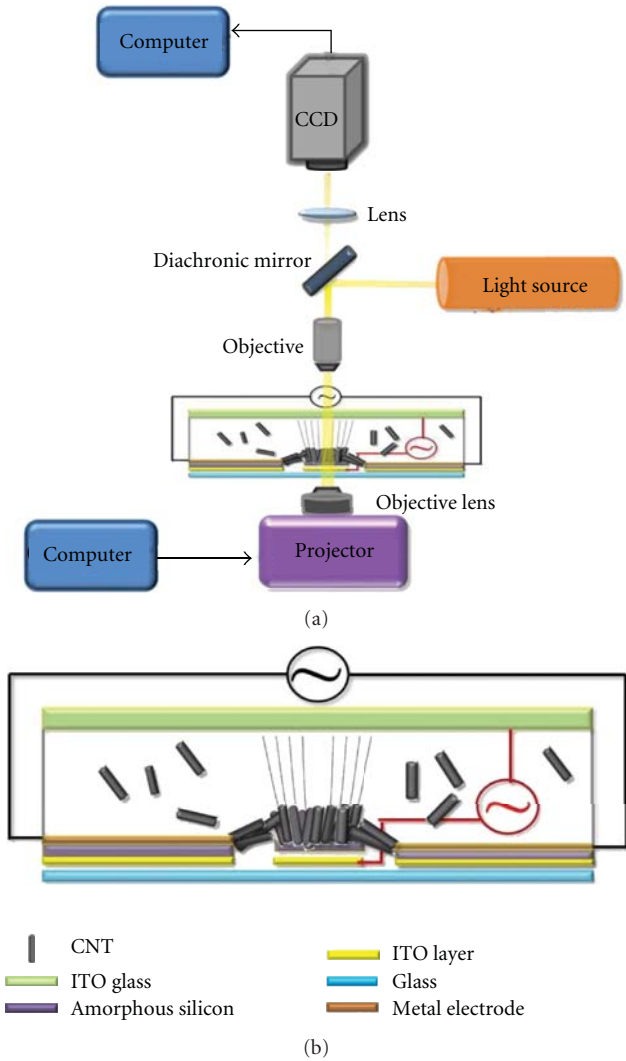


FIGURE 2: Schematic illustration of the experimental setup and the assembly process of CNTs between ITO electrodes by using a positive ODEP force and a DEP force.

diacrylate (PEGDA) and 0.2% w/v photoinitiator (Irgacure 2959) [18] so that the electrical conductivity of the solution formed was around  $80 \mu\text{S}/\text{cm}$ . PEGDA is an ultraviolet (UV)-curable polymer [22, 23] that forms a three-dimensional polymer matrix in the presence of an UV source. CNTs with purity not less than 90% were chosen as the solute in this study. Since CNTs are hydrophobic and tend to bundle together, it was difficult to achieve well-dispersed CNTs. After mixing, the CNTs solution was bath sonicated for 1 hour to become more dispersed CNTs and then centrifuged for 3 min at 1500 rpm. Around  $5 \mu\text{L}$  of the solution was then pipetted into the ODEP chip.

Figure 2 shows the experimental setup. A digital projector (PJ1172, Viewsonic, Japan) was used to illuminate preprogrammed light patterns as virtual electrodes onto the ODEP platform. A 50x objective lens (Nikon, Japan) was fixed between the projector and the ODEP chip to focus the projected light onto the chip to form light patterns. It was

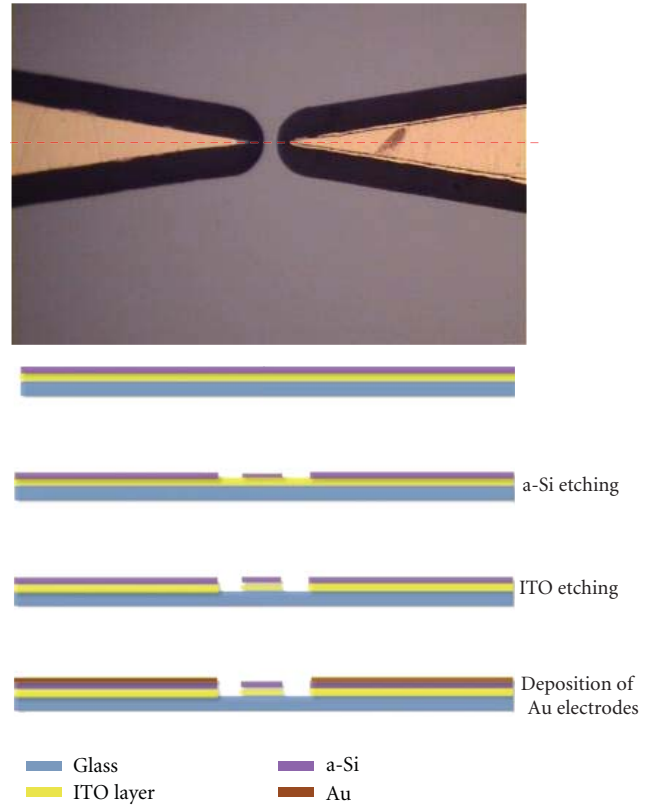


FIGURE 3: The simplified fabrication process of the ODEP chip.

composed of a charge-coupled device (CCD) camera (SSC-DC80, Sony, Japan), an optical microscope (Zoom 125C, OPTEM, USA), and a computer equipped with an image acquisition interface card. The AC voltage was supplied by using two function generators (Model 195, Wavetek, UK; AFG310 TEKTRONIX, USA), and a power amplifier (790 Series, AVC Instrumentation, USA). In this study, an AC power source with a frequency of 100 kHz and a magnitude of 20 Vpp was applied across the top and bottom layers of the ODEP chip to generate an electrical field. Similarly, the voltage applied across the metal electrodes was 30 Vpp with a frequency of 110 kHz. Note that the operating frequencies of these two applied voltages must be different. If the two applied frequencies were the same, the CNTs connected to the electrodes would move up and down, which is a result of the interference between the simultaneous DEP and ODEP forces.

### 3. Results and Discussion

As mentioned previously, moving light patterns can be used to attract and collect dispersed CNTs in the medium to the center of the electrodes when using ODEP forces. Figure 4 shows a series of photographs for prealigned CNTs at the electrodes. First, an AC potential was applied to the metal electrodes to generate the required electric field for the DEP alignment process (Figure 4(a)). The CNTs would adhere to the electrodes temporarily. Second, the CNTs

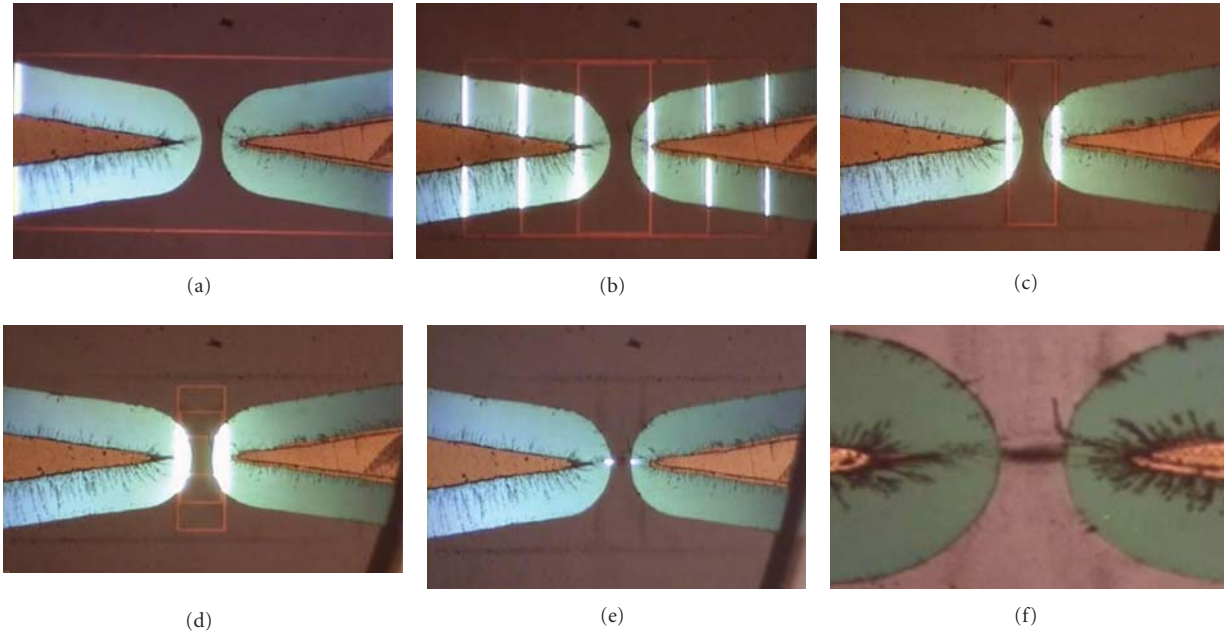


FIGURE 4: A series of snapshot photographs for collecting CNTs to the central area between metal electrodes by using moving optical images and DEP forces.

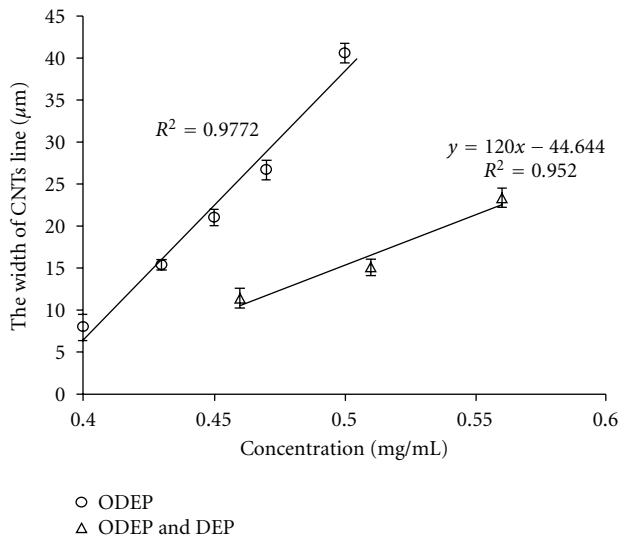


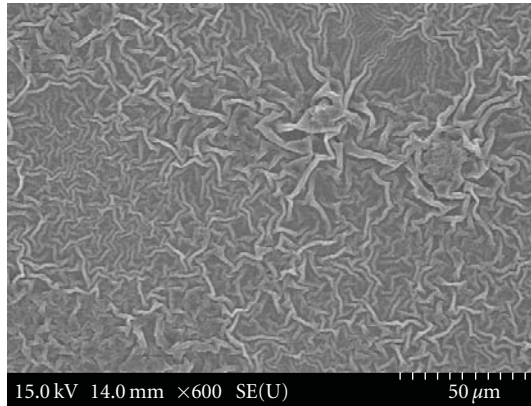
FIGURE 5: The relationship between the width of the line of CNTs and the concentration of the CNTs.

were successfully collected by using the ODEP force. CNTs were attracted and collected to a specific area through the manipulation of the moving optical images designed by the computer program (Figures 4(b)–4(e)). A specific light track to collect suspended CNTs was generated as follows. First, six vertical lines inside a big square were used to collect CNTs. Then, these six lines moved toward the center and then collapsed into two lines to define the width of the CNTs line between two electrodes such that the suspended CNTs were collected horizontally. Finally, another six horizontal lines were generated to collect the suspended CNTs. These

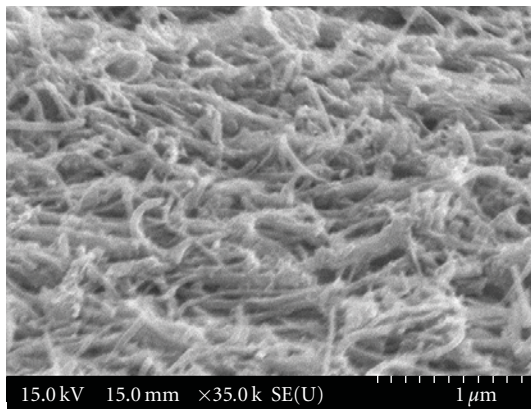
six lines moved and then collapsed again to only one line. With this approach, suspended CNTs can be collected and aligned into a thin line across two electrodes. The patterns of the light track were flexible and could be finetuned based on the required line width. Note that the moving speed of the light track should be controlled appropriately. If the light track moved too fast, the CNTs cannot move with the light track so that the collected CNTs may not be enough.

It was clearly observed that most of the CNTs in the manipulation area can be successfully collected by animated optical images. In this case, the concentration of the CNTs was 0.51 mg/mL, and the resulting line width of the CNTs was measured to be 15  $\mu\text{m}$  by utilizing both the DEP and ODEP forces (Figure 4(f)). The operating times for applying the DEP and ODEP forces were five minutes and three minutes, respectively. It was found that the line width of the CNTs can be adjusted by controlling the initial concentrations of CNTs. Figure 5 shows the relationship between the width of CNTs lines and the concentrations of the CNTs at an applied voltage of 20 Vpp. It can be clearly observed that at higher concentrations, the width of the line of CNTs line increases. Note that lower initial CNT concentrations were tested. However, the line of CNTs cannot be formed at concentrations lower than 0.45 mg/mL, indicating that the narrowest width of the nanosensor was 8  $\mu\text{m}$  in our current experimental configuration. The width of CNT line also depended on the light width from the projector. The minimum line width provided by this ODEP platform was approximately 5  $\mu\text{m}$ . By adopting a higher power projector and a better optical setup, this minimum line width could be further minimized.

Nevertheless, utilizing the ODEP force only cannot connect the CNTs to the electrodes. Hence, the DEP force was



(a)



(b)

FIGURE 6: SEM images of CNTs in the photoresist (a) before and (b) after the ashing process.

further used before the CNTs were collected. The relationship between the width of the CNT lines and the concentrations of the CNTs using a combination of the ODEP and DEP is also shown in Figure 5. Some CNTs would connect to the electrode when using DEP so that the CNTs in the neighboring area would decrease. Consequently, the line width will be narrower if utilizing the DEP and the ODEP simultaneously at the same concentration. The fewer number of CNTs connected, the narrower the resulting line width. The coefficients of variation for the measurements of the widths were 10%, 4%, and 6% for CNTs concentrations of 0.45, 0.51, and 0.56 mg/mL, respectively, indicating that the CNT-based nanosensors can be fabricated by using the proposed method with good reproducibility.

Another issue after the alignment of the CNTs is to fix them to the original location. As mentioned previously, an UV illumination (UV-A) through a metal mask for 10 minutes was used to immobilize the CNTs once the nanowires were positioned at the desired location. The UV-curable polymer was then removed by a photoresist asher such that the prealigned CNTs can be used. Note that the time and the power of the photoresist asher need to be controlled carefully to avoid the oxidation and damage of

the prealigned CNTs. Figure 6(a) shows a scanning electron microscopy (SEM) image of CNTs in the photoresist before using the ashing process. After the ashing process, most of the polymers were ashed and the CNTs were exposed for the subsequent sensing applications (Figure 6(b)).

#### 4. Conclusion

This study, for the first time, reports a new approach for assembly of carbon nanotubes between electrodes by utilizing optically induced dielectrophoresis and the dielectrophoresis forces. An animated optical pattern was designed to collect the CNTs in the medium. The widths of the CNTs were reasonably controlled. The minimum line width of the CNTs was measured to be  $8 \mu\text{m}$ . Furthermore, the prealigned CNTs were immobilized by exposure to an UV source. This developed platform may be promising for controlling the width of CNTs in nanosensors.

#### Abbreviation and Nomenclature

AC:	Alternating current
a-Si:	Hydrogenated amorphous silicon
CCD:	Charge-coupled device
CM:	Clausius-Mossotti factor
CNTs:	Carbon nanotubes
DEP:	Dielectrophoretic
$E$ :	Intensity of the applied electric field
$\epsilon m$ :	Electrical permittivity of the surrounding medium
Fdep:	Dielectrophoretic force
ITO:	Indium-tin-oxide
$l$ :	Length of the nanotubes
ODEP:	Optically induced dielectrophoresis
OET:	Optoelectronic tweezers
OT:	Optical tweezers
PEGDA:	Poly(ethylene glycol) diacrylate
$r$ :	Radius of the nanotubes
$\text{Re}[K * (\omega)]$ :	Real part of Clausius-Mossotti factor
SEM:	Scanning electron microscopy.

#### Acknowledgment

The authors gratefully acknowledge the financial support provided to this study by the National Science Council in Taiwan (NSC 96-2120-M-007-015).

#### References

- [1] S. Iijima, "Helical microtubules of graphitic carbon," *Nature*, vol. 354, no. 6348, pp. 56–58, 1991.
- [2] D. Tasis, N. Tagmatarchis, A. Bianco, and M. Prato, "Chemistry of carbon nanotubes," *Chemical Reviews*, vol. 106, no. 3, pp. 1105–1136, 2006.
- [3] A. Jorio, M. S. Dresselhaus, and G. Dresselhaus, *Carbon Nanotubes*, Springer, Berlin, Germany, 2008.
- [4] J. Suehiro, G. Zhou, and M. Hara, "Fabrication of a carbon nanotube-based gas sensor using dielectrophoresis and its application for ammonia detection by impedance spectroscopy," *Journal of Physics D*, vol. 36, no. 21, pp. L109–L114, 2003.

- [5] M. Trojanowicz, "Analytical applications of carbon nanotubes: a review," *Trends in Analytical Chemistry*, vol. 25, no. 5, pp. 480–489, 2006.
- [6] B. Q. Wei, R. Vajtai, Y. Jung et al., "Organized assembly of carbon nanotubes," *Nature*, vol. 416, no. 6880, pp. 495–496, 2002.
- [7] J. Hu, M. Ouyang, P. Yang, and C. M. Lieber, "Fabricating carbon nanotube transistor device," *Nature*, vol. 399, pp. 48–51, 1999.
- [8] J. E. Fischer, W. Zhou, J. Vavro et al., "Magnetically aligned single wall carbon nanotube films: preferred orientation and anisotropic transport properties," *Journal of Applied Physics*, vol. 93, no. 4, pp. 2157–2163, 2003.
- [9] Y. Huang, X. Duan, Q. Q. Wei, and C. M. Lieber, "Directed assembly of one-dimensional nanostructures into functional networks," *Science*, vol. 291, no. 5504, pp. 630–633, 2001.
- [10] S. G. Rao, L. Huang, W. Setyawan, and S. Hong, "Large-scale assembly of carbon nanotubes," *Nature*, vol. 425, no. 6953, pp. 36–37, 2003.
- [11] D. G. Grier, "A revolution in optical manipulation," *Nature*, vol. 424, no. 6950, pp. 810–816, 2003.
- [12] Z. Liu, Z. Shen, T. Zhu et al., "Organizing single-walled carbon nanotubes on gold using a wet chemical self-assembling technique," *Langmuir*, vol. 16, no. 8, pp. 3569–3573, 2000.
- [13] S. Tan, H. A. Lopez, C. W. Cai, and Y. Zhang, "Optical trapping of single-walled carbon nanotubes," *Nano Letters*, vol. 4, no. 8, pp. 1415–1419, 2004.
- [14] H. W. Seo, C. S. Han, D. G. Choi, K. S. Kim, and Y. H. Lee, "Controlled assembly of single SWNTs bundle using dielectrophoresis," *Microelectronic Engineering*, vol. 81, no. 1, pp. 83–89, 2005.
- [15] S. Tung, H. Rokadia, and W. J. Li, "A micro shear stress sensor based on laterally aligned carbon nanotubes," *Sensors and Actuators A*, vol. 133, no. 2, pp. 431–438, 2007.
- [16] A. Vijayaraghavan, S. Blatt, D. Weissenberger et al., "Ultra-large-scale directed assembly of single-walled carbon nanotube devices," *Nano Letters*, vol. 7, no. 6, pp. 1556–1560, 2007.
- [17] P. Y. Chiou, A. T. Ohta, and M. C. Wu, "Massively parallel manipulation of single cells and microparticles using optical images," *Nature*, vol. 436, no. 7049, pp. 370–372, 2005.
- [18] A. Jamshidi, P. J. Pauzauskie, P. J. Schuck et al., "Dynamic manipulation and separation of individual semiconducting and metallic nanowires," *Nature Photonics*, vol. 2, no. 2, pp. 86–89, 2008.
- [19] P. J. Pauzauskie, A. Jamshidi, J. K. Valley, J. H. Satcher, and M. C. Wu, "Parallel trapping of multiwalled carbon nanotubes with optoelectronic tweezers," *Applied Physics Letters*, vol. 95, no. 11, Article ID 113104, 3 pages, 2009.
- [20] M. W. Lee, Y. H. Lin, and G. B. Lee, "Manipulation and patterning of carbon nanotubes utilizing optically induced dielectrophoretic forces," *Microfluidics and Nanofluidics*, vol. 8, no. 5, pp. 609–617, 2010.
- [21] T. B. Jones, *Electromechanics of Particles*, Cambridge University Press, Cambridge, UK, 1995.
- [22] D. J. Beebe, J. S. Moore, J. M. Bauer et al., "Functional hydrogel structures for autonomous flow control inside microfluidic channels," *Nature*, vol. 404, no. 6778, pp. 588–590, 2000.
- [23] M. Law, L. E. Greene, J. C. Johnson, R. Saykally, and P. Yang, "Nanowire dye-sensitized solar cells," *Nature Materials*, vol. 4, no. 6, pp. 455–459, 2005.

## Review Article

# From Spheric to Aspheric Solid Polymer Lenses: A Review

**Kuo-Yung Hung,<sup>1</sup> Po-Jen Hsiao,<sup>2</sup> Fang-Gang Tseng,<sup>3,4</sup> and Miao-Chin Wei<sup>1</sup>**

<sup>1</sup>*Institute of Mechanical and Electrical Engineering, Ming Chi University of Technology, Taipei 24301, Taiwan*

<sup>2</sup>*iVIEW SBU/CIS-Pixel, Novatek Microelectronics Corporation, Hsinchu 300, Taiwan*

<sup>3</sup>*Engineering and System Science Department, NanoEngineering and MicroSystems Institute, National Tsing Hua University, Hsinchu 30013, Taiwan*

<sup>4</sup>*Division of Mechanics, Research Center for Applied Sciences, Academia Sinica, Taipei 115, Taiwan*

Correspondence should be addressed to Kuo-Yung Hung, kuoyung@mail.mcut.edu.tw  
and Fang-Gang Tseng, fangang@ess.nthu.edu.tw

Received 9 May 2011; Accepted 27 June 2011

Academic Editor: Eric Pei Yu Chiou

Copyright © 2011 Kuo-Yung Hung et al. This is an open access article distributed under the Creative Commons Attribution License, which permits unrestricted use, distribution, and reproduction in any medium, provided the original work is properly cited.

This paper presents a new approach in the use of MEMS technology to fabricate micro-optofluidic polymer solid lenses in order to achieve the desired profile, focal length, numerical aperture, and spot size. The resulting polymer solid lenses can be applied in optical data storage systems, imaging systems, and automated optical inspection systems. In order to meet the various needs of different applications, polymer solid lenses may have a spherical or aspherical shape. The method of fabricating polymer solid lenses is different from methods used to fabricate tunable lenses with variable focal length or needing an external control system to change the lens geometry. The current trend in polymer solid lenses is toward the fabrication of microlenses with a high numerical aperture, small clear aperture (<2 mm), and high transmittance. In this paper we focus on the use of thermal energy and electrostatic force in shaping the lens profile, including both spherical and aspherical lenses. In addition, the paper discusses how to fabricate a lens with a high numerical aperture of 0.6 using MEMS and also compares the optical characteristics of polymer lens materials, including SU-8, Norland Optical Adhesive (NOA), and cyclic olefin copolymer (COC). Finally, new concepts and applications related to micro-optofluidic lenses and polymer materials are also discussed.

## 1. Introduction

Microlens arrays are currently utilized in a wide array of applications, including projection [1], smart phone cameras [2], data storage [3] and imaging devices [4]. Most of the lenses used in these types of applications have a fixed focal length and require precision positioning and high-resolution imaging. Because of this, the size, profile uniformity, numerical aperture, and focal length of microlens arrays are very important factors in relation to system integration. The focuses of optical systems employing fixed-focus lenses are generally accomplished using a servo control system. Solid fixed-focus lens fabrication concepts and methods are quite different from those of microtunable lenses. As a consequence, this paper only compares the fabrication and design methods for fixed-focus spherical and aspherical lenses. The method of fabricating polymer solid lenses is different from methods used to fabricate tunable lenses with

variable focal length or needing an external control system to change the lens geometry.

A variety of techniques for the fabrication of microlenses already exist. Recently, a variety of fabrication techniques for microlenses have been proposed and demonstrated, such as resist melting [5], electrowetting [6], and micro inkjet printing [7]. These methods have various restrictions, such as difficulty of controlling numerical aperture due to intrinsic fabrication limitations or numerous control variables. One low-cost method is to use a modified ink-jet printer to produce lenses. However, this nonlithographic technique suffers from limitations in alignment accuracy and minimum lens size. An alternative technique to using lithography is that of resist reflow [5], in which photoresist is patterned at specific locations and then melted so that the resist changes its shape under the influence of surface tension to form a portion of a sphere. Although this technique is used to

manufacture high-quality lenslets, it has several drawbacks: high processing temperatures and the etch-transfer process being required to produce high transmittance components. In addition, there are many variables in the resist melting method which must be taken into account during photolithography, and melting-cooling cycles must be seriously considered in order to determine numerical aperture. For its part, the electrodeposition proposed by Sakurai et al. [8] requires a conducting substrate, is relatively complicated, and needs a very precise processing environment in terms of such factors as current density homogeneity if surface smoothness of optimal quality is to be attained; this method is not suitable for integration with the CMOS process. Jeong et al. [9] proposed the use of SU-8 photoresist to define lens formation locations ahead of time, but since the lens material must be applied using a pipette, this method cannot readily be used in batch manufacturing. Wu et al. [10] relied on mechanical processing of polystyrene ball lens focus light to achieve tiny photoresist structures and then employed reflow technology to produce microlenses; although this method allowed relatively small lenses to be produced, it is not suitable for application in processes requiring precise alignment due to the fact that the ball lens could not be precisely positioned.

Due to lower costs and good performance, the use of a single aspheric lens has been considered in applications such as inexpensive consumer cameras, laser diode collimation, and coupling light into and out of optical fibers. In addition, a single aspheric lens has also been considered for use in optical data storage systems because of its low aberration, small size, high numerical aperture, and short focal length. While aspheric surfaces can be made by polishing with a small tool with a compliant surface that conforms to the optical surface, precise control of the surface profile and quality is difficult and results may vary as the tool wears. Single-point diamond turning is an alternative process in which a computer-controlled lathe uses a diamond tip to directly cut the desired profile into a piece of glass or other optical material. Diamond turning is slow and has limitations in terms of the materials on which it can be used as well as the degree of surface accuracy and smoothness attainable.

An electrostatic modulation is usually used in liquid zoom lens fabrication. For example, Philips Inc. [2] proposed the use of electrowetting of oil and water and applied the electric field while changing the contact angle of the oil and water. This shapes the curvature of the lens to achieve the lens profile modulation or to refer the dielectric electrophoresis methodology [11] on two different dielectric materials, in order to achieve microlens zoom effects. In a dielectric lens, under a gradient electric field, the generated dielectric force causes the dielectric liquid to be shaped towards the region with the lowest electric field strength. One distinct advantage is that electrolysis, joule heating, and microbubble formation often occurs in electrowetting lenses due to the transportation of the free electric charges and the alternating electric fields [12], but dielectric lenses do not possess these problems; they require only a patterned electrode to generate a gradient electric field [13–15].

This paper presents different ideas for fabricating spherical and aspherical solid polymer lenses. In addition, this paper discusses how the profile of a spherical lens can be modified so as to transform it into an aspherical lens through the use of MEMS technology. The self-assembly, heating for concentrating, and surface tension force are discussed for the formation of spherical lenses. The hybrid gradient electrostatic force and thermal energy in a dynamic fluidic are compared for the formation of aspherical lenses. This paper mainly focuses on describing both the fabrication of microlenses and the shaping of lens profiles.

## 2. Design Concepts of the Spherical or Aspherical Lenses by Polymer Lens

This paper proposes three ideas concerning the design and fabrication of microlenses employing the methods of gathering-shrinking, self-assembly, thermal energy, and surface tension. Profile or optical tests are then performed to verify our design.

*2.1. Self-Assembly Process to Change the Focal Length of Solid Spherical Lenses.* Recently, several authors have proposed and demonstrated techniques for the fabrication of microlenses using the hydrophilic/hydrophobic effect [16]. This method can produce microlenses with a large area and high coverage and can be applied to display backlight or light-guide panel modules. However, the self-alignment method using hydrophilic and hydrophobic effects has a drawback: the numerical aperture of a microlens formed on a hydrophilic surface will be small due to the high surface energy. As such, this paper proposes a novel method for utilizing self-assembly characteristics that can yield microlenses with a high numerical aperture and high coverage.

*2.1.1. Self-Assembly.* This paper proposes a method of using the hydrophilic/hydrophobic difference of surfaces to produce microlenses by self-assembly, where the microlens material consists of SU-8, the high-transmittance and high-refractive-index negative photoresist material. Because SU-8 has a much higher coefficient of viscosity than AZ positive photoresist and can readily produce relatively high aspect ratio structures, it is very suitable for the production of microlenses with a high numerical aperture.

The microlens fabrication process proposed in this paper employs a self-alignment mechanism and consists of either a fixed focal length process (Figure 1(a)) or a variable focal length process (Figure 1(b)). Both design types employ hydrophilic/hydrophobic interface characteristics to form areas with different surface tension. When lens material is applied, the material will tend to remain in hydrophilic zones with high surface free energy. The goal of the variable focal length process is to resolve the problem of excessively small numerical aperture (NA) that occurs when the conventional self-alignment method is employed.

After being heated to a temperature higher than its boiling point, Teflon (DuPont, USA) has extremely stable physical characteristics and cannot be readily removed or

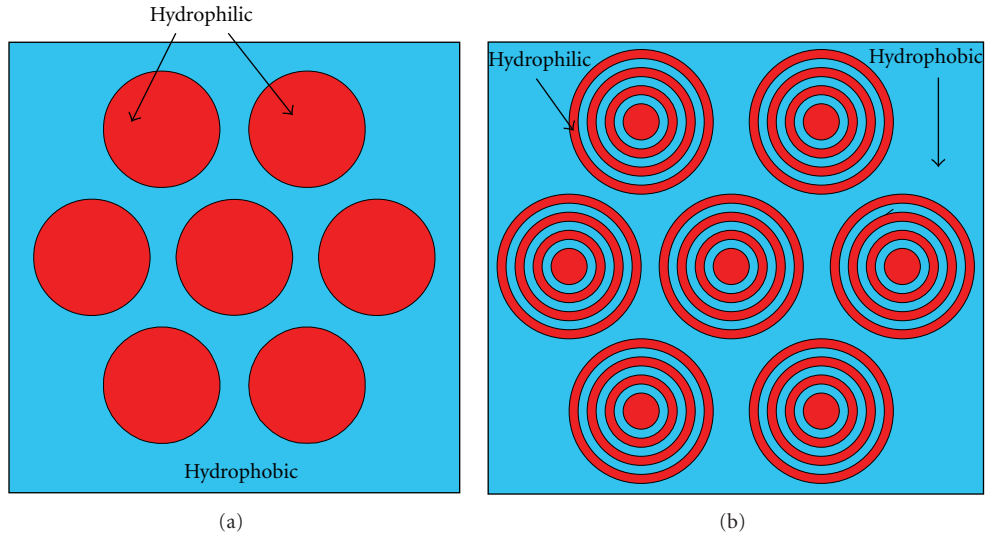


FIGURE 1: Schematic diagram of the self-assembly mechanism of the lenses: (a) fixed focal length and (b) variable focal length methods. Both types of design employ hydrophilic/hydrophobic interface characteristics to form areas with different surface tension. When lens material is applied, the material will tend to remain in hydrophilic zones with high surface free energy. The goal of the variable focal length process is to resolve the problem of excessively small numerical aperture (NA) that occurs when the conventional self-alignment method is employed.

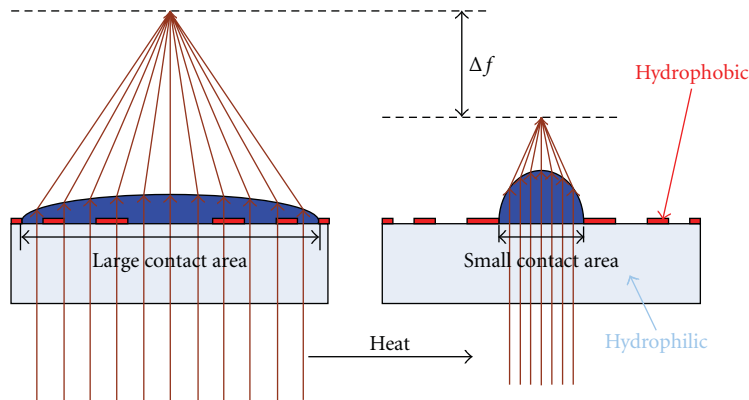


FIGURE 2: Schematic diagram of the principle of lens fabrication for a higher numerical aperture.

scraped off. Furthermore, Teflon has an extremely high contact angle (implying low surface energy). Because of this, Teflon is extremely suitable for the lift-off process, which completes the definition of the Teflon hydrophobic zone.

The most direct method of judging the hydrophilic/hydrophobic characteristics of a surface is by examining the contact angle, which is correlated with surface tension. The surface tension, which constantly tries to cause the surface to contract, is represented by  $\gamma$ ; surface tension exists between the liquid, solid, and gas phases. Assume that  $\gamma_{LV}$  is the surface tension between liquid and gas phases,  $\gamma_{SV}$  is the surface tension between solid and gas phases,  $\gamma_{SL}$  is the surface tension between solid and liquid phases, and  $\theta$  is the contact angle. These three forces are in a state of balance when the system is stable:  $\gamma_{SL} - \gamma_{SV} + \gamma_{LV} \cdot \cos \theta = 0$ , where

$$\theta = \cos^{-1} \frac{\gamma_{SL} - \gamma_{SV}}{\gamma_{LV}}. \quad (1)$$

The relationship between the hydrophilic/hydrophobic characteristics of different surfaces and contact angles can be clarified by using  $\theta = 90^\circ$  as a dividing line:  $\theta < 90^\circ$  signifies a hydrophilic surface that is easily moistened by liquids and adheres readily to solid surfaces, such as by forming a liquid film on a glass surface;  $\theta > 90^\circ$  signifies a hydrophobic surface that is not easily moistened by liquids and will not adhere readily to solid surfaces; this phenomenon is known as the *lotus effect*. As a consequence, if a surface possesses different hydrophilic and hydrophobic zones, a liquid will tend to remain in the hydrophilic zones. This is the principle of self-assembly in microlens design.

**2.1.2. Enhancing the Surface Energy at the Center.** In the case of specific hydrophilic/hydrophobic surfaces and microlens materials, the surface energy difference will be fixed. Because of this, the numerical aperture of a microlens cannot change unless the coefficient of viscosity of the microlens materials or the area of the hydrophilic/hydrophobic interface

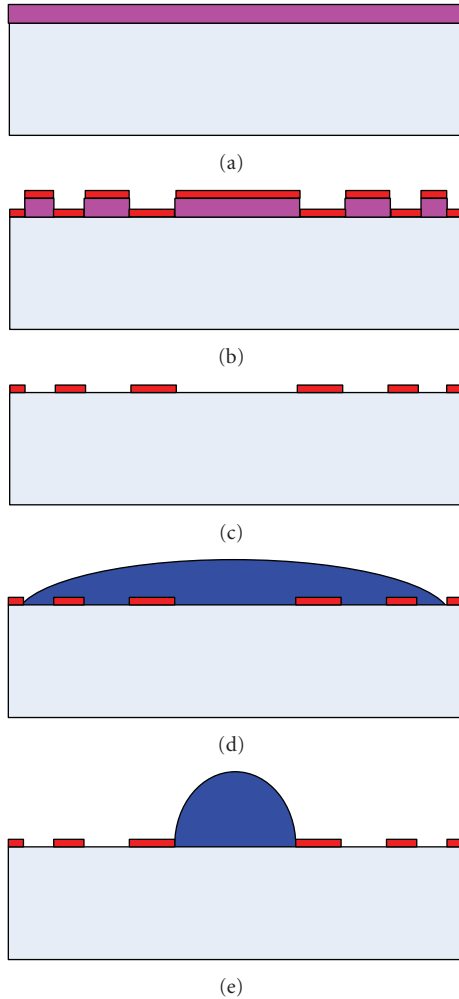


FIGURE 3: Microspherical lens fabrication processes for higher numerical aperture.

is changed, or a hydrophobic layer with an even lower surface energy is used. As a consequence, in order to effectively integrate these technologies, this paper uses heat treatment in microlens fabrication. Apart from inducing the extremely small quantities of solvent in the optical materials to volatilize and thereby cause the lens to shrink (this is a relatively small effect), heat treatment also causes the hydrophilic zone (high surface energy) in the center of the hydrophilic/hydrophobic interface pattern to exhibit strong cohesion; this enables the use of multiple hydrophilic/hydrophobic interfaces in the design of the optical materials to achieve inward shrinking, which will then increase numerical aperture (see the schematic diagram in Figure 2). This method does entail many design considerations, however, such as (1) the ratio of the widths of adjacent hydrophilic and hydrophobic zones; when the hydrophilic zone is wide on the outside and narrow on the inside, the hydrophobic zone will be fixed and must be larger than or equal to the smallest hydrophilic zone to ensure that the thermal energy will overcome the constraining surface tension of the hydrophobic layer, enabling the fabrication

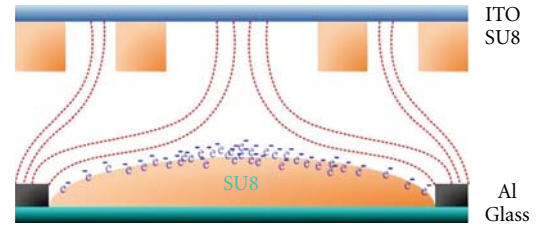


FIGURE 4: The gradient electrostatic field modulation system 1 developed in this paper. This paper consequently modifies the electrode structure to design electrodes structurally similar to Fresnel zone plate, which can be used to modify the shape of the lens margin. The upper and lower electrodes both consisted of transparent ITO electrodes in this paper's initial design. Nevertheless, due to the approximately 2 mm distance between the upper and lower electrodes, the excessively large depth of field caused difficulty in aligning the upper and lower electrodes. Because of this, the upper electrodes were modified to include an SU-8 3010 insulating layer (SU-8 has a dielectric coefficient of approximately 3.28), and Teflon was used on the aluminum lower electrodes to define the hydrophilic/hydrophobic interface, inducing liquid droplets to perform self-assembly; the Teflon also served as an insulating layer (Teflon has a dielectric coefficient of approximately 2.1–2.5). In addition, the SU-8 3010 design formed hollow round concavities with different radii and width, which caused different electric field effects and gave the edge of the lens an aspherical profile.

of lenses with high numerical apertures. (2) The smaller the diameter, the harder it is to achieve shrinking, because even more surface energy must be provided. Because this experiment employed SU-8 as a lens material, heating to the Tg point caused fluidity to increase and the material to shrink inward from the hydrophilic zone in the outermost ring. While some of the solvent is volatilized during the heating process, the surface tension of the shrinking lens still overcome the volatilization effect due to the fact that the lens has a smaller diameter after shrinkage. This causes the overall height of the microlens to increase (Figure 2), the numerical aperture to increase, and the focal length  $f$  to shorten. If the diameter of a lens is  $D$  and the height  $s$ , the radius of curvature will be  $R = (s^2 + D^2/4)/2s$  and the focal length  $f = R/(n - 1)$ , where  $n$  is the index of refraction (for SU-8  $n = 1.67$ ), and the numerical aperture is  $NA = D/2f$ .

**2.1.3. Microspherical Lens Fabrication Processes.** In order to verify the concepts described above, a test was used for this study which employed the following fabrication processes and parameters.

- (a) AZ9260 photoresist was spin-coated on a substrate at 2500 rpm for 30 sec., forming a layer with a thickness of approximately  $6 \mu\text{m}$ . The material was then soft-baked at  $100^\circ\text{C}$  for 2 minutes (Figure 3(a)).
- (b) An exposure and developing process was used to produce a pattern opposite to that of the desired Teflon pattern. The Teflon (with 0.66% FC43 thinner) was then evenly spun-coated at 3000 rpm for 30 sec. The material was then baked at  $180^\circ\text{C}$  for 9 min. (Figure 3(b)).

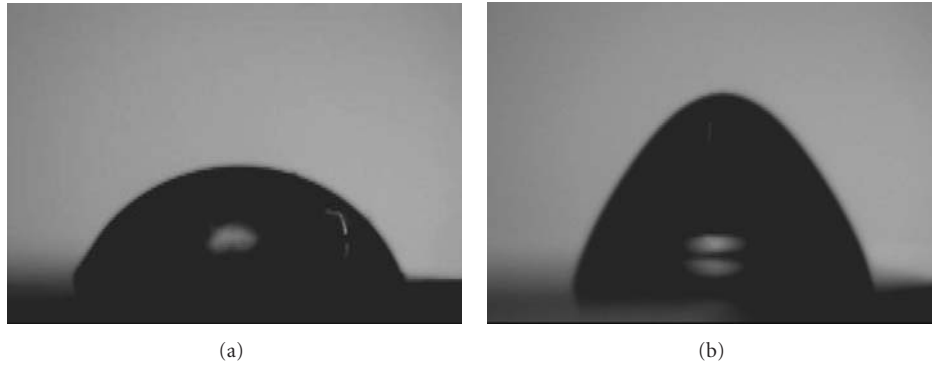


FIGURE 5: (a) The unmodified lens profile (b), the modified profile [16].

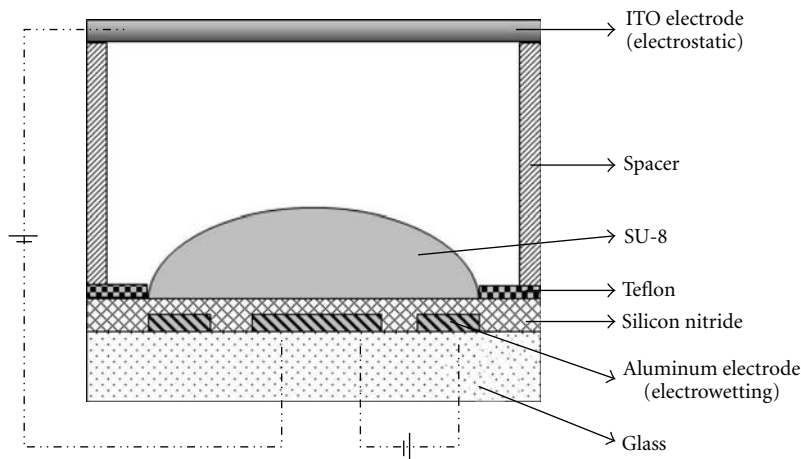


FIGURE 6: Schematic diagram of electrostatic force extension mechanism 2.

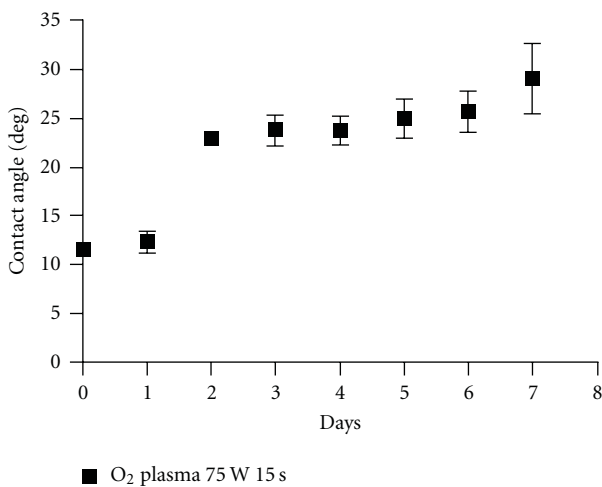


FIGURE 7: Restoration of the Teflon contact angle after O<sub>2</sub> plasma treatment.

- (c) The lift-off technique was used to remove the photoresist, yielding the desired Teflon pattern (Figure 3(c)).
- (d) After the lens material SU-8 had flowed across the hydrophilic/hydrophobic pattern that had been

produced on the Teflon, the material remained on the glass substrate bounded by Teflon, completing the lens self-alignment process (the material will remain in the outermost ring if there are many hydrophilic/hydrophobic rings) (Figure 3(d)).

- (e) Slow, multistaged heating can be employed if there are many hydrophilic/hydrophobic rings. After heating to the material's glass transition temperature ( $T_g$ ), the temperature is then maintained at that level. The heating increases the material's energy, allowing it to overcome Teflon's surface free energy constraints, and causes the lens material to shrink inward. This shrinkage becomes more apparent after time. Different hydrophilic/hydrophobic patterns can be used to produce different lens profiles. This completes the fabrication of a self-aligning microlens with thermally modified focal length (Figure 3(e)).

2.2. Hybrid Aspherical Lens Produced Using Electrostatic Force.

The biggest difference between high-level aspherical lenses and spherical lenses lies in the area close to the edge of the lens aperture; because there is relatively little change in the curvature near the on-axis of a spherical lens, spherical aberration will not be significant in this area. Nevertheless,

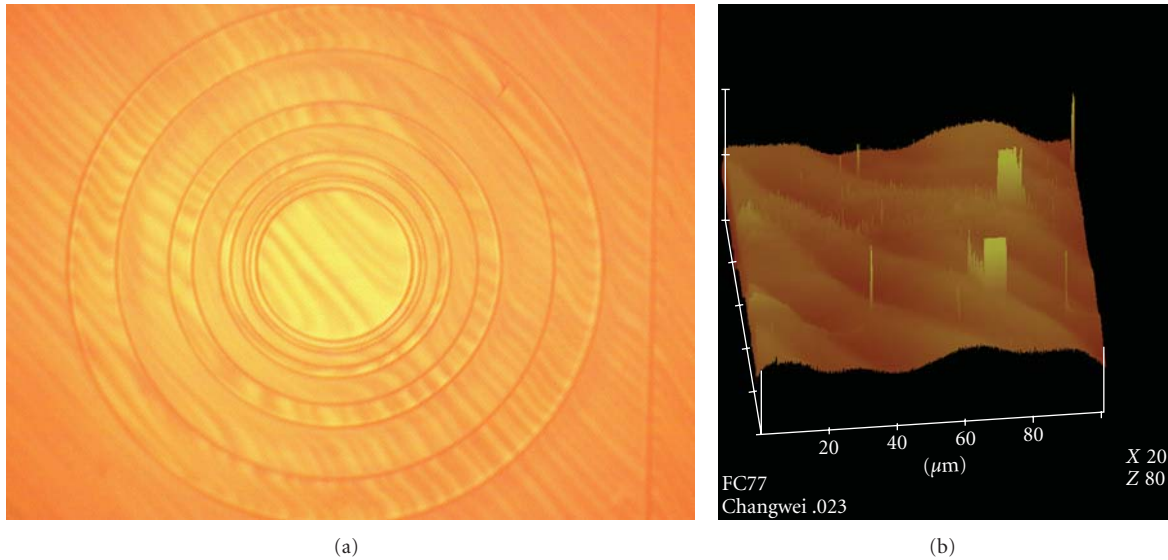


FIGURE 8: (a) Optical microscope and (b) AFM measurements after FC-77 thinner has been applied to a structural surface. FC-77 (3 M, USA) was originally used as a Teflon thinner at a concentration of 1%. The Teflon was spun-coated on a chip with a predefined photoresist pattern and dry-baked at 120°C for 10 min. However, because the saturated vapor pressure of the FC-77 thinner was relatively high (42 torr) [17], it volatilized too rapidly during spin coating which resulted in a wrinkled surface.

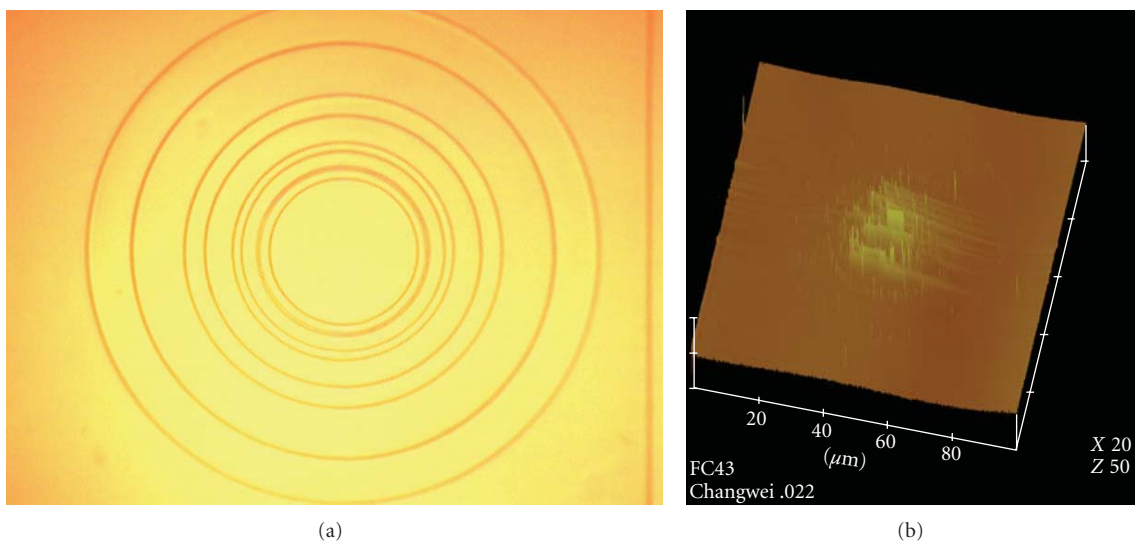


FIGURE 9: (a) Optical microscope and (b) AFM measurements after FC-43 thinner has been applied to a structural surface. FC-43 (3 M, USA) was originally used as a Teflon thinner at a concentration of 1%. The Teflon was spun-coated on a chip with a predefined photoresist pattern, and dry-baked at 180°C. We could find that no wrinkle surface is present on the Teflon surface.

because the curvature increases farther away from the lens off-axis, spherical aberration will occur in this region. One method of reducing spherical aberration is to reduce the difference in the light path between rays of light near to and distant from the lens axis.

This paper employs the difference in index of refraction between a liquid polymer and an optical glass substrate and uses adjustable electrodes to produce an electrostatic field with a two-dimensional gradient, to produce a hybrid aspherical lens. The design first simulates the hydrophilic/hydrophobic characteristics on different glass

substrates and indices of refraction of the polymer SU8-3050 to obtain optimized parameters and then employs an adjustable design involving self-positioning alignment and parallel-plate electrodes to obtain a hybrid high-level aspherical lens with an extremely large change in curvature. This paper relies on the adjustment of parameters, such as electrode size (Figure 4) and contact angle, to investigate how aspherical lens profile affects (Figure 5) optical performance.

This paper consequently modifies the electrode structure to design electrodes structurally similar to Fresnel Zone Plate (FZP), which can be used to modify the shape of the lens

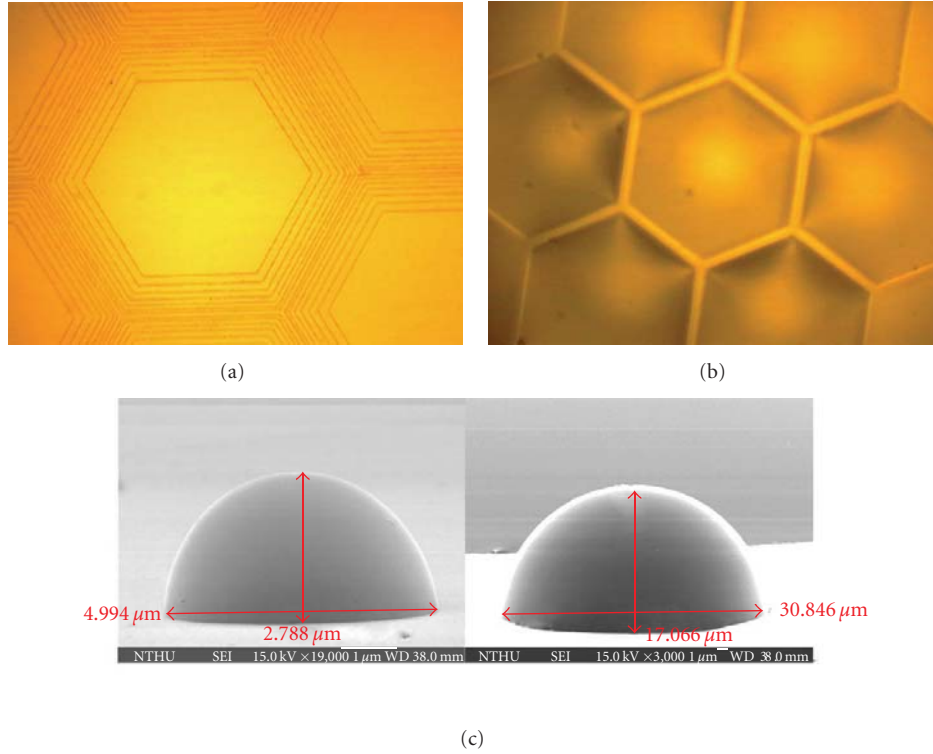


FIGURE 10: (a) Resultant hexagonal shape lens resulting after successful lift-off. (b) Photograph of a high-density hexagonal microlens array. (c) SEM of the Micro lens with different diameters (5 and 30 μm).

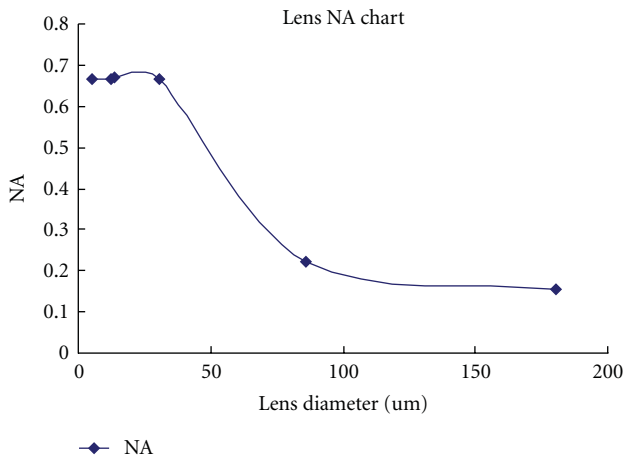


FIGURE 11: Relationship between different lens sizes and NA value.

margin. The upper and lower electrodes both consisted of transparent ITO electrodes in this paper’s initial design, and an oxidized layer served as the insulating layer, facilitating alignment and avoiding lens eccentricity. Nevertheless, due to the approximately 2 mm distance between the upper and lower electrodes, the excessively large depth of field caused difficulty in aligning the upper and lower electrodes. Because of this, the upper electrodes were modified to include an SU-8 3010 insulating layer (SU-8 has a dielectric coefficient of approximately 3.28), and Teflon was used on the aluminum

lower electrodes to define the hydrophilic/hydrophobic interface, inducing liquid droplets to perform self-assembly; the Teflon also served as an insulating layer (Teflon has a dielectric coefficient of approximately 2.1–2.5). In addition, the SU-8 3010 design formed hollow round concavities with different radii and width (Figure 4), which caused different electric field effects and gave the edge of the lens an aspherical profile.

The lower electrodes employ a lateral design to ensure that the lines of electrostatic field are not distributed vertically. As a result, the gradient electrostatic field is weak in the center and only exerts control over the edge of the lens. The surface tension still causes the surface of the lens to form a smooth curve (Figure 5(a)). This paper assesses the effect of different electrodes on optical performance, including the lens hydrophilic/hydrophobic angle, focusing ability, and light spot size.

The relationship between the electrostatic energy, electrostatic force, voltage, and distance is as follows [18]:

$$\text{the electrostatic energy } W = \frac{1}{2} \left( \frac{\epsilon xy}{d} \right) \times V^2, \quad (2)$$

$$\text{electrostatic forces } F_Z = - \left( \frac{dW}{dZ} \right) = \left( \frac{\epsilon xy V^2}{2d^2} \right). \quad (3)$$

It can be seen from these two equations that the electrostatic force is inversely proportional to the square of the distance  $d$ , where  $x$ ,  $y$  are the staggering length and width of the upper and lower electrodes, and  $V$  is the applied voltage. If modulation is implemented using electrodes that

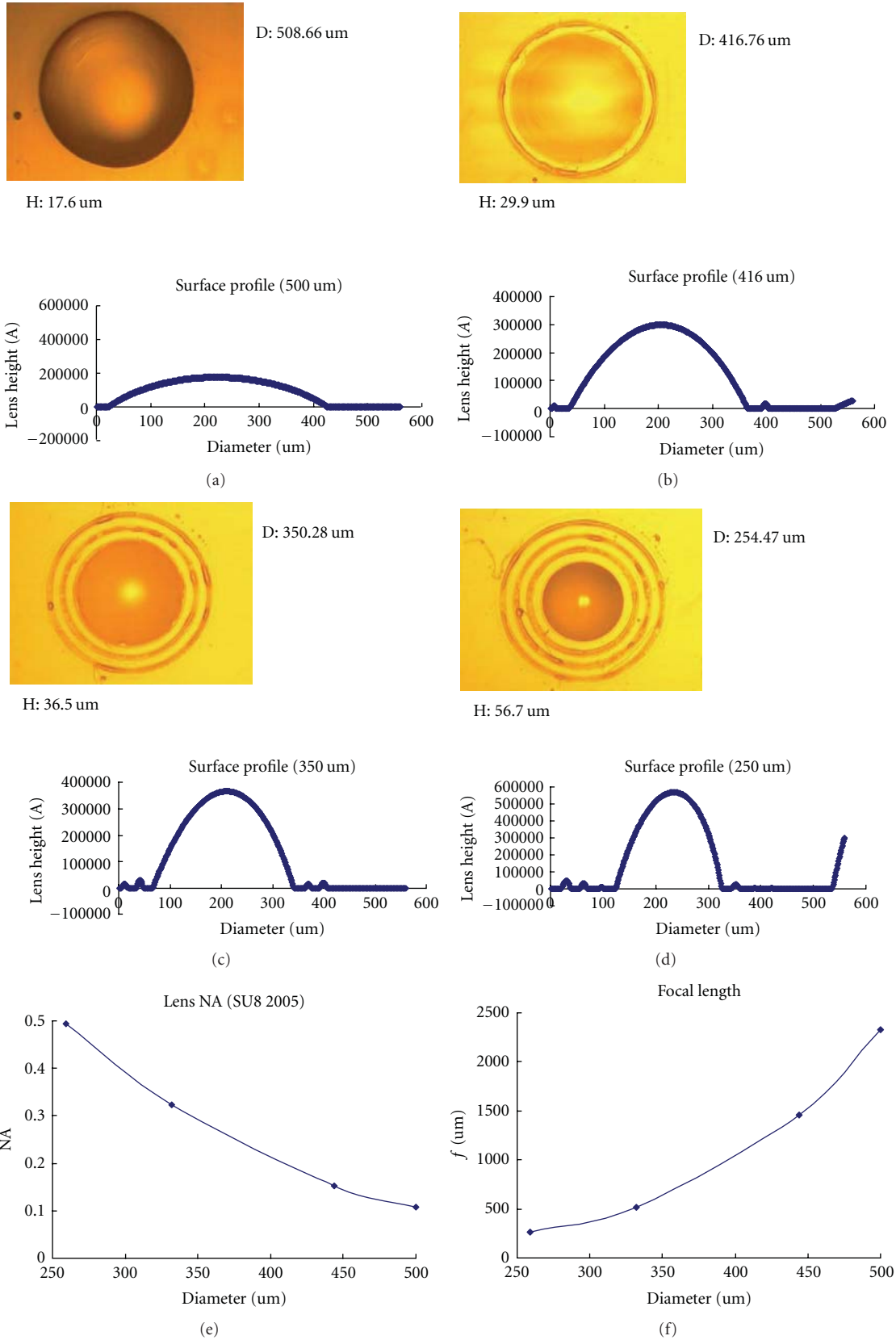


FIGURE 12: Micrograph of a multiring microlens and thickness measurements; relationship between size, NA value, and focal length (a) before heat treatment; (b) after first heat treatment; (c) after second heat treatment; (d) after third heat treatment; (e) relationship between multiring Teflon pattern size and NA value; (f) relationship between multiring Teflon pattern size and focal length.

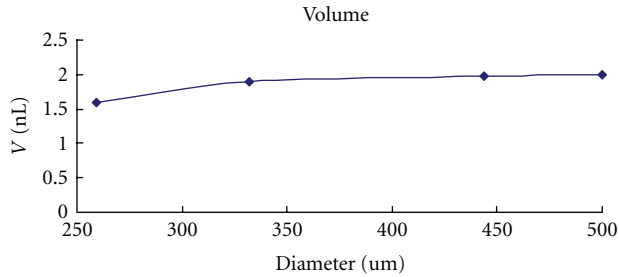


FIGURE 13: Change in volume of contracting microlens with different diameters.

are not specially designed, the closer the upper electrode to the tip of the lens, the greater the charge that will accumulate in the center of the lens, forming a pyramidal structure with severe spherical aberration (Figure 5(b)).

The following explains how a gradient electrostatic force induced by upper and lower electrodes was employed to produce hybrid aspherical microlenses.

(i) *Upper Electrode.*

- (1) Piranha (sulfuric acid: hydrogen peroxide = 7 : 1) was used to wash the glass substrate, which was then heated (90°C, 10 minutes) using a hot plate.
- (2) After sputter deposition ITO 1000 Å on the glass substrate, the application of negative SU-8 3010 photoresist by spin coating at 3000 rpm for 30 sec., yielding a thickness of approximately 10 μm.
- (3) Soft baking at 100°C for 2 min.
- (4) Exposure with a dose of 130 mJ.
- (5) After exposure, baking at 65°C for 1 min. and at 95°C for 3 min.
- (6) Developing with SU-8 developer for approximately 1 min. and 40 sec.

This completes the upper electrode pattern.

(ii) *Lower Electrode.*

- (1) Deposition of a 3000 Å layer of aluminum on the glass substrate using an electron gun vapor deposition machine.
- (2) Application of positive photoresist AZ 5214 (spin coating at 3000 rpm for 30 sec.).
- (3) Soft baking at 100°C for 1 min.
- (4) Exposure and baking at 100°C for 1 min.
- (5) Exposure to ten times the dose, completing the positive to negative conversion process.
- (6) AZ developer: H<sub>2</sub>O = 1 : 2, developing time approximately 45 sec. Because the AZ photoresist is used to protect the aluminum electrodes, overdeveloping should be avoided.

- (7) Etching of the aluminum: the etching fluid consists of H<sub>3</sub>PO<sub>4</sub> : HNO<sub>3</sub> : CH<sub>3</sub>COOH : H<sub>2</sub>O = 4 : 1 : 4 : 1. Etching is performed after heating to 50°C; etching time is approximately 25–30 sec.
- (8) Application of another layer of AZ 9260 positive photoresist (2500 rpm for 30 sec.) in order to define the hydrophilic/hydrophobic interface.
- (9) Soft baking at 100°C for 2 min.
- (10) Developing after exposure: to avoid dislocation in the hydrophilic/hydrophobic interface defined on the Teflon from causing an asymmetrical structure, the alignment precision must be less than the acceptable surface eccentricity.
- (11) Developing with AZ : H<sub>2</sub>O = 1 : 2 for approximately 6–8 min.
- (12) Application of Teflon (Teflon FC 43, 0.66%) at 3000 rpm for 30 sec.
- (13) Hard baking at 120°C for 10 min.
- (14) Use of acetone to lift off the AZ 9260; time is approximately 1 min.

The microlens fabrication process begins after the electrodes have been produced. In this paper, the volume under the curve is integrated to obtain the optimal lens volume. Two lower electrode sizes were designed in this paper; the electrodes had diameters of 0.91 mm and 0.8 mm, respectively. It can be seen from (3) that the electrostatic force is directly proportional to the square of the voltage and is inversely proportional to the distance between the electrodes. Different electrode designs were employed to investigate the lens profile after modulation. Figure 6 is a schematic diagram of the extension of the gradient electrostatic force 2. Process testing was based on a spherical lens with the foregoing multiple ring electrodes, and modulation employing electrostatic force was used to create aspherical lenses. The optical quality of the aspherical lenses was then tested and a comparison made with the aspherical lenses created employing single-ring electrodes.

### 3. Experimental Results

**3.1. Method 1: Spherical Microlens.** Because difference in surface hydrophilicity and hydrophobicity is used to produce microlenses in this paper, Teflon (contact angle of approximately 120°) and a glass substrate (contact angle of approximately 10°) are used because of the extreme difference in their contact angle. Unlike photoresist, a Teflon pattern cannot be produced directly using microimaging; therefore an indirect method consisting of etching and developing had to be used.

A reactive ion etching (RIE) machine was used in this experiment to produce a Teflon pattern via dry etching. When dry etching was used, the pattern could be very precisely converted from photoresist to Teflon. However, because of the excellent hydrophobicity of Teflon, photoresist could not be directly coated on the Teflon surface. Because of this, a low-power (75 W, 15 sec.) O<sub>2</sub> plasma was applied

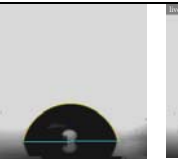
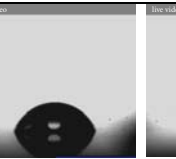
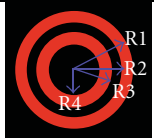
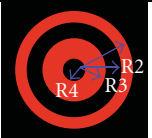
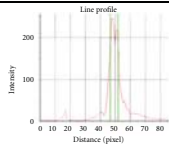
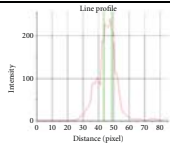
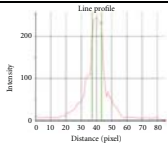
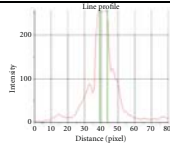
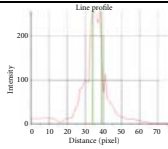
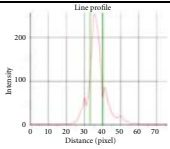
	Lens 01	Lens 02	Lens 03	Lens 04	Lens 05	Lens 06
Lenses						
Contact angles	83.7°	75.93	75.54	77.2	69.08	70.46
Concept of the designed radii						
Design radii	R1 = 400 $\mu$ m R2 = 700 $\mu$ m R3 = 900 $\mu$ m R4 = 1100 $\mu$ m	R1 = 400 $\mu$ m R2 = 600 $\mu$ m R3 = 800 $\mu$ m R4 = 1000 $\mu$ m	R1 = 200 $\mu$ m R2 = 500 $\mu$ m R3 = 700 $\mu$ m R4 = 900 $\mu$ m	R1 = 200 $\mu$ m R2 = 400 $\mu$ m R3 = 500 $\mu$ m R4 = 700 $\mu$ m R5 = 800 $\mu$ m R6 = 1000 $\mu$ m	R1 = 300 $\mu$ m R2 = 500 $\mu$ m R3 = 600 $\mu$ m R4 = 800 $\mu$ m R5 = 900 $\mu$ m R6 = 1100 $\mu$ m	R1 = 400 $\mu$ m R2 = 600 $\mu$ m R3 = 700 $\mu$ m R4 = 900 $\mu$ m R5 = 1000 $\mu$ m R6 = 1200 $\mu$ m
Spot diagram						
Beam profiler						
RMS spot size ( $\mu$ m)	0.8249	1.076	0.8724	0.8468	0.7575	0.9366

FIGURE 14: Showing the design radii, the resulting lens, spot size, beam profiler, and contact angle of the lenses.

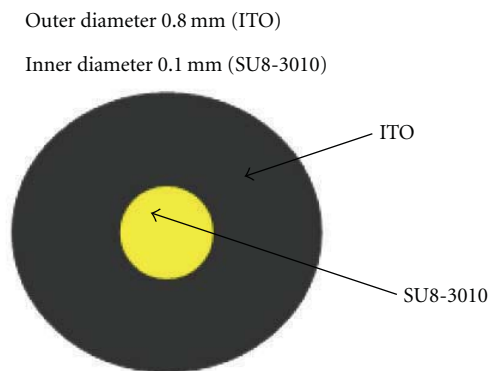


FIGURE 15: Schematic diagram of the upper electrode design.

to the surface as a hydrophilic treatment, allowing the AZ 5214 photoresist to be spun-coated on the Teflon. After soft baking, exposure, developing, and hard baking, a high-power (200 W, 200 sec.) O<sub>2</sub> plasma was used to perform etching. Although this method can be used to produce a desired

pattern on Teflon, the relatively good hydrophilicity of the Teflon surface after O<sub>2</sub> plasma surface treatment is unfavorable for lens shaping. Furthermore, the hydrophilicity is maintained for too long a time (Figure 7), which makes this method inappropriate for batch-type manufacturing. Figure 7 shows the contact angle at about 30° after seven days.

Another method is to use the lift-off technique to define the hydrophilic/hydrophobic interface. FC-77 (3M, USA) was originally used as a Teflon thinner at a concentration of 1%. The Teflon was spun-coated on a chip with a predefined photoresist pattern and dry-baked at 120°C for 10 min. However, because the saturated vapor pressure of the FC-77 thinner was relatively high (42 torr) [17], it volatilized too rapidly during spin coating which resulted in a wrinkled surface (Figure 8). As a consequence, the thinner FC-43 was used instead because of its relatively low saturated vapor pressure of 1.3 torr [17], which is only one-thirtieth that of FC-77. The switch to FC-43 brought about a clear improvement in the surface, which no longer had any visible spin coating marks (Figure 9). Nevertheless,

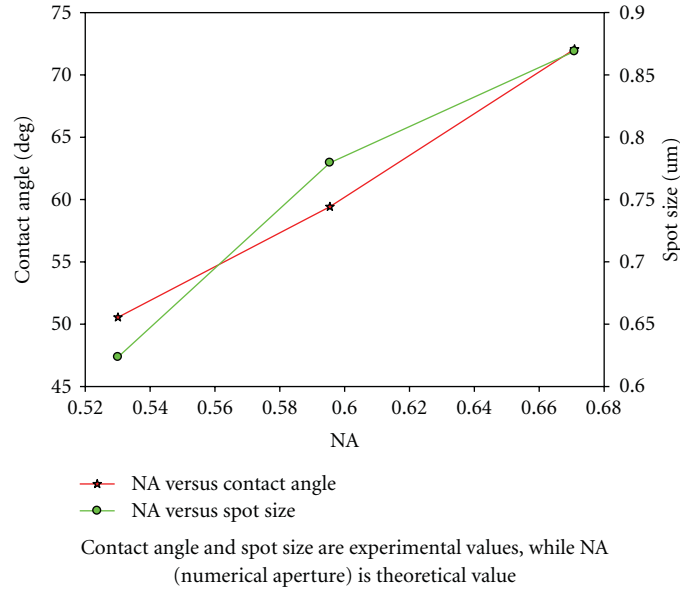


FIGURE 16: Relationship between contact angle, NA, and light spot size after the experiment.

due to its relatively high boiling point of 174°C (FC-77 has a boiling point of 97°C), FC-43 needed to be dry-baked at 180°C, after which acetone and Aleg-310 were used to remove the photoresist. Figures 10(a) and 10(b) show a high-density hexagonal microlens array produced successfully in this paper. Figure 10(c) shows the SEM of the microlens with different diameters (5 and 30 μm). When testing for different lens diameter, we could get the relationship between different lens sizes and NA in Figure 11.

With the addition of a suitable amount of thermal energy to the multiring variable focus lenses produced in this paper, the lens can be shrunk from the 500 μm diameter of the outermost ring to the 250 μm diameter of the innermost ring. Figure 12 shows a micrograph of a lens and the results of lens profile measurements. Here Figure 12(a) shows a microlens that has not yet undergone heat treatment; the SU-8 remains in the hydrophilic zone of the outermost ring, the lens diameter is 508.66 μm, and its height is 17.6 μm. Figure 12(b) shows a lens after the first heat treatment; the lens diameter shrank to 416.76 μm, and its height increased to 29.9 μm. Figure 12(c) shows a lens after the second heat treatment; the lens diameter continued to shrink to 350.28 μm, and its height increased to 36.5 μm. Figure 12(d) shows a lens after the third heat treatment; the lens diameter further shrank to 254.47 μm, and its height increased to 56.7 μm. The decreasing diameter of the lens causes its height to increase, which also increases its NA and shortens the focal length. The foregoing equation reveals that the relationship between the NA, focal length, and lens size before and after heat treatment is as shown in Figures 12(e) and 12(f). The lens’s NA has increased from 0.1 to 0.5, while its focal length has decreased from 2.5 mm to 0.3 mm. The change in SU-8 lens volume before and after heat treatment reveals the volatilization of solvent. Volume can be estimated using the equation  $V_{cap} = \pi s^2((3R - s)/3)$ , and the volume change correlation is as

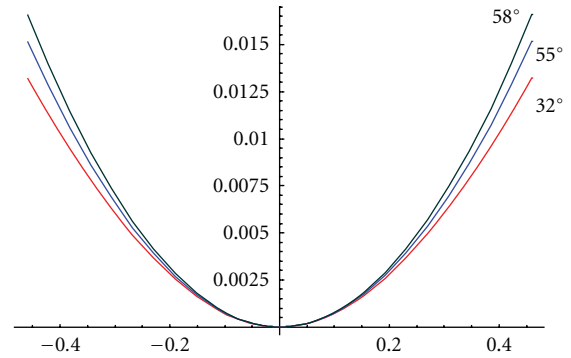


FIGURE 17: Lens profile curve for different contact angles.

shown in Figure 13. The foregoing experiment reveals that a hydrophilic/hydrophobic multiple-interface design can effectively resolve the problem of insufficient NA caused by lens material and lens size. By employing this design, when the original lens is relatively small, the problem of surface free energy shifts from the horizontal direction to the vertical direction, making it difficult to achieve a variable focus.

**3.2. Method 2: Aspherical Microlens.** This paper then investigates the relationship between contact angle and focal light spot size for the different contact angles obtained when the electrode distance and voltage are fixed, the lens volume is fixed, and the radii of the multiring electrodes are varied. Figure 14 shows the design radii, the resulting lens, spot diagram, spot size, beam profiler, and contact angle.

*Case 1* (Changing the lower multiring electrode radius (mechanism 2)). It can be seen from the foregoing optical testing results (Figure 14) that, although varying the multiple

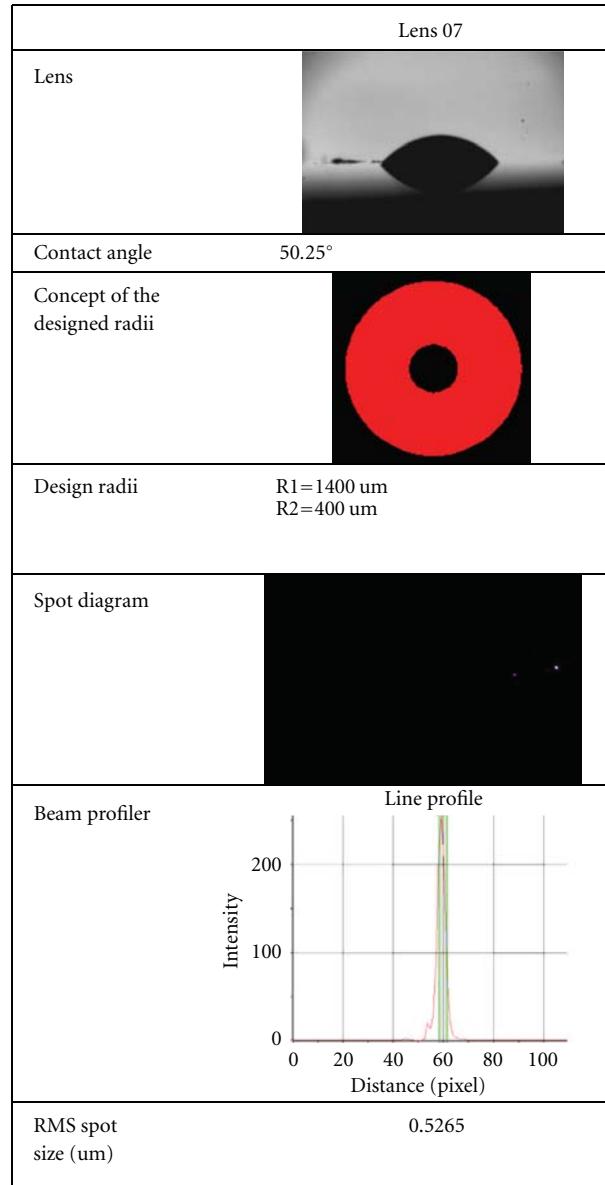


FIGURE 18: Shows the spot size and light energy distribution after modulation.

electrodes can indeed change the lens's contact angle to within a range of 69–83°, the light spot size is always around 0.75–0.9  $\mu\text{m}$  when multiple electrode modulation is employed. It can be inferred from these experimental results that this multiring electrode design chiefly changes the curvature near the lens axis, but does not change the lens profile near the edge of its aperture. Because of this, spherical aberration near the edge cannot be effectively corrected, and the light spot cannot be shrunk.

*Case 2* (Changing the upper multiring electrode radius (mechanism 1)). This paper also investigates the relationship between contact angle and focal light spot size for the different contact angles obtained when the electrode distance and voltage are fixed, the lens diameter is fixed, and the lens volume is varied. The parameters employed here

include an upper electrode ITO outer diameter of 0.8 mm, a lens outer diameter (ITO inner diameter) of 0.1 mm (Figure 15), a distance fixed at 2 mm ( $1.5 \pm 0.2$  mm), a voltage of 4000 V, and a volume varying from 0.2  $\mu\text{L}$  to 0.45  $\mu\text{L}$ . The minimum light spot size was approximately 0.62  $\mu\text{m}$  ( $\lambda = 632.8$  nm), the rear focal length was roughly 0.24 mm, and the contact angle was approximately 59°. These results show that the larger the contact angle, the greater the off-axis spherical aberration, and consequently the larger the light spot. The hydrophilic/hydrophobic angle and the NA are directly proportional and are inversely proportional with the rear focal length (Figure 16). In accordance with the experimental results for lenses with different contact angles, the profile fits the relation curve shown in Figure 17. The foregoing results indicate that correcting off-axis spherical aberration requires achieving a smaller contact angle, which

TABLE 1: The comparison of lens specifications in relevant literature.

Reference	Lens type	Tuning concept	$D$ (mm)	$n$	$f$	Spot size
[18]	Plane-convex	Electrostatic force	1.4 mm	1.67 (SU-8)	1.525 mm	0.778 $\mu\text{m}$ (for 632.8 nm)
[19]	Hybrid aspheric lens	Hybrid, electrostatic force	0.92 mm	1.53 (BK7); 1.58 (NOA-63)	0.385 mm	0.504 $\mu\text{m}$ (for 405 nm)
[20]	Biconvex	Thermal energy, electrostatic force	1.14 mm	1.53 (COC)	4.97 mm	0.588 $\mu\text{m}$ (for 405 nm)
[21]	Polymer Plane-convex	Hot embossing	1 mm	1.53 (COC)	$X$	0.98 $\mu\text{m}$ (for 405 nm)

requires a stronger electrostatic field around the lens margin and a weaker electrostatic field in the center of the lens.

*Case 3* (Modulating the outside electrode—aluminum electrodes have no defined hydrophilic/hydrophobic interface). It can be seen from Case 2 that off-axis aberration can be reduced by changing the magnitude of the marginal off-axis electrostatic field and reducing the contact angle. Experimental test results are shown in Figure 18. The results of light spot testing show that when contact angle is reduced to roughly  $50^\circ$ , the off-axis spherical aberration can be lessened and the light spot shrunk to around 0.5265 microns, which is close to the light spot size of the aspherical lenses used in commercial DVD players. Please refer to [17–21] concerning other shaping methods or the use of other materials such as COC and NOA in conjunction with electrostatic force to produce aspherical lenses. This paper provides the comparison of lens specifications in relevant literature shown in Table 1.

#### 4. Conclusions

This paper presents many new micro-optofluidic polymer solid lens fabrication methods that are capable of achieving the desired profile, focal length, numerical aperture, and spot size through the utilization of MEMS technology. The resulting polymer solid lenses have spherical or aspherical shapes. The method of fabricating polymer solid lenses is different from methods used to fabricate tunable lenses with variable focal length or needing an external control system to change the lens geometry. In this paper, we focus on the use of thermal energy and electrostatic force to shape lens profiles, including both spherical and aspherical lenses. Furthermore, this paper also discusses how to achieve a lens with a high numerical aperture of 0.6 by means of MEMS.

The polymer used in this study, SU8-3050, has high transmittance in the blue light waveband ( $\lambda = 405$  nm), and the resulting curvature change in aspherical lenses is  $C = 0.3 - 1.5$  (L/mm). The use of electrodes with different designs can also produce many types of conical curves.

As far as optical characteristics are concerned, the smallest light spot measured for a micro-aspherical lens was approximately  $0.62 \mu\text{m}$  ( $\lambda = 632.28$  nm), and the rear focal length was 0.24 mm. In the blue light ( $\lambda = 405$  nm) waveband, the smallest measured light spot is approximately  $0.56 \mu\text{m}$ , and the rear focal length is roughly 0.38 mm; these

values are all close to the requirement for blue light DVD players.

Although the MEMS techniques discussed in this paper are not currently able to fully meet the requirements of existing optical systems, as higher density DVDs are developed in the future, there will be much greater need for precision lenses. Since the methods presented in this paper can provide a high degree of precision, they may be employed to make lenses for pickup heads in the near future.

#### References

- [1] J. W. Pan, C. M. Wang, W. S. Sun, and J. Y. Chang, "Portable digital micromirror device projector using a prism," *Applied Optics*, vol. 46, no. 22, pp. 5097–5102, 2007.
- [2] S. Kuiper and B. H. W. Hendriks, "Variable-focus liquid lens for miniature cameras," *Applied Physics Letters*, vol. 85, no. 7, pp. 1128–1130, 2004.
- [3] B. H. W. Hendriks, M. A. J. Van As, and A. A. M. Van Alem, "Miniaturised high-numerical aperture singlet plastic objective for optical recording," *Japanese Journal of Applied Physics A*, vol. 44, no. 9, pp. 6564–6567, 2005.
- [4] C. Ke, X. Yi, J. Lai, and S. Chen, "Research on hybrid integration technology between charge-coupled devices and diffractive microlens arrays," *Journal of Micromechanics and Microengineering*, vol. 14, no. 1, pp. 125–128, 2004.
- [5] D. Daly, R. F. Stevens, M. C. Hutley, and N. Davies, "The manufacture of microlenses by melting photoresist," *Measurement Science and Technology*, vol. 1, no. 8, article 016, pp. 759–766, 1990.
- [6] C. Cheng and J. A. Yeh, "Dielectrically actuated liquid lens," *Optics Express*, vol. 15, no. 12, pp. 7140–7145, 2007.
- [7] H. Yang, C. K. Chao, T. H. Lin, and C. P. Lin, "Fabrication of microlens array with graduated sags using UV proximity printing method," *Microsystem Technologies*, vol. 12, no. 1-2, pp. 82–90, 2005.
- [8] Y. Sakurai, S. Okuda, H. Nishiguchi, N. Nagayama, and M. Yokoyama, "Microlens array fabrication based on polymer electrodeposition," *Journal of Materials Chemistry*, vol. 13, no. 8, pp. 1862–1864, 2003.
- [9] K. H. Jeong, G. L. Lin, N. Chronis, and L. P. Lee, "Tunable microdoublet lens array," in *Proceedings of the 17th IEEE International Conference on Micro Electro Mechanical Systems (MEMS '04)*, pp. 37–40, 2004.
- [10] M. H. Wu, K. E. Paul, and G. M. Whitesides, "Patterning flood illumination with microlens arrays," *Applied Optics*, vol. 41, no. 13, pp. 2575–2585, 2002.

- [11] C. C. Cheng, C. A. Chang, and J. A. Yeh, "Variable focus dielectric liquid droplet lens," *Optics Express*, vol. 14, no. 9, pp. 4101–4106, 2006.
- [12] M. Vallet, B. Berge, and L. Vovelle, "Electrowetting of water and aqueous solutions on poly(ethylene terephthalate) insulating films," *Polymer*, vol. 37, no. 12, pp. 2465–2470, 1996.
- [13] C. Cheng and J. A. Yeh, "Dielectrically actuated liquid lens," *Optics Express*, vol. 15, no. 12, pp. 7140–7145, 2007.
- [14] H. Ren and S. T. Wu, "Tunable-focus liquid microlens array using dielectrophoretic effect," *Optics Express*, vol. 16, no. 4, pp. 2646–2652, 2008.
- [15] H. Ren, H. Xianyu, S. Xu, and S. T. Wu, "Adaptive dielectric liquid lens," *Optics Express*, vol. 16, no. 19, pp. 14954–14960, 2008.
- [16] K. -Y. Hung, F. -G. Tseng, and H. -S. Khoo, "Integrated three-dimensional optical MEMS for chip-based fluorescence detection," *Journal of Micromechanics and Microengineering*, vol. 19, no. 4, Article ID 045014, pp. 1–10, 2009.
- [17] <http://www.3m.com/index.jhtml> .
- [18] K. Y. Hung, F. G. Tseng, and T. H. Liao, "Electrostatic-force-modulated microspherical lens for optical pickup head," *Journal of Microelectromechanical Systems*, vol. 17, no. 2, pp. 370–380, 2008.
- [19] K. Y. Hung, L. W. Chang, F. G. Tseng, J. C. Chiou, and Y. Chiu, "Optimum electrostatic force control for fabricating a hybrid UV-curable aspheric lens," *Journal of Micromechanics and Microengineering*, vol. 20, no. 7, Article ID 075001, 2010.
- [20] K. Y. Hung, C. C. Fan, F. G. Tseng, and Y. K. Chen, "Design and fabrication of a copolymer aspheric bi-convex lens utilizing thermal energy and electrostatic force in a dynamic fluidic," *Optics Express*, vol. 18, no. 6, pp. 6014–6023, 2010.
- [21] K.-Y. Hung, Y.-K. Chen, S.-H. Huang, and D.-C. Shye, "Molding and hot forming techniques for fabricating plastic aspheric lenses with high blue-light transmittance," *Microsystem Technologies*, vol. 16, no. 8-9, pp. 1439–1444, 2010.

## Research Article

# Moldless PEGDA-Based Optoelectrofluidic Platform for Microparticle Selection

Shih-Mo Yang,<sup>1</sup> Tung-Ming Yu,<sup>1</sup> Ming-Huei Liu,<sup>2</sup> Long Hsu,<sup>1</sup> and Cheng-Hsien Liu<sup>3</sup>

<sup>1</sup> Department of Electrophysics, National Chiao Tung University, Hsinchu 30010, Taiwan

<sup>2</sup> R & D Division, SINONAR Corporation, Hsinchu 30078, Taiwan

<sup>3</sup> Department of Power Mechanical Engineering, National Tsing Hua University, Hsinchu 30010, Taiwan

Correspondence should be addressed to Cheng-Hsien Liu, liuch@pme.nthu.edu.tw

Received 6 March 2011; Revised 20 May 2011; Accepted 4 June 2011

Academic Editor: Aaron T. Ohta

Copyright © 2011 Shih-Mo Yang et al. This is an open access article distributed under the Creative Commons Attribution License, which permits unrestricted use, distribution, and reproduction in any medium, provided the original work is properly cited.

This paper reports on an optoelectrofluidic platform which consists of the organic photoconductive material, titanium oxide phthalocyanine (TiOPc), and the photocrosslinkable polymer, poly (ethylene glycol) diacrylate (PEGDA). TiOPc simplifies the fabrication process of the optoelectronic chip due to requiring only a single spin-coating step. PEGDA is applied to embed the moldless PEGDA-based microchannel between the top ITO glass and the bottom TiOPc substrate. A real-time control interface via a touch panel screen is utilized to select the target 15  $\mu\text{m}$  polystyrene particles. When the microparticles flow to an illuminating light bar, which is oblique to the microfluidic flow path, the lateral driving force diverts the microparticles. Two light patterns, the switching oblique light bar and the optoelectronic ladder phenomenon, are designed to demonstrate the features. This work integrating the new material design, TiOPc and PEGDA, and the ability of mobile microparticle manipulation demonstrates the potential of optoelectronic approach.

## 1. Introduction

The microparticle manipulation by using either optical forces or electrokinetics has been getting important and popular, especially in fields like lab-on-a-chip. The former utilize a laser beam to trap microparticles toward the focal point. The invention of optical tweezers [1–3] and the various development of the holographic optical tweezers [4, 5] have established a convenient platform to manipulate either single or multimicroparticles. However, the requirement of high N.A. value lens in optical tweezers to perform a high focal laser beam highly reduces the working distance and constrains the application [6, 7]. The latter such as dielectrophoresis (DEP) induces microparticle polarized in a non-uniform electric field to either attract or repel toward the field maximum or minimum [8, 9]. General methods to generate nonuniform electric field are to fabricate metal electrodes on the glass substrate. The fixed metal pattern limits the flexibility to manipulate microparticle. Recently, Chiou et al. integrated the optical flexibility and the electronic approach to present optoelectronic tweezers (OETs) [10]. Its

various applications have been applied in biological field [11].

Photoconductive material is a key character of the OET. The amorphous silicon (a-Si) is usually fabricated on an ITO glass to prevent the charges [12]. While the light pattern with proper absorbing wavelength is projected onto the a-Si layer, the resistance within the illumination region is reduced and the charges transport through the a-Si layer to form a virtual electrode. Due to the flexibility of light pattern, the nonuniform electric field induced by illuminating method is able to manipulate the microparticle within the region which the light can cover. Polystyrene particles [10, 13], biological sample [10, 11, 13–15] DNA [16, 17], and other microparticles [18–21] are able to be manipulated by this optoelectronic approach.

The micromolding approach of photocrosslinkable polymers has been widely applied in cells patterning and three-dimensional artificial tissue [22–25]. The structure of photolithographically patterned poly(ethylene glycol) diacrylate (PEGDA) enables to fabricate microwell array [26, 27], cultures cells inside hydrogels [28], and forms cell-laden

microgels for the fabrication of 3D tissue constructs [29]. The high-resolution feature of photolithographically patterned PEGDA hydrogel has been also applied to photoresist-based patterns [30] as master molds for generating poly(dimethylsiloxane), PDMS, microstructures [31]. Comparing to the methods of turning the PDMS microfluidics from PEGDA-based mold, here we present the approach of fabricating the microchannel which is directly embedded into the optoelectrofluidic chip.

Polymer-based and organic material OET devices have been reported [32, 33]. Herein, we use the simplified fabrication process with the photoconductive material, titanium oxide phthalocyanine (TiOPc), to fabricate our optoelectrofluidic chip. Comparing with a-Si deposition process, a single spin-coating step is able to finish the fabrication of our TiOPc-based OET chip. We also demonstrate the PEGDA microchannel used for pumping and injecting the medium containing polystyrene particles. This integration providing a tunable and constant liquid flow velocity promotes the optoelectronic technology as a optoelectrofluidic platform for the microparticle manipulation. By utilizing dynamic optical images to generate the light-induced DEP force, this platform demonstrates the feature of microparticle selection which can be done by the design of either the switching oblique light bar or the fixed slanting in-parallel light bars.

## 2. Principle of TiOPc-Based Light-Induced Dielectrophoresis Chip

DEP was investigated by H. A. Pohl (1951), who performed the early significant experiments with the small plastic microparticles suspended in insulating dielectric liquid and found that they could be driven in response to the application of a nonuniform electric field [34, 35]. This phenomenon has been applied to manipulate the microparticles such as virus, bacteria, neurons, and limited cells in microfluidics [36]. The time-averaged DEP force,  $F_{\text{DEP}}$ , acting on a spherical microparticle of radius  $r$  suspended in the insulating medium of relative permittivity  $\epsilon_m$  is given by

$$F_{\text{DEP}} = 2\pi r^3 \epsilon_m \text{Re}[f_{\text{CM}}(\omega)] \nabla E_{\text{rms}}^2. \quad (1)$$

Here,  $E_{\text{rms}}^2$  is the root mean square of the ac electric field, and  $f_{\text{CM}}(\omega)$  is the Clausius-Mossotti factor [36, 37].

In our PEGDA-based optoelectrofluidic platform, the microparticles are suspended in the insulating medium and sandwiched between the top indium tin oxide (ITO) conductive glass and the bottom photoconductive layer substrate. The feature of photoconductivity is that its conductivity can be enhanced when the suitable wavelength light illuminates on it. In the illumination region, the charges transport the conductivity layer and assemble on its surface to form a virtual electrode. The size of virtual electrode on the photoconductivity surface is much smaller than the top ITO plane, relatively. Therefore, the electric field intensity within the illumination region is the maxima, while ac voltage is applied between the top and the bottom ITO glasses. The microparticle experiences either the positive DEP force attracting toward the light pattern or the negative DEP force

repelling toward the nonilluminated region. In this paper, the microparticles, polystyrene beads, always experience the negative DEP force [13] under our operation condition setup.

## 3. Chip Fabrication

The general method to fabricate microfluidic channel takes the advantage of convenience of polydimethylsiloxane- (PDMS-) based microstructure. Utilizing standard photolithography process to fabricate SU-8 negative photoresist on the silicon substrate and turning the case mold with PDMS are widely used to form the designed microchannels. It is a convenient approach for a microchannel with any complex component. However, for our optoelectrofluidic platform with the top ITO glass and the bottom TiOPc substrate, a thin PDMS film is easy to remain on the top ITO glass above the microchannel. That would limit the electric field distribution within the microchannel.

The oxygen plasma treatment would help the bonding of the PDMS surface and the glass substrate, but the conductivity of indium oxide layer on the glass plane would reduce the bonding force between itself and PDMS surface. Therefore, PDMS microchannel is not the first choice for our light-induced dielectrophoresis chip.

This research integrates the OET system and the microchannel structure. Professor Lee's group utilizes a light bar switch to select the polystyrene beads of specific diameter into the desired channel [38]. Professor Wu's group uses the dynamic nonuniform electric field to induce the cells electroporation and get the fluorescent tags through the membrane into the cell [39]. Both of them utilize positive photoresist SU-8 to fabricate the microchannels. Besides, the latter applies the UV-curable epoxy to seal the SU8 microchannel. Although the SU-8 provides a convenient way to guide the liquid flow on a-Si-based OET chip, it is not the good choice for our organic photoconductive TiOPc-based chip. The hardened TiOPc layer would be dissolved in the alcoholic solution. Besides, the solvent to develop the SU-8 structure on TiOPc surface would also destroy the TiOPc characters. TiOPc would be washed out by these two organic solutions. Therefore, we develop the PEGDA material to fabricate the microchannel in this research. Besides, it is much convenient to fabricate PEGDA-based microchannels because there is no need to make the mold first. Moreover, there are usually three PDMS walls for the PDMS channel, two sides and one top cover. The PEGDA-based channel only has two side PEGDA walls. It keeps the features of the top ITO glass and the bottom substrates. This is suitable for our TiOPc-based optoelectronic chip.

The schematic of the process to fabricate the moldless PEGDA-based microchannel on the TiOPc-based optoelectrofluidic chip is shown in Figure 1. The TiOPc liquid is dropped on a 3 cm  $\times$  8 cm ITO glass substrate. The thin TiOPc layer of about 500 nm is spin coated at 1000 rpm for 10 sec (Figures 1(a) and 1(b)). After baking at 130°C for 30 min to remove the organic solvent and harden the photoconductivity structure, the thin TiOPc layer stays stable for

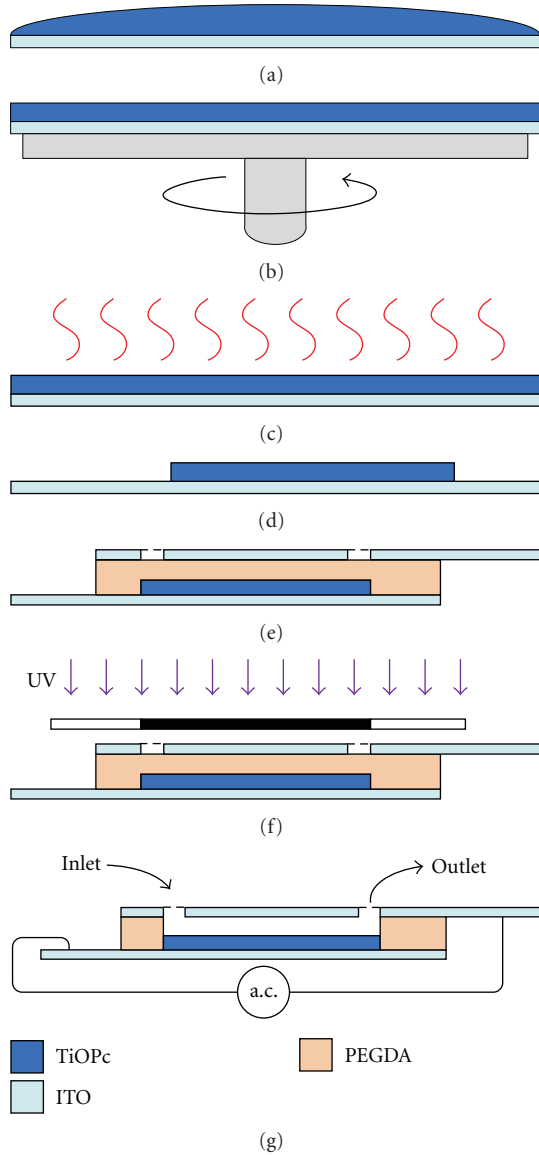


FIGURE 1: Fabrication process of the TiOPc-based light-induced DEP chip and the moldless PEGDA-based microchannel.

months on the ITO glass surface under normal operation (Figure 1(c)). Because our operation area is about  $3\text{ cm} \times 8\text{ cm}$ , the ethanol-water solution (70 : 30) is utilized to wipe out the unused area and remain the suitable operation area of TiOPc surface (Figure 1(d)). The PEGDA prepolymer solution, which is prepared by mixing 5 mL of PEGDA (MW 258 Da, 99%) with 150 mg of 2,2-dimethoxy-2-phenyl-acetophenone (DMPA, 99%) photoinitiator, is sandwiched between the top ITO glass and the bottom TiOPc-coated substrate (Figure 1(e)). The UV light of 350~500 nm wavelength illuminates on the chip for several seconds (Figure 1(f)). After photocrosslinking, microchannel is developed by utilizing DD-water to remove the noncrosslinked prepolymer and dried with  $\text{N}_2$  blowing. Finally, the chip is placed on the hotplate at  $40^\circ\text{C}$  for 30 min to remove the water vapour and harden the PEGDA-based microstructure.

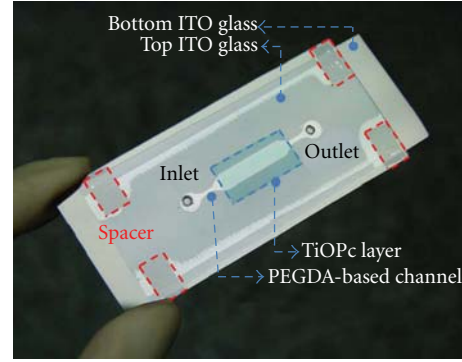


FIGURE 2: The moldless PEGDA-based optoelectrofluidic chip prototype. The overlapping area of TiOPc layer and PEGDA-based channel is the working region.

The moldless PEGDA-based optoelectrofluidic chip prototype is shown in Figure 2. The TiOPc layer is spincoated on the bottom ITO glass. Inlet and outlet holes are drilled on the top ITO glass. Before the UV light exposure, the four square spacers of  $60\ \mu\text{m}$  height are placed at the corners of the exposure region. The prepared PEGDA solution is sandwiched between bottom and top ITO glasses. After photocrosslinking of UV light illuminating, the microchannel is formed between the two ITO glasses.

#### 4. The Operation System Setup for the TiOPc-Based Light-Induced Dielectrophoresis Chip

The optoelectrofluidic platform consists of three parts, the optical system, the optoelectronic chip, and the liquid pumping setup. The light source is provided by a Philips UHP mercury lamp and concentrated as a straight beam when it passes through a pair of focusing lenses, an optical alignment. The light illuminates on a digital micromirror display (DMD, with a spatial resolution of  $1024 \times 768$  pixels). The pattern of micromirror is controlled by a touch-panel device, MSI AE 2000, and the manipulation interface is programmed by using Flash software (Adobe Systems Co., Ltd.). After the illuminating light reflects from the DMD surface, the light pattern is formed as the designed pattern on the controlled surface. A pair of focus lenses, which consist of two lenses with 200 and 10 mm focal lengths respectively, are utilized to concentrate the pattern size as 1/20 times and project the light pattern onto the TiOPc surface. The chip is placed on an XYZ translation stage for tuning the projected image. A function generator (33120A, Agilent) is used to provide the out-of-phase ac voltage required for the DEP operation on the optoelectrofluidic platforms. A syringe pump (SP230IW, WPI, FL, USA) is utilized to pump and regulate the flow streams containing with the microparticles polystyrene beads. The motion of microparticles manipulated by light image is captured and recorded by a 10x object lens and a digital CCD camera connecting to a desktop computer (Figure 3).

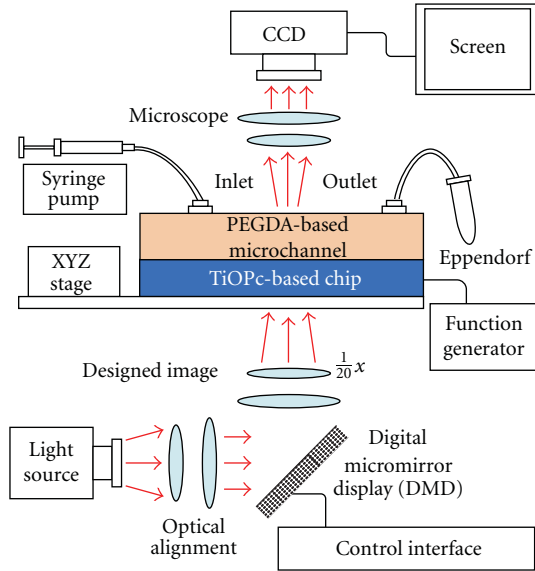


FIGURE 3: Schematic diagram of the optoelectrofluidic system. The optical system, the optoelectrofluidic platform, and the liquid driving pump are three main parts.

## 5. PEG-Based Microchannel

Here, we design the T junction pattern for the PEGDA-based microchannel. The channel width in Figures 4(a) and 4(b) is  $100\ \mu\text{m}$  and  $300\ \mu\text{m}$ , respectively, for two different microchannel designs. Before UV light illuminating, the PEGDA solution of about  $50\ \mu\text{l}$  is sandwiched between the top and the bottom glasses. After 7 seconds of UV photopolymerization process, the microchannel is fabricated and exhibits a good optical transparency and robust package. The DMPA ratio in PEGDA solution determines the exposure time and the later microstructure expansion. The diffraction influence of UV illuminating is a significant phenomenon when the PEGDA solution is exposed. According to our experimental results, we could easily fabricate the microchannel of about  $100\ \mu\text{m}$  width.

## 6. Optical Virtual-Electrode Switch for Microparticle Selection

When the light pattern is projected on the photoconductivity material, the conductivity is reduced, and the charges transport to the TiOPc layer to form a virtual electrode, on its surface. Microparticles would be either attracted toward the light pattern due to the positive DEP force or repelled to the nonilluminated region due to the negative DEP force. If the microfluidics system is integrated with this DEP operation, the microparticle would experience liquid driving force dominated by the liquid flow. This integration of microfluidics and light-induced DEP increases the operation flexibility.

Here, we combine the convenience of light-driven operation with the feature of moldless PEGDA-based microfluidics channel to develop the optical virtual switch approach for

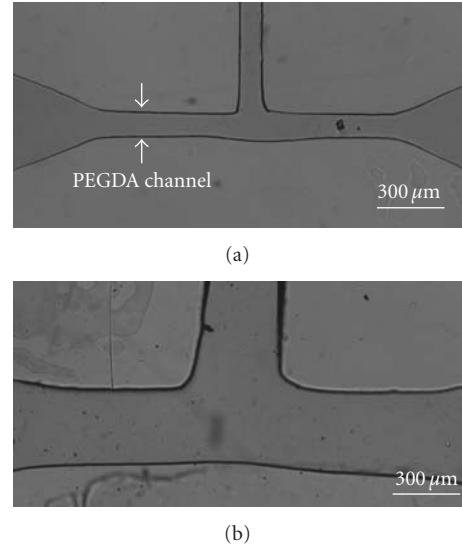


FIGURE 4: T junction of PEGDA-based microchannel. (a)  $100\ \mu\text{m}$  wide microchannel and (b)  $300\ \mu\text{m}$  wide microchannel.

microparticle selection as shown in Figure 4(a). The light pattern projected on the TiOPc surface has two different functional regions, alignment part and virtual switch part. The liquid flows rightward in the PEGDA-based microchannel containing with the dispersedly suspended microparticles. In order to arrange the microparticle as a line one by one, the light pattern with the funnel-like geometry is designed for the entrance guiding. When the microparticle reaches the edge of light pattern, it experiences a repelling force (negative DEP) toward nonilluminated region. In Figure 5(a), the direction of flow-driving force is rightward, and the direction of OET force is in the upper left. These two forces dominate the net force,  $F_{\text{Net}}$ , which is in the direction of the up right at the entrance of the switch. Then, the microparticle is able to be selected into the specific downstream pathway based on our virtual switch command. The upper channel and down channel are two flash models, as shown in Figures 5(c) and 5(d), to guide the microparticle into different pathway. The polystyrene bead experiences negative DEP force and only moves within the minimum electric field region which is the nonilluminated region on the TiOPc surface. To preverify the DEP effect induced by the light pattern for predicting the trajectory of moving microparticles, a commercial finite element software CFD-ACE+ (CFDRC, Huntsville, Ala) is utilized to simulate the steady-state electric field, which dominates the DEP force to drive the mobile microparticles. Figure 5(b) shows the simulation result of electric field distribution,  $E_{\text{square}}$ , on the chip. The illumination region has the large electric field, and the nonilluminated region provides the minimum electric field for polystyrene bead. The negative DEP force guides the bead at the nonilluminated region, and the liquid flow drives it to move rightward as the black-dotted line shown in Figure 5(b). This research work integrates touch panel for the convenient and intuitive microparticle manipulation. The real-time controlling interface is programmed by using Flash

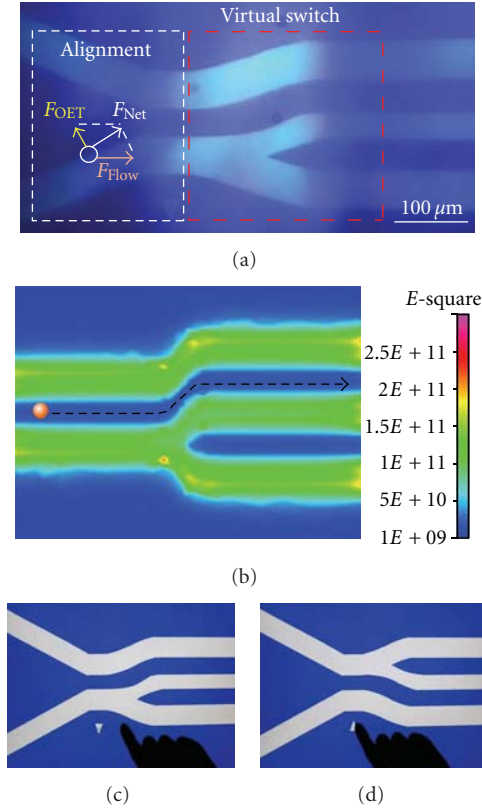


FIGURE 5: (a) Optical virtual-electrode switch. (b) Numerical simulation of the virtual-electrode switch. (c) The upperchannel model and (d) downchannel model light image on the touch panel for control interface. The black shape is the finger for triggering the model switch.

software. The light pattern switch between upper-channel and down-channel models is triggered by the functional triangle image shown in Figures 5(c) and 5(d). The touch panel screen and the feature of Flash software provide a user-friendly interface. We switch the light image of different modes on the TiOPc surface by the finger shown in Figures 5(c) and 5(d). As a mobile microparticle moving from the entrance, we can select the microparticle to move in the desired downstream pathway by the simple finger operation.

The selection process of microparticles based on the optical virtual-electrode switch is demonstrated and recorded as shown in Figures 6(a)–6(f). The different color arrows/dotted circles indicate the moving path of the individual bead in the microchannel. The microparticles are arranged one by one toward the entrance by the funnel-shaped light pattern, which generates negative DEP force. The microparticle enters the selection region with a characterized velocity of  $100 \mu\text{m/s}$ . When the light pattern is in upper-channel model, the polystyrene bead will be guided to the upper pathway.

When the light pattern is in down-channel model, the polystyrene bead will be guided to the lower pathway. The light pattern mode is switched from the under-channel model to the down-channel mode by touching the triangle

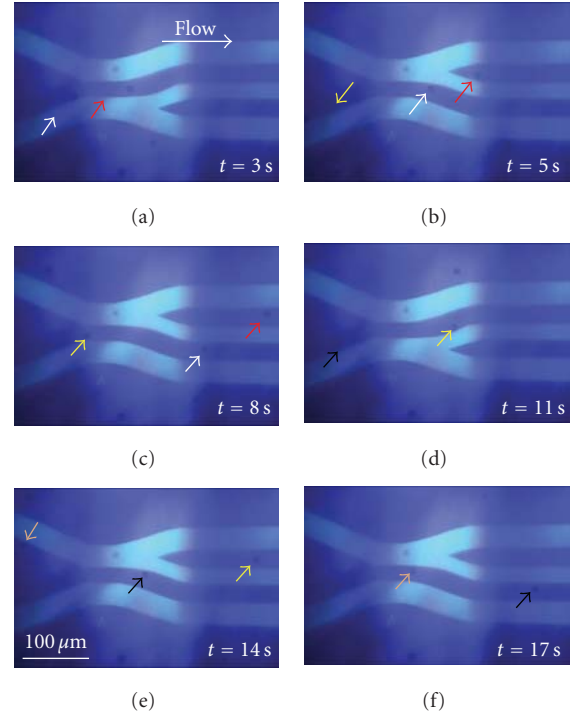


FIGURE 6: (a)–(f) The microparticle selection process. The microparticles with the velocity of  $100 \mu\text{m/s}$  are selected toward different downstream channel by our designed light pattern.

on the touch panel screen to trigger operation mode switch. Figures 6(a)–6(f) demonstrate the switch and selection process for different microparticles. The beads indicated by yellow, black, and orange colors are arranged in order to the entrance and selected to different desired channels. These processes demonstrate that utilizing light pattern projecting onto the TiOPc chip to select desired mobile polystyrene bead provides a convenient platform for microparticle selection.

## 7. Optoelectronic Ladder Effect for Microparticle Sorting

Optoelectronic ladder effect is another application utilizing the virtual electrode to sort mobile microparticles. As a line-shape light pattern projected onto the TiOPc chip surface, a virtual electrode like a line is formed on the TiOPc surface, and a nonuniform electric field is generated in space. When a moving microparticle encounters this electric field, it would experience an either attracting or repelling DEP force. The force from liquid flow,  $F_{\text{Flow}}$ , drives the microparticle rightward. The second force,  $F_{\text{OET}}$ , acting on the microparticle is provided from the nonuniform electric field with the DEP direction perpendicular to the linear light pattern. The net force,  $F_{\text{Net}}$ , as illustrated in Figure 6(a) drives the microparticle toward the right-up direction along the virtual electrode, the linear light bar. Because the electric field distribution of the nonuniform electric field is three dimensions as shown in Figure 7, the microparticle is elevated to stride

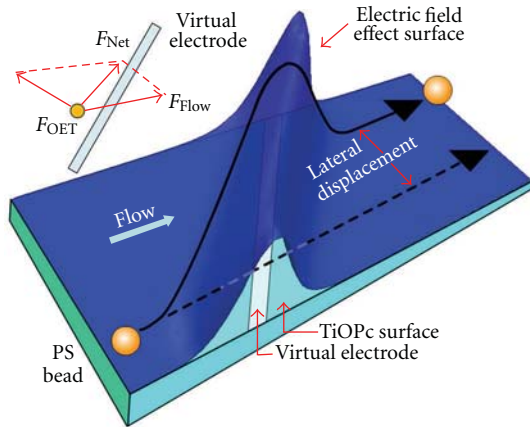


FIGURE 7: The simulation of nonuniform electric field distribution generated due to the linear light-induced virtual electrode pattern.

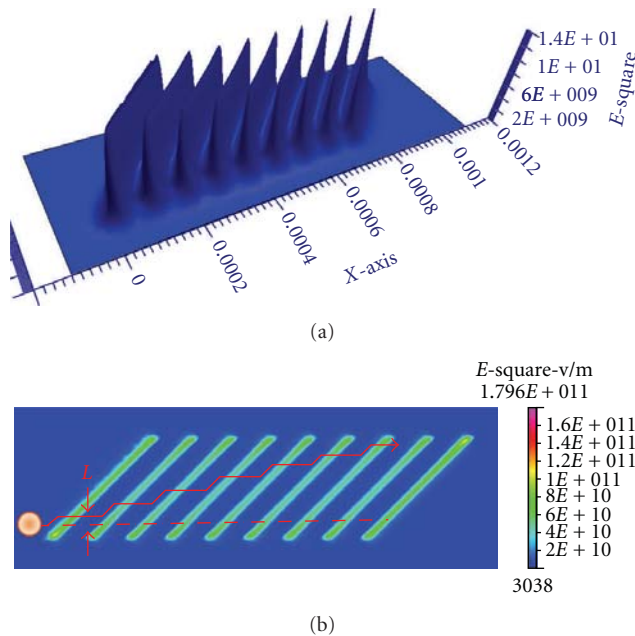


FIGURE 8: Electric field simulation for the optoelectronic ladder effect induced by the in-parallel slanting light bars. (a) Side view and (b) top view of the induced electric field distribution.

across the virtual electrode like climbing a mountain. As it passes and falls down to the TiOPc surface and keeps moving, this process generates a lateral displacement between the original and final moving directions.

Utilizing a series of slanting linear light image to generate three-dimensional nonuniform electric field for the lateral displacement of microparticles is the concept of our optoelectronic ladder effect. When a microparticle passes one light image, the microparticle particle has a one-step lateral displacement,  $L$ , between the original and the final moving direction. Several slanting linear light bars in parallel would enlarge these lateral displacements. The trace of the microparticle crossing over these series of in-parallel light images is just like a ladder. Figure 8(a) shows the simulation of

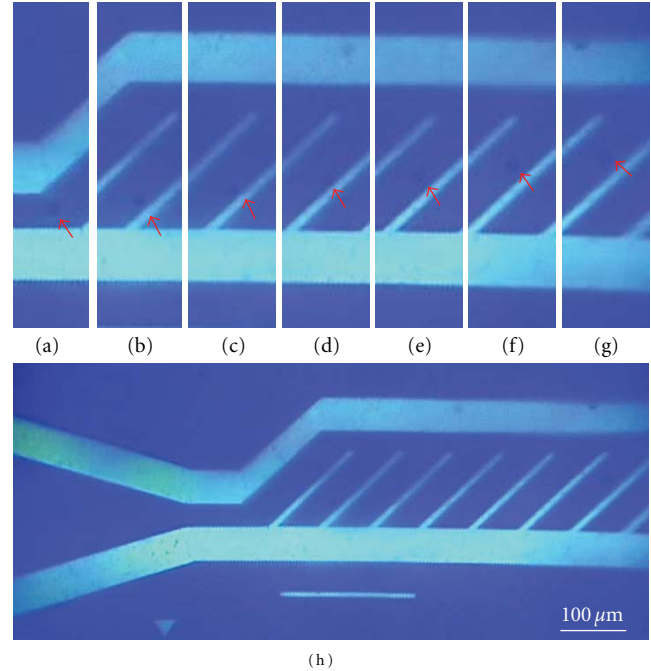


FIGURE 9: (a)–(g) The red arrow/dotted circle indicates the position of microparticle along the microchannel. The lateral displacement is enlarged by a series of DEP forces generated due to TiOPc-based light-induced dielectrophoresis. The time interval of each image is 0.5 sec. (h) The light image projected on the TiOPc surface.

electric field distribution for a series of slanting light-bar pattern, which is utilized to enlarge the lateral displacement of the microparticle. Figure 8(b) illustrates the moving trajectory of the microparticle when it passes the in-parallel slanting light-bar pattern. As the flow velocities are  $520 \mu\text{m/s}$ ,  $260 \mu\text{m/s}$ , and  $150 \mu\text{m/s}$ , the average lateral displacements of microparticles crossing the slating light bar are  $5.2 \mu\text{m}$ ,  $8.1 \mu\text{m}$ , and  $11.9 \mu\text{m}$ , respectively. The distance of lateral displacement could be assigned and tuned via the flow velocity.

The experimental recording for the trajectory of the moving microparticle experiencing the nonuniform electric field is shown in Figure 9(a)–9(g). Figure 9(h) is the light pattern projected on the TiOPc surface. The front part with the shape similar to a funnel is utilized to line up the microparticles to enter the entrance. While the microparticle moving rightward encounters the slanting light-bar image, the negative DEP force would push it upward to make a lateral distance between the original and the final direction. The red arrow/dotted circle indicates the microparticle position. The more slanting light bars more the microparticle passes, the more lateral displacement would be enlarged.

The microparticle lateral displacement is dominated by the TiOPc-based light-induced DEP force and the liquid flow driving force. Therefore, the tuning of the liquid flow would also influence the lateral displacement of the microparticle. The relationship between the lateral displacement and the flow velocity is characterized and shown in Figure 10. The time of the microparticle moving from TiOPc surface to the DEP-force-constrained height in the nonuniform electric

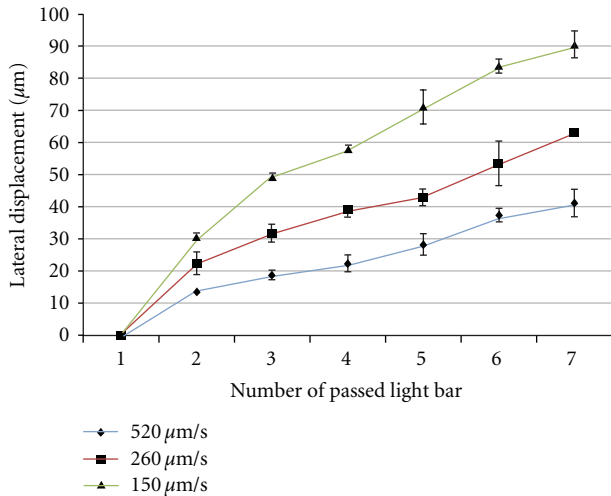


FIGURE 10: The relationship of lateral displacement in different flow velocity. The lateral displacement is enlarged in the low flow velocity.

field determines the lateral displacement. If the microparticle spends more time climbing the mountain-shape nonuniform electric field, the net force,  $F_{\text{net}}$ , has more time to act on it to generalize the larger lateral displacement. A mobile microparticle with the slow velocity would have a large lateral displacement. After passing seven slanting light bars, a microparticle with  $520 \mu\text{m/s}$  velocity has only  $40 \mu\text{m}$  lateral displacement. For a slow velocity,  $150 \mu\text{m/s}$ , its lateral displacement is  $90 \mu\text{m}$ .

## 8. Conclusions

We report the development of the moldless PEGDA-based optoelectrofluidic platform for the demonstration of microparticle selection. The negative DEP force is induced by the virtual electrode which is formed due to the illuminating light pattern. The application of the organic photoconductivity material, TiOPc, simplifies the chip fabrication process. PEGDA-based microchannel is embedded onto the TiOPc layer to provide the required liquid flow. The target mobile microparticle is able to be selected by the virtual switch. The different lateral displacements of a moving polystyrene particle encountering a series of slanting light bars under distinct flow velocity are measured. With this integration, this optoelectrofluidic platform provides a suitable approach to fabricate a microfluidic system on the TiOPc-based OET chip and to supply a functional manipulation of microparticle under the continuous flow.

## Acknowledgment

This research is financially sponsored by National Science Council (Grants nos. 98-2120-M-007-003 and NSC 99-2221-E-007-125-MY3). The authors extend special thanks to Professor Hwan-You Chang at Institute of Molecular Medicine, National Tsing Hua University for the biological

knowledge support. They also thank Professor Ming C. Wu at University of California, Berkeley, Prof. Pei-Yu Chiou at University of California, Los Angeles, and Professor Gwo-Bin Lee at National Tsing Hua University for sharing OET experience and helpful discussion.

## References

- [1] P. S. Dittrich and A. Manz, "Lab-on-a-chip: microfluidics in drug discovery," *Nature Reviews Drug Discovery*, vol. 5, no. 3, pp. 210–218, 2006.
- [2] A. Ashkin, J. M. Dziedzic, and T. Yamane, "Optical trapping and manipulation of single cells using infrared laser beams," *Nature*, vol. 330, no. 6150, pp. 769–771, 1987.
- [3] K. C. Neuman and S. M. Block, "Optical trapping," *Review of Scientific Instruments*, vol. 75, no. 9, pp. 2787–2809, 2004.
- [4] E. R. Dufresne and D. G. Grier, "Optical tweezer arrays and optical substrates created with diffractive optics," *Review of Scientific Instruments*, vol. 69, no. 5, pp. 1974–1977, 1998.
- [5] B. Sun, Y. Roichman, and D. G. Grier, "Theory of holographic optical trapping," *Optics Express*, vol. 16, no. 20, pp. 15765–15776, 2008.
- [6] J. R. Moffitt, Y. R. Chemla, S. B. Smith, and C. Bustamante, "Recent advances in optical tweezers," *Annual Review of Biochemistry*, vol. 77, no. 1, pp. 205–228, 2008.
- [7] D. G. Grier, "A revolution in optical manipulation," *Nature*, vol. 424, no. 6950, pp. 810–816, 2003.
- [8] R. Pethig, "Dielectrophoresis: status of the theory, technology, and applications," *Biomicrofluidics*, vol. 4, no. 2, article 022811, 35 pages, 2010.
- [9] C. Zhang, K. Khoshmanesh, A. Mitchell, and K. Kalantar-Zadeh, "Dielectrophoresis for manipulation of micro/nano particles in microfluidic systems," *Analytical and Bioanalytical Chemistry*, vol. 396, no. 1, pp. 401–420, 2010.
- [10] P. Y. Chiou, A. T. Ohta, and M. C. Wu, "Massively parallel manipulation of single cells and microparticles using optical images," *Nature*, vol. 436, no. 7049, pp. 370–372, 2005.
- [11] Y. S. Lu, Y. P. Huang, J. A. Yeh, C. Lee, and Y. H. Chang, "Controllability of non-contact cell manipulation by image dielectrophoresis (iDEP)," *Optical and Quantum Electronics*, vol. 37, no. 13–15, pp. 1385–1395, 2005.
- [12] H.-Y. Hsu, A. T. Ohta, P. Y. Chiou, A. Jamshidi, S. L. Neale, and M. C. Wu, "Phototransistor-based optoelectronic tweezers for dynamic cell manipulation in cell culture media," *Lab on a Chip*, vol. 10, no. 2, pp. 165–172, 2010.
- [13] A. T. Ohta, P. Y. Chiou, T. H. Han et al., "Dynamic cell and microparticle control via optoelectronic tweezers," *Journal of Microelectromechanical Systems*, vol. 16, no. 3, pp. 491–499, 2007.
- [14] A. T. Ohta, P. Y. Chiou, H. L. Phan et al., "Optically controlled cell discrimination and trapping using optoelectronic tweezers," *IEEE Journal on Selected Topics in Quantum Electronics*, vol. 13, no. 2, pp. 235–242, 2007.
- [15] A. T. Ohta, M. Garcia, J. K. Valley et al., "Motile and non-motile sperm diagnostic manipulation using optoelectronic tweezers," *Lab on a Chip*, vol. 10, no. 23, pp. 3213–3217, 2010.
- [16] M. Hoeb, J. O. Rädler, S. Klein, M. Stutzmann, and M. S. Brandt, "Light-induced dielectrophoretic manipulation of DNA," *Biophysical Journal*, vol. 93, no. 3, pp. 1032–1038, 2007.
- [17] P.-Y. Chiou, A. T. Ohta, A. Jamshidi, H. Y. Hsu, and M. C. Wu, "Light-actuated AC electroosmosis for nanoparticle manipulation," *Journal of Microelectromechanical Systems*, vol. 17, no. 3, pp. 525–531, 2008.

- [18] A. Jamshidi, P. J. Pauzauskie, P. J. Schuck et al., "Dynamic manipulation and separation of individual semiconducting and metallic nanowires," *Nature Photonics*, vol. 2, no. 2, pp. 86–89, 2008.
- [19] A. T. Ohta et al., "Trapping and transport of silicon nanowires using lateral-field optoelectronic tweezers," in *Proceedings of the Conference on Lasers and Electro-Optics (CLEO '07)*, 2007.
- [20] A. T. Ohta, S. L. Neale, H. Y. Hsu, J. K. Valley, and M. C. Wu, "Parallel assembly of nanowires using lateral-field optoelectronic tweezers," in *Proceedings of the 2008 IEEE/LEOS International Conference on Optical MEMS and Nanophotonics (OPT MEMS '10)*, pp. 7–8, August 2008.
- [21] M.-C. Tien, A. T. Ohta, K. Yu, S. L. Neale, and M. C. Wu, "Heterogeneous integration of InGaAsP microdisk laser on a silicon platform using optofluidic assembly," *Applied Physics A*, vol. 95, no. 4, pp. 967–972, 2009.
- [22] A. Khademhosseini, G. Eng, J. Yeh et al., "Micromolding of photocrosslinkable hyaluronic acid for cell encapsulation and entrapment," *Journal of Biomedical Materials Research*, vol. 79, no. 3, pp. 522–532, 2006.
- [23] D. T. Chiu, N. L. Jeon, S. Huang et al., "Patterned deposition of cells and proteins onto surfaces by using three-dimensional microfluidic systems," *Proceedings of the National Academy of Sciences of the United States of America*, vol. 97, no. 6, pp. 2408–2413, 2000.
- [24] J. Fukuda, A. Khademhosseini, Y. Yeo et al., "Micromolding of photocrosslinkable chitosan hydrogel for spheroid microarray and co-cultures," *Biomaterials*, vol. 27, no. 30, pp. 5259–5267, 2006.
- [25] J. W. Nichol, S. T. Koshy, H. Bae, C. M. Hwang, S. Yamanlar, and A. Khademhosseini, "Cell-laden microengineered gelatin methacrylate hydrogels," *Biomaterials*, vol. 31, no. 21, pp. 5536–5544, 2010.
- [26] Y. S. Hwang, G. C. Bong, D. Ortmann, N. Hattori, H. C. Moeller, and A. Khademhosseini, "Microwell-mediated control of embryoid body size regulates embryonic stem cell fate via differential expression of WNT5a and WNT11," *Proceedings of the National Academy of Sciences of the United States of America*, vol. 106, no. 40, pp. 16978–16983, 2009.
- [27] H. C. Moeller, M. K. Mian, S. Shrivastava, B. G. Chung, and A. Khademhosseini, "A microwell array system for stem cell culture," *Biomaterials*, vol. 29, no. 6, pp. 752–763, 2008.
- [28] J. A. Burdick and K. S. Anseth, "Photoencapsulation of osteoblasts in injectable RGD-modified PEG hydrogels for bone tissue engineering," *Biomaterials*, vol. 23, no. 22, pp. 4315–4323, 2002.
- [29] Y. Du, E. Lo, S. Ali, and A. Khademhosseini, "Directed assembly of cell-laden microgels for fabrication of 3D tissue constructs," *Proceedings of the National Academy of Sciences of the United States of America*, vol. 105, no. 28, pp. 9522–9527, 2008.
- [30] A. Revzin, R. J. Russell, V. K. Yadavalli et al., "Fabrication of poly(ethylene glycol) hydrogel microstructures using photolithography," *Langmuir*, vol. 17, no. 18, pp. 5440–5447, 2001.
- [31] C. M. Hwang, W. Y. Sim, S. H. Lee et al., "Benchtop fabrication of PDMS microstructures by an unconventional photolithographic method," *Biofabrication*, vol. 2, no. 4, Article ID 045001, 2010.
- [32] G.-B. Lee, Y. H. Lin, W. Y. Lin, W. Wang, and T. F. Guo, "Optically-induced dielectrophoresis using polymer materials for biomedical applications," in *Proceedings of the The 15th International Conference on Solid-State Sensors, Actuators and Microsystems (TRANSDUCERS '09)*, pp. 2135–2138, June 2009.
- [33] S. M. Yang, T. M. Yu, H. P. Huang, M. Y. Ku, L. Hsu, and C. H. Liu, "Dynamic manipulation and patterning of microparticles and cells by using TiOPc-based optoelectronic dielectrophoresis," *Optics Letters*, vol. 35, no. 12, pp. 1959–1961, 2010.
- [34] R. Pethig, "Dielectrophoresis: using inhomogeneous AC electrical fields to separate and manipulate cells," *Critical Reviews in Biotechnology*, vol. 16, no. 4, pp. 331–348, 1996.
- [35] T. B. Jones, "Basic theory of dielectrophoresis and electrorotation," *IEEE Engineering in Medicine and Biology Magazine*, vol. 22, no. 6, pp. 33–42, 2003.
- [36] C.-T. Ho, R. Z. Lin, W. Y. Chang, H. Y. Chang, and C. H. Liu, "Rapid heterogeneous liver-cell on-chip patterning via the enhanced field-induced dielectrophoresis trap," *Lab on a Chip*, vol. 6, no. 6, pp. 724–734, 2006.
- [37] B. H. Lapizco-Encinas and M. Rito-Palomares, "Dielectrophoresis for the manipulation of nanobiotparticles," *Electrophoresis*, vol. 28, no. 24, pp. 4521–4538, 2007.
- [38] Y.-H. Lin and G.-B. Lee, "Optically induced flow cytometry for continuous microparticle counting and sorting," *Biosensors and Bioelectronics*, vol. 24, no. 4, pp. 572–578, 2008.
- [39] J. K. Valley, S. Neale, H. Y. Hsu, A. T. Ohta, A. Jamshidi, and M. C. Wu, "Parallel single-cell light-induced electroporation and dielectrophoretic manipulation," *Lab on a Chip*, vol. 9, no. 12, pp. 1714–1720, 2009.